

**Dynamics of Transneptunian Objects under the Influence of  
a Rogue Planet**

by

Yukun Huang

B.S., Harbin Institute of Technology, China, 2016

M.S., Tsinghua University, China, 2019

A THESIS SUBMITTED IN PARTIAL FULFILLMENT  
OF THE REQUIREMENTS FOR THE DEGREE OF

**Doctor of Philosophy**

in

THE FACULTY OF GRADUATE AND POSTDOCTORAL STUDIES  
(Astronomy)

The University of British Columbia  
(Vancouver)

July 2023

© Yukun Huang, 2023

The following individuals certify that they have read, and recommend to the Faculty of Graduate and Postdoctoral Studies for acceptance, the thesis entitled:

**Dynamics of Transneptunian Objects under the Influence of a Rogue Planet**

submitted by Yukun Huang in partial fulfillment of the requirements for the degree of Doctor of Philosophy in Astronomy.

**Examining Committee:**

Brett Gladman, Professor, Department of Physics and Astronomy, UBC  
*Supervisor*

Aaron Boley, Associate Professor, Department of Physics and Astronomy, UBC  
*Supervisory Committee Member*

J.J. Kavelaars, Adjunct Professor, Department of Physics and Astronomy, University of Victoria  
*Supervisory Committee Member*

Jess McIver, Assistant Professor, Department of Physics and Astronomy, UBC  
*Supervisory Committee Member*

Joerg Rottler, Professor, Department of Physics and Astronomy, UBC  
*Supervisory Committee Member*

Paul Hickson, Professor, Department of Physics and Astronomy, UBC  
*University Examiner*

Takamasa Momose, Professor, Department of Chemistry, UBC  
*University Examiner*

# Abstract

Over the past two decades, our knowledge of the Solar System’s transneptunian region (often called the Kuiper Belt) has been gradually increasing. Observational surveys have greatly expanded the inventory of Trans-Neptunian Objects (TNO), which are distant icy bodies thought to be relics from the giant planet formation era.

In the main Kuiper Belt region, a complex bimodal inclination structure is present, leading to the common assertion that current TNOs may have accreted in different regions of the protoplanetary disk. To study this blended inclination structure, I develop an improved semi-analytical method to compute TNO ‘free’ inclinations, which are well conserved and thus better represent the primordial inclination profile.

In the implanted Kuiper Belt, a semimajor axis power law distribution is observed in the outer Solar System surveys. I show that in a patched-conic model, the power law is a natural outcome after multiple flybys of the perturbing planet homogenize the directions of planetary relative-velocity vectors. This model allows one to analytically compute the diffusion coefficient in closed form.

In the distant Kuiper Belt, several striking features seem to challenge our previous understanding of the early Solar System: 1) a very large population of objects in distant mean-motion resonances with Neptune, 2) a substantial detached population that are not dynamically coupled with Neptune’s effects, and 3) the existence of three very-large perihelion objects. I demonstrated in this thesis, that a super-Earth-mass planet temporarily present in the Solar System on a Neptune crossing orbit (referred to as a ‘Rogue Planet’), is able to create all these structures in the distant Kuiper Belt. Such a planet would have formed in the giant planet region

and gotten scattered to a highly-eccentric orbit with a few hundred au semimajor axis with a typical lifetime of 100 Myr. Additionally, I showed this transient planet would not have heated the cold belt's very low free inclinations to larger than observed. Both the structures in the distant belt and the existence of an unheated cold belt provide constraints to narrow down the mass and possible dynamical histories the rogue might have taken.

# Lay Summary

My thesis proposes a hypothesis that a rogue planet existed in the early Solar System to explain puzzling features in the observable Kuiper Belt (a band of objects orbiting beyond Neptune). This planet was most likely a planet the size of the Earth formed between the giant planets and then ejected to a distant orbit where its gravity sculpted the orbits of small celestial bodies. By simulating the evolutions of transneptunian objects under the influence of this temporarily-present rogue planet, I demonstrate that it could explain their spatial distribution. This research sheds new light on the early history of our Solar System and provides a possible explanation for some of the mysteries in the Kuiper Belt. The findings of this thesis may also inspire future astronomical discoveries in the uncharted territory of the Solar System.

# Preface

The text of this dissertation includes a combination of the author's original studies and modified reprints of previously published material.

## Chapter 1 (introduction):

This chapter introduces the scientific background of Solar System's known structures, as well as the analytical and numerical tools that I utilized throughout this dissertation. The GLISSER integrator, the main numerical N-body integrator I used in this thesis, was mainly developed by Kevin Zhang (then an undergraduate student at UBC) and Brett Gladman (Zhang & Gladman, 2022). I contributed to the integrator by improving its planetary orbit interpolation algorithm, extending its capability to write out close encounters, and fixing several bugs in the original code.

## Chapter 2 (published):

- Y. Huang, B. Gladman & K. Volk, *Free Inclinations for Trans-Neptunian Objects in the Main Kuiper Belt*. The Astrophysical Journal Supplement Series **259**, 2 (2022)

This paper presents a robust method to accurately compute the constant free inclinations for cold classical Kuiper Belt objects. The original idea came out of Brett Gladman's experience at a TNO seminar, in which he found many Kuiper Belt observers and spectroscopists lacked a consensus of how to differentiate cold and hot classical Kuiper Belt objects through their inclinations. A superior way, however, is not using the ecliptic inclination but the free inclination, a constant quantity from the Laplace-Lagrange secular theory. This soon became a collaborative project be-

tween me, Brett Gladman, and Kat Volk (a planetary dynamicist at the Planetary Science Institute). Kat Volk carried out the numerical simulations for main-belt TNOs using a pre-existing pipeline. I wrote the code and manually inspected the orbital histories of 2,018 objects in order to categorize them based on their dynamical class. I tried different analytical methods to compute their free inclinations, and realized that because of the presence of a nearby secular resonance, the most robust and accurate way is to compute their precession rates by averaging the dominant Hamiltonian over two fast angles (the so-called ‘double average’ method). I then computed the free inclinations for the 2,018 TNOs and tabulated them in a datatable. I wrote the manuscript, with editing by Brett Gladman and Kat Volk, and produced all the figures. I also self-released a searchable datatable on my personal academic website ([link](#)), with which people can quickly find the free inclinations for objects they’re interested in.

### Chapter 3 (unpublished):

This chapter is an origin study by me and Brett Gladman. During my early numerical experiments on the rogue planet theory, Brett Gladman pointed out to me that the  $a^{-2.5}$  distribution observed in the current implanted population (Petit et al., 2011) was probably related to the power law in Levison & Duncan (1997)’s cometary dynamics simulations. Upon closer inspection of the literature, we realized the steady state was actually an  $a^{-1.5}$  power law in the number density (the  $r^{-2.5}$  power law in Levison & Duncan 1997 is actually a surface density, one index lower), which came from Yabushita (1980)’s exact solutions of a diffusion equation. This piqued my interest of finding a simple interpretation to the power law in summer 2022, when I soon realized that from the viewpoint of flyby dynamics, the  $a^{-1.5}$  power law is equivalent to a uniform distribution in the directions of incoming velocities  $\theta$ . I derived the equations, produced all the figures and wrote the chapter, with valuable guidance and edits from Brett Gladman. Sam Hadden (a postdoctoral researcher at the Canadian Institute for Theoretical Astrophysics) coincidentally also worked on a similar topic but from the perspective of a diffusion problem. Brett, Sam, and I had meaningful discussions during our visit at CITA, and Sam and I also had a meaningful discussion during his visit at UBC. Our works provide complementary ways to study the scattering dynamics and collectively, they depict

a broad picture to the cometary scattering problem.

**Chapter 4** (introduction):

This chapter introduces the scientific background of planetary formation theory and the early history of the Solar System.

**Chapter 5** (published):

- Y. Huang, B. Gladman, M. Beaudoin & K. Zhang, *A Rogue Planet Helps to Populate the Distant Kuiper Belt*. *The Astrophysical Journal Letters* **938**, L23 (2022)

This paper presents a close inspection of the rogue planet's dynamical effect on populating resonant and detached TNOs in the  $a < 100$  au Kuiper Belt. The idea for this project came from my preliminary numerical experiments with the rogue planet in 2021. I showed that in simulations with the rogue planet, vertical spikes appear on the  $a - q$  plot which clearly correspond to neptunian resonances. I carried out more GLISSER simulations and demonstrated that it is the rogue planet's encounter effect that help populate the  $a < 100$  au Kuiper Belt. I derived analytical estimates for the rogue's encounter frequency and the semimajor axis change it induces. Meanwhile, UBC undergraduate student Matthew Beaudoin was working with Brett on a separate project about the perihelion distribution and population estimate of the detached TNOs. I provided Matthew with the orbital distribution of the distant Kuiper generated from my rogue planet simulation, which helped him improve his population estimate. He also provided me with the code to quickly simulate detections from an intrinsic model using the OSSOS survey simulator (Lawler et al., 2018b), which I used to validate my own simulation. I wrote the majority of the manuscript, with major edits and improvements done by Brett Gladman to suit the format of an ApJ Letter. I also produced all the figures and animations.

**Chapter 6** (unpublished):

This chapter is an origin study by me and Brett Gladman and is the main investigation of the rogue planet's dynamical history and parameters. The idea of explaining high- $q$  detached bodies with a temporarily-present planet was first hypothesized in Gladman et al. (2002) and demonstrated in Gladman & Chan (2006).

Brett brought up this hypothesis during my PhD interview in 2018, and it quickly piqued my curiosity after I arrived at UBC and was deciding on my thesis project with Brett. While working on the new dynamical phenomenon we found in Chapter 5, I also started numerically experimenting with the rogue planet’s history using the REBOUND package (Rein & Liu, 2012). I used REBOUNDX (Tamayo et al., 2019) to model planetary migrations. Subsequent test particle simulations showing the dynamical sculpting induced by the rogue were also carried out by me with GLISSER. I wrote the entire chapter, derived analytical constraints, produced all the figures and tables, presented the rogue planet model, and performed all the analyses. Brett Gladman provided helpful comments and suggestions on the text and figures. Matthew Beaudoin’s script was used to simulate detections with the OSSOS survey simulator (Lawler et al., 2018b).

# Table of Contents

<b>Abstract</b> . . . . .	<b>iii</b>
<b>Lay Summary</b> . . . . .	<b>v</b>
<b>Preface</b> . . . . .	<b>vi</b>
<b>Table of Contents</b> . . . . .	<b>x</b>
<b>List of Tables</b> . . . . .	<b>xiv</b>
<b>List of Figures</b> . . . . .	<b>xv</b>
<b>List of Abbreviations</b> . . . . .	<b>xix</b>
<b>List of Symbols</b> . . . . .	<b>xxi</b>
<b>Acknowledgments</b> . . . . .	<b>xxiv</b>
<b>Dedication</b> . . . . .	<b>xxvi</b>
<b>1 Introduction</b> . . . . .	<b>1</b>
1.1 Celestial Mechanics Tools . . . . .	<b>1</b>
1.1.1 Orbital Elements . . . . .	<b>2</b>
1.1.2 Hamiltonian Formalism . . . . .	<b>6</b>
1.1.3 Restricted Three-Body Problem . . . . .	<b>8</b>
1.1.4 Mean-Motion Resonances . . . . .	<b>10</b>
1.1.5 Secular Resonances . . . . .	<b>12</b>

1.2	Numerical Tools . . . . .	16
1.2.1	Solar System Small-Body Integrators . . . . .	16
1.2.2	The GLISSER Integrator . . . . .	18
1.3	The Known Structures of the Solar System . . . . .	23
1.3.1	Small Body Populations Inside the Orbit of Neptune . . . . .	24
1.3.2	Transneptunian Space . . . . .	26
1.3.3	Oort Cloud and Comets . . . . .	29
1.3.4	Other Stable Niches in the Solar System . . . . .	31
1.4	Thesis Outline . . . . .	32
<b>2</b>	<b>Free Inclinations for TNOs in the Main Kuiper Belt . . . . .</b>	<b>34</b>
2.1	Introduction . . . . .	35
2.2	Computation of Free Inclinations . . . . .	38
2.2.1	Dynamical Classification of TNOs . . . . .	38
2.2.2	Free Inclination with the Correct Precession Rate . . . . .	40
2.2.3	Free Inclination Results . . . . .	47
2.3	Discussion . . . . .	52
2.4	Data Release . . . . .	55
<b>3</b>	<b>Steady-state Distribution of the Scattering Disk . . . . .</b>	<b>58</b>
3.1	Comet Dynamics and the Diffusion Approximation . . . . .	59
3.2	A Patched-Conic Point of View . . . . .	64
3.3	Estimating the Relaxation Time . . . . .	74
3.4	Comparison with Numerical Simulations . . . . .	80
3.5	Discussion . . . . .	85
<b>4</b>	<b>Introduction to the Early history of the Solar System . . . . .</b>	<b>88</b>
4.1	Planetesimals . . . . .	89
4.2	Planet Formation . . . . .	92
4.3	Planetary Migration . . . . .	94
4.3.1	Gas-Driven Migration . . . . .	94
4.3.2	Planetesimal-Driven Migration . . . . .	96
4.3.3	Planetary Instability . . . . .	100
4.4	Stellar Environment . . . . .	102

4.5	Additional Planets . . . . .	105
4.5.1	Still-Existing planets . . . . .	106
4.5.2	Rogue planets . . . . .	108
4.6	Important Metrics of an Outer Solar System Model . . . . .	110
<b>5</b>	<b>A Rogue Planet Helps to Populate the Distant Kuiper Belt . . . . .</b>	<b>115</b>
5.1	Introduction . . . . .	116
5.2	Dynamics from the 4 Giant Planets . . . . .	118
5.3	Dynamical Effects Induced by the Rogue Planet . . . . .	121
5.4	Estimating Observation Bias . . . . .	127
5.5	Discussion . . . . .	128
<b>6</b>	<b>Rogue Planet Parameters . . . . .</b>	<b>133</b>
6.1	Dynamics Induced by an Distant Rogue Planet . . . . .	134
6.1.1	Rogue Encounters . . . . .	134
6.1.2	Secular Effect . . . . .	136
6.1.3	Analytical Constraints from the Making of Sednoids . . . . .	146
6.1.4	Analytical Constraints from the Cold Classical Belt . . . . .	150
6.2	Planetary simulations with rogue planet(s) . . . . .	155
6.2.1	Rogues Scattered by Neptune . . . . .	156
6.2.2	Rogues Scattered by Saturn . . . . .	164
6.3	GLISSER Simulations with a Rogue Planet . . . . .	170
6.3.1	Reference Simulations . . . . .	170
6.3.2	Uranus-coupled Distant Rogue Planet . . . . .	175
6.3.3	Neptune-coupled Distant Rogue Planet . . . . .	180
6.4	The Rogue Planet Model . . . . .	184
6.4.1	Detached Objects with $a = 48\text{--}200$ au . . . . .	186
6.4.2	Other Implanted Populations within $a < 200$ au . . . . .	190
6.4.3	Detached Objects with $a > 200$ au, the ‘Iceberg’ Population .	193
6.4.4	Stability of the Cold Classical Belt . . . . .	198
6.4.5	Orbital Clustering . . . . .	200
6.5	Discussion . . . . .	203
<b>7</b>	<b>Future Work . . . . .</b>	<b>207</b>

<b>A GLISSER Validation of Performance</b>	<b>237</b>
A.1 Validation of the GLISSER Integrator	237
A.2 Efficiency Comparison Between GLISSER and Other Integrators	240
<b>B Dynamical Effects of Rogue Encounters</b>	<b>243</b>
B.1 Encounter Frequency from a Highly-Eccentric Planet	243
B.2 Orbital Element Changes Due to Rogue Encounters	245

# List of Tables

Table 2.1	Barycentric elements and $I_{\text{free}}$ for main-belt TNOs . . . . .	56
Table 2.2	$q, p$ components of the forcing pole for various orbital elements . .	57
Table 3.1	Relaxation time $t_R$ for planets in the Solar System . . . . .	78
Table 4.1	barycentric orbital elements of TNO with $a > 200$ au and $q >$ 38 au. . . . .	104
Table 4.2	Comparison between different outer Solar System formation hy- potheses . . . . .	114
Table 6.1	Implantation (or retention) fractions for each TNO population in the rogue planet model (Figure 6.28) and their relative ratios .	186
Table 6.2	Comparison between different outer Solar System formation hy- potheses . . . . .	206
Table A.1	Comparison between SWIFT, MERCURY, and GLISSER on differ- ent machines . . . . .	242

# List of Figures

Figure 1.1	Keplerian orbits with different eccentricities . . . . .	3
Figure 1.2	Spacial orientation of the elliptic orbit . . . . .	4
Figure 1.3	Circular restricted three-body problem in the co-rotating frame	9
Figure 1.4	5:2 mean-motion resonance with Neptune . . . . .	13
Figure 1.5	Secular resonance . . . . .	15
Figure 1.6	GLISSER Flowchart . . . . .	19
Figure 1.7	Comparison of the orbital distributions of 1,000 test particles using MERCURY and GLISSER . . . . .	21
Figure 1.8	80,000 test particles integration with GLISSER . . . . .	22
Figure 1.9	Known TNOs with dynamical classifications . . . . .	27
Figure 2.1	Free inclination diagram . . . . .	42
Figure 2.2	Inclination evolutions of a TNO near the $\nu_{18}$ secular resonance .	46
Figure 2.3	$I_{\text{free}}$ for each TNO as a function of $a$ . . . . .	48
Figure 2.4	$I_{\text{free}}$ evolution of a classical and a resonant TNO . . . . .	49
Figure 2.5	$\Delta I_{\text{free}}$ measured across 4 Gyr as a function of $a$ . . . . .	51
Figure 2.6	Free inclinations and ecliptic inclinations histogram . . . . .	54
Figure 3.1	Diffusion model diagram . . . . .	60
Figure 3.2	Diffusion timescales . . . . .	63
Figure 3.3	Planet-crossing scheme diagram . . . . .	65
Figure 3.4	Close encounter diagram . . . . .	67
Figure 3.5	Velocity vectors before and after a planetary close flyby . . . . .	68
Figure 3.6	Dimensionless semimajor axis $a$ as a function of $\theta$ . . . . .	69

Figure 3.7	Constant Tisserand lines on the $a$ - $q$ space . . . . .	70
Figure 3.8	Dynamical evolution of a Neptune-scattered test particle . . . . .	72
Figure 3.9	Gravitational focusing diagram . . . . .	76
Figure 3.10	Relaxation time $t_R$ estimates as a function of the Tisserand parameter $\mathcal{T}$ . . . . .	80
Figure 3.11	Snapshots . . . . .	82
Figure 3.12	Time evolution of the $a$ distribution power law index for an external scattering disk of Neptune . . . . .	83
Figure 3.13	Time evolution of the $a$ distribution power law index for an external scattering disk of Jupiter . . . . .	84
Figure 4.1	Proplyds in the Orion Nebula (HST image) . . . . .	89
Figure 4.2	Composite image of Arrokoth from New Horizons spacecraft data . . . . .	91
Figure 4.3	The outward migrations of Neptune and its outer mean-motion resonances . . . . .	99
Figure 5.1	$a, q, i$ distributions of TNOs at 100 Myr in the reference simulation . . . . .	119
Figure 5.2	$a, q, i$ distributions and histograms of test particles under 100-Myr gravitational influences of a $2 M_{\oplus}$ rogue . . . . .	121
Figure 5.3	Dynamical evolutions of two particles initially near the 4:1 resonance . . . . .	123
Figure 5.4	$a, q, i$ distributions of the detached, the simulated detections, and the real $q > 38$ au detached objects . . . . .	126
Figure 5.5	Orbital excitation of the cold classical Kuiper Belt by a rogue planet . . . . .	130
Figure 6.1	Estimate the excitations of the cold classical belt with rogue encounters . . . . .	135
Figure 6.2	Apsidal precession period $P_{\varpi}$ for objects in the distant Kuiper Belt . . . . .	138
Figure 6.3	$q - \Delta\varpi$ phase-space portraits for distant TNOs ( $a < a_r$ ) under the presence of an additional rogue planet . . . . .	141

Figure 6.4	$q - \Delta\varpi$ phase-space portraits for distant TNOs ( $a > a_r$ ) with the presence of an additional rogue planet . . . . .	142
Figure 6.5	Comparison between analytical estimates of $q$ raising and the numerical simulation with a $2M_{\oplus}$ rogue . . . . .	147
Figure 6.6	Comparison between analytical estimates of $q$ raising and the numerical simulation with a $5M_{\oplus}$ rogue . . . . .	148
Figure 6.7	Timescales for making the three Sednoids . . . . .	151
Figure 6.8	Timescales for overheating the cold classical Kuiper Belt . . . . .	152
Figure 6.9	Histogram of the dynamical lifetimes of the rogue planet when initially coupled with Neptune . . . . .	157
Figure 6.10	Planetary evolution histories of the four giant planets and a scattering rogue planet (Sim-N-1) . . . . .	158
Figure 6.11	Planetary evolution histories of the four giant planets and a scattering rogue planet (Sim-N-2) . . . . .	160
Figure 6.12	Scatter plot showing statistics of Sim-N-2 . . . . .	161
Figure 6.13	GLISSER simulation snapshots showing the destruction of the cold classical belt by a Neptune-scattered rogue. . . . .	163
Figure 6.14	Scatter plot showing statistics of Sim-S-1 and Sim-S-2 . . . . .	165
Figure 6.15	Planetary evolution histories of the four giant planets and two scattering rogue planets (Sim-S-1) . . . . .	167
Figure 6.16	Planetary evolution histories of the four giant planets and two scattering rogue planets (Sim-S-2) . . . . .	168
Figure 6.17	$a, q, i$ distributions of TNOs in the reference simulation (replotted) . . . . .	171
Figure 6.18	Dynamical history of the four giant planets in a two-stage eccentric migration simulation. . . . .	173
Figure 6.19	$a, q, i$ distributions of TNOs in a reference migration simulation	174
Figure 6.20	Planetary history of the first Uranus-coupled rogue planet simulation (Sim-U-Mig-1) . . . . .	176
Figure 6.21	$a, q, i$ distributions of TNOs in Sim-U-Mig-1 . . . . .	177
Figure 6.22	Planetary history of the second Uranus-coupled rogue planet simulation (Sim-U-Mig-2) . . . . .	178
Figure 6.23	$a, q, i$ distributions of TNOs in Sim-U-Mig-2 . . . . .	179

Figure 6.24	Planetary history of the first Neptune-coupled rogue planet simulation (Sim-N-Mig-1) . . . . .	181
Figure 6.25	$a, q, i$ distributions of TNOs in Sim-N-Mig-1 . . . . .	182
Figure 6.26	Planetary history of the second Neptune-coupled rogue planet simulation (Sim-N-Mig-2) . . . . .	183
Figure 6.27	$a, q, i$ distributions of TNOs in Sim-N-Mig-1 . . . . .	184
Figure 6.29	$a, q, i$ distributions of the detached, the simulated detections based on the rogue planet model, and detached objects discovered by OSSOS . . . . .	188
Figure 6.30	$a$ histogram of the implanted population from 40 au to 200 au .	192
Figure 6.31	$a, q, i$ distributions of the intrinsic ‘iceberg’ population, the simulated detections, and the real detached objects . . . . .	196
Figure 6.32	The preservation of an underheated cold classical belt in the rogue planet model . . . . .	199
Figure 6.33	Distributions of $\varpi$ and $\Omega$ at 4 Gyr for iceberg TNOs . . . . .	200
Figure 6.34	Rewinding the longitudes of perihelion ( $\varpi$ ) of three Sednoids back to 4 Gyr ago shows the primordial orbital clustering . . . . .	202
Figure A.1	A GLISSER simulation with an Earth-scattered particle showing the conservation of the Jacobi constant and the Tisserand parameter for 100 kyr . . . . .	238
Figure A.2	A GLISSER simulation with an Neptune-scattered particle showing the conservation of the Tisserand parameter for 100 kyr . .	239
Figure A.3	Comparison between GLISSER and SWIFT for a 3:2 resonant TNO with Neptune. . . . .	239
Figure A.4	Comparison between GLISSER and SWIFT for a 5:2 resonant TNO with Neptune. . . . .	240

# List of Abbreviations

**3D** Three-Dimensional

**CFEPS** Canada-France Ecliptic Plane Survey

**CLASSY** Classical and Large-a Distant Solar SYstem

**CPU** Central Processing Unit

**CRTBP** Circular Restricted Three-Body Problem

**DES** Dark Energy Survey

**GLISSE** GPU Long-term Integrator for Solar System Evolution

**GLISSER** GPU Long-term Integrator for Solar System Evolution: Regularized

**GPU** Graphics Processing Unit

**HST** Hubble Space Telescope

**IAU** International Astronomical Union

**IOC** Inner Oort Cloud

**JFC** Jupiter-Family Comets

**JPL SBDB** Jet Propulsion Laboratory Small-Body DataBase

**KBO** Kuiper Belt Objects

**LHB** Late Heavy Bombardment

**LPC** Long-Period Comets

**LSST** Legacy Survey of Space and Time

**MMR** Mean-Motion Resonance

**MPC** Minor Planet Center

**MVS** Mixed Variable Symplectic

**NEO** Near Earth Objects

**OSSOS** Outer Solar System Origins Survey

**RMVS** Regularized Mixed Variable Symplectic

**RTBP** Restricted Three-Body Problem

**SPC** Short-Period Comets

**TNO** Trans-Neptunian Objects

# List of Symbols

- au** - Astronomical unit. Roughly the distance from Earth to the Sun. Defined as exactly 149,597,870,700 meters.
- yr** - Year. 365.25 days or 31,557,600 seconds.
- kyr** - A thousand years.  $10^3$  yr.
- Myr** - A million years.  $10^6$  yr.
- Gyr** - A billion years (or a Giga year).  $10^9$  yr.
- $\mathcal{G}$**  - Gravitational constant.  $6.67430 \times 10^{-11} \text{ m}^3 \text{ kg}^{-1} \text{ s}^{-2}$ .
- $M_{\oplus}$**  - The mass of the Earth.  $5.97219 \times 10^{24} \text{ kg}$ .
- $M_{\odot}$**  - The mass of the Sun.  $1.9886 \times 10^{30} \text{ kg}$ .
- $R_{\oplus}$**  - The radius of the Earth. 6,378.1 km.
- $R_{\odot}$**  - The radius of the Sun. 695,500 km.
- $\mu$**  - Gravitational parameter. Defined as  $\mu = \mathcal{G}M$ , where  $M$  is the mass of the central body.
- $a$**  - Semimajor axis of an orbit. Defined as half of the longest diameter of an ellipse.
- $e$**  - Eccentricity, which is a measure of how much a conic section deviates from being circular. A perfect circle has  $e = 0$ , and ellipse has  $0 < e < 1$ , a parabolic orbit has  $e = 1$ , and a hyperbolic orbit has  $e > 1$ .
- $q$**  - Pericenter distance. Pericenter (also called perihelion for orbits around the Sun in our solar system) is the point of the conic section orbit where the object is closest to the central body.  $q = a(1 - e)$ .
- $Q$**  - Apocenter distance. Apocenter (also called aphelion for orbits around the Sun in our solar system) is the point of the elliptical orbit where the object is farthest to the central body.  $Q = a(1 + e)$ .
- $i$**  - The inclination of the plane of an orbit to a reference plane. For objects in our

solar system, the reference plane is the ecliptic plane, which is the plane through Earth's orbit around the Sun. A prograde orbit has  $i < 90^\circ$  and a retrograde orbit has  $i > 90^\circ$ .

$I_{\text{free}}$  - Free inclination. A conserved inclination quantity independent of the chosen reference frame.

$\Omega$  - The longitude of the ascending node. The angle from the reference direction (this is the vernal equinox direction in the solar system) to where the orbit passes upward through the reference plane, measured in the reference plane.

$\omega$  - The argument of pericenter. The angle from the ascending node of the orbit to its location of pericenter, measured in the direction of motion.

$\varpi$  - The longitude of pericenter. Defines as  $\varpi = \omega + \Omega$  for prograde orbits and  $\varpi = \omega - \Omega$  for retrograde orbits.

$P$  - The orbital period. Defined as the amount of time a give object takes to complete one orbit.  $P = 2\pi \sqrt{\frac{a^3}{GM_\odot}}$  for solar system bodies.

$n$  - The mean motion. The angular speed required for a body to complete the orbit. Defined as  $n = \frac{2\pi}{P}$ .

$\mathcal{M}$  - The mean anomaly. A fictitious angle that describes the average change in position of an object over time and is defined by  $\frac{2\pi}{P} t_{\text{peri}}$ , where  $P$  is the orbital period, and  $t_{\text{peri}}$  is the time since the last pericenter passage.

$\lambda$  - The mean longitude. Define as  $\lambda = \mathcal{M} + \varpi$ .

$f$  - The true anomaly. The angle between the direction of the pericenter and the current position of the object.

$\epsilon$  - The specific orbital energy. Defined as  $\epsilon = -\frac{\mu}{2a}$ .

$R_H$  - The Hill sphere radius. For  $M_{\text{planet}}/M_\odot \ll 1$ , the sphere around a planet where the gravitational dominance of the planet exceeds that of the sun.  $R_H = r \sqrt[3]{\frac{M_{\text{planet}}}{3M_\odot}}$ .

$\mu'$  - Secondary to primary mass ratio in the Restricted Three-Body Problem (RTBP). Defined as  $\mu' = M_{\text{planet}}/(M + M_{\text{planet}})$ .

$\mathcal{C}_J$  - Jacobi integral in the Circular Restricted Three-Body Problem (CRTBP).

$\mathcal{T}$  - Tisserand parameter. A conserved quantity for a small body in CRTBP. This quantity has to be computed with respect to a certain planet (e.g. Neptune with the semimajor axis of  $a_N$ ), where  $\mathcal{T}_N = \frac{a_N}{a} + 2\sqrt{(1 - e^2)\frac{a}{a_N}} \cos i \approx \mathcal{C}_J$ .

$\varphi_{j:k}$  - The nominal resonant angle for the  $j:k$  mean-motion resonance.  $\varphi_{j:k} = j\lambda - k\lambda_{\text{planet}} - (j - k)\varpi$ .

- $g_i$  - The  $i$ -th eigenfrequency of the solar system related to the eccentricity solution.  
E.g.,  $g_5$  is the fifth  $e$  eigenfrequency.
- $f_i$  - The  $i$ -th eigenfrequency of the solar system related to the inclination solution.  
E.g.,  $f_8$  is the eighth  $i$  eigenfrequency.
- $\nu_i$  - The  $i$ -th eccentricity secular resonance of the solar system.
- $\nu_{1i}$  - The  $i$ -th inclination secular resonance of the solar system.
- $A$  - The expected  $\Omega$  precession rate of a small body in the solar system.
- $B$  - The expected  $\varpi$  precession rate of a small body in the solar system.
- $L$  - The first action of the canonical Delaunay variables.  $L = \sqrt{\mu a}$ .
- $G$  - The second action of the canonical Delaunay variables.  $G = L\sqrt{(1 - e^2)}$ .
- $H$  - The third action of the canonical Delaunay variables.  $H = G \cos i$ .
- $\mathcal{H}$  - Hamiltonian of a dynamical system.
- $H$ -magnitude - Absolute magnitude. The apparent magnitude an object would have if it were located in an equilateral triangle 1 au from the Sun and the Earth and at zero phase angle.

# Acknowledgments

I would like to express my sincere gratitude to my thesis advisor, Brett Gladman, for being the best mentor that I could have hoped for. An ancient Chinese quote from *Shi Shuo* (师说) by Han Yu (韩愈) says, “师者， 所以传道授业解惑也。”; which basically translates to “A teacher is one who transmits knowledge, provides for study, and dispels confusion”. Brett Gladman is a fantastic “老师” for fulfilling these duties (though he doesn’t read ancient Chinese) and patiently providing me with the support and opportunities I needed over the past four years. Furthermore, Brett Gladman is a very good friend of mine. Thank you for inviting me to your house; your culinary skills really impressed my picky stomach. Thank you for recommending all the magnificent galleries and museums in Italy; the “Renaissance tour” is still an unforgettable memory for me. Thank you for recommending *A Fire Upon the Deep* by Vernor Vinge, one of the best novels I have read in so many years.

Thank you to the Chinese Scholarship Counsel and Dr. Edwin S.H Leong for providing me with financial support.

Thank you to my supervisory committee members, Aaron Boley, J.J. Kavelaars, Jess McIver, and Joerg Rottler for providing support and guidance along the way.

Thank you to my colleagues Simone Hagey, Shiming Gu (顾时铭), Ryley Hill, Edward Ashton, and Simran Kaur for sharing exciting astronomy news (and cakes). Thank you to my co-authors Matthew Beaudoin and Kat Volk for their valuable work and discussions. Thank you to Kevin Zhang, without the first version of the Glisser integrator you developed, this thesis would not have been completed in time. Thank you to my good friend Jane Peng for spending time with me finding delicious food in Vancouver.

Thank you to my friends in Neptune, Snake, Kouren, 【BPC】 , Refl, Kanata,

and Tiger, and my friends in Uranus, Ying, carrot, Teru, Mero, and moe for chatting and playing party games with me. Thank you to all *Earthlings* in Nexus for always supporting the robot boy, no matter what planet he is exploring. Without all of you, I can hardly survive the lockdown.

Thank you to my parents for always being so supportive of my childhood dream of studying space and the universe.

Most importantly, thank you, Ben. Without your love (<3), understanding (T T), and curiosity (0 0), I could never have finished this thesis.

# Dedication

To Ben, for your curiosity.  
楚天寥阔，星宇参商。

# Chapter 1

## Introduction

The early Solar System was a chaotic environment, with multiple forces shaping the orbits of planets and small bodies in it. One intriguing possibility is that a ‘rogue planet’, temporarily present in the Solar System, could have played a role in shaping the current orbital structure of Trans-Neptunian Objects (TNO). This hypothesis is the focus of this thesis, which aims to investigate the dynamics of transneptunian objects under the influence of a rogue planet. By utilizing a combination of numerical simulations and analytical tools in celestial mechanics, my study sheds light on the potential impact of a rogue planet on the evolution of the Kuiper Belt and the formation of its observed structures. The results of this research will contribute to our understanding of the early Solar System and the role of rogue planets in shaping planetary systems. This thesis not only provides valuable insights into the dynamics of TNOs, but also constrains the parameter space of the hypothetical rogue planet, providing valuable information for future studies on rogue planets and their role in shaping planetary systems.

### 1.1 Celestial Mechanics Tools

My dissertation mainly involves the use of analytical and numerical methods to study the orbital distribution and dynamical evolution of TNO, for which a basic understanding of celestial mechanics is needed. In this section, I will briefly introduce the definition of orbital elements, the Hamiltonian formalism of celestial

mechanics, Mean-Motion Resonance (MMR), and secular resonance. I will refer to textbooks, such as *Solar System Dynamics* by Murray & Dermott (1999), an unpublished celestial mechanics book by Burns et al. (2022), and *Modern Celestial Mechanics* by Morbidelli (2002).

### 1.1.1 Orbital Elements

The vast majority of Solar System objects orbit a central dominant massive body under Newtonian gravity. In 1609, Kepler first discovered that “the orbit of every planet is an ellipse with the Sun at a focus”, which became the famous first law of planetary motion. The term ‘Keplerian orbit’ is now used to describe the motion of one body relative to the massive body, or their common center of mass (a.k.a the barycenter). More generally, the path of an object under the gravity of a central mass follows a ellipse, a parabola, or a hyperbola, which all belong to a group of curves known as conic sections.

The size and shape of a Keplerian orbit is defined by its eccentricity ( $e$ ) and semi-major axis ( $a$ ). The trajectory is a perfect circle if  $e = 0$ , an ellipse if  $0 < e < 1$ , a parabola if  $e = 1$ , and a hyperbola if  $e > 1$ . For Solar System bodies, bound orbits are essentially ellipses. Only gravitationally unbound comets and interstellar objects have hyperbolic orbits relative to the Sun. Additionally, small bodies during planetary flybys have hyperbolic orbits relative to the planet, which will be discussed in Section 3.2. Figure 1.1 shows an bounded elliptic orbit and an unbounded hyperbolic orbit. Semimajor axis ( $a$ ) is one half of the longest axis of the ellipse, and periapsis ( $q$ ) is the distance between the point of closest approach and the central body. For objects orbiting the Sun, ‘perihelion’ is more commonly used, while for objects orbiting the Earth, ‘perigee’ is used. The three quantities,  $a$ ,  $e$ , and  $q$  satisfy the following relationship:

$$q = a(1 - e) \quad \text{or} \quad e = 1 - \frac{q}{a}. \quad (1.1)$$

To describe the spatial orientation of the orbit and the object’s orbital position relative to some reference plane, the following angles are often used (Figure 1.2):

- $i$  - Inclination. The tilt angle between the orbital plane and the reference plane. Prograde orbits move counterclockwise and have  $i < 90^\circ$ . Retrograde orbits

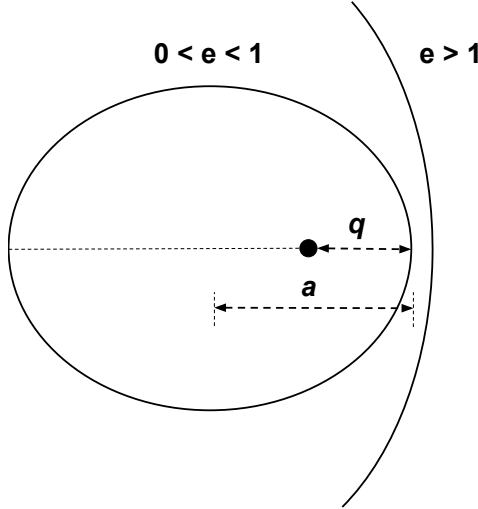


**Figure 1.1:** A diagram describing an elliptic orbit ( $0 < e < 1$ ) and a hyperbolic orbit ( $e > 1$ ). The dashed line connecting the periapsis and the central body (black dot) is the apsidal line.  $a$  is the semimajor axis and  $q$  is the pericenter distance. Only elliptic orbits have well-defined semimajor axis and apoapsis.

move clockwise and have  $i > 90^\circ$ .

- $\Omega$  - Longitude of the ascending node. The intersection between the orbital and reference planes is called the line of nodes. The ascending node is where the orbit passes upward through the reference plane, and  $\Omega$  is the orientation of this node in the reference plane, as an angle measured from the ascending node to the vernal point  $\Upsilon$ .
- $\omega$  - Argument of pericenter. The orientation of the ellipse in the orbital plane, as an angle measured from the ascending node to the pericenter.
- $f$  - True anomaly. The position in orbit at a specific time, as an angle measured from the pericenter to the orbiting object.

The six orbital elements,  $a$ ,  $e$ ,  $i$ ,  $\Omega$ ,  $\omega$ , and  $f$  are a set of independent coordinates that defines the size, shape, and spatial orientation of an elliptic orbit, as well as the celestial body's exact location. They can be interconverted to the Cartesian coordi-

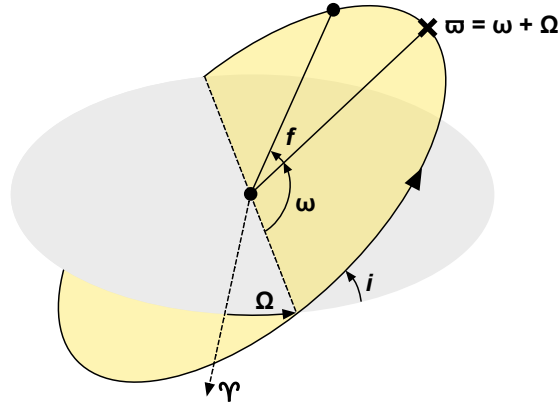


**Figure 1.2:** A diagram describing the spacial orientation of a prograde orbit (yellow) in a reference plane (gray). The intersection between the two planes is the line of nodes (dashed line with no arrowhead). The cross marks the pericenter, and the dashed arrow points to the reference direction, which is normally the vernal equinox  $\Upsilon$  in the Solar System.  $i$  is the orbital inclination,  $\Omega$  the longitude of the ascending node,  $\omega$  the argument of pericenter,  $\varpi$  the longitude of pericenter, and  $f$  the true anomaly.

nates, uniquely corresponding to a specific state vector that consists of position ( $x, y, z$ ) and velocity vectors ( $\dot{x}, \dot{y}, \dot{z}$ ).

Some orbital elements are often expressed in alternative forms to avoid singularities. For example, if the orbital inclination  $i$  is precisely  $0^\circ$  or  $180^\circ$ , then the longitude of the ascending node  $\Omega$  becomes ill-defined. In co-planar case, the longitude of pericenter  $\varpi$  (pronounced “curly pi”) is often used to describe the orientation of the apsidal line that connects the periapsis, the central body, and the apoapsis (the dashed line in Figure 1.1). In the Three-Dimensional (3D) case, the longitude of pericenter is also used, defined as  $\varpi = \Omega + \omega$  for prograde orbits and  $\varpi = \Omega - \omega$  for retrograde orbits (Huang et al., 2018), despite the fact that the angles  $\Omega$  and  $\omega$  lie in different planes. In general, therefore,  $\varpi$  is just a broken angle used to describe the azimuthal orientation of the apsidal line, *not* the precise longitude. When the orbital plane approaches the reference plane (i.e.  $i \approx 0^\circ$  or  $180^\circ$ ),  $\varpi$  approaches the real longitude of pericenter.

As the object moves on an elliptic orbit, the time-varying distance  $r$  between the

central body and the object can be expressed as a function of the true anomaly  $f$ :

$$r = \frac{a(1 - e^2)}{1 + e\cos f}. \quad (1.2)$$

This equation is often called the orbit equation of the two-body problem, but is also the polar coordinates equation for an ellipse, with the origin at one focus and  $f = 0$  corresponding to periapsis.

The orbital period  $P$  is the time between two consecutive pericenter passages, given by the Kepler's third law:

$$P = 2\pi \left( \frac{a^3}{\mu} \right)^{\frac{1}{2}}, \quad (1.3)$$

where the gravitational parameter  $\mu$  is the product of the gravitational constant  $G$  and the mass of the central body  $M$ :

$$\mu = GM. \quad (1.4)$$

For any Keplerian orbit, the vis-viva equation, or the orbital-energy-invariance equation, is as follows:

$$v^2 = \mu \left( \frac{2}{r} - \frac{1}{a} \right), \quad (1.5)$$

where  $v$  is the relative speed of the two bodies. This comes directly from the conservation of the specific orbital energy  $\epsilon$ , which is the sum of the mutual potential energy and the total kinetic energy per mass

$$\epsilon = \frac{v^2}{2} - \frac{\mu}{r} = -\frac{\mu}{2a}. \quad (1.6)$$

When it comes to solving the orbiting body's movement with time, mean anomaly  $\mathcal{M}$  is more convenient, which is defined as

$$\mathcal{M} = nt_{\text{peri}}, \quad (1.7)$$

where  $t_{\text{peri}}$  is the time since the last pericenter passage, and  $n$  is called the 'mean motion' of the body. Mean motion  $n$  denotes the average angular speed required

for that body to complete one orbit. It is simply one full revolution ( $2\pi$ ,  $360^\circ$  or 1) divided by the orbital period  $P$ :

$$n = \frac{2\pi}{P}. \quad (1.8)$$

For a circular orbit, the orbiting body's mean motion is equal to the constant angular velocity, so the true anomaly  $f$  is also equal to the mean anomaly  $\mathcal{M}$ . For an elliptic orbit, however, the orbital body speeds up near the pericenter and slows down near the apocenter, as described by the Kepler's second law. To solve for  $f$  as a function of time, Kepler's equation is needed:

$$\begin{aligned} \mathcal{M} &= \mathcal{E} - e \sin \mathcal{E}, \\ \tan \frac{\mathcal{E}}{2} &= \sqrt{\frac{1-e}{1+e}} \tan \frac{f}{2}, \end{aligned} \quad (1.9)$$

where  $\mathcal{E}$  is the eccentric anomaly. Calculating  $\mathcal{M}$  for a given value of  $f$  is straightforward. However, solving for  $\mathcal{E}$  and  $f$  when  $\mathcal{M}$  is given can be considerably challenging, as Kepler's equation is a transcendental equation. Newton's iterative method and series expansions are generally used to evaluate  $\mathcal{E}$ , of which I will not get into details.

### 1.1.2 Hamiltonian Formalism

The Hamiltonian formalism is commonly used in celestial mechanics to analyze and simplify a dynamical problem (Murray & Dermott, 1999; Morbidelli, 2002). In Hamiltonian mechanics, a dynamical system's state is described in  $2n$ -dimensional canonical phase space coordinates  $(\mathbf{p}, \mathbf{q})$ , where  $n$  is the number of degrees of freedom. In such coordinates, the Hamilton's equations of motion is given by

$$\frac{d\mathbf{q}}{dt} = \frac{\partial \mathcal{H}}{\partial \mathbf{p}}, \quad \frac{d\mathbf{p}}{dt} = -\frac{\partial \mathcal{H}}{\partial \mathbf{q}}, \quad (1.10)$$

when  $\mathcal{H}$  does not depend on time. There only exists a limited number of Hamiltonian systems that are fully solvable and does not possess chaos, such as the simple harmonic oscillator and the two-body system. They are often called integrable Hamiltonian systems. For integrable systems, of crucial importance is the *Arnold*–

*Liouville theorem*, which states that there exists a canonical transformation to action-angle coordinates in which the transformed Hamiltonian is dependent only upon the ‘action’ coordinates  $\mathbf{p}$  and the ‘angle’ coordinates  $\mathbf{q}$  evolve linearly in time.

As an example of the application of the Arnold–Liouville theorem, let’s introduce the following variables for the two-body problem:

$$\begin{aligned} L &= \sqrt{\mu a}, & l &= \mathcal{M}, \\ G &= L\sqrt{1-e^2}, & g &= \omega, \\ H &= G\cos i, & h &= \Omega. \end{aligned} \tag{1.11}$$

The canonical variables  $L, G, H$  (actions) and  $l, g, h$  (angles) are usually called the Delaunay variables. With this choice, the integrable Hamiltonian of the two-body problem will be dependent solely on the first action variable  $L$ :

$$\mathcal{H} = -\frac{\mu^2}{2L^2}, \tag{1.12}$$

and  $\mathcal{H}$  is also the specific orbital energy  $-\frac{\mu}{2a}$  (1.6).

With Equation (1.10), the Hamilton’s equations of motion are simply

$$\begin{aligned} \dot{L} &= 0, & \dot{l} &= \left(\frac{a^3}{\mu}\right)^{-\frac{1}{2}}, \\ \dot{G} &= 0, & \dot{g} &= 0, \\ \dot{H} &= 0, & \dot{h} &= 0. \end{aligned} \tag{1.13}$$

These equations of motion trivially state that in the two-body problem, orbital elements  $a, e, i, \Omega$ , and  $\omega$  are all constant while the mean anomaly  $\mathcal{M}$  evolves linearly with the speed of mean motion  $\dot{l} = n$  (1.8).

To avoid the same singularity problem when  $i$  and/or  $e$  are zero, the following Poincaré variables (also known as the *modified Delaunay variables*) are often used

for prograde orbits:

$$\begin{aligned}\Lambda &= L = \sqrt{\mu a}, & \lambda &= l + g + h = \mathcal{M} + \varpi, \\ P &= L - G = L(1 - \sqrt{1 - e^2}), & p &= -g - h = -\varpi, \\ Q &= G - H = 2G\sin^2 \frac{i}{2}, & q &= -h = -\Omega,\end{aligned}\tag{1.14}$$

where  $\lambda = \mathcal{M} + \Omega + \omega$  is called the mean longitude, evaluating the orbiting body's azimuthal location on the reference plane. For  $i > 0^\circ$ , it is another broken angle as  $\varpi$ . In this new set of coordinates, the Hamiltonian (1.12) and the resulting equations of motion (1.13) remain unchanged.

The orbital elements and canonical coordinates are derived from the two-body problem, where Keplerian orbits are fixed and unchanged under the Newton's gravity, which, by definition, is precisely proportional to the inverse square of the distance  $F \propto r^{-2}$ . Bertrand's theorem, on the other hand, states that any small perturbation off a purely  $r^{-2}$  central-force law (either from the general relativity correction or the gravity of a planet) will result in the particle orbits not closing, causing orbits to precess in physical space (i.e. non-zero  $\dot{\Omega}$ ,  $\dot{\omega}$ , or  $\dot{\varpi}$ ). If the perturber's gravitational effect is significantly smaller than the central body's, the induced orbital element variations will have longer timescales than the Keplerian orbital period  $P$ . One can thus still use the instantaneous orbital elements (called the 'osculating orbit') to study orbital evolutions of small bodies under such perturbations.

### 1.1.3 Restricted Three-Body Problem

A dynamical problem in celestial mechanics commonly investigated is the Restricted Three-Body Problem (RTBP), in which a massless particle moves under the influence of two massive bodies, in our case, the Sun (the *primary*, with the mass  $m_1 = 1 - \mu'$ ) and the planet (the *secondary*, with the mass  $m_2 = \mu'$ ). Having negligible mass, the force that the particle exerts on the two massive bodies may be neglected, and the system can therefore be described in terms of a two-body motion. It is thus a *restricted* approximation to the original three-body problem for analyzing the motions of spacecrafts and small bodies whose masses are negligible compared to those of the Sun and planet.

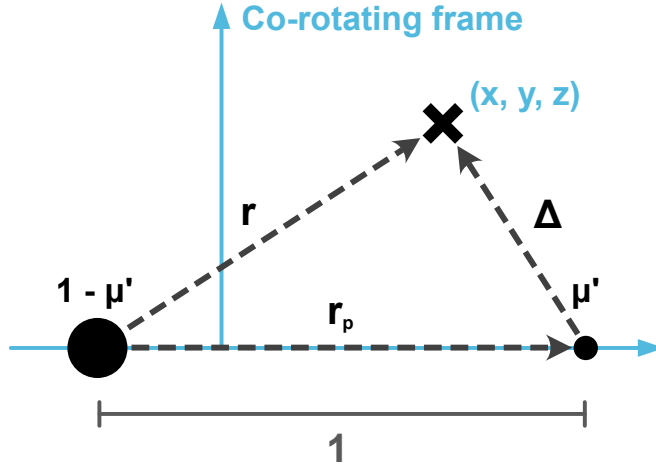


**Figure 1.3:** The circular restricted three-body problem as described in the co-rotating  $(x, y)$  coordinate system (blue). The two primaries  $m_1 = 1 - \mu'$  and  $m_2 = \mu'$  always lie on the  $x$  axis which, due to their mutual circular orbits, rotates around the center of mass (origin) uniformly with the mean motion  $n$ . The massless particle is marked with the black cross, whose distances from the two. The total mass and the constant distance between the two masses are both normalized to unity.

The Hamiltonian of the restricted problem can be written in Delaunay's variables (1.11) as (choosing the time unit so that  $\mathcal{G} = 1$ )

$$\begin{aligned}\mathcal{H} &= \underbrace{\mathcal{H}_0}_{\text{Keplerian term}} + \underbrace{\mathcal{H}_1(L, G, H, l, g, h, t)}_{\text{disturbing term}}, \\ \mathcal{H} &= -\frac{1}{2L^2} - \mu' \left( \frac{1}{\|\Delta_p\|} - \frac{\mathbf{r} \cdot \mathbf{r}_p}{\|\mathbf{r}_p\|^3} \right),\end{aligned}\tag{1.15}$$

where  $\mathbf{r}$  is the heliocentric position vector of the small body, and  $\mathbf{r}_p$  that of the perturber, and  $\Delta_p = \mathbf{r} - \mathbf{r}_p$ . The Keplerian term  $\mathcal{H}_0$  is the two-body Hamiltonian of the test particle with respect to the central body, and the disturbing term  $\mathcal{H}_1$  (also known as the *disturbing function*) represents the gravitational perturbation induced by the additional mass. This Hamiltonian  $\mathcal{H}$  can be explicitly written and used for practical computations, such as computing the expected precession frequency in Chapter 2.

If the planet orbits the Sun on a circular orbit, or its eccentricity is so small that the orbit is close to a circle, the RTBP can be simplified to the Circular Restricted Three-Body Problem (CRTBP), which is depicted in Figure 1.3. I will not go into the analytical details, but it is important to know that there exists a ‘first integral of the motion’  $\mathcal{C}_J$ , which is called the Jacobi integral or Jacobi constant of the CRTBP (Szebehely & Jefferys, 1968):

$$\begin{aligned}\mathcal{C}_J &= 2U(x, y, z) - v^2, \\ \mathcal{C}_J &= \underbrace{x^2 + y^2}_{\text{rotational potential}} + 2(\underbrace{\frac{1 - \mu'}{r_1} + \frac{\mu'}{r_2}}_{\text{gravitational potential}}) - \underbrace{(\dot{x}^2 + \dot{y}^2 + \dot{z}^2)}_{\text{kinetic energy}},\end{aligned}\quad (1.16)$$

where  $v$  is the particle’s velocity in the co-rotating frame and the mean motion is normalized to  $n = 1$ .  $U(x, y, z)$  is the ‘effective potential’ of the system, which is a combination of the rotational and gravitational potentials.

The Jacobi constant is effectively a conserved “energy” of the motion in the CRTBP. If we re-write Equation (1.16) in the inertial frame, substituting the velocity and position vectors with Keplerian elements, we get

$$\begin{aligned}\frac{1}{A} + 2\sqrt{A(1 - e^2)\cos i} + 2\mu'(\frac{1}{r_2} - \frac{1}{r_1}) &= \mathcal{C}_J, \\ \mathcal{T} \equiv \frac{1}{A} + 2\sqrt{A(1 - e^2)\cos i} &\approx \mathcal{C}_J,\end{aligned}\quad (1.17)$$

where  $\mathcal{T}$  is the Tisserand parameter and  $A = a/a_p$  is the normalized semimajor axis with respect to the planet ( $a_p$ ). The Tisserand parameter remains approximately unchanged given the mass parameter  $\mu'$  is small and when the particle is far from both the Sun and the planet (i.e.  $1/r_1$  and  $1/r_2$  are both small). This quality is widely used in cometary dynamical classification (Levison, 1996) and I will demonstrate that it also provides valuable information for the Kuiper Belt (see Section 3.2 and Chapter 5).

#### 1.1.4 Mean-Motion Resonances

A mean-motion resonance between two celestial bodies orbiting the same central body occurs when they have orbital periods very close to a simple integer ratio (a.k.a

mean-motion commensurability). I will mainly focus on mean-motion resonances between TNOs and Neptune, which happens when the mean motions  $n_p/n \approx k/k_p$ , or

$$kn - k_p n_p \approx 0, \quad (1.18)$$

where  $k$  and  $k_p$  are positive integers. We call such resonance a ‘ $k:k_p$  resonance’ and  $k_p:k$  the ‘resonant ratio’. For exterior resonance where  $a > a_p$ , the resonant order is defined as  $k - k_p$ .

The nominal resonant location  $a_{\text{res}}$ , which is the semimajor axis (of the small body) that would give itself the orbital period commensurate with that of the planet, is given by

$$a_{\text{res}} = \left( \frac{k}{k_p} \right)^{\frac{2}{3}} a_p. \quad (1.19)$$

When the small body is in resonance with the planet, the critical resonant angle

$$\varphi = k\lambda - k_p\lambda_p - (k - k_p)\varpi \quad (1.20)$$

will oscillate around an equilibrium point, which is often called ‘libration’ in resonant dynamics. This libration center is usually located at  $0^\circ$  or  $180^\circ$ , but for exterior  $n:1$  resonances, asymmetric libration centers (such as  $\pm 60^\circ$ ) also exist (Beaugé, 1994).

The evolution of the resonant angle  $\varphi$  is related to the long-term variation of the orbital orientation in the reference frame co-rotating with the planet’s mean motion. As an example,  $a$  and  $\varphi$  evolutions and the orbit of a resonant TNO – (472235) Zhulong – are shown in Figure 1.4 to demonstrate the geometry encoded in the resonant angle. The 5:2 mean-motion commensurability between Zhulong and Neptune creates the two-fold symmetry in the rotating frame, and  $\varphi$  is related to the angular location of each perihelion passage with respect to Neptune (denoted by those ‘curly wires’ around the gray dashed circle). This can also be seen from Equation (1.20). By noting that  $\varpi = \lambda$  when the particle is at perihelion, we get  $\varphi = k_p(\lambda - \lambda_p)$ , where  $\lambda - \lambda_p$  is the difference in true longitude between the object and the planet (Volk & Malhotra, 2022). This states that the orbit’s circumferential oscillation amplitude in the rotating frame must be equal to  $\Delta\varphi/k_p$ .

Bounded by the geometrical relationship between the resonant angle  $\varphi$  and the orbital orientation with respect to the planet, a resonant small body is less likely to experience strong close encounters with the planet, as illustrated in Figure 1.4's right panel. This dynamical mechanism is often called the 'phase protection' of a resonance, stabilizing the small body's orbit even if its perihelion crosses the planet's orbit. I will dive deep into resonant dynamics in Chapter 5.

### 1.1.5 Secular Resonances

In the restricted three-body problem, when the small body is not in mean-motion resonance and not able to approach the planet (characterized by perihelion beyond the planet's orbit), it generally experiences extremely tiny  $a$  variation and small  $e$ , and  $i$  oscillations, with the pericenter moving in a prograde sense (termed *precession*, denoted by  $\dot{\varpi}$  increasing linearly) and the node moving retrograde (termed *regression*, denoted by  $\dot{\Omega}$  decreasing linearly). This motion is often called *secular variations* or *secular drifts*, because the precession rate is significantly slower than the small body's mean motion<sup>1</sup>.

The secular precession rates can be computed analytically. By directly expanding the disturbing function into secular (i.e. non-resonant) terms, one can solve for the precession rates ( $\dot{\varpi}$  and  $\dot{\Omega}$ ) with Lagrange's planetary equations (see Brouwer & Clemence 1961; Murray & Dermott 1999; Mardling 2013). In the approximation that the planet and the small body both have low- $e$  and low- $i$  orbits, the planet-induced apsidal and nodal processing rate are nearly equal in magnitude. For external small bodies perturbed by an internal planet (like TNOs), the precession rates are given by

$$\begin{aligned}\dot{\varpi} &\approx -\dot{\Omega} \approx \frac{1}{4} \frac{m_p}{M_\odot} n \alpha b_{3/2}^{(1)}(\alpha), \\ &\approx \frac{3}{4} \frac{m_p}{M_\odot} n \alpha^2, \quad \text{if } \alpha \ll 1,\end{aligned}\tag{1.21}$$

where  $\alpha$  is the semimajor axis ratio of the two bodies (always  $< 1$ )

$$\alpha = \frac{a_p}{a},\tag{1.22}$$

---

<sup>1</sup>so is the regression rate, but for the sake of simplicity, I will now start to call both drifts 'precession'.

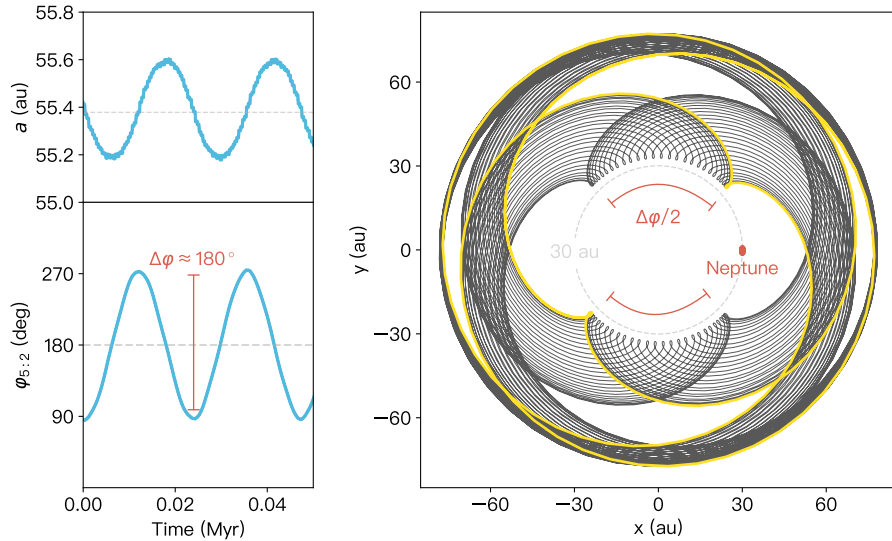


**Figure 1.4:** Orbital evolution of TNO (472235) Zhulong over 50 kyr in Neptune's 5:2 mean-motion resonance. **Left:** The time evolution of  $a$  and the resonant angle  $\varphi$ . **Right:** Zhulong's position projected on a reference  $x$ – $y$  plane that co-rotates around the Solar System's barycenter at the rate of Neptune's mean motion; Neptune thus remains nearly fixed along the  $x$  axis (red dot), whereas Zhulong follows the black trajectory clockwise, except at perihelia (represented by those ‘curly wires’) where the object moves faster than Neptune. Zhulong completes two orbits (an example of two orbits is shown in yellow) for every five Neptune orbits, creating the two-fold symmetry in the rotating frame. The  $\Delta\varphi \approx 180^\circ$  libration amplitude corresponds to a circumferential oscillation of the perihelion location in the rotating frame of  $\Delta\varphi/2 \approx 90^\circ$  (both labeled in red). Despite its perihelion distance being very close to Neptune's orbit (gray circle with a 30 au radius), the TNO never approaches the planet at perihelion passages. This is known as the ‘phase protection’ mechanism of a resonance.

and  $b_s^{(j)}(\alpha)$  is the Laplace coefficient, defined as

$$b_s^{(j)}(\alpha) = \frac{1}{\pi} \int_0^{2\pi} \frac{\cos j\psi \, d\psi}{(1 - 2\alpha \cos \psi + \alpha^2)^s}. \quad (1.23)$$

Now let's turn to the planet. If the planetary system only consists of a single planet, its Keplerian orbit is fixed in physical space. Adding another planet, the two planets' mutual gravitational forces pull on each other as they orbit the Sun. This causes both of them to acquire forced eccentricities and inclinations (assuming they're not co-planar) and to precess both nodally and apsidally.

In this two-planet case, a *secular resonance* occurs when the particle's natural precession rate, which is the sum of the rates induced by the two planets, is close to either planet's. This is because the magnitude of the particle's forced eccentricity ( $e_{\text{forced}}$ ) and inclination ( $i_{\text{forced}}$ ) has a term

$$\begin{aligned} e_{\text{forced}} &\propto \sum_{j=1}^2 \frac{1}{A - g_j}, \\ i_{\text{forced}} &\propto \sum_{j=1}^2 \frac{1}{B - f_j}, \end{aligned} \quad (1.24)$$

where  $A$  and  $B$  are the small body's expected apsidal and nodal precession rates, and  $g_j$  and  $f_j$  are the two planets' respectively. Noting that  $A - g_j$  or  $B - f_j$  (which are called "small divisors") appears in the denominators, when  $A$  or  $B$  approaches the corresponding planetary secular frequencies, the forced elements in Equation (1.24) diverge in the linear theory, which does not reflect the real orbital dynamics.

An example is shown in Figure 1.5. When an apsidal precession of  $\dot{\varpi}_p \approx \dot{\varpi}$  is imposed on Neptune's orbit, the small body will be subjugated to a much larger  $e$  oscillation, driving its  $q$  down to Neptune's scattering region (highlighted in red). Similarly, when the small body's node precesses at the same rate as the planet, its  $i$  will be pumped to a larger value by the inclination secular resonance.

In the the Solar System, the eight planets influence each other's orbits in a much more complex manner. The precession of each planet is composed of a series of frequencies with varying magnitudes, and each frequency corresponds to a specific secular resonance. Brouwer & Woerkm (1950) analyzed the secular variations of

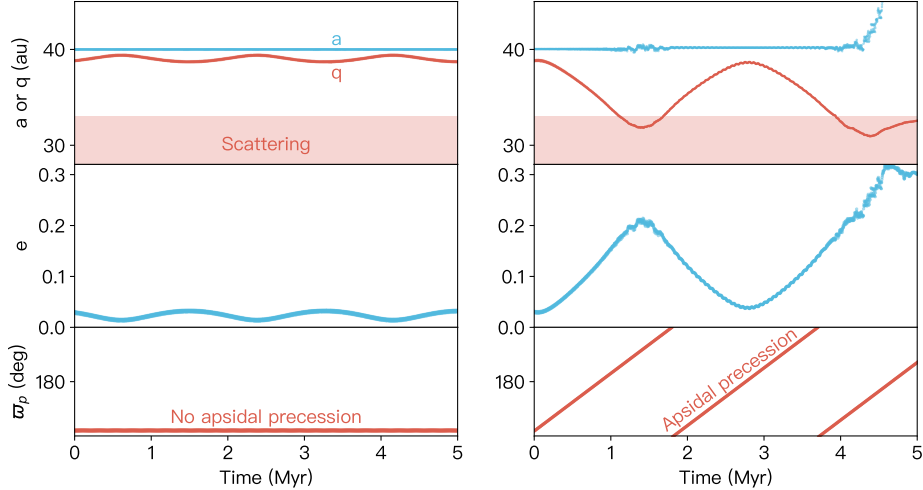


**Figure 1.5:** Orbital evolutions of two identical test particles under the gravity of a planar and near-circular ( $e_N \sim 0.01$ ) Neptune orbit. These two particles demonstrate wildly different secular evolution histories, due to the difference in Neptune's apsidal precession rates and the secular resonance. **Left:** With Neptune on a fixed orbit and no apsidal precession, the secular oscillation of the particle's eccentricity is so small that it does not pump the particle to the region where strong semimajor axis scattering can occur (red highlighted). **Right:** When an apsidal precession rate very close to that of the particle ( $\sim 0.68''/\text{yr}$ ) is artificially given, Neptune's gravity induces a much more powerful  $e$  excitation to the small body, despite having the same small initial eccentricity. As shown in the top-right panel, the secular resonance allows objects initially starting from near-circular orbits to couple with Neptune and likely get ejected from the Solar System eventually.

orbital elements of the eight planets and obtained the *eigenfrequencies* and *eigenmodes* of the Solar System, where ten frequencies for the  $e-\varpi$  solution ( $g_1-g_{10}$ ) and eight frequencies for the  $i-\Omega$  solution  $f_1-f_8$  are given. The corresponding resonances are often referred as as the  $\nu_n$  secular resonance, where the subscript denotes the  $i$ -th value of the eigenfrequency involved ( $\nu_1 = g_1, \dots, \nu_{10} = g_{10}, \nu_{11} = f_1, \dots, \nu_{18} = f_8$ ).

Secular resonances play vital roles in shaping the structures of small body populations. For example, the inner edge of the cold classical Kuiper Belt at  $\sim 41$  au is

largely set by the presence of the  $\nu_8$  resonance, which destabilizes nearby low- $e$  and low- $i$  TNOs by pumping their  $e$  to Neptune-crossing orbits (similar to the orbital evolution shown in Figure 1.5’s right panel). Additionally, an extra planet’s secular effect is able to raise perihelia of scattering TNOs and detach them. I will examine the secular evolution of main-belt TNOs in more depth in Chapter 2, and study the extra planet’s secular forcing in Chapter 6.

## 1.2 Numerical Tools

Long-term N-body numerical integrations are playing a vital role in dynamical astronomy. In the context of planetary system dynamics, one of the most common problems is to study the motion of a large number ( $N$ ) of low-mass small bodies under the gravitational field of a central star and several planets ( $N_p$ ) on hierarchical orbits. While the star and planets need to be evolved considering their mutual gravities, which requires an algorithm with  $N_p^2$  complexity, the small bodies can be treated as massless test particles and thus the calculation expense scales as  $NN_p$ . Once the number of particles greatly exceeds the number of planets, the total complexity is  $N_p^2 + NN_p \approx NN_p$ .

In this section, I will briefly introduce several frequently-used N-body numerical integrators in planetary dynamics and their underlying algorithms. I will also talk about GPU Long-term Integrator for Solar System Evolution: Regularized (GLISSER), a Graphics Processing Unit (GPU)-based integrator I helped improve based on GLISSE (Zhang & Gladman, 2022) during my PhD study. This fast and efficient integrator will be the main numerical tool I use in Chapter 3, 5, and 6 to study various dynamical problems in the Solar System.

### 1.2.1 Solar System Small-Body Integrators

While generic ordinary differential equations solvers, such as the Bulirsch-Stoer and the Runge-Kutta algorithms (Stoer & Bulirsch, 1980) can be applied in planetary dynamics, they are not suitable for propagating orbits for millions of years. This is because most of the generic integrators are non-symplectic, where small numerical errors would lead to the gradual drift in the system’s total energy. Symplectic methods, on the other hand, conserve the total energy of a Hamiltonian system by

design. One of the most commonly-used algorithm in solving gravitational N-body problems is the Wisdom-Holman Mixed Variable Symplectic (MVS) method (Wisdom & Holman, 1991), in which the Hamiltonian is split into the following two terms

$$\mathcal{H} = \mathcal{H}_{\text{Kepler}} + \mathcal{H}_{\text{Interaction}}, \quad (1.25)$$

where  $\mathcal{H}_{\text{Kepler}}$  is the Keplerian term that describes the central force of the star and thus can be propagated forward by numerically solving the Kepler's equation (1.9);  $\mathcal{H}_{\text{Interaction}}$  is the planetary interaction term that updates the planet/particle's velocities using the Newtonian accelerations evaluated on their positions. When planets are far away from each other or test particles are far away from the planets (i.e. no planet-planet or particle-planet close encounters), the interaction terms are so small that the problem can be approximately solved through the second-order 'leapfrog' time step scheme: a half step following  $\mathcal{H}_{\text{Kepler}}$ , followed by successive whole steps alternately following  $\mathcal{H}_{\text{Interaction}}$  and  $\mathcal{H}_{\text{Kepler}}$ , ending with a half step of  $\mathcal{H}_{\text{Kepler}}$ .

When close encounters do occur in the planetary system (when a planet/particle enters another planet's Hill sphere  $R_H$ , see Equation 3.13), the assumption that  $\mathcal{H}_{\text{Interaction}} \ll \mathcal{H}_{\text{Kepler}}$  breaks down and the integrator must switch to a planet-centric reference frame to resolve the close encounter with a much smaller time step  $\Delta t$ . Different Solar System small body integrators apply different algorithms to approach this problem. The SWIFT integrator (Levison & Duncan, 1994) uses the Regularized Mixed Variable Symplectic (RMVS) method, which approximates a test particle flyby with a hyperbola centered about the planet. The SYMBA integrator (Duncan et al., 1998) is able to handle planet-planet close encounters by employing a variant of the standard MVS with a multiple time step technique. The MERCURY integrator (Chambers, 1999) solves close encounters with the standard Bulirsch-Stoer method (Stoer & Bulirsch, 1980) while handling the long-term evolutions with Wisdom-Holman MVS.

A latest and more comprehensive N-body package is REBOUND developed by Rein & Liu (2012). It is written in both C++ and PYTHON and contains several numerical integrators, such as Bulirsch-Stoer, IAS15 (Rein & Spiegel, 2014), WHFAST (a fast and accurate implementation of the Wisdom-Holman MVS integrator, Rein & Tamayo, 2015), and MERCURIUS (an optimized implementation of the original

hybrid symplectic method in MERCURY, Rein et al., 2019b). For comparison between various symplectic N-body algorithms, one can refer to Wisdom (2016) and Rein et al. (2019a).

### 1.2.2 The GLISSER Integrator

While most of the N-body integrators implement the Wisdom-Holman MVS algorithm on the Central Processing Unit (CPU), the GPU Long-term Integrator for Solar System Evolution (GLISSE) integrator (Zhang & Gladman, 2022) is an implementation of the same algorithm but on the GPU, which fully utilizes its capability of parallel computing. In this section, I will introduce GLISSE, the GPU integrator I helped improve and test based on GLISSE and Kevin Zhang's extended codes. GLISSE handles particle-planet close encounters on CPU cores while propagating thousands of the non-encountering particles on the GPU.

As shown in the flowchart 1.6, the GLISSE integrator primarily consists of two parts:

1. GLISSE on the GPU (green): GLISSE utilizes the GLISSE code as its core to propagate test particles on GPU using the Wisdom-Holman MVS algorithm (green component in Figure 1.6). The details of the implementation can be read in Zhang & Gladman (2022).
2. SWIFT subroutines on the CPU (yellow): GLISSE separates the particles that are having close encounters from the non-encountering majority. For each ‘time chunk’<sup>2</sup>, close-encounter particles are handed over to SWIFT subroutines that resolve encounters on one or more CPU cores, after which they are re-inserted back onto the GPU.

Unlike most integrators that evolve planets and test particles simultaneously, GLISSE utilizes a pre-computed planetary history lookup file, in which the Cartesian coordinates of each planet are logged at each time chunk. The advantage is that it can read a planetary history generated by other programs (where more complex dynamical effects are considered, such as planetary migration and collision) and only simulate the small-body distributions shepherded by that history.

---

<sup>2</sup>time chunk is the basic unit, of which test particles get sent to GPU and propagated in parallel. It consists of a few hundred to thousands time steps depend on the problem GLISSE is resolving

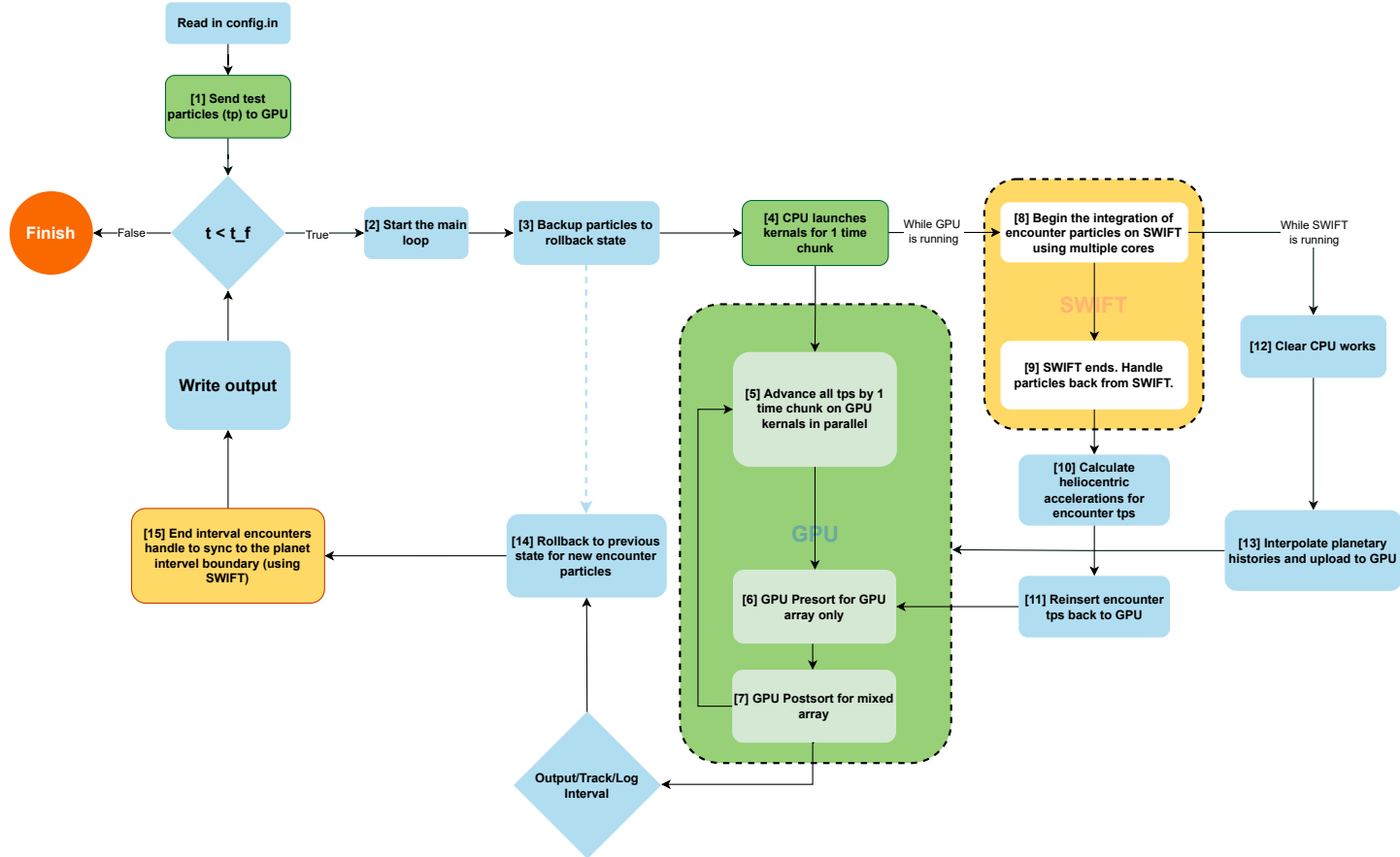


**Figure 1.6:** A conceptual flowchart for the GLISSER integrator. Blue, green, and yellow boxes are related to program processes that occur on the bookkeeping CPU core, the GPU, and SWIFT cores, respectively.

The history file is read at each time chunk and interpolated for every time step. I helped improve GLISSER’s interpolation algorithm, switching from heliocentric orbital elements to barycentric ones which greatly reduce the errors in the interpolated position vectors. I also expand the code to output the flyby distance and timing for each close encounter. With several bugs in the original code fixed, the overall usefulness of GLISSER has been greatly improved.

To illustrate its power, I have run two identical test simulations (on both GLISSER and MERCURY) and compared their results and execution speed. In both simulations, I put the four giant planets on their current orbits and also a  $2 M_{\oplus}$  additional planet on an orbit with  $a = 300$  au,  $q = 50$  au, and  $i = 10^\circ$ . This case is intended to show that both secular and close encounter dynamics are reproduced by GLISSER. As a first calculation, 1,000 test particles are randomly generated from  $a=50$  to 600 au with heliocentric  $q$  ranging from 32 to 38 au. The simulations were run for 100 Myr with GPU time step of 100 days (during close encounters the SWIFT code may decrease this time step to resolve a very close planetary passage). In both integrators, the close encounter portion of the algorithm is activated when a test particle is within  $3.5 R_H$  of any planet. Snapshots at the end of the 100 Myr integration are shown in Fig. 1.7; the simulations show very similar orbital distributions. Dynamical effects with different timescales, such as particles with  $q < 38$  au being rapidly scattered in semimajor axis by Uranus and Neptune and the long-range averaged gravity of the additional planet lifting the perihelia of objects between  $a=100$  to 800 au, are present in both integrators (also shown in the supplemental video). The rate of particle’s being eliminated (by scattering out to the Oort Cloud with heliocentric distances beyond 2,000 au, or striking planets) is statistically the same.

Fig. 1.8 shows the results of the aforementioned test-particle initial condition, but with the much larger particle count of 80,000. There are estimates in the literature that the retention probability for outer Solar System bodies may be only  $10^{-4}$ – $\sim 10^{-3}$  (Nesvorný, 2018), so as to have any reasonable statistics it is necessary to to integrate  $\sim 10^5$  initial conditions. Execution times and merit measurement are in Table A.1. It is clear that the presence of such a planet imposes significant  $e$  (and thus  $q$ ) oscillations on objects beyond  $\simeq 150$  au, forming a pyramid structure around itself on the  $a - q$  plot. This gigantic high- $q$  structure is created by the extra planet’s secular effects, which I will investigate in depth in Chapter 6. Upon closer inspec-

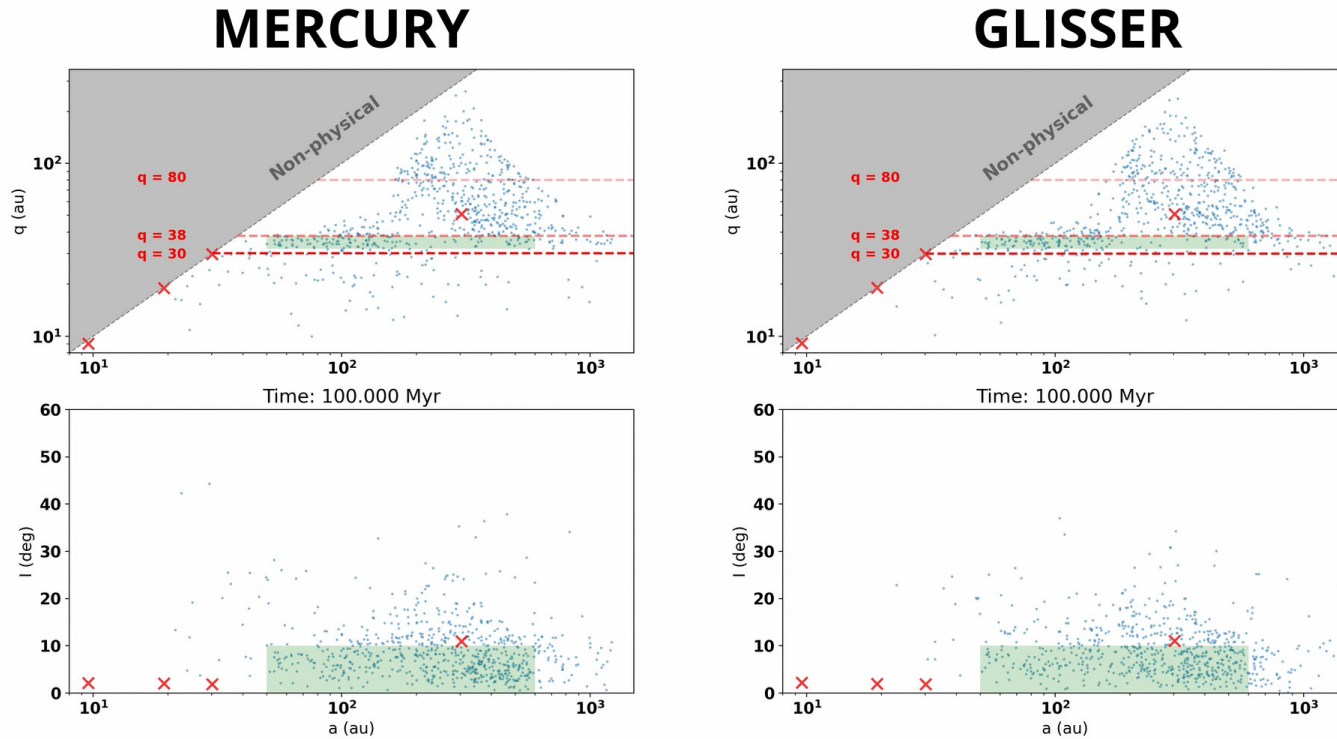


**Figure 1.7:** Comparison of the orbital distributions of 1,000 test particles after 100 Myr of simulation time using the CPU code MERCURY (left panel) and GLISSER (right panel). Planets are shown as red crosses (Jupiter is not indicated), while particle's initial conditions are confined in green boxes. Three horizontal dashed lines denote where  $q = 30$  (crossing the orbit of Neptune),  $q = 38$  (roughly the boundary between the scattering and the detached population), and  $q = 80$  au (the highest perihelion (2012 VP<sub>113</sub>) so far observed). The orbital distributions are obviously very similar but on this calculation GLISSER is 40 times faster. See Table A.1 for timings.

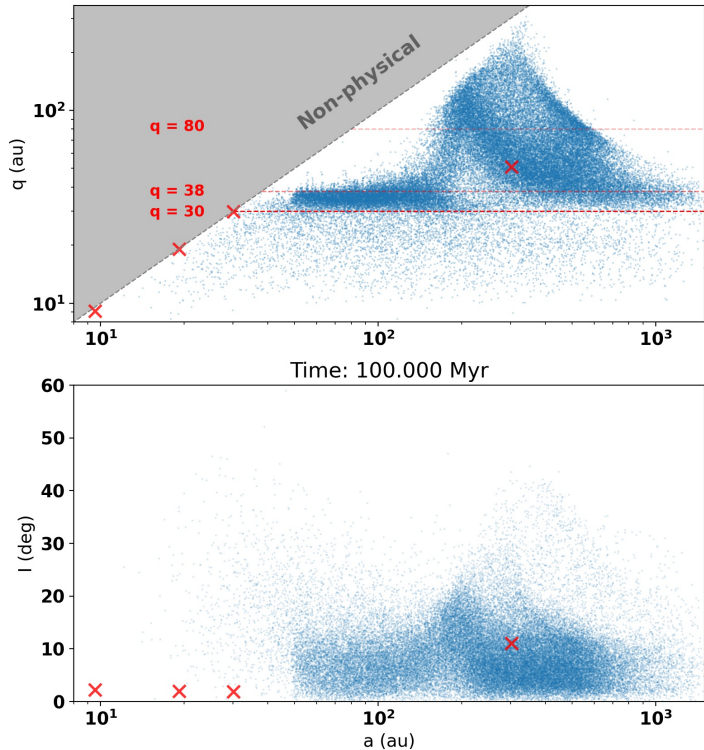


**Figure 1.8:** Same numerical simulation as in Figure 1.7. But instead of integrating only 1,000 test particles, GLISSER is able to propagate 80,000 test particles in parallel with only  $\sim 4 \times$  the integration time. See Table A.1 for timings. One noticeable feature with a larger sample size is the ‘vertical spikes’ above the  $q = 38$  au red dashed line inside 100 au. Their locations in  $a$  are close to where strong neptunian resonances lie, suggesting that the temporarily-present extra planet has enhanced the resonant capture efficiency. This feature is only seeable in simulations with tens of thousands of particles and it demonstrates the necessity of using GLISSER to study small body orbital distributions in greater details.

tion, I also notice that in the top  $a - q$  panel of Figure 1.8, there are a few ‘vertical spikes’ above the  $q = 38$  au red dashed line inside 100 au. These features are not visible in simulations without the additional planet or a vast amount of test particles, and they seem to suggest the extra planet’s role in enhancing the resonant capture efficiency. This new dynamical effect coming out of preliminary GLISSER simulations demonstrating its capability has been studied in Huang et al. (2022a) and will appear in Chapter 5. For additional GLISSER simulations showing the conservation of the Jacobi constant (Section 1.1.3) and orbital evolution comparisons with SWIFT, see Appendix A.1.

### 1.3 The Known Structures of the Solar System

The history of humanity’s understanding of the Solar System bears witness to the scientific and technological advances of the last few hundred years. Although almost all ancient civilization knew the existence of the five ‘wandering stars’ (or *planètes astères* in ancient Greek, from which today’s word *planet* was derived), it was not until 1781 that a new planet – Uranus – was discovered by Herschel, expanding the known boundaries of the Solar System for the first time. Motivated by the abnormal orbital motion of Uranus, the mathematical determination of Neptune’s existence by Le Verrier (Le-Verrier, 1846b,a) and Adams (Adams, 1846) in 1846 and its subsequent discovery represents one of the most significant theoretical predictions in the history of astronomy (see a recent review by Krajnović, 2016). This remarkable discovery further stimulated the search for more planets and solar system bodies, which led to the discovery of Pluto by Tombaugh in 1930 (see search history for Pluto in Tombaugh, 1946). This long-sought planet-sized body coincided with the proposed *Planet X* by Lowell (1915), and was soon after granted the *Ninth Planet of the Solar System* for the next 70 years. The ‘planet’ title of Pluto stood unchallenged until growing number of Pluto-sized objects were found in the millennium (e.g. Eris by Brown et al. 2005). This led to the redefinition of Pluto as a ‘dwarf planet’ in the 2006 International Astronomical Union (IAU) General Assembly. The consensus of eight known planets in the Solar System – Mercury, Venus, Earth, Mars, Jupiter, Saturn, Uranus, Neptune – was surprisingly only established in the past two decades, and may keep on expanding as our understanding of the Solar System increases.

Besides planets, the Solar System also hosts a swarm of small celestial bodies (sometimes called minor planets), including comets, asteroids, icy bodies in the outer Solar System, planetary satellites, and interplanetary dust. Small bodies are mainly located in four major reservoirs – the main asteroid belt, Jupiter’s co-orbital space, the Kuiper Belt (a.k.a Transneptunian space), and the Oort Cloud. These objects are more frequently known as asteroids if from the inner Solar System, Jovian Trojans if from the co-orbital space of Jupiter, Trans-Neptunian Objects (TNOs) if from the Kuiper Belt, and Oort Cloud objects if from the Oort Cloud. They are thought to be remnant debris from the Solar System’s ancient past. Their orbital distributions, physical characteristics, and spectral properties provide invaluable tools for understanding the formation, migration, and evolution history of the planets. In my thesis, I will use the orbital distributions of TNOs to study the formation history of the outer Solar System, with a focus on the hypothesis that additional Earth-scale planet(s) may have existed in the past and left permanent traces in the observed TNO populations.

### 1.3.1 Small Body Populations Inside the Orbit of Neptune

Small bodies in the inner Solar System ( $a < 5.2$  au, the orbit of Jupiter) that do not have cometary activities (e.g. outgassing) are named ‘asteroids’. They are rocky bodies thought to be relics left over from the early formation of the Solar System about 4.6 Gyr ago. The largest asteroid reservoir is the main asteroid belt, located between the orbits of Mars and Jupiter, spanning semimajor axis from 2.0 to 3.5 astronomical units (au). It currently holds  $\sim 1$  million objects with diameter  $D > 1$  km (Bottke et al., 2005) and has a total mass only  $\approx 3\%$  of Earth’s moon (Pitjeva & Pitjev, 2018).

Most asteroids within the belt have orbital eccentricities  $e < 0.4$ , and inclinations  $i < 30^\circ$ . The vast majority of them are dynamically stable for the age of the Solar System, as their eccentricities place their orbits away from the orbits of Mars and Jupiter, where strong planetary close encounters cannot occur (i.e. ‘decoupled’). There are also unstable regions embedded in the main asteroid belt, opening gateways for them to escape and couple with planets. Unstable regions in the main belt are mainly associated with resonances that pump asteroid eccentricities.

Two particularly important such resonances are the 3:1 MMR with Jupiter (see Section 1.1.4) and the  $\nu_6$  secular resonance (see Section 1.1.5). Dynamical lifetimes insides these resonances are only a few million years, with the majority destroyed by being transferred to Jupiter-crossing orbits or being driven into the Sun (Gladman et al., 1997). Some of the escaped main-belt asteroids enter the near-Earth space and form the steady-state Near Earth Objects (NEO) population (Bottke et al., 2002; Greenstreet et al., 2012; Granvik et al., 2018), of which the recently-discovered member (594913) 'Ayló' chaxnim even has an orbit completely inside that of Venus (Greenstreet, 2020).

Beyond the main asteroid belt, the Hilda asteroids are a dynamical group in 3:2 MMR with Jupiter (Brož & Vokrouhlický, 2008). The Jupiter Trojans are a large group of asteroids that share Jupiter's orbit and librate around one of the Jupiter's triangular Lagrange points L4/L5, which are equilibrium points of the CRTBP (Section 1.1.3). Trojans are the majority of Jupiter's co-orbital, which are asteroids in 1:1 MMR, or co-orbital resonance with Jupiter<sup>3</sup>. While most of the Jupiter Trojans are dynamically stable for the age of the Solar System, long-term dynamical integrations show that those along the stability boundaries will escape Jupiter's co-orbital region and roam the Solar System (Levison et al., 1997). A recent estimate shows the total mass the Jupiter Trojans is  $\approx 0.08\%$  of the moon (Vinogradova & Chernetenko, 2015), nearly two orders of magnitude smaller than the main belt.

Between orbits of Jupiter ( $a = 5.2$  au) and Neptune ( $a = 30.2$  au), almost no small bodies evolve on long-term stable orbits due to strong gravitational interactions with giant planets. The term 'Centaurs' is used to refer to those short-lived objects whose orbits cross the orbits of one or more giant planets (Jewitt, 2009). Centaurs are a transient population of icy bodies that dynamically link the outer Solar System's transneptunian objects with the Jupiter-Family Comets (JFC) and Short-Period Comets (SPC) (Sarid et al., 2019). They only have  $\approx 3$  Myr mean dynamical lifetime and the total number of Centaurs with  $D > 1$  km is estimated as  $\approx 40,000$ ; a flux of one new object into the Centaur region from the Kuiper Belt every 125 yr is required to maintain the steady-state population (Horner et al., 2004).

---

<sup>3</sup>Except for Trojans that orbit the Sun on tadpole orbits relative to Jupiter, other co-orbital configurations include horseshoe orbits, quasi-satellites, and retrograde co-orbitals. See Morais & Namouni (2017).

### 1.3.2 Transneptunian Space

Transneptunian space is the outer region of the Solar System beyond Neptune. In the last century, this region was more commonly known as the ‘Kuiper Belt’, named after Gerard Kuiper, who envisioned a swarm of planetesimals spreading over a ring from  $\sim 30$  to  $50$  au (Kuiper, 1951). The idea of having a continuing protoplanetary disk outside the orbit of Neptune was initially proposed by Edgeworth (1949). Both Edgeworth and Kuiper’s works were prompted by the discovery of Pluto by Tombaugh in 1930.

The existence of the conceptualized Kuiper Belt was not verified until more Kuiper Belt Objects (KBO) were discovered in the late 90s, such as (15760) Albion (with initial provisional designation 1992 QB<sub>1</sub>) and 1993 FW by Jewitt & Luu (1993). Unlike Pluto, which is locked into the 3:2 MMR with Neptune and has moderate  $e$ , these two objects were found to have low-eccentricity orbits and semimajor axes ( $a$ ) around 44 au, which were soon realized to be just the tip of the vast Kuiper Belt population.

Starting around the millennium, various Kuiper Belt surveys have been carried out to find more TNOs. Since then, the population of discovered TNOs has been steadily increasing, reaching the number of  $\sim 4200$  as of the year 2022<sup>4</sup>. Major contributing surveys include the Deep Ecliptic Survey from 1999 to 2005 that yielded 382 designated TNOs (Elliot et al., 2005), the Canada-France Ecliptic Plane Survey (CFEPS) from 2003 to 2006 that yielded  $\sim 200$  characterized TNOs (Jones et al., 2006), the Outer Solar System Origins Survey (OSSOS) from 2013 to 2017 that yielded  $\sim 800$  characterized TNOs (Bannister et al., 2018), and the most recent Dark Energy Survey (DES) from 2013 to 2019 that yielded  $\sim 800$  TNOs (Bernardinelli et al., 2022). In the next few years, future Solar System surveys like the Legacy Survey of Space and Time (LSST), run by the Vera C. Rubin observatory, are likely to discover 40,000 TNOs. This number is an order of magnitude higher than all the current discoveries combined (Collaboration et al., 2021).

TNOs in different parts of the Kuiper Belt experience different dynamical behaviours. Their orbital stability times vary from millions of years to the age of the Solar System (Gladman et al., 2008). Therefore, dynamical classification is the first

---

<sup>4</sup>Data retrieved from JPL Small-Body Database ([https://ssd.jpl.nasa.gov/tools/sbdb\\_query.html](https://ssd.jpl.nasa.gov/tools/sbdb_query.html)) on September 12th, 2022.

step towards understanding the long-term evolution and origin of TNOs. Based on dynamics in the current environment (i.e., all planets on their current orbits and no extra planet-mass bodies), TNOs are divided into the following four categories (Fig. 1.9) in the most recent review article by Gladman & Volk (2021):

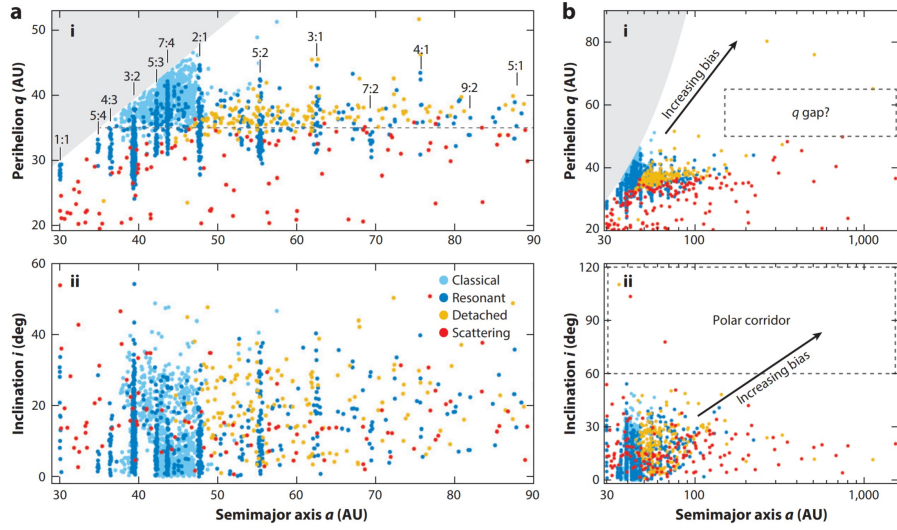


**Figure 1.9:** Known TNOs with dynamical classifications and perihelia beyond Uranus ( $q > 19.2$  au), in barycentric orbital elements. Major mean-motion orbital resonances with Neptune are marked in the upper left panel. Figure from Gladman & Volk (2021).

- **Resonant:** a TNO in a mean-motion resonance with Neptune, which allow survival even if  $q < a_N \approx 30$  au. Example: the 2:1 resonance at  $a \simeq 47$  au has TNOs with twice the orbital period of Neptune.
- **Scattering:** a TNO for which Neptune can *currently* significantly alter its semimajor axis  $a$  on timescales  $\ll 1$  Gyr; typically  $q \lesssim 38$  au. This is often called ‘scattered disk’ in other literature, but this term more precisely applies to objects which are currently dynamically scattering with Neptune.
- **Detached:** a non-resonant and non-scattering TNO with  $a > 47.4$  au (the location of the 2:1 resonance)<sup>5</sup>.

<sup>5</sup>In Gladman & Volk (2021), a detached TNO must also have  $e > 0.24$  to separate itself from

- **Classical:** a TNO that falls into none of the above categories.

The resonant population is subdivided into different groups based on their resonant ratios with Neptune. TNOs with 1:1 MMR with Neptune are also called Neptune Trojans, and those with 3:2 are usually called *Plutinos*, named after the largest TNO in the 3:2 population. As illustrated in Section 1.1.4, MMRs with Neptune protect TNOs from planetary close encounters, which stabilizes orbits even for TNOs with perihelia inside the orbit of Neptune (although many resonant TNOs have  $q > 30.2$  au). The formation mechanism related to the resonant population will be reviewed in Chapter 4 and studied in 5.

The current scattering population, whose present mass is of order  $0.05 M_{\oplus}$  (Trujillo et al., 2000), is the decaying remnant of a giant primordial population with initial mass of  $\approx 5 M_{\oplus}$  (Duncan & Levison, 1997) and is most likely the source of SPCs and JFCs (Dones et al., 2004; Volk & Malhotra, 2008). The dynamical lifetime of scattering disk objects is a few hundred million years, but numerical simulations show that scattering objects are often trapped near the boundaries of a resonant island, a phenomenon known as *resonance sticking* (Duncan & Levison, 1997; Gladman et al., 2002; Lykawka & Mukai, 2007). Resonance sticking with Neptune seems to significantly prolong the dynamical lifetimes of scattering objects (Duncan & Levison, 1997; Malyshkin & Tremaine, 1999). The dynamical nature and property of the scattering process will be studied in Chapter 3.

The classical Kuiper Belt is defined as the semimajor axis range between the 3:2 resonance (39.4 au) and the 2:1 resonance (47.7 au). All the non-resonant TNOs within this  $a$  range belong to the classical population. The ‘dynamically cold’ population are TNOs from the *cold classical Kuiper Belt*, with low- $e$  and low- $i$  orbits from  $a = 42.5$ –47.4 au. The current understanding is that they most likely formed in-situ, keeping their primordial state by remaining largely untouched by planetary perturbations and collisional evolution (Kavelaars et al., 2021). The hot classicals, on the other hand, are thought to be transported onto higher- $e$  and  $i$  orbits during the epoch of giant planet migration (Malhotra, 1995; Morbidelli et al., 2003). To separate the cold and hot classical TNOs that occupy the same semimajor axis

---

any potential primordial cold population beyond 47.4 au. Because there is not yet direct evidence to support the existence of a cold outer disk, I call all non-resonant and non-scattering TNOs beyond 47.4 au detached in this thesis.

range but originated from different places, an improved method to compute the ‘free inclinations’, a conserved quality for classical TNOs, is proposed in Chapter 2. Moreover, the dynamically unheated (relative to  $e = i = 0$ ) cold classical belt also provides a critical constraint on the evolutional histories of planets scattered out from the giant planet region, which will be discussed in Chapter 5 and 6.

The detached population refers to all non-resonant and non-scattering TNOs beyond the 2:1 resonance. It was first recognized by Gladman et al. (2002), in which the term *extended scattered disk* was first proposed to focus on the existence of those high- $q$  TNOs that are not experiencing strong gravitational interactions with Neptune, such as 2000 CR<sub>105</sub> and 1995 TL<sub>8</sub>. Emel’yanenko et al. (2003) demonstrates the long-term orbital stability of these objects with numerical integrations, in which they experience little semimajor axis variations for the entire 4-Gyr integration time (their figure 2). Later-discovered Sedna (Brown et al., 2004) also has perihelion so large ( $q \simeq 76$  au) that it cannot have been emplaced by only the four giant planets. Delsanti & Jewitt (2006) first used the word *detached* to describe TNOs that are currently away from Neptune’s scattering and resonant dynamics, and this was adopted by Gladman et al. (2008). Their emplacement might have been due to perturbations associated with extra bodies, either from a planet or a passing star, which will be studied in Chapter 5 and 6.

The entirety of hot TNOs, including the scattering, resonant, detached, and hot classicals, is often called the ‘implanted’ population. It is thought that these objects formed interior to 30 au and were implanted at their current locations by planetary migration and potentially other external perturbations. The process of the implantation will be overviewed in Chapter 4 and studied in Chapter 6.

### 1.3.3 Oort Cloud and Comets

A comet is an icy small Solar System body that, when passing close to the Sun, warms and begins to release gases, which produces a visible coma and sometimes a tail. Comets have relatively short lifespans, due to their orbital instability and volatile depletion during near-Sun perihelion passage (Fernandez, 1981; Levison & Duncan, 1994). Historically, known comets have been classified into two groups based on their orbital periods  $P$ : spc, defined as those having  $P < 200$  yr, and

Long-Period Comets (LPC), whose  $P > 200$  yr. The orbital inclinations of LPCs are nearly isotropic, whereas SPCs have inclinations strongly concentrated toward prograde orbits.

There are two primary comet reservoirs in the Solar System: the scattering disk for SPCs (see Section 1.3.2), and the Oort Cloud for LPCs. Oort (1950) first suggested a distant spherical and isotropic comet cloud to explain the apparent overabundance of LPCs with  $a > 10^4$  au in the catalog. While the observable Oort Cloud hypothesized by Oort himself starts at tens of thousands of au, a more populous inner reservoir is required to replenish the observable Oort Cloud (Hills, 1981). This came to be known as the inner Oort Cloud, ranging from 2,000 to 20,000 au (Weissman, 1990).

Duncan et al. (1987) first used numerical simulations to show the formation of the Oort Cloud (inner + outer) is mainly driven by a two-step dynamical processes:

1. The planetary perturbations (mainly from Uranus and Neptune) scattered objects to large semimajor axis  $a$  at nearly constant perihelion distance  $q$ ;
2. Those objects that went beyond a few thousand au had their  $q$  raised nad Q shrunk at fixed  $a$  by the galactic tidal field and/or stellar encounters, making comets exit the planetary region and forming the Oort Cloud.

Duncan et al. (1987) also estimated various timescales involving the building of the Oort Cloud (their figure 2). It was shown that the boundary of the inner Oort Cloud is determined by the diffusion timescale for planetary perturbations and the tidal torquing timescale from the Galactic disk, where  $\approx 2,000$  au is the distance at which the two timescales are equal. The boundary between the inner and the observable Oort Cloud of  $\approx 20,000$  au is set by the tidal torquing timescale and the comet's orbital period (also see Figure 3.2 in Section 3.1 for details). Estimates for the Oort Cloud's current mass and primordial implantation efficiency are highly uncertain (Portegies-Zwart et al., 2021), and I will come back to formation of Oort Cloud in Chapters 4 and 6.

### 1.3.4 Other Stable Niches in the Solar System

In addition to the regions which are dynamically stable for 4.5 Gyr and are known to host small-body populations, there are a few dynamical niches that numerical studies have shown to be stable for the age of the Solar System but which have no known members with demonstrated 4 Gyr stability.

The first such established case is for the ‘Uranus–Neptune’ belt near 26 au. Gladman & Duncan (1990) demonstrated some stable orbits for their 22.5 Myr maximum integration time, which Holman & Wisdom (1993) pushed to 800 Myr and demonstrated continued survival for this time. Holman (1997) extended the integration time to 4.5 Gyr, and found 0.3% of initially near-circular and near-planar orbits between the orbits of Uranus and Neptune (24–27 au) survive for the age of the Solar System. Zhang & Gladman (2022) thoroughly explored this region, proving 4.5 Gyr stability. There are still no known bodies discovered in the stable region (despite great sensitivity to them in trans-neptunian surveys), and Holman (1997) and Brunini & Melita (1998) argue that by the end of giant planet formation, it is likely that no bodies would remain at low  $e$  and  $i$  in this region.

Evans & Tabachnik (1999) mapped stable orbits in a hypothetical belt between Earth and Mars ( $a = 1.08\text{--}1.28$  au). They investigated the structure of those two belts in greater detail with 100 Myr simulations, exploring the role of mean-motion resonances with terrestrial planets, as well as the  $\nu_6$  and  $\nu_{16}$  secular resonances, in sculpting the belts (Evans & Tabachnik, 2002). In my study (Huang & Gladman, 2020, which is not part of this thesis), I demonstrated the Earth–Mars belt is only stable over 4.5 Gyr timescale over a restricted region of  $a = 1.09\text{--}1.17$  au and this low- $e$  and low- $i$  region is nearly unreachable by the continuous flux of NEOs from the main belt. The fact that it is unoccupied today provides an additional constraint to terrestrial planet formation models.

Based on numerical integrations of hypothetical Earth Trojan asteroids, Tabachnik & Evans (2000) demonstrated 50 Myr orbital stability of these objects and speculated by extrapolation of the decay rate that some orbits could survive for the age of the Solar System. Earth co-orbitals in horseshoe orbits (that is, not librating around a single Lagrange point like Trojans, but instead encompassing three points) have even longer stability time ( $\sim$ Gyr) than Earth Trojans have (Ćuk et al., 2012). It may

be thus more likely to find a primordial Earth horseshoe (Zhou et al., 2019), but all *known* Earth co-orbitals (of any type) have much shorter dynamical lifespans than the Solar System’s age (see references listed in Greenstreet et al. 2020). Recently, Zhou et al. (2019) concluded that the dynamical erosion over 4 Gyr, especially when accounting for Yarkovsky drift, would eliminate a population of sub-km primordial Earth co-orbitals surviving to the present day, but that km-sized could survive. Direct observational searches by Ye et al. (2020) and Markwardt et al. (2020) provided no Trojan detections down to sizes of a few hundred meters, leading to the conclusion that it is unlikely that any Earth Trojans still exist.

Thus, simply demonstrating that the dynamics permit a portion of phase space to be stable does not imply that a population currently exists; again, the perturbations inherent in planet formation likely resulted in no large stable Earth co-orbitals being present at the end of planet formation. The only temporary Earth Trojan 2011 TK<sub>7</sub> (Connors et al., 2011) is dynamically unstable and not consistent with a primordial origin. The known co-orbitals of the Earth are best explained as temporarily trapped near-Earth asteroids (Morais, 2002).

Inside Mercury’s orbit, the hypothesized population of small bodies, known as the Vulcanoids, was first proposed by Weidenschilling (1978). Evans & Tabachnik (1999) numerically studied the stability of the intra-mercurial region and found that the dynamical niche where Vulcanoids may exist is from 0.09 au to 0.21 au. However, accounting for Vulcanoid evolution under the Yarkovsky thermal force shows that objects with the diameter  $< 1$  km would be removed over the age of the Solar System (Vokrouhlický et al., 2000). A recent search for Vulcanoids with NASA’s STEREO spacecraft (Steffl et al., 2013) returned no detection, and thus the existence of Vulcanoids larger than 5.7 km in diameter was ruled out.

## 1.4 Thesis Outline

In this thesis, I will concentrate on exploring dynamical puzzles in trans-Neptunian space to better understand the formation and evolutionary history of the Solar System. In Chapter 2, I analyze the free inclinations of TNOs in the main Kuiper Belt, offering insight into their primordial inclination distribution. In Chapter 3, I examine a possible origin for the power-law distribution of semimajor axes for scattering

TNOs. Chapter 4 provides an introduction to planet formation and the early history of the Solar System. In Chapter 5, I conduct a detailed investigation of the weak encounter effect of a hypothesized rogue planet, which was temporarily present in the early Solar System, on the resonant and detached TNO populations within the Kuiper Belt at  $a < 100$  au. In Chapter 6, I elaborate on the rogue planet model and offer a more comprehensive study of the rogue planet's possible dynamical histories. This model, based on numerical integrations, aims to explain several long-standing puzzles in the outer Solar System, including the production of large- $a$  and high- $q$  TNOs like Sedna. In Chapter 7, I discuss potential improvements to the current study and explore new opportunities emerging from the findings of this thesis.

## Chapter 2

# Free Inclinations for TNOs in the Main Kuiper Belt

There is a complex inclination structure present in the Trans-Neptunian Object (TNO) orbital distribution in the main classical belt region (between orbital semi-major axes of 39 and 48 au). The long-term gravitational effects of the giant planets make TNO orbits precess, but non-resonant objects maintain a nearly constant ‘free’ inclination ( $I_{\text{free}}$ ) with respect to a local forced precession pole. Because of the likely cosmogonic importance of the distribution of this quantity, we tabulate free inclinations for all main-belt TNOs, each individually computed using barycentric orbital elements with respect to each object’s local forcing pole. We show that the simplest method, based on the Laplace-Lagrange secular theory, is unable to give correct forcing poles for objects near the  $\nu_{18}$  secular resonance, resulting in poorly conserved  $I_{\text{free}}$  values in much of the main belt. We thus instead implemented an averaged Hamiltonian to obtain the expected nodal precession for each TNO, yielding significantly more accurate free inclinations for non-resonant objects. For the vast majority (96%) of classical belt TNOs, these  $I_{\text{free}}$  values are conserved to  $< 1^\circ$  over 4 Gyr numerical simulations, demonstrating the advantage of using this well-

---

This chapter is based on the following published work: Y. Huang, B. Gladman & K. Volk, *Free Inclinations for Trans-Neptunian Objects in the Main Kuiper Belt*. The Astrophysical Journal Supplement Series **259**, 2 (2022)

conserved quantity in studies of the TNO population and its primordial inclination profile; our computed distributions only reinforce the idea of a very co-planar surviving ‘cold’ primordial population, overlain by a large  $I$ -width implanted ‘hot’ population.

## 2.1 Introduction

The outer region of our Solar System beyond Neptune hosts a large swarm of icy bodies that are planetesimals left over after the planet formation era. They contain valuable information about the Solar System’s distant past.

Over the past two decades, there is growing consensus that current transneptunian objects may have accreted from different regions in the protoplanetary disk: the cold population likely formed locally around  $a \approx 44$  au and hasn’t experienced significant subsequent dynamical excitation or collisional evolution, whereas the hot population likely formed closer to the Sun ( $a < 30$  au) and was implanted at the current locations during the late stages of planet formation. These two populations are mixed in the main Kuiper Belt ( $42 \lesssim a \lesssim 47$  au) radially and vertically, with the inclination being a rough proxy to separate them (see Gladman & Volk 2021 for a detailed review).

Brown (2001) first fit the inclination distribution of all classical TNOs (i.e. main belt TNOs not in mean motion resonances with Neptune) using a functional form of  $\sin I$  multiplied by a sum of two Gaussians consisting of a cold component (of width  $\sim 2.2^\circ$ ) and a hot component ( $\sim 17^\circ$ ). Levison & Stern (2001) noticed the observed cold population lacks large objects, which was later further confirmed by several independent Kuiper belt surveys showing the cold population has a significantly steeper absolute magnitude (H) distribution than the hot population (Bernstein et al., 2004; Elliot et al., 2005; Fraser et al., 2010; Petit et al., 2011; Kavelaars et al., 2021). The perihelion distance distribution of the cold population is more confined than those of the hot (Petit et al., 2011). The cold classicals are also known to have a higher abundance of binary TNOs (see, e.g. Noll et al., 2020), especially those with comparable sizes. Furthermore, a statistically significant correlation between the color and inclination of the classical objects has been observed, with low-inclination objects more likely to be red and high-inclination objects likely to be more neutral

in color (Doressoundiram et al., 2002; Trujillo & Brown, 2002; Doressoundiram, 2003; Peixinho et al., 2008). High-precision colors from optical and near-infrared observations have demonstrated that the cold classicals have different surface properties than the hot members (Pike et al., 2017b; Schwamb et al., 2019; Müller et al., 2020; Fernández-Valenzuela et al., 2021). All of these properties are consistent with the two populations having distinct formation histories. As a result, the orbital distributions, especially the inclination distributions, of the two populations shed light upon their dynamical past and deserve detailed investigation with the most recent sample.

A common practice in TNO research is to split the classical TNOs into hot and cold populations with a simple inclination cut to facilitate, for example, physical property studies of the two populations or comparisons between observationally derived population estimates and those from dynamical models.

For example, Bernstein et al. (2004), Petit et al. (2011) and Fraser et al. (2014) all used a cut of  $I < 5^\circ$  in ecliptic inclination to identify a dominantly cold population, while Peixinho et al. (2008) used  $12^\circ$ . The ecliptic  $I$ , however, varies over time as an artifact of the reference frame choice: a TNO's orbit precesses around its local forcing pole with a fixed  $I_{\text{free}}$  and a constant frequency, the result of which, in ecliptic space, is a non-constant precession (sometimes not even a precession but a confined oscillation in the longitude of ascending node  $\Omega$ ) with a varying  $I$  (see section 7.4 of Murray & Dermott 1999 or figure 1 of Gladman & Volk 2021). This naturally makes  $I_{\text{free}}$ , a conserved quantity regardless of the choice of reference frame, preferable to the ecliptic inclination, which is the commonly tabulated quantity and useful for orbit comprehension.

We note that because the real classical belt TNO distribution is a sum of two overlapping components that each have different inclination widths, there will always be some level of contamination when using a simple cut (see figure 2 of Dawson & Murray-Clay (2012), for example). Cutting in  $I_{\text{free}}$  rather than ecliptic  $I$ , however, dramatically improves how well the two components are isolated.

Van-Laerhoven et al. (2019) showed that when using a free inclination cut of  $4^\circ$ , the cold classical TNOs are best fit with a narrower width of  $\simeq 1.75^\circ$ , strongly limiting its past perturbation. Gladman & Volk (2021) also found this cut results in a cleaner separation in TNO colors (their figure 6). Because of this superiority, the

$4^\circ$  cut in free inclination is also adopted in Kavelaars et al. (2021).

With today’s large TNO sample, including survey data from the Canada-France Ecliptic Plane Survey (CFEPS, Jones et al. 2006), the Deep Ecliptic Survey (Adams et al., 2014), the Outer Solar System Origins Survey (OSSOS, Bannister et al. 2018), and the Dark Energy Survey (Bernardinelli et al., 2022), it is thus desireable to compute  $I_{\text{free}}$  for each main belt TNO. To do this, the local forcing planes or the forcing poles, relative to which  $I_{\text{free}}$  is measured, must be correctly calculated. Brown & Pan (2004) first realized the apparent mean plane of the TNOs differs significantly from the Solar System’s invariable plane (the plane defined by the average angular momentum of the larger planets). In contrast, Elliot et al. (2005) found the mean plane of the classical TNOs is more consistent with the invariable plane than with the local Laplacian plane (the latter being the plane perpendicular to the local forcing pole discussed below). In a subsequent study, Chiang & Choi (2008) investigated the theoretically predicted locations of forcing poles, pointing out that the classical belt plane is significantly warped by the  $\nu_{18}$  secular resonance near  $a = 40.5$  au; i.e., the local forcing plane in the main belt changes significantly with semimajor axis. They also confirmed the conservation of TNO free inclination with respect to their calculated time-variable poles for 4 Gyr, but only for objects away from the singularity associated with the secular resonance.

Given that the calculation of the forcing poles (and thus the free inclinations) is somewhat complicated near secular resonances and that a non-negligible portion of the classical belt is affected by this, a better approach to calculating free inclinations is warranted. In the present work, we implement a new method based on doubly averaging the Hamiltonian to obtain the expected nodal precession rates and the correct forcing pole for each TNO. The free inclinations generated by this new algorithm represent a significant improvement over those given by the often-used linear secular theory, especially for objects within a few au of the  $\nu_{18}$  secular resonance singularity (see Section 2.2.2). We thus tabulated the correct  $I_{\text{free}}$  of each main-belt TNO along with its barycentric orbital elements in Table 2.1.

## 2.2 Computation of Free Inclinations

Because of the cosmogonic significance of the cold and hot populations, both for the dynamical structure of the transneptunian region and the interpretation of surface properties inferred from photometry and spectra, we chose to compute and publish TNO free inclinations. Because as a *population* the cold objects exist only in the main belt between the 3:2 and 2:1 mean motion resonances with Neptune, our interpretation is that this component split is only sensible in this semimajor axis range (objects that might have low inclinations at other semimajor axes are best interpreted as the low- $I$  tail of the implanted hot component's inclination distribution); we thus confine ourselves to the main belt objects in this work. In Section 2.2.1, we describe how we selected the observed TNOs to include in our analysis. Section 2.2.2 describes our approach to calculating free inclinations, and Section 2.2.3 demonstrates that the newly calculated free inclinations are a better-conserved quantity than those calculated using linear theory.

### 2.2.1 Dynamical Classification of TNOs

We began by downloading the most recent sample of main belt TNOs from the Jet Propulsion Laboratory Small-Body DataBase (JPL SBDB)<sup>1</sup>. We constrained the *heliocentric* semimajor axis  $a$  to the range of (39.4, 47.7) au and the 1-sigma uncertainty in  $a$  to  $\delta a < 0.1$  au. This  $a$  range is the region between the 3:2 and the 2:1 neptunian MMRs, which is frequently referred to as the ‘main Kuiper Belt’ in literature (e.g., Gladman & Volk, 2021). We also added two additional TNOs to the sample: 486958 Arrokoth (2014 MU<sub>69</sub>), the target TNO visited by the New Horizons spacecraft on Jan. 1, 2019 (Stern et al., 2019) whose orbit-fit accuracy is not accurately reflected in JPL’s database, and 2005 JY<sub>185</sub>, an OSSOS object whose  $a$  uncertainty given by JPL is slightly above the 0.1 au but our own estimate is  $\delta a \simeq 0.05$  au (Bannister et al., 2018). This resulted in 2018 objects being selected.

The JPL SBDB provides orbital elements in the heliocentric IAU76/J2000 ecliptic reference frame. However, for the study of TNO dynamics, barycentric orbital elements are preferable to heliocentric ones. TNOs are relatively far away from the Sun, and the small wobbling of the Sun’s position under planetary perturbations

---

<sup>1</sup>[https://ssd.jpl.nasa.gov/sbdb\\_query.cgi](https://ssd.jpl.nasa.gov/sbdb_query.cgi), retrieved on October 5th, 2021.

(mainly from the giant planets) leads to variation of TNO heliocentric orbital elements on timescales of each giant planet's orbital period (Gladman & Volk, 2021). The barycenter of the Solar System, on the other hand, is far more stable in the eyes of TNOs. As a result, orbital elements in this paper and the appended table are all barycentric elements.

These TNOs are distributed across the whole main classical belt, starting from the 3:2 neptunian mean-motion resonance ( $a = 39.4$  au) and ending at the 2:1 resonance (47.7 au). Several low-order resonances are also embedded in the main belt, the most important of which are the 5:3 (42.3 au), the 7:4 (43.7 au), and the 9:5 (44.6 au). We classified the 2018 TNOs in our sample according to their current dynamical state (Gladman et al., 2008), separating the classical TNOs from the resonant objects and the scattering objects (note that by definition detached objects have  $a > 47.7$  au, therefore they cannot be in this sample). To do this, we integrated the best-fit orbit for each TNO forward 10 Myr in time under the influence of the Sun and the four giant planets. We used the MERCURIUS algorithm within the REBOUND orbital integration software package (Rein & Liu, 2012); this algorithm uses REBOUND's WHFAST symplectic integrator (Rein & Tamayo, 2015) for the majority of time steps and the adaptive-stepsize IAS15 integrator (Rein & Spiegel, 2014) to resolve close encounters between test particles and planets. We used a base time step of 0.25 years and an output interval of 1,000 years for these integrations.

After the integration, the TNO classification was carried out manually: each particle's  $a$ , eccentricity ( $e$ ), and critical angle for the closest resonance ( $\varphi$ ) are plotted. A human operator then decided to tag it as *scattering* ( $a$  alters more than 1 au), *resonant* ( $\varphi$  ceases to circulate at any moment in the 10 Myr integration), or *classical* (for a non-scattering and non-resonant particle). Although recent papers have described TNO classification using automatic pipelines (Khain et al., 2020) or machine learning algorithms (Smullen & Volk, 2020), we decided to do the job manually as the sample was not too large and this remains the most accurate method. Our criterion for resonant objects is quite loose; this is motivated by the fact that even a brief interaction with a mean-motion resonance can significantly alter  $I_{\text{free}}$  (see Section 2.2.3). For the resonant identification, we searched through resonances  $i:j$  with  $i = 1 \dots 20$  and  $j = 1 \dots 20$  in the  $a$  range of (39.4, 47.7) au, which includes 23 distinct resonances with the 20:11 being the highest-order one.

Among the sample of 2018 objects we integrated and classified, 66% (1332/2018) are classical, 31% (622/2018) are resonant, and only 3% (64/2018) are scattering. These percentages have biases and should not be interpreted as the intrinsic or cosmogonic dynamical distribution in this semimajor axis range<sup>2</sup>. Note that our TNO classification is conducted with the purpose of better presenting our results in the next section; it should not be treated as the ‘definitive’ classification for these objects because we are not considering orbital uncertainties by integrating clone orbits.

### 2.2.2 Free Inclination with the Correct Precession Rate

In Laplace-Lagrange secular theory, the barycentric inclination vector (also called the orbit pole) of a TNO (typically measured from the ecliptic plane) constantly rotates around its *local forcing pole* under the perturbations of planets. When perturbed by a single planet, an object’s forcing pole is constant and simply perpendicular to the planet’s orbital plane. However, when perturbed by multiple planets, the local forcing pole constantly changes with time. The time-dependent location of the forcing pole is predicted by the Laplace-Lagrange secular theory, which gives the following rectangular components of the forcing pole

$$\begin{aligned} q &= I \cos \Omega, \\ p &= I \sin \Omega, \end{aligned} \tag{2.1}$$

at any given semimajor axis induced by the orbits of all planets:

$$\begin{aligned} q &= I_{\text{free}} \cos(Bt + \gamma) + q_{\text{forced}}(t), \\ p &= I_{\text{free}} \sin(Bt + \gamma) + p_{\text{forced}}(t), \end{aligned} \tag{2.2}$$

where  $I_{\text{free}}$  is the free inclination,  $B$  denotes the expected precession rate of the small body’s node, and  $q_{\text{forced}}$  and  $p_{\text{forced}}$  are components of the forcing poles imposed by planetary perturbations (see Section 1.1.5). In the present work, only the four giant

---

<sup>2</sup>In particular, many of the scattering objects in this semimajor axis range have perihelia well inside of Neptune and were only detected with their faint absolute magnitudes because of their small current heliocentric distances; they are thus over-represented in our sample compared to the classical and resonant objects with brighter absolute magnitudes.

planets are taken into account, so the resulting forced terms are given by

$$\begin{aligned} q_{\text{forced}}(t) &= - \sum_{j=5}^8 \frac{\chi_j}{B - f_j} \cos(f_j t + \gamma_j), \\ p_{\text{forced}}(t) &= - \sum_{j=5}^8 \frac{\chi_j}{B - f_j} \sin(f_j t + \gamma_j), \end{aligned} \quad (2.3)$$

where  $j$  denotes the index of the inclination eigenfrequencies/eigenvectors ( $f_j$  and  $I_{ji}$  below) of the Solar System. In Laplace-Lagrange secular theory,  $B$  is the summation of precession rates contributed by each planet ( $B_j$ ), which depend on both the planetary and the small body's semimajor axes ( $a_j$  and  $a$ ).

For TNOs in the main belt (where  $\alpha_j = a_j/a < 1$  always holds),  $B$ ,  $B_j$ , and  $\chi_j$  are given by:

$$\begin{aligned} B_j &= \frac{1}{4} \frac{m_j}{M_\odot} n \alpha_j b_{3/2}^{(1)}(\alpha_j), \\ B &= - \sum_{j=5}^8 B_j, \\ \chi_j &= \sum_{j=5}^8 B_j I_{ji}, \end{aligned} \quad (2.4)$$

where  $m_j$  is the mass of the  $j$ -th planet, and  $n$  is the mean motion of the small body.  $b_{3/2}^{(1)}(\alpha_j)$  is the Laplace coefficient (Equation 1.23).

The Laplace-Lagrange secular theory predicts a nodal precession rate for each TNO, under the assumption that both the planets and the TNOs have near circular and planar orbits. As a result, the forced inclination  $I_{\text{forced}}$  and the longitude of ascending node  $\Omega_{\text{forced}}$  are both functions of the semimajor axis only.

Chiang & Choi (2008) showed that in the main classical belt, the forcing poles at various semimajor axes form a line in  $(q, p)$  space, rotating around the location of the Solar System's invariable pole with a 1.9 Myr period. As the semimajor axis goes to infinity (although in practice needs only  $a > 45$  au), the forcing pole approaches the invariable plane pole and is therefore fixed.

A TNO's current osculating orbital inclination is a sum of this locally forced inclination and its free inclination (also sometimes called the 'proper' inclination, see

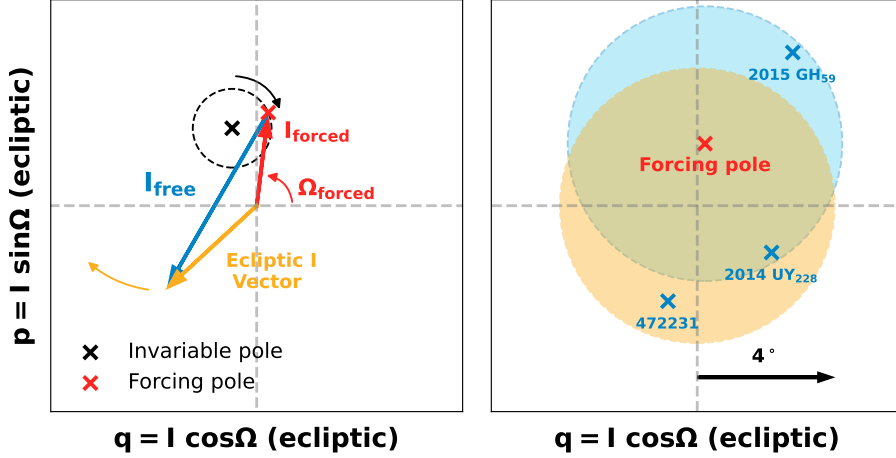


**Figure 2.1:** Left panel: Polar and rectangular coordinate depiction of the ecliptic (orange), the forced (red), and the resultant free (blue) inclination vectors of a TNO in the main classical belt. For this object, the forcing center (red cross) rotates around the Solar System's invariable pole (black cross) with a  $\simeq 2$  Myr period, the path of which is the black dashed circle. The free inclination (blue) vector rotates around the time-varying forcing center at a constant nodal precession rate  $B$ , keeping its magnitude  $I_{\text{free}}$  unchanged. The composition of these two movements gives rise to a more complicated inclination evolution in the ecliptic reference frame (orange vector with arrow denoting its approximate sense of motion). Right panel: The difference between a 4° cut in ecliptic inclination (orange circle centered at origin) and a 4° cut in free inclination (blue circle centered at the forcing pole). Three TNOs with almost identical forcing centers are marked in blue crosses, with light blue being colds object ( $I_{\text{free}} < 4^\circ$ ) and dark blue being the hot object ( $I_{\text{free}} > 4^\circ$ ). If one were to use ecliptic inclinations to split the populations, 472231 (2014 FU<sub>71</sub>) would be misclassified as cold while 2015 GH<sub>59</sub> (see Figure 2.4) would be misclassified as hot. TNOs in the overlapping area will maintain  $I_{\text{free}} < 4^\circ$  and are correctly classified currently but some with  $I_{\text{free}} > 2^\circ$ , such as 2014 UY<sub>228</sub>, will cycle to ecliptic  $I > 4^\circ$  on Myr timescales.

Equation 2.2). By calculating and then subtracting the forced pole from an object’s ecliptic inclination, the resultant free inclination vector components are obtained. The magnitude of the free inclination vector is  $I_{\text{free}}$ , and the phase provides the free ascending node  $\Omega_{\text{free}}$ . In Figure 2.1, we illustrate the geometric relationship between the ecliptic (orange) inclination, the forced pole (red), and the free (blue) inclination in the rectangular  $(q, p)$  space. We also refer the reader to Gladman & Volk (2021)’s figure 1 and their supplemental video for more details.

In theory, the free inclination of a non-resonant, non-scattering object is constant over time. The conservation of  $I_{\text{free}}$  at 38.6 au and at 43 au for 4 Gyr has been verified by numerical integrations (Chiang & Choi, 2008). However, we find that near the  $\nu_{18}$  secular resonance at  $a = 40.5$  au, the  $I_{\text{free}}$  of TNOs calculated by the linear theory are not conserved even over our much shorter 10 Myr integrations. Figure 2.2 shows the barycentric ecliptic  $a$  and  $I$  evolutions (blue curves) of 2014 QU<sub>510</sub> as well as its  $I_{\text{free}}$  calculated by the linear theory (red dotted curve). To compute the linear secular  $I_{\text{free}}$  evolution of this object over our simulation, we recalculate the eigenmodes of the Solar System at each time output, based on the constantly-evolving orbits of the 4 giant planets (using the method described in Murray & Dermott 1999) and use those to determine 2014 QU<sub>510</sub>’s forced plane and thus free inclination. As shown in Figure 2.2, the linear theory  $I_{\text{free}}$  of this object is not conserved at all; its amplitude even exceeds the variation of its osculating ecliptic inclination.

The varying  $I_{\text{free}}$  computed from linear theory near  $a = 40.5$  au demonstrates that the forcing pole is not correctly predicted near the secular resonance. The reason for this failure is that in the linear theory, the expected precession rate ( $B$  in Equation 2.4) of a TNO is only a function of its semimajor axis. The real nodal precession rate, however, also depends on the object’s eccentricity and inclination. Ignoring high-order terms in  $e$  and  $I$  produces an inaccurate precession rate, resulting in the incorrect determination of its forcing pole. This effect is particularly strong near a secular resonance, due to the fact that the term  $B - f_j$  (where  $f_j$  is an eigenfrequency) exists in the denominator of the forcing pole expression (Equation 2.3).

To get the correct  $I_{\text{free}}$ , especially near the  $\nu_{18}$ , we adopt a semi-analytical method to recalculate the correct precession rate at every time step. It’s based on numerically averaging the TNO’s Hamiltonian over two ‘fast angles’ (called the *double average* method hereafter), which avoids any truncation in powers of the small body’s ec-

centricity and inclination (Williams, 1969). This approach has been commonly used in Solar System studies (Henrard, 1990; Morbidelli & Henrard, 1991; Froeschlé & Morbidelli, 1994; Michel & Froeschlé, 1997), in order to compute the locations of secular resonances over a large range of  $e$  and  $I$ . We summarize the major steps to obtain the correct precession rates ( $B$  and  $B_j$ ) using the double average method (see Michel & Froeschlé 1997 and chapter 8 of Morbidelli 2002 for more complete details).

Assuming all the planets to be on co-planar circular orbits and the gravitational constant  $\mathcal{G} = 1$ , the Hamiltonian  $\mathcal{H}$  of a TNO perturbed by the  $j$ -th planet can be written as

$$\mathcal{H} = -\frac{1}{2L^2} - \underbrace{\mu_j \mathcal{P}_j}_{\mathcal{H}_{\text{kep}}} (L, G, H, L_j; l, g, h, l_j) + \underbrace{\mathcal{H}_{\text{sec}}^{(j)}}_{\mathcal{H}_{\text{sec}}}, \quad (2.5)$$

where  $\mathcal{H}_{\text{kep}}$  is the integrable Keplerian motion of the TNO around the Sun and  $\mathcal{H}_{\text{sec}}^{(j)}$  accounts for the planetary perturbation by the  $j$ -th planet, in which  $\mu_j = \mathcal{G}m_j$  and  $\mathcal{P}_j$  is the normalized term that only depends on the Delaunay variables (defined in 1.11). Assuming the TNO is not trapped inside a mean-motion resonance, then the secular Hamiltonian  $\mathcal{H}_{\text{sec}}^{(j)}$  can be averaged over the two unrelated fast angles,  $l$  and  $l_j$  (a ‘double average’), which yields

$$\bar{\mathcal{H}}_{\text{sec}}^{(j)} = -\mu_j \mathcal{P}_j (G, H; g, h), \quad (2.6)$$

To write the averaged Hamiltonian in explicit form (1.15):

$$\bar{\mathcal{H}}_{\text{sec}}^{(j)} = -\frac{\mu_j}{(2\pi)^2} \int_0^{2\pi} \int_0^{2\pi} \left( \frac{1}{\|\mathbf{r} - \mathbf{r}_j\|} - \frac{\mathbf{r} \cdot \mathbf{r}_j}{\|\mathbf{r}_j\|^3} \right) dl dl_j, \quad (2.7)$$

in which the vectors  $\mathbf{r}$  and  $\mathbf{r}_j$  denote the heliocentric positions of the small body and of the  $j$ -th planet, respectively, and  $\Delta_j = \mathbf{r} - \mathbf{r}_j$ . Under the approximation that eccentricities and inclinations of the planets are zero, one of the integrals can

be analytically computed using the complete elliptic function of the first kind  $K$ :

$$\int_0^{2\pi} \left( \frac{1}{\|\mathbf{r} - \mathbf{r}_j\|} - \frac{\mathbf{r} \cdot \mathbf{r}_j}{\|\mathbf{r}_j\|^3} \right) dl_j = \int_0^{2\pi} \frac{1}{\|\Delta_j\|} dl_j = \frac{4}{\sqrt{r^2 + a_j^2}} \sqrt{1 - \frac{\eta}{2}} K(\eta), \quad (2.8)$$

where

$$\eta = \frac{4a_j \sqrt{x^2 + y^2}}{r^2 + a_j^2 + 2a_j \sqrt{x^2 + y^2}}, \quad (2.9)$$

and  $x$  and  $y$  are the coordinates of  $\mathbf{r}$ 's projection on the plane of the planetary orbit, with  $r = \|\mathbf{r}\|$ . It is worth noting that Equation 2.8 has the physical interpretation of the potential from a homogeneous ring (averaging the Hamiltonian over a planet's mean anomaly  $l_j$  is equivalent to spreading out the planetary mass on a circular ring of radius  $a_j$ ). Combining Equation 2.7 through 2.9, we have

$$\begin{aligned} \bar{\mathcal{H}}_{\text{sec}}^{(j)} &= -\frac{\mu_j}{\pi^2} \int_0^{2\pi} \sqrt{\frac{1-\eta/2}{r^2 + a_j^2}} K(\eta) dl, \\ \bar{\mathcal{H}}_{\text{sec}} &= \sum_{j=5}^8 \bar{\mathcal{H}}_{\text{sec}}^{(j)}, \end{aligned} \quad (2.10)$$

where  $\bar{\mathcal{H}}_{\text{sec}}$  is the Hamiltonian accounts for the total planetary perturbations. The expected nodal precession rate contributed by each planet  $B_j$  and the total precession rate  $B$  can thus be obtained through numerical differentiation

$$\begin{aligned} B_j &= \dot{h}^{(j)} = \frac{\partial \bar{\mathcal{H}}_{\text{sec}}^{(j)}}{\partial H}, \\ B &= - \sum_{j=5}^8 B_j, \end{aligned} \quad (2.11)$$

and the resulted  $B_j$  and  $B$  are not only functions of  $a$  and  $a_j$ , but also functions of  $e$ ,  $I$ , and  $\omega$ . Replacing the nodal precession rates from Equation 2.2 to 2.4, we get the correct forcing pole ( $q_{\text{forced}}$ ,  $p_{\text{forced}}$ ) and thus the correct  $I_{\text{free}}$  for each TNO.

In summary, the double average method calculates the precession rate as a function of  $a$ ,  $e$ ,  $I$ , and  $\omega$ , instead of just  $a$  as in the linear theory. As a result, the method

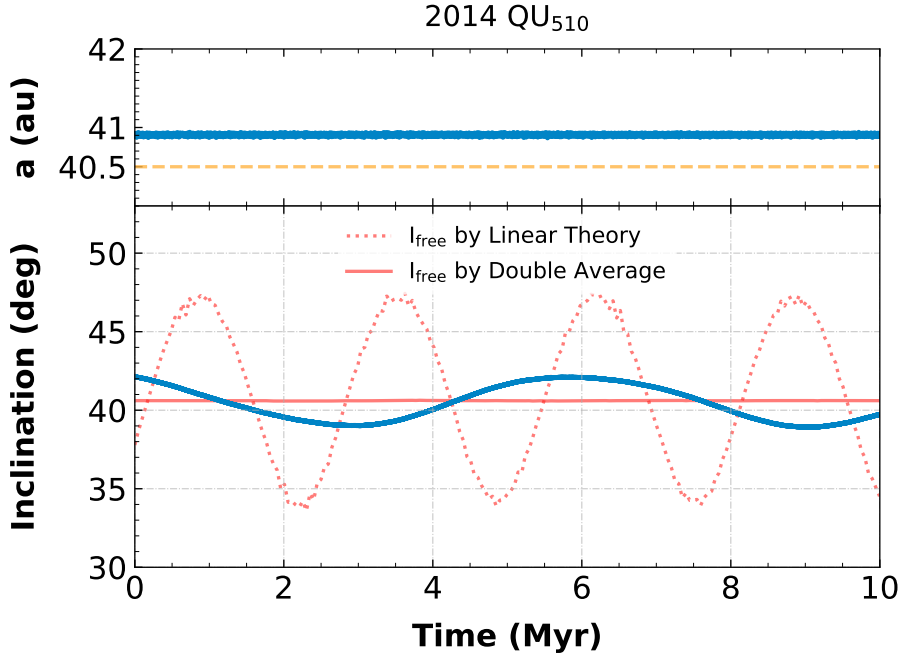


**Figure 2.2:** Blue curves: barycentric  $a$  (top panel) and ecliptic  $I$  (bottom panel) evolution of 2014 QU<sub>510</sub> over 10 Myr. The orange dashed line in the upper panel marks the semimajor axis of the  $\nu_{18}$  secular resonance for circular and planar orbits. Red curves:  $I_{\text{free}}$  calculated by the linear theory (dotted curve) and the semi-analytical double average method (solid curve). The ranges of the blue curve, the dotted curve, and the solid line are  $3.2^\circ$ ,  $14.4^\circ$ , and  $0.06^\circ$ , respectively; the double average method yields a much better-conserved value of  $I_{\text{free}}$ .

produces a rate closer to the TNO's true precession rate, and thus a more accurate forcing pole and a better conserved free inclination. Taking the object from Figure 2.2 as an example: the linear theory predicts a nodal rate of  $-0.63''/\text{yr}$ , which is very close to the  $f_8 = -0.68''/\text{yr}$  inclination eigenfrequency of the Solar System (Brouwer & Woerkm, 1950). In contrast, the real precession rate according to numerical integration is only  $-0.206''/\text{yr}$ , which is much closer to what the double average method predicts (a rate varying between  $-0.19''/\text{yr}$  to  $-0.21''/\text{yr}$  as the orbit evolves). The  $\sim 40^\circ$  inclination makes the TNO precess slower than a planar orbit

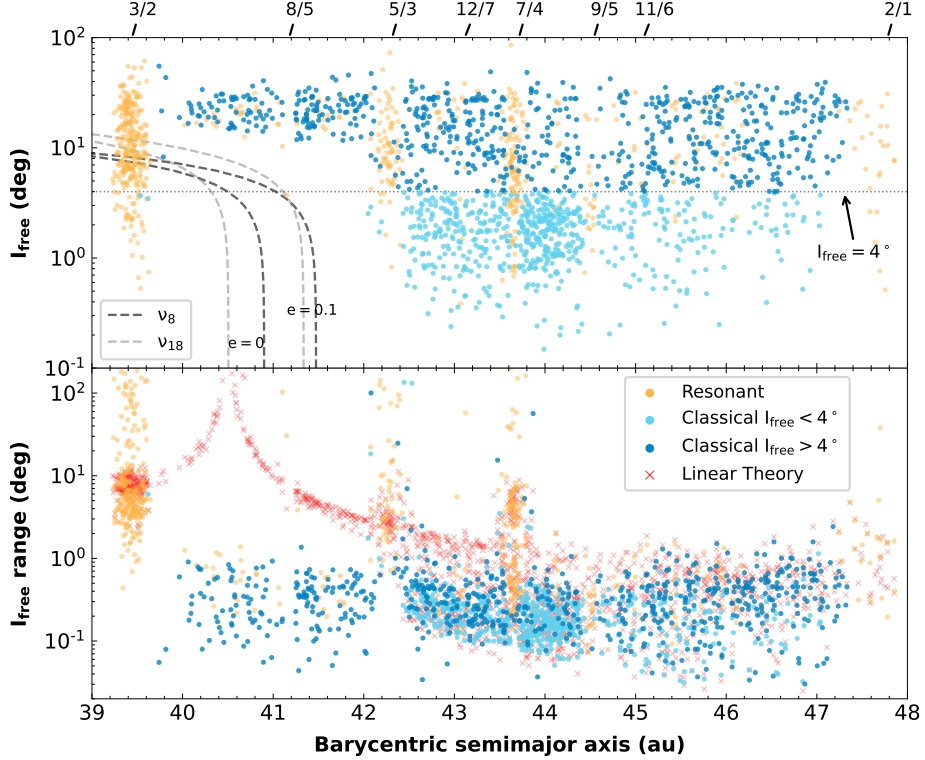
of the same  $a$ , pulling itself away from the  $\nu_{18}$  secular resonance despite being near  $a = 40.5$  au. Obviously, the double average method provides a more accurate precession rate, resulting in a much better conserved  $I_{\text{free}}$  for the TNO (red solid line in Figure 2.2).

### 2.2.3 Free Inclination Results

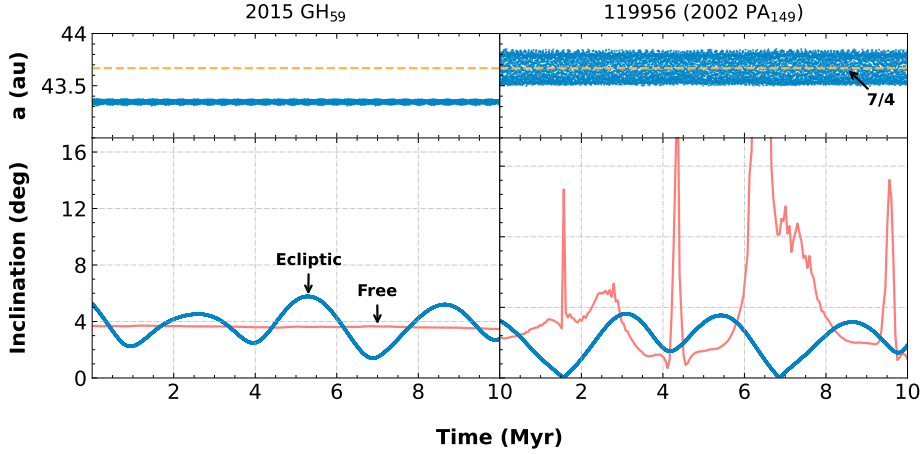
We applied both the linear theory and the double average method to the calculation of  $I_{\text{free}}$  for each of the non-scattering TNOs in our sample. Figure 2.3’s upper panel shows the double-averaging  $I_{\text{free}}$  as a function of  $a$ . To illustrate the conservation of  $I_{\text{free}}$  over 10 Myr timescales, the bottom panel shows the variation,  $I_{\text{free}}$  range  $\equiv \max(I_{\text{free}}) - \min(I_{\text{free}})$ , over the integration for both methods. The  $I_{\text{free}}$  range values show that, as expected, near the  $\nu_{18}$  resonance at 40.5 au, the linear theory fails to produce a well-conserved  $I_{\text{free}}$  (red crosses in Figure 2.3), whereas even near the secular resonance our method (blue dots) provides free inclinations that are as well conserved as for the rest of main-belt classicals. The vast majority of classicals have  $I_{\text{free}}$  conserved to better than  $1^\circ$ , although this is not the case for resonant objects (orange dots) and a handful of near-resonant objects. Because the averaging method doesn’t take into account the Hamiltonian’s resonant terms, it cannot predict the correct nodal precession rate for objects affected by the mean motion commensurabilities. As a result, TNOs near and in the 3:2 and the 5:3 resonances have a significantly large  $I_{\text{free}}$  range (bottom panel of Figure 2.3). The 7:4 resonance, however, hosts TNOs with both large and small  $I_{\text{free}}$  ranges; the latter group are all objects with relatively small eccentricities ( $e < 0.15$ ) and the vast majority have  $I_{\text{free}} < 10^\circ$ . Higher-order resonances in the main belt seem to have no clear effect on the object’s  $I_{\text{free}}$  range, presumably due to their relatively weak strength.

Figure 2.3’s lower panel aligns with our expectations: classical TNOs not affected by resonant dynamics generally have very small  $I_{\text{free}}$  variations, while resonant TNOs (especially those in strong, low-order resonances) have significantly large  $I_{\text{free}}$  ranges. In other words, in Figure 2.3’s upper panel, only for the classical objects (blue dots) can  $I_{\text{free}}$  be trusted to be cosmogonically relevant.

If we limit our scope only to the classical TNOs in the  $I_{\text{free}} - a$  distribution, there are a few things worth pointing out:



**Figure 2.3: Upper panel:** Our computed values of current  $I_{\text{free}}$  for each TNO as a function of its barycentric semimajor axis  $a$  (note the log scale on the y-axis). Resonant objects are shown in orange and classical TNOs in blue, with light blue and dark blue denoting classical TNOs with  $I_{\text{free}} < 4^\circ$  and  $I_{\text{free}} > 4^\circ$ , respectively. The dashed curves in the lower left portion of the plot give the center of the  $\nu_8$  (black) and  $\nu_{18}$  (gray) secular resonances, with curves on the left being  $e = 0$  and those on the right being  $e = 0.1$  (see text). **Bottom panel:** The range in calculated  $I_{\text{free}}$  values (log scale) over our 10 Myr integrations as a function of  $a$ . For objects with  $a \simeq 39.7$ – $42.5$  au, the proximity of the  $\nu_{18}$  secular resonance results in the TNO's expected precession rate being dramatically incorrect, resulting in widely-varying values of  $I_{\text{free}}$  when calculated using the linear theory (red crosses). When the nodal precession rate for non-resonant TNOs is corrected (using the double average method), well-preserved free inclinations are obtained for the classical TNOs (blue dots); resonant TNOs (orange dots) can have highly-variable values for their calculated  $I_{\text{free}}$  even with the double average method because the resonant dynamics are not accounted for.



**Figure 2.4:** Evolution in  $a$  (upper panels; blue curves), ecliptic  $I$  (lower panels; blue curves) and  $I_{\text{free}}$  (lower panels; red curves) over 10 Myr for classical TNO 2015 GH<sub>59</sub> (left) and resonant TNO 119956 (2002 PA<sub>149</sub>; right). The classical TNO has initial J2000  $I > 5^\circ$ , but its  $I_{\text{free}}$  is always less than  $4^\circ$  (see also Figure 2.1's right panel). The resonant object is in the 7:4 resonance and its  $I_{\text{free}}$  (as calculated by the double average method) is not conserved; this is expected because neither linear secular theory nor the double average method is appropriate for resonant TNOs.

1. Almost every classical TNO between the 3:2 and the 5:3 neptunian resonances has  $I_{\text{free}}$  larger than  $10^\circ$ , due to the presence of  $\nu_8$  and  $\nu_{18}$  secular resonances in the low- $I$  region. The  $\nu_8$  resonance will excite eccentricities for lower- $I$  orbits to Neptune crossing, resulting in TNO removal. We computed the positions of these resonances (gray and black dashed curves) by iteratively converging (for a given  $e$ ) to the resonant secular frequency ( $g_8$  or  $f_8$ ) by varying  $I_{\text{free}}$ ; the  $e = 0.1$  curve is very similar to those shown in Knežević et al. (1991) and Morbidelli (2002).
2. The 8:5 resonance might be viewed as surprisingly devoid of TNOs, leaving a semimajor axis gap in the hot population at  $a = 41.2$  au. We integrated five of the 8:5 resonant objects to 4 Gyr; none of them survives for the age of the Solar System, with a median dynamical lifetime of only 700 Myr. None of the real objects is thus deeply embedded and stabilized by the mean-motion

resonance for the age of the Solar System. Given that the nearby third-order 7:4 resonance does not deplete on this same timescale (even at large  $I_{\text{free}}$ ), this contrast seems puzzling. It is plausible that the proximity to the two secular resonances is contributing to this instability, but may instead imply something about capture into this resonance out of the abundant ancient scattering population.

3. There is a few-degree wide sparsely populated region in the free inclination distribution (sitting just above  $I_{\text{free}} = 4^\circ$ ) in the semimajor axis range between the 5:3 and the 7:4 resonances in the main belt. This ‘gap’ is nearly devoid of TNOs and exists only in the  $I_{\text{free}}$  space; it would be completely hidden if one were to plot the distribution using ecliptic  $I$ . This explains why Van-Laeerhoven et al. (2019) found isolating  $I_{\text{free}} < 4^\circ$  is an excellent way to reduce contamination between hot and cold, minimizing interlopers when measuring the width of the cold population’s inclination distribution. We expand upon this in the Discussion section.

To show how the resonant dynamics affects  $I_{\text{free}}$ , we plot (Figure 2.4) the orbital evolution of an object (119956 = 2002 PA<sub>149</sub>) trapped in the 7:4 resonance with moderate  $e \simeq 0.17$  and a nearby cold classical TNO (2015 GH<sub>59</sub>). Despite maintaining a relatively low ecliptic inclination, the resonant object’s calculated free inclination is extremely variable (right panel of Figure 2.4) because the assumptions underlying the linear secular or the double average  $I_{\text{free}}$  calculation are not valid for resonant objects; this highlights why we needed to classify our TNO sample prior to determining free inclinations. In contrast, the classical TNO in the left panel of Figure 2.4 demonstrates why  $I_{\text{free}}$  is superior to the ecliptic inclination in separating objects into cold versus hot populations: 2015 GH<sub>59</sub> is an object with a  $5.3^\circ$  ecliptic inclination currently, which would place it in the hot population according to most ecliptic inclination cuts. In addition, the 10-Myr average of its ecliptic inclination is  $4.4^\circ$ , still above a typical  $4^\circ$  cut. However, our calculation shows its free inclination is only  $3.69^\circ$  with a range of  $0.25^\circ$ , which keeps it always below a  $4^\circ$  cut and thus always a cold object.

We demonstrated above the conservation of  $I_{\text{free}}$  for classical objects over 10 Myr timescales. But what one truly cares about is whether  $I_{\text{free}}$  is stable for the age

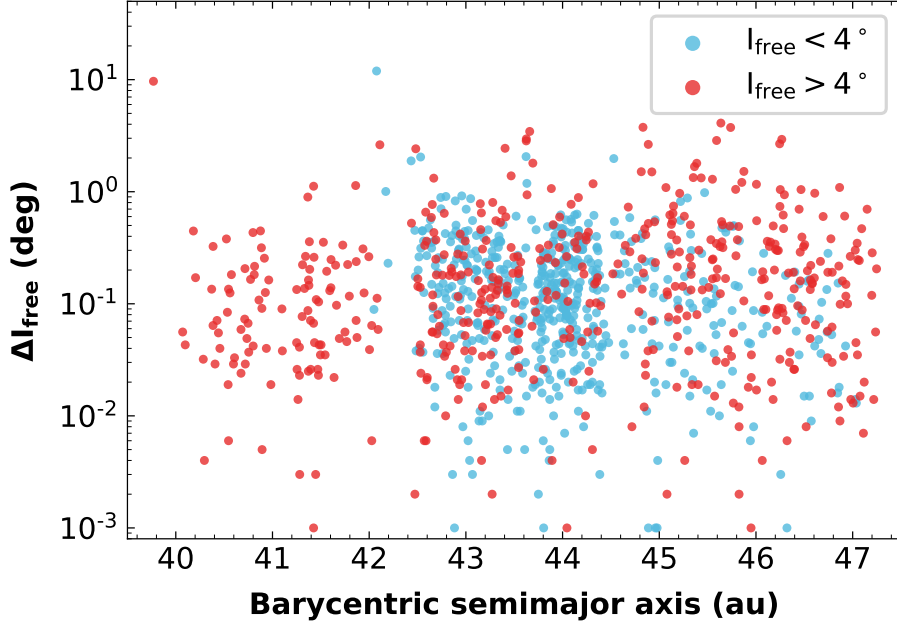


**Figure 2.5:**  $\Delta I_{\text{free}}$  measured across a 4 Gyr integration as a function of barycentric  $a$  for main-belt classical TNOs. The blue and red dots represent  $I_{\text{free}} < 4^\circ$  and  $I_{\text{free}} > 4^\circ$ , respectively. The majority of TNOs in both categories have values of  $I_{\text{free}}$  that are conserved to within  $1^\circ$  even over 4 Gyr.

of the Solar System. In other words, will the current  $I_{\text{free}}$  of classical TNOs reflect their  $I_{\text{free}} \sim 4$  billion years ago, at end of the giant planet formation and migration/-transport to their present-day orbits? To answer this, we extended the numerical integrations of the observed objects for 4 Gyr and plotted the surviving particles'  $\Delta I_{\text{free}}$  (the absolute difference between each object's current  $I_{\text{free}}$  and that at 4 Gyr) in Figure 2.5. The vast majority of classical TNOs, no matter what their current inclinations are, have  $\Delta I_{\text{free}} < 1^\circ$ . The very few outliers are mainly distributed around major mean-motion resonances, indicating some occasional interactions with the resonances during the 4 Gyr evolution in which the secular conservation is lost. Figure 2.5 thus shows that the  $I_{\text{free}}$  distribution we compute today for the classical TNOs can be taken to be representative of the primordial distribution.

Last but not least, we also explored the idea of whether the (easily calculated) mean ecliptic inclination from numerical integrations can serve as a good proxy for  $I_{\text{free}}$ . We find that for classical TNOs whose  $I_{\text{free}} > 4^\circ$ , the mean ecliptic inclination over 10 Myr is a good approximation to  $I_{\text{free}}$ , with the median absolute difference being only  $0.2^\circ$ . However, in the cold population ( $I_{\text{free}} < 4^\circ$ ), the median absolute difference is  $0.6^\circ$ , which renders the mean ecliptic inclination a low-quality estimate of the free inclination for this population (see the example discussed above from Figure 2.4). Moreover, we point out if one intended to study the main belt's inclination distribution through the mean ecliptic inclination, this averaging would result in all objects with  $I_{\text{free}}$  smaller than the local forced inclination being assigned a mean ecliptic inclination of roughly the forced value of about  $2^\circ$ ; the distribution of very low  $I_{\text{free}}$  objects would be completely erased. These same arguments apply if one tried to use the invariable plane as the reference (rather than the ecliptic); the cold population's median absolute inclination difference is still  $0.5^\circ$ . It is thus superior to use  $I_{\text{free}}$  computed by the double average to studying the main belt's inclination distribution.

## 2.3 Discussion

As a summary, the free inclination distribution we have computed for the main belt (Figure 2.3) illustrates several points:

1. The innermost boundary of the cold population at  $a \simeq 42$  au is being set by the existence of the secular resonances. The absence of low- $I$  TNOs here does not imply that the cold belt did not exist here before the giant planets finished formation and migration. How and when these secular resonances reached their current location is a subject of much speculation (e.g. Batygin et al. 2011, Dawson & Murray-Clay 2012, Gladman et al. 2012, Nesvorný 2018, Baguet et al. 2019, and references therein)
2. The double averaging method removes the apparent forced-inclination singularities that occur in the linear secular theory. If one wished to study the secular effects of additional planets on the ancient or current structure of the Solar System (e.g. Volk & Malhotra, 2017; Batygin et al., 2019), this method

is to be preferred to estimate the inclination perturbations produced by the planet.

3. The preservation of the  $I_{\text{free}}$  calculated via this method over 4 Gyr allows us to study the ancient inclination structure of the belt (that is, the structure existing at the end of the the planet formation epoch). This reinforces the idea that there was a cold ( $I_{\text{free}} < 4^\circ$ ) population present at that time which (at least in the  $a < 44.5$  au region of the main belt) is well separated from the presumably implanted hot population.
4. The main-belt TNO population clearly has multiple superposed components (see Brown, 2001, and citations to it) and, because there is evidence that these components have different physical properties due to different formation locations, there needs to be some way to easily separate observed TNOs for spectrophotometric studies. Due to the narrow width of the cold component, TNOs with large ecliptic inclinations (larger than  $10^\circ$ , say) will almost all be from the hot component with very few interlopers. At small inclinations, the majority of the TNOs will be from the cold population, with the interloper fraction depending on the component  $I$  distributions and relative populations. The often-used but still reasonable  $5^\circ$  cut in ecliptic inclination to separate the cold and hot components was proposed by Bernstein et al. (2004), although no justification for that particular value was given.

Here we have demonstrated the superiority of using a cut in  $I_{\text{free}}$  to isolate the hot and cold populations. Van-Laerhoven et al. (2019) found that the cold population is tightly confined (in  $I_{\text{free}}$ ) around the local forcing pole; this is especially true in the inner part of the main belt, where they found the cold population has an inclination width of just  $\simeq 1.8^\circ$ . Figure 2.6 shows histograms of ecliptic and free inclination for the non-resonant main belt TNOs in this work. The low- $I$  peak in the free inclination histogram is sharper than in the ecliptic histogram, and there is a noticeable drop-off in the observed population at  $I_{\text{free}} = 4^\circ$  (roughly twice the cold population's inclination width). We note that observational biases are not accounted for in Figure 2.6, though they were accounted for in Van-Laerhoven et al. (2019)'s analysis of the cold population's inclination width. Based on that inclina-

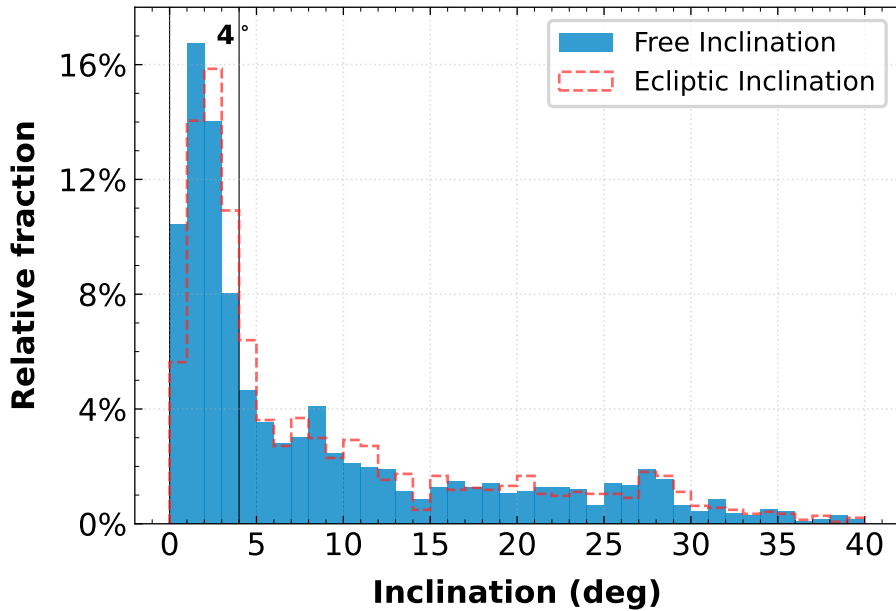


**Figure 2.6:** A fractional histogram of free inclinations (blue bars) and ecliptic inclinations (red outlines) for 1450 main-belt classical TNOs beyond the 5:3 resonance ( $a > 42.3$  au). Only a few such objects (not shown) have  $> 40^\circ$  inclinations. Note that because most TNO surveys have been conducted at relatively low latitudes, there is an observational bias against the large-inclination TNOs; thus the high- $I$  tail in this histogram should not be taken to represent the true hot TNO inclination distribution. However, the dramatic spike at low inclinations (which is due to the cold population) is still clear in the observed population, and even more obvious in the  $I_{\text{free}}$  histogram (which is shifted towards zero due to the true secular dynamics of the belt). A 4-degree cut is shown by the vertical line; few TNOs in the  $0\text{--}4^\circ$  range would be hot-population interlopers.

tion width and our analysis here, we suggest that  $I_{\text{free}} < 4^\circ$  is a reasonable choice when using a simple cut to separate the hot and cold populations in the main TNO belt.

## 2.4 Data Release

The purpose of this work is to provide tabulated barycentric orbit elements and  $I_{\text{free}}$  for the currently observed main classical belt TNOs as a resource for studies comparing the hot and cold populations. We do this in Table 2.1. We identify each TNO in our sample by their primary Minor Planet Center (MPC) designation, but we also include OSSOS++ and DES designations for objects that appear in either survey so that one could more easily use the survey simulators of those surveys for quantitative de-biasing. The absolute magnitude  $H$  in Table 2.1 is taken from the JPL Small body database; we note that these  $H$  values use approximate color transformations and should not be used with the survey simulators mentioned above as they are not linked to a specific filter.

In addition, to help the reader quickly estimate the correct  $I_{\text{free}}$  for future TNOs, we provide Table 2.2, in which the forcing pole components  $(q, p)$  are pre-computed in a  $(a, e, I, \omega)$  4-dimensional grid. We also provide a Python script to read the file and find the closest data point for any given orbit, which the reader can then use to estimate the  $I_{\text{free}}$  that would be given by the double average method. However, it's important to note that this simplified approach of evaluating  $I_{\text{free}}$  can only be trusted if the TNO:

1. is a non-resonant and non-scattering object within the given orbital ranges,
2. stays away from the  $\nu_{18}$  secular resonance (in other words, the forcing pole is relatively small), and
3. has a current inclination computed at the current epoch.

We have tested the file and confirmed that for TNOs that meet these three requirements, this script yields  $I_{\text{free}}$  to a precision of  $\sim 0.1^\circ$  compared to that computed by double average.

With accurate values of  $I_{\text{free}}$  and the knowledge of a cleaner separation between hot and cold population with a  $4^\circ$  boundary in this variable, one can use our tabu-

**Table 2.1:** Barycentric elements and  $I_{\text{free}}$  for main-belt TNOs

Column names	Units	Descriptions
$a$ (a)	au	Semimajor axis of the nominal orbit
$e$ (e)		Eccentricity
$I$ (inc)	deg	Inclination
$\Omega$ (Omega)	deg	Longitude of ascending node
$\omega$ (omega)	deg	Argument of perihelion
$M$ (M)	deg	Mean anomaly
$d$ (dist)	au	Distance from the barycenter
$H$ (H)	mag	Absolute magnitude
RESO		Dynamics flag: -1 for scattering, 0 for non-resonant/classical, $> 0$ for the exactly resonant ratio (e.g. ‘74’ stands for the 7:4 mean-motion resonance with Neptune)
$I_{\text{free}}$ ( $I_{\text{free}}$ )	deg	Free inclination, computed via double averaging
$I_{\text{free}}$ range ( $I_{\text{freeRange}}$ )	deg	Free inclination range over 10-Myr integration time
$q_{\text{forced}}$ ( $q_{\text{Forced}}$ )	deg	q component of the forcing pole. $q_{\text{forced}} = I_{\text{forced}} \cos(\Omega_{\text{forced}})$
$p_{\text{forced}}$ ( $p_{\text{Forced}}$ )	deg	p component of the forcing pole. $p_{\text{forced}} = I_{\text{forced}} \sin(\Omega_{\text{forced}})$
OSSOS		OSSOS++ internal designation ('x' for non-OSSOS++ objects)
DES		DES internal designation ('x' for non-DES objects)
ID		ID downloaded from JPL Small-Body Database: For a numbered TNO, ID gives its designated number; For an unnumbered TNO, ID gives its compact provisional designation
Name		Full name (designation in bracket)

**Note.** The first six orbital elements and the distance are barycentric and in the IAU76/J2000 ecliptic reference frame, referring to epoch JD 2459400.5. Both  $I_{\text{free}}$  and  $I_{\text{free}}$  range are independent of the choice of reference frame. The absolute magnitude  $H$ , id and full name are directly retrieved from JPL on October 5th, 2021; these values could change as the MPC receives additional observations. This table is available as a downloadable, machine readable file at <https://yukunhuang.com>.

**Table 2.2:**  $q, p$  components of the forcing pole for various orbital elements

Axis names	Range	Grid sizes	Dimensions
$a$	(39.4, 47.7) au	0.1 au	84
$e$	(0, 0.25)	0.01	26
$I$	(0, 40) deg	2 deg	21
$\omega$	(0, 90) deg	10 deg	10
<b>Total Size</b>			458,640

**Note.** In the double average method, the forcing pole vector is a function of  $(a, e, I, \omega)$ . For each data point on grid, we give the  $q, p$  components of the forcing pole in degrees, which can be used to estimate the  $I_{\text{free}}$  of nearby orbits.  $\omega$  is only in the range of  $(0, 90)$  deg due to its two-fold reflection symmetries in both the orbital plane and the central axis.

lated  $I_{\text{free}}$  values to reduce the occurrence of cross-contamination between the two groups in photometric and spectroscopic studies of those populations whose goal is to constrain primordial TNO surface properties. Lastly, we provide a rapid method allowing anyone to easily estimate the correct  $I_{\text{free}}$  for future TNO discoveries in the main Kuiper Belt.

## Chapter 3

# Steady-state Distribution of the Scattering Disk

The TNO orbital distribution provides constraints on the early migration history of the giant planets. In Chapter 2, I established the primordial free inclination distribution of main-belt TNOs, which can also be used to differentiate the cold classicals from the hot component in this region. In this chapter, I turn my attention to the semimajor axis distribution of the implanted non-resonant TNOs, including hot classicals in the main Kuiper Belt and detached TNOs beyond 50 au.

The CFEPS survey first discovered that a continuous  $dN/da \propto a^{-2.5}$  power law could account for the entirety of the implanted population within 100 au (Petit et al., 2011, their figure 8). Beaudoin et al. (2023, submitted to PSJ) measured the semi-major axis distribution of the detached sample from the OSSOS survey, concluding it follows  $a^{-2.5}$  all the way to at least  $\sim 200$  au. These results suggest that these hot Kuiper Belt components are a single dynamical population that formed around the same time.

The power-law nature in  $a$  of the implanted TNOs begs the following questions:

1. What is the physical interpretation and implication of the  $a$  power law?
2. Is  $a^{-2.5}$  the expected steady-state distribution of scattering TNOs, which are thought to be the ‘primordial source’ of the implanted populations?

To answer these two questions, I first summarize relevant literature about comet

dynamics in Section 3.1, where the expected  $a$  distribution of ecliptic comets was derived using a diffusion equation. In Section 3.2, I approach this problem from a completely different perspective: the patched-conic approximation that is commonly used in flyby dynamics. The patched-conic model surprisingly reaches the same steady-state distribution as the diffusion approximation. In Section 3.3, I estimate the diffusion coefficient and timescale analytically, and I confirm the validity of the power law and the analytically-computed scattering timescales through numerical integrations in Section 3.4. Section 3.5 discusses possible applications of my results.

### 3.1 Comet Dynamics and the Diffusion Approximation

One of the early results of planetary scattering dynamics appears in comet dynamics, in which comets with extremely large semimajor axis ( $200 < a < 20,000$  au) were studied under planetary perturbations, stellar encounters, and the galactic tide. Duncan et al. (1987) studied the timescales of the three dynamical effects, and established the idea that the formation of the current comet cloud (inner + outer Oort cloud) was driven mainly by an interaction between planetary perturbations and torquing due to galactic tides. In this paradigm, planetary perturbations first sent cometary objects to large  $a$  with almost constant  $q$ , and torques from the galactic tide then lead to changes in  $q$ , raising objects from the giant planet region to the Oort cloud.

To estimate timescales for planetary perturbations, Duncan et al. (1987) adopted an energy-diffusion approximation model from Yabushita (1980), in which ecliptic comets (with sufficiently large  $a$  and planet-coupled  $q$ ) random walk in energy space ( $x \equiv 1/a$ <sup>1</sup>) at each perihelion passage (Figure 3.1). The exact locations of giant planets during the comet's closest approach is not modeled, instead, the diffusion coefficient  $D$ , which denotes the root-mean-square energy change per encounter with given  $q$  and  $i$ , determines the diffusion speed or scattering efficiency by the ensemble of planets. In the Solar System,  $D$  increases as  $q$  drops due to stronger planetary interactions (Duncan et al., 1987, figure 1).

Under this approximation, Yabushita (1980) shows that if  $n(x, t)dx$  is the num-

---

<sup>1</sup>The special energy in the two-body system has the form of  $-\mu/(2a)$  (Equation 1.6).

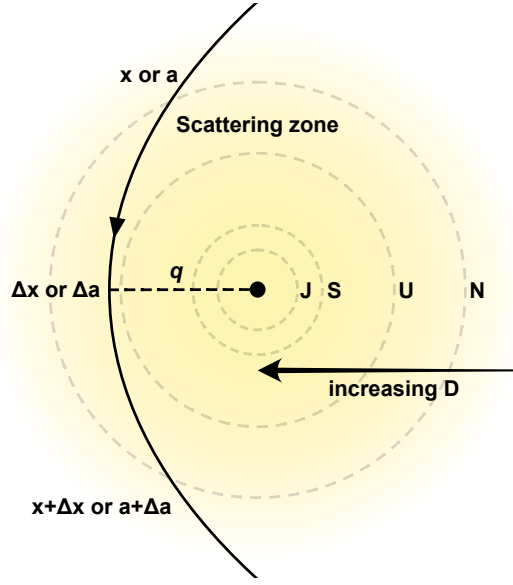


**Figure 3.1:** An ecliptic comet has near-parabolic orbit with sufficiently large semimajor axis  $a$  and specific orbital energy  $x$  slightly greater than 0 (solid curve). In the energy-diffusion approximation of the comet dynamics (Yabushita, 1980), the comet experiences a random energy kick  $\Delta x$  in the scattering zone (yellow), regardless of the planets' exact locations (dashed circles).

ber of comets at time  $t$  with energies in the range  $(x, x + dx)$ , then  $n$  satisfies the diffusion equation

$$\frac{\partial n}{\partial \tau} = \frac{1}{2} \sqrt{x_0} \frac{\partial^2 (nx^{3/2})}{\partial x^2}, \quad (3.1)$$

where  $x_0$  is an arbitrary initial energy with corresponding dimensionless time unit  $\tau = t/t_D(x_0)$ , where the diffusion timescale is

$$t_D \equiv \frac{P(x)x^2}{D^2} = \frac{2\pi}{D^2} \sqrt{\frac{x}{\mu}}, \quad (3.2)$$

where  $P(x)$  is the orbital period. In practice, the diffusion coefficient is mostly dependent on  $q$ , but also depends on  $i$ . In this model,  $q$  and  $i$  of the comet are assumed to remain constant, and thus  $D$  is constant also.

The solution of the diffusion equation (3.1) for a delta-function initial distribu-

tion  $n(x, t = 0) = \delta(x - x_0)$ , corresponding to all comets at a single initial energy  $x_0$ , is given by (Yabushita, 1980)

$$n(x, t) = \frac{4}{x\tau} \exp\left[-\frac{8}{\tau}\left(1 + \sqrt{\frac{x}{x_0}}\right)\right] I_2\left[\frac{16}{\tau}\left(\frac{x}{x_0}\right)^{1/4}\right], \quad (3.3)$$

where  $I_2$  is the modified Bessel function of the first kind, which can be computed using

$$I_2(z) = \frac{z^2}{4} \sum_{k=0}^{\infty} \frac{(\frac{1}{4}z^2)^k}{k!(2+k)!}. \quad (3.4)$$

Note that

$$\lim_{z \rightarrow 0} I_2(z) \approx z^2/8, \quad (3.5)$$

when  $t \rightarrow \infty, z \rightarrow 0$  and Equation (3.3) indicates the number density function can be simplified to

$$\lim_{t \rightarrow \infty} n(x, t) \sim x^{-0.5}, \quad (3.6)$$

whereas the total number of objects  $N(t)$  at given time is given by

$$N(t) = \int_0^\infty n(x, t) dx. \quad (3.7)$$

At large times,  $\lim_{t \rightarrow \infty} N(t) \sim t^{-2}$  (Yabushita, 1980; Malyshkin & Tremaine, 1999). The comet's removal is mainly due to the lossy boundary condition at  $x < 0$  in the diffusion, corresponding to objects getting ejected from the Solar System.

Equation (3.6) gives the steady-state<sup>2</sup> energy distribution for comets only interacting with planets. Given  $x \equiv 1/a$ , to convert this into a semimajor axis distribution, one uses the transformation  $dx = -da/a^2$ . Therefore, the steady-state  $a$

---

<sup>2</sup>I use the word 'steady-state' here to describe an constant relative distribution. The total number of objects  $N(t)$  in the steady-state distribution decays steadily.

distribution under the diffusion approximation is

$$\begin{aligned}\frac{dN}{da} &= \frac{dN}{dx} \left| \frac{dx}{da} \right|, \\ &\sim \left( \frac{1}{x} \right)^{\frac{1}{2}} a^{-2}, \\ &\sim a^{-1.5},\end{aligned}\tag{3.8}$$

which is one index shallower than the  $a^{-2.5}$  power law observed in the implanted Kuiper Belt. In other words, there are observed to be relatively more TNOs at smaller  $a$  compared to the expected steady-state distribution that would eventually result from pure planetary perturbations.

Duncan et al. (1987) computed several relevant timescales for the evolution of Solar System comets. This includes the planetary scattering diffusion timescale  $t_D$  and the perihelion torquing timescale from the galactic tide  $t_q$ , which are given by

$$\begin{aligned}t_D &= 1 \text{ Myr} \left( \frac{10^4 \text{ au}}{a} \right)^{\frac{1}{2}} \left( \frac{10^{-4} \text{ au}^{-1}}{D} \right)^2, \\ t_q &= 13 \text{ Myr} \left( \frac{\Delta q}{10 \text{ au}} \right) \left( \frac{25 \text{ au}}{q} \right)^{\frac{1}{2}} \left( \frac{10^4 \text{ au}}{a} \right)^2,\end{aligned}\tag{3.9}$$

where the diffusion coefficient  $D$  for a given  $q$  and  $i$  can be evaluated numerically (e.g. figure 1 in Fernandez 1981; Duncan et al. 1987; Malyshkin & Tremaine 1999), and  $t_q$  gives the timescale on which the galactic tides change perihelion distance by  $\Delta q$ .

I reconstruct figure 2 from Duncan et al. (1987) in Figure 3.2, with  $a$  ranging from 3 to 50,000 au. Equation (3.3) also indicates the timescale for the number density to approach the  $x^{-0.5}$  ( $a^{-1.5}$ ) steady state is  $t_D$ , which decreases with semi-major axis as  $t_D \propto a^{-0.5}$  for constant  $D$  (blue lines in Figure 3.2). To estimate the timescales for initially near-circular and co-planar small bodies near a planet to reach their steady-state distributions, I plot four lines corresponding to perihelia at the four giant planets, on which the black circle marks the diffusion timescale for initial circular orbits at each planet:  $\sim 70$  kyr for Jupiter-scattered,  $\sim 2$  Myr for Saturn-scattered,  $\sim 100$  Myr for Uranus-scattered, and  $\sim 500$  Myr for Neptune-scattered

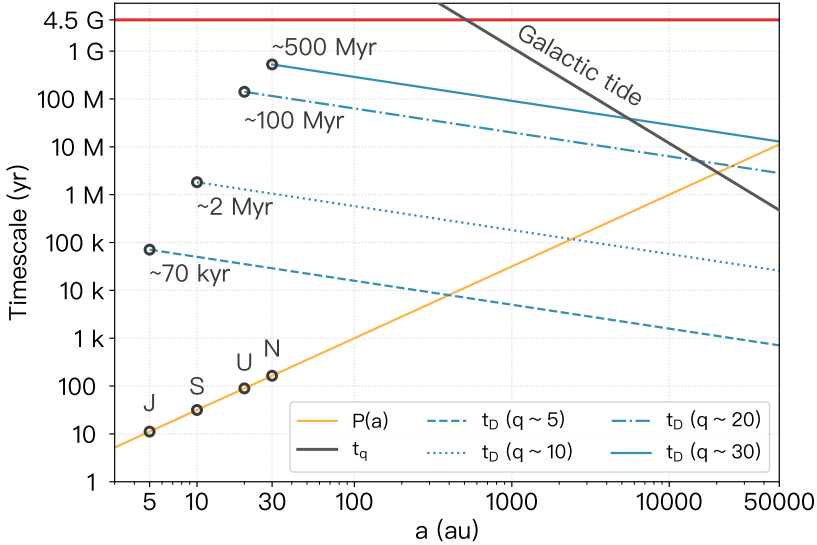


**Figure 3.2:** Diffusion timescales  $t_D$  for various perihelion distance  $q$  are plotted as a function of  $a$  (Equation 3.2). The solid, dash-dotted, dotted, and dashed blue lines, from top to bottom, correspond to Neptune, Uranus, Saturn, and Jupiter-coupled orbits, respectively. The black circle on each line marks the  $t_D$  for initially circular heliocentric orbits near that planet.  $P(a)$  is the orbital period (orange).  $t_q$  is the tidal torquing time from the galactic disk for  $\Delta q = 10$  au and  $q = 30$  au (black), whose intersection with  $t_D$  ( $q \sim 30$ ) naturally defines the boundary between the Kuiper Belt and the Oort cloud. The age of the Solar System (4.5 Gyr) is indicated by the red horizontal line. Adapted from Duncan et al. (1987)'s figure 2.

objects. The diffusion coefficients used to calculate these timescales are directly obtained from Duncan et al. (1987)'s figure 1, assuming  $q = 5, 10, 20, 30$  au, respectively. The black line in Figure 3.2's top-right corner represents the tidal torquing timescale for  $\Delta q = 10$  au, starting at  $q = 30$  au; this amount of  $q$  lifting is enough to remove a particle from strong planetary coupling. The intersection between  $t_q$  (black) and  $t_D$  ( $q \sim 30$ , solid blue) at several thousand au roughly defines the boundary between the Kuiper Belt and the inner Oort cloud, and the intersection between  $t_q$  and  $P(a)$  (gold) at  $\sim 20,000$  au defined the boundary of the Oort cloud.

In conclusion, under the diffusion approximation, the scattering process is mod-

eled as random walks in energy space  $x$  with constant  $D$ . Note that this approximation only holds if the scattering orbit is assumed to have fixed  $q$  and  $i$  (therefore constant  $D$ ), which may not be the case in reality (see the next section for more discussion). Figure 3.2 shows that the scattering disk should have reached the  $a^{-1.5}$  steady-state distribution at  $\sim 500$  Myr. This is one index shallower than the observed implanted Kuiper Belt. I will discuss cosmogonic implications of this disagreement in Chapter 6.

### 3.2 A Patched-Conic Point of View

In this section, I try to approach the same problem from a completely different perspective – the patched-conic approximation – which is often applied in spacecraft trajectory design. I show that under some simple assumptions, the  $a^{-1.5}$  power law is a natural outcome after multiple flybys of the perturbing planet homogenize the directions of planetary relative-velocity vectors ( $V_\infty$ ). This provides a physical interpretation (at least in the patched-conic model) for the steady-state distribution of scattering objects.

The patched-conic formalism is only unequivocally defined when the small body's orbit intersects the planet's; in other words  $q < a_p$  at all times. To begin with, we consider the following CRTBP model, where the planet orbits the Sun on a circular orbit of radius 1, and the particle is on a planet-crossing orbit with semimajor  $a$ , eccentricity  $e$ , and inclination  $i$ . For  $i \approx 0^\circ$  orbit, the two phase angles  $\omega$  and  $\Omega$  do not influence the dynamics due to symmetry and thus can be dropped.

As shown in Figure 3.3, when the particle has a close encounter with the planet at the intersection  $r = a_p$ , the relative velocity vector  $\mathbf{V}_\infty$  is the vector subtraction between the two heliocentric velocities

$$\mathbf{V}_\infty = \mathbf{V}_{\text{cross}} - \mathbf{V}_p. \quad (3.10)$$

Defining the positive apex angle between  $\mathbf{V}_p$  and  $\mathbf{V}_\infty$  as  $\theta$ , one obtains the following relationship by applying the cosine formula

$$\begin{aligned} V_{\text{cross}}^2 &= V_\infty^2 + V_p^2 - 2V_\infty V_p \cos(\pi - \theta), \\ &= V_\infty^2 + V_p^2 + 2V_\infty V_p \cos\theta, \end{aligned} \quad (3.11)$$

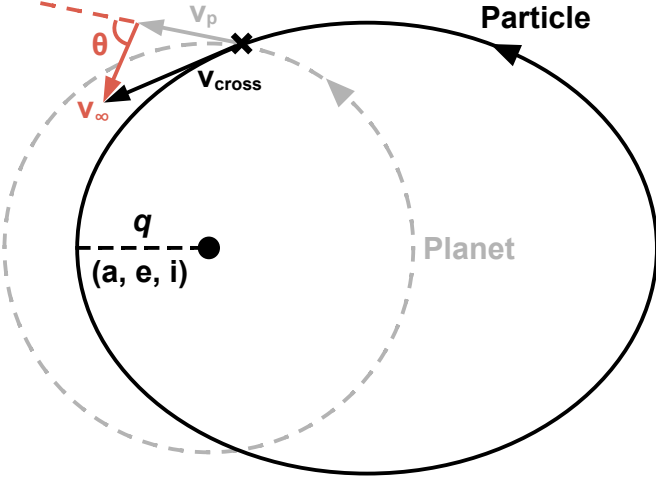


**Figure 3.3:** In the planet-crossing case, the particle’s perihelion on its orbit (black) is inside that of the planet (gray). A planetary close encounter can only happen at  $r = a_p$  (black cross), where  $\mathbf{V}_{\text{cross}}$  (black vector) and  $\mathbf{V}_p$  (gray vector) are the particle and the planetary heliocentric velocity vectors at the intersection, and  $\mathbf{V}_{\infty} = \mathbf{V}_{\text{cross}} - \mathbf{V}_p$  (red vector) represents the particle’s relative velocity with respect to the planet.  $\theta$  denotes the positive apex angle between  $\mathbf{V}_p$  and  $\mathbf{V}_{\infty}$ , ranging from  $0^\circ$  to  $180^\circ$ .

The magnitude of the particle’s crossing velocity  $V_{\text{cross}}$  is directly linked to its semi-major axis  $a$  by the vis-visa equation (1.5, where  $\mu = 1$ ,  $r = 1$ , and  $v_{\text{cross}} = V_{\text{cross}}/V_p$  is the particle’s speed in units of planet’s heliocentric speed.)

$$v_{\text{cross}}^2 = 2 - \frac{1}{a}, \quad (3.12)$$

where at  $a \rightarrow \infty$ ,  $v_{\text{cross}} \rightarrow \sqrt{2}$ <sup>3</sup> which is the escape speed at the planet’s heliocentric orbit.

Now, let’s study the flyby dynamics in the planet-centered frame and temporarily ignore the Sun’s gravity. This approximation is valid if the flyby object is well inside the planet’s Hill sphere ( $R_H$ )<sup>4</sup>, where it experiences a stronger gravitational force

<sup>3</sup>In this chapter, I use the capital letter  $V$  to denote dimensional velocity and the lowercase  $v$  to denote velocity in units of planet’s heliocentric speed.

<sup>4</sup>Note that in spacecraft dynamics, the sphere of influence  $R_{\text{SOI}} = r_p(m_p/M_{\odot})^{2/5}$  is also commonly used. It is shown below that the choice of sphere does not affect the results.

from the planet than from the Sun. The Hill sphere of a planet is given by (Hill, 1878)

$$R_H = r_p \sqrt[3]{\frac{m_p}{3M_\odot}}, \quad (3.13)$$

where  $m_p$  is the planet mass and  $r_p$  is the heliocentric distance. Inside the planet's Hill sphere, the object's path can be approximated as a hyperbolic trajectory with  $v_\infty$  being its incoming planetocentric speed. The term *v infinity* is used here because it describes the 'velocity at infinity' for the hyperbolic trajectory. Although the relative speed at intersection is not exactly the velocity at infinity in the eye of the planet, it is a decent approximation as long as the mass of the planet is much smaller than that of the Sun ( $m_p/M_\odot \ll 1$ ).

As shown in Figure 3.4, a hyperbolic planet flyby can only do one thing: reorienting the  $v_\infty$  vector without changing its magnitude. This can be immediately understood using the conservation of orbital energy (Equation 1.6) in the planetocentric frame

$$\frac{v_{\infty,\text{in}}^2}{2} - \frac{\mu_p}{R_H} = \frac{v_{\infty,\text{out}}^2}{2} - \frac{\mu_p}{R_H}, \quad (3.14)$$

$$v_{\infty,\text{in}} = v_{\infty,\text{out}},$$

where  $\mu_p = Gm_p$  is the gravitational parameter of the planet. The direction and amount of  $\Delta\theta$  depends on exactly where the object enters the planet's Hill sphere (i.e. the impact parameter  $b$  and its location), which is extremely sensitive to the exact flyby timing. For example, if the red trajectory in Figure 3.4 were to enter the hill sphere on the left side, the resultant reorientation of  $v_\infty$  is in the opposite direction. If the object and the planet are not in any mean-motion resonance, the flyby timing is essentially random, which results in significant differences in subsequent orbital elements and naturally introduces a highly random factor –  $\Delta\theta$  – into this problem.

If  $v_\infty = \sqrt{2} - 1$ , one can see from Figure 3.5 that at  $\theta = 0$ ,  $v_{\text{cross}} = \sqrt{2}$  ( $v_p$  is also set to 1 for simplicity), which is the escape velocity at  $r = 1$ . Consequently, if  $v_\infty > \sqrt{2} - 1$ , a forward 'loss cone' (derived below) will open on the unit sphere, where particles can escape from the planetary system.

Therefore, it is reasonable to model the scattering problem from a different perspective: each planetary close encounter forces a random walk in  $\theta$ , reducing  $a$  when

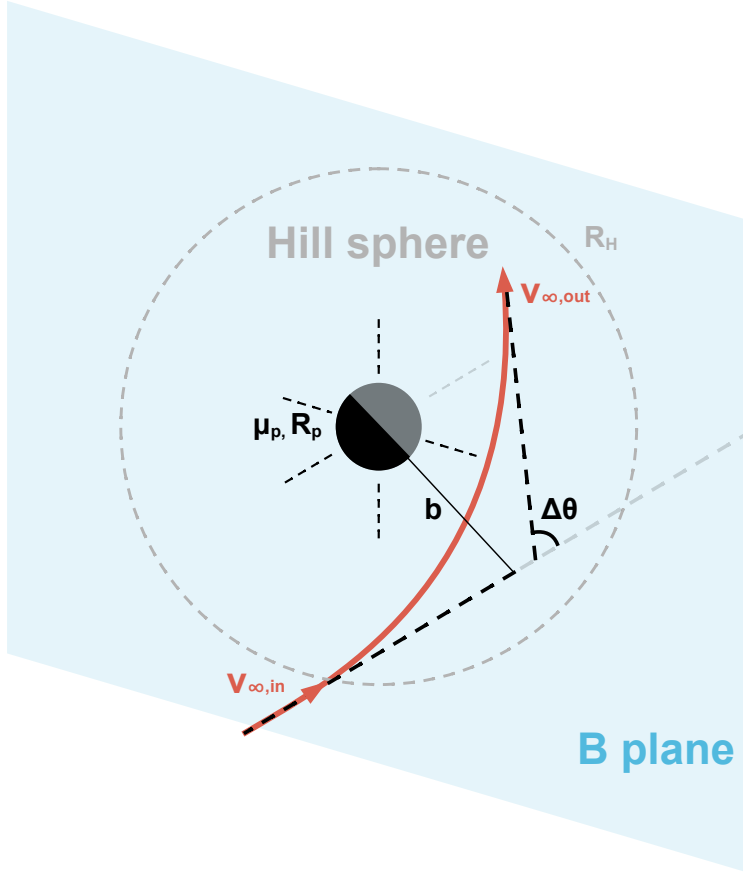


**Figure 3.4:** Diagram for a planetary close encounter in the planet-centered reference frame. In the patched-conic model, an object entering the planet's Hill sphere (dashed circle) can be approximated as a hyperbolic flyby, with the incoming speed equal to the outgoing speed. The B plane is defined as the plane that crosses the planet and is perpendicular to the incoming  $v_{\infty,in}$ . The impact parameter  $b$  is the ‘unperturbed’ closest distance between the incoming velocity and the planet. Each planetary flyby causes in a change in  $v_{\infty}$ ’s direction (represented by  $\Delta\theta$ ) without modifying its magnitude, the result of which is changes in the object’s orbital elements (see also Figure 3.5).

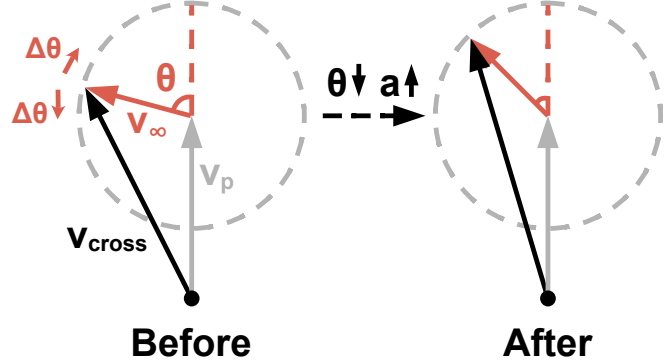


**Figure 3.5:** Velocity vectors,  $\mathbf{v}_p$ ,  $\mathbf{v}_\infty$ , and  $\mathbf{v}_{\text{cross}}$  before and after a planetary close flyby. The relative velocity  $\mathbf{v}_\infty$ 's magnitude does not change as a result of the encounter, but its orientation does, with the direction and amount of change set by the details of the flyby. If the particle's direction when leaving the Hill sphere is more aligned with the planet's velocity vector  $\mathbf{v}_p$  ( $\theta$  drops), the flyby increases heliocentric  $a$ , and vice versa.

$\theta$  increases or boosting  $a$  when  $\theta$  decreases (Figure 3.5). As a result,  $\mathbf{v}_\infty$  rotates randomly but is confined to remain on a circle centered on the tip of  $\mathbf{v}_p$ , giving rise to the change in the heliocentric velocity vector (Equation 3.11) and thus orbital elements. The magnitude of the relative velocity  $v_\infty$  not only is a constant before and after a single close encounter, but also keeps its length unchanged for *all* the planetary flybys. To demonstrate this, one examines the Jacobi integral  $\mathcal{C}_J$  (1.16) and the Tisserand parameter  $\mathcal{T}$  (1.17) at  $r = 1$ :

$$\mathcal{C}_J|_{r=1} = 1 + 2 \left( \frac{1 - \mu'}{1} + \frac{\mu'}{\Delta} \right) - v_{\text{rel}}^2 \approx \mathcal{T}, \quad (3.15)$$

where  $v_{\text{rel}} = v_\infty$  and (Burns et al., 2022)

$$v_\infty \approx \sqrt{3 - \mathcal{T}}, \quad (3.16)$$

where the relative velocity is in the unit of the planet's heliocentric circular speed and the  $\mathcal{T} < 3$  condition corresponds to that of orbit crossing in the co-planar case.

Equating Equation (3.11) with (3.12), one gets a one-to-one mapping from  $\theta$  to

$a$  (or  $x$ ) as

$$\frac{1}{a} = x = 1 - 2v_\infty \cos\theta - v_\infty^2, \quad (3.17)$$

The vast majority of objects scattered by a planet have  $2.5 < \mathcal{T} < 3$  (e.g. Jupiter-Family Comets (JFCs), see Levison & Duncan, 1997), thus the typical  $v_\infty$  ranges from 0 to  $\sqrt{2}/2$  (3.16). I plot  $a$  as a function of  $\theta$  in Figure 3.6. Depending on the value of  $v_\infty$ , the scattering problem can be divided into the following five cases:

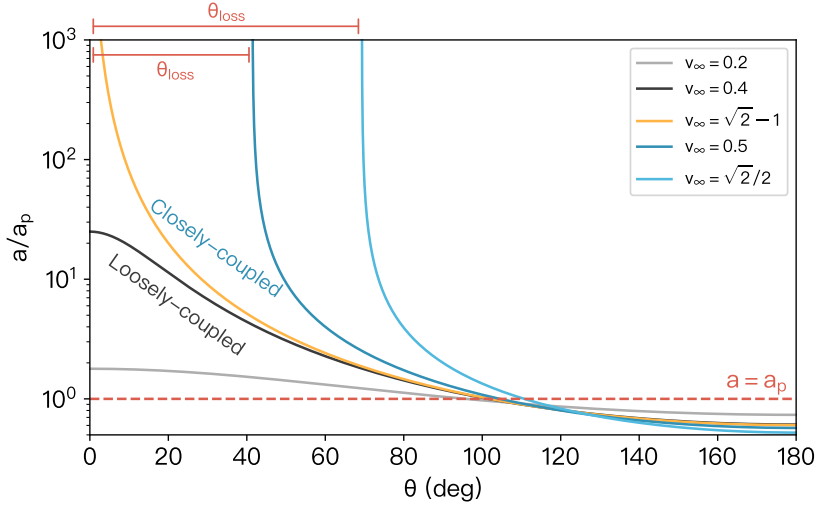


**Figure 3.6:** Dimensionless  $a$  as a function of  $\theta$  for various  $v_\infty$  (all units are in terms of the planet's value). The horizontal dashed line marks  $a = a_p$ . In a loosely-coupled case (gray and black), there is a maximum  $a$  the particle can reach in the planet-crossing state. For the boundary case  $v_\infty = \sqrt{2} - 1$  (orange),  $\theta \rightarrow 0^\circ$  corresponds to  $a \rightarrow \infty$  and  $\theta = 102^\circ$  corresponds to  $a = a_p$ . In closely-coupled cases (blue), the object will escape the Solar System once  $\theta < \theta_{loss}$ , which is defined in Equation 3.21. A larger  $v_\infty$  corresponds to a bigger loss cone (red line segments).

### 1. Diffusion case: $v_\infty$ undefined ( $\mathcal{T} > 3$ ).

The small body and the planet's orbits do not intersect. Either the small body is completely outside the planet ( $q > a_p$ ) or completely inside ( $Q < a_p$ ). The patched-conic approach fails.

2. Loosely-coupled case:  $v_\infty \leq \sqrt{2} - 1$ , for which  $\sqrt{8} < \mathcal{T} < 3$ .

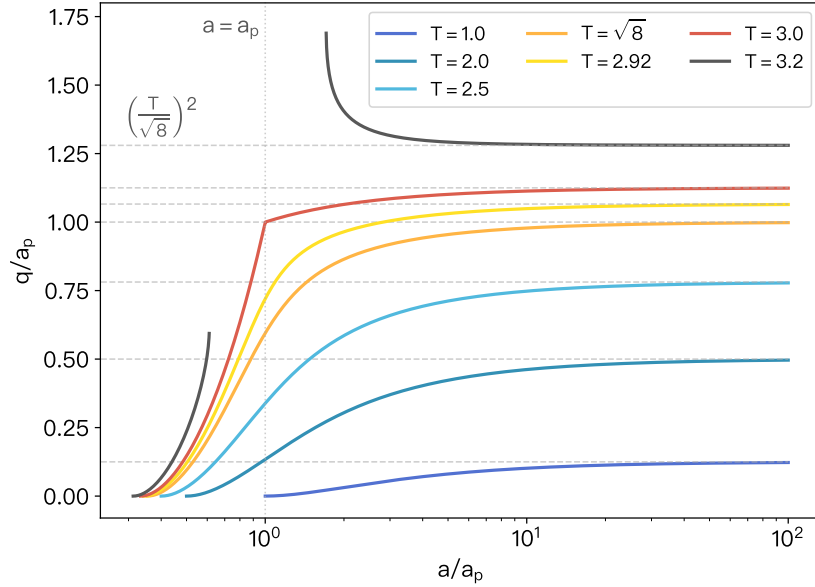


**Figure 3.7:** Constant  $\mathcal{T}$  curves on the  $a$ - $q$  space (3.19), assuming  $i = 0^\circ$ . In the large  $a$  limit, the perihelion  $q$  asymptotically approach the value  $(\mathcal{T}/\sqrt{8})^2$  (gray dashed lines). For  $\mathcal{T} < \sqrt{8}$ ,  $\lim_{a \rightarrow \infty} q < 1$  and the particle can never decouple from the planet in the co-planar case (curves in blue). For  $\mathcal{T} > \sqrt{8}$ ,  $\lim_{a \rightarrow \infty} q > 1$  and spontaneous decoupling when the particle reaches large  $a$  is required (yellow and red curves). Equation (3.19) is partially undefined near the planet for  $\mathcal{T} > 3$  (blue). The loosely-coupled case and the closely-coupled cases defined in text are separated by the critical value of  $\mathcal{T} = \sqrt{8}$  (orange), which has  $q \rightarrow a_p$  as  $a \rightarrow \infty$ . The vertical dotted line marks where  $a = a_p$ .

Each  $\theta \in (0^\circ, 180^\circ)$  corresponds to a unique value of  $a$  (gray and black lines in Figure 3.6), with the maximum set by

$$a_{\max} = \frac{1}{2 - (v_\infty + 1)^2}. \quad (3.18)$$

The maximum semimajor axis, however, is only the upper limit for the patched-conic assumption. In practice, the particle can still raise its  $a$  above  $a_{\max}$  and

escape from the Solar System; this is accomplished when encounters raise  $q > a_p$ , which breaks the patched-conic formulation.

One can see a condition on this outward escape route from the Tisserand parameter. Re-writing Equation 1.17 as a function of  $a$  and  $q$  (assuming  $i = 0$ )

$$\mathcal{T} = \frac{1}{a} + 2\sqrt{q\left(2 - \frac{q}{a}\right)}, \quad (3.19)$$

and when  $a \rightarrow \infty$

$$\begin{aligned} \lim_{a \rightarrow \infty} \mathcal{T} &= 2\sqrt{2q}, \\ \lim_{a \rightarrow \infty} q &= \left(\frac{\mathcal{T}}{\sqrt{8}}\right)^2. \end{aligned} \quad (3.20)$$

I plot values of  $q$  as a function of  $\mathcal{T}$  in Figure 3.7. For  $\sqrt{8} < \mathcal{T} < 3$ , a co-planar orbit is coupled with the planet at lower  $a$  while uncoupled at larger  $a$ , which is why I labeled it as the loosely-coupled case (see the yellow curve in Figure 3.7).

To show that an initially-crossing object can indeed spontaneously uncross the planetary orbit, I show in Figure 3.8 one example of a Neptune-scattered particle with  $\mathcal{T} = 2.9$ . When  $a < a_p$  (in this case  $a < 30$  au, denoted by the gray dashed line), the scattering particle's aphelion  $Q$  (orange dots) is close to Neptune, whereas when it gets scattered outward ( $a > a_p$ ), its perihelion  $q$  (blue dots in the lower panel) is close to Neptune. Spontaneous orbital detachment occurs at  $a \gtrsim 110$  au, consistent with Figure 3.7's analytical prediction <sup>5</sup>.

3. **Closely-coupled case:**  $\sqrt{2} - 1 < v_\infty < \sqrt{2} + 1$ , for which  $-\sqrt{8} < \mathcal{T} < \sqrt{8}$ .

When the relative velocity is greater than  $\sqrt{2} - 1$ , if the small body's heliocentric velocity vector after a flyby, it can exceed  $v_{\text{cross}} = \sqrt{2}$ , the escape velocity at  $r = 1$ . The object is then ejected from the planetary system when the condition  $\theta < \theta_{\text{loss}}$  is satisfied, which is denoted as a *loss cone* on Figure 3.5's unit

---

<sup>5</sup>Specifically, the semimajor axis beyond which an orbit has  $q > a_q$  can be analytically computed by solving Equation 3.19 (assuming  $q = 1$ ). For the  $\mathcal{T} = 2.9$  scattering particle shown in Figure 3.8, this occurs at  $a = 3.74a_q \approx 110$  au.

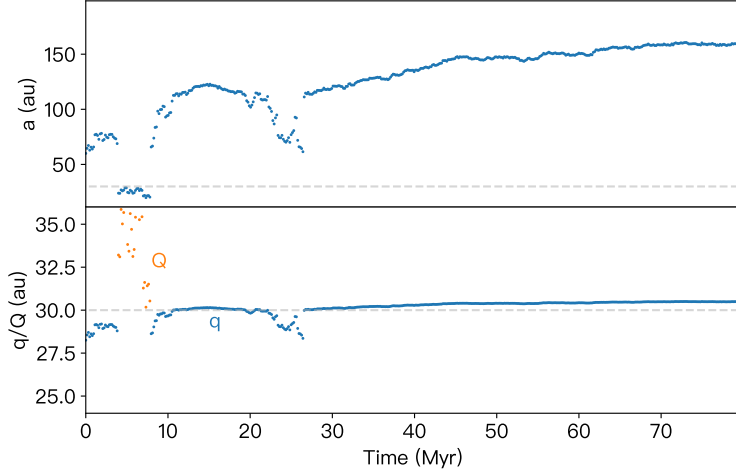


**Figure 3.8:** Dynamical evolution of a Neptune-scattered test particle with  $\mathcal{T} = 2.9$  (loosely-coupled case) integrated in the strictly 2D case. The bottom panel shows its aphelion ( $Q$ ) and perihelion ( $q$ ) evolutions, in which spontaneous orbital detachment from Neptune (defined as  $q > a_p$ , the gray dashed line) occurs when  $a \gtrsim 110$  au.

circle. The opening angle of the loss cone  $\theta_{\text{loss}}$  is given by

$$\theta_{\text{loss}} = \arccos \frac{1 - v_\infty^2}{2v_\infty}, \quad \text{if } v_\infty > \sqrt{2} - 1. \quad (3.21)$$

This can also be generalized to the 3D case, where instead being confined to an unit circle,  $v_\infty$  moves around on a unit sphere, and the angle  $\theta_{\text{loss}}$  defines a 3D loss cone in which orbits are unbound. Additionally, in the closely-couple case, the maximum  $q$  is always inside the orbit of the planet (blue curves in Figure 3.7), and the small body can hardly uncross the planet's orbit unless it gets ejected.

#### 4. Critical case: $v_\infty = \sqrt{2} - 1$ , for which $\mathcal{T} = \sqrt{8}$ .

The critical value of  $\mathcal{T} = \sqrt{8}$  has  $q \rightarrow a_p$  at  $a \rightarrow \infty$  (orange curve in Figure 3.7). The small body's orbit can never decouple from the planet and there is no loss cone for the critical case. This serves as a separatrix between the

loosely-coupled and the closely-coupled cases.

5. **Unbound case:**  $v_\infty = \sqrt{2} + 1$ , for which  $\mathcal{T} = -\sqrt{8}$ .

This case corresponds to  $v_{\text{cross}} > \sqrt{2}$  for all  $\theta$ . All orbits are all unbound.

As shown in the above discussion, the patched-conic approximation is not always valid for the scattering problem, especially in the loosely-coupled case where the small body can slightly raise its perihelion when getting into large- $a$  orbits. In the trans-Neptunian region I'm interested in, most of the objects in the current scattering disk are loosely coupled with Neptune, namely  $\mathcal{T}_N > \sqrt{8}$ . However, I discovered that a Taylor expansion can be made at the critical value of  $v_\infty = \sqrt{2} - 1$ , which leads to the simple  $a^{-1.5}$  distribution at large semimajor axis.

Equation (3.17) gives a one-to-one mapping from  $\theta$  to  $a$  (or  $x$ ). Therefore, any presumed  $\theta$  distribution will naturally result in an  $a$  (or  $x$ ) distribution. Since the amount and direction of  $\theta$  change is a highly randomized parameter which does not depend on  $\theta$  itself, it is reasonable to assume that any initial  $\theta$  distribution (e.g. a  $\delta(\theta)$  function corresponding to all orbits initialized at the same  $\theta$ ) will eventually approach a steady-state uniformity.

Supposing the expected steady state for  $\theta$  is a uniform distribution from 0 to  $\pi$  (that is,  $dN = K d\theta$ ), one obtains the steady-state  $x$  distribution

$$\frac{dN}{dx} = \frac{dN}{d\theta} \left| \frac{d\theta}{dx} \right| = K \frac{1}{2v_\infty \sin \theta}, \quad (3.22)$$

where  $K$  is a normalization constant that doesn't affect the shape of the distribution. Replacing  $\theta$  with  $x$  using Equation 3.17, one obtains a function of  $x$  and  $v_\infty$  that is expandable around  $x = 0$  and  $v_\infty = \sqrt{2} - 1$  for the critical case. I define a temporary variable  $v' = v_\infty - (\sqrt{2} - 1)$  that allows  $v_\infty$  to be expanded around the

critical value:

$$\begin{aligned}
\frac{1}{2v_\infty \sin \theta} &= \frac{1}{\sqrt{(2v_\infty)^2 - (1 - v_\infty^2 - x)^2}}, \\
&= \frac{1}{\sqrt{4(v' - 1 + \sqrt{2})^2 - (1 - (v' - 1 + \sqrt{2})^2 - x)^2}}, \\
&\approx \left( \frac{1}{2(\sqrt{2} - 1)^{1/2} \sqrt{x}} + \sqrt{O[x]} \right) + \\
&\quad v' \left( -\frac{1}{\sqrt{2}(\sqrt{2} - 1)^{1/2} x^{3/2}} + \frac{\sqrt{2} - 4}{16(\sqrt{2} - 1)^{3/2} \sqrt{x}} + \sqrt{O[x]} \right) + \\
&\quad O[v']^2.
\end{aligned} \tag{3.23}$$

It is evident that in the large- $a$  limit ( $x \rightarrow 0$ ), Equation (3.23)'s leading factor is  $1/\sqrt{x}$  given  $v'$  is small. The number density of  $a$  can be obtained by

$$\frac{dN}{da} = \frac{dN}{dx} \left| \frac{dx}{da} \right| \propto \frac{1}{\sqrt{x}} \frac{1}{a^2} \propto a^{-1.5}. \tag{3.24}$$

It is perhaps surprising that both the diffusion and patched-conic approximations reach the same  $a^{-1.5}$  steady-state distribution, despite the fact that the two methods approach this problem from very different perspectives. Although technically speaking, the  $a^{-1.5}$  power law just derived only holds for  $\mathcal{T} = \sqrt{8}$ , I will demonstrate in Section 3.4 that for other values of  $\mathcal{T}$ , this power law is still a very good approximation to the semimajor axis distribution that develops.

### 3.3 Estimating the Relaxation Time

In the patched-conic model, a uniform distribution of the angle  $\theta$  is equivalent to an  $a^{-1.5}$  power law distribution of the semimajor axis in the large  $a$  limit. This result provides a novel perspective to approach the scattering problem using flyby dynamics. In this section, I will estimate the relaxation timescale  $t_R$ , defined as the time for which an ensemble of small bodies initially in the proximity of the planet approaches the  $a^{-1.5}$  steady-state distribution (similar to the diffusion timescale  $t_D$  in Equation 3.2). This timescale can serve as the characteristic timescale for the scattering problem consisting of a Sun and a planet on a circular orbit, thus I also

address it as the *scattering timescale* in this thesis. Note that in the diffusion model, past works have had to estimate the diffusion coefficient numerically.

Considering a hyperbolic planetary flyby with  $v_\infty$  (Figure 3.4), one can compute  $\Delta\theta$  from

$$\sin\left(\frac{\Delta\theta}{2}\right) = \frac{1}{\sqrt{1 + v_\infty^4 b^2 / \mu_p^2}}, \quad (3.25)$$

where the impact parameter  $b$  (solid line in Figure 3.4) is the ‘unperturbed’ closest distance between the incoming  $v_\infty$  vector and the planet. For a given planet and  $v_\infty$ , the magnitude of the deflection angle  $\Delta\theta$  solely depends on  $b$ . The more distant a flyby is, the smaller the deflection angle is, as well as the induced orbital element change. When the impact parameter  $b \gg \mu_p/v_\infty^2$ <sup>6</sup> and the deflection angle is small, Equation (3.25) can be simplified to

$$\Delta\theta \simeq \frac{2\mu_p}{v_\infty^2 b}. \quad (3.26)$$

The ‘B plane’ (blue plane in Figure 3.4), defined as the plane that crosses the planet center and is perpendicular to the incoming  $v_\infty$ , cuts through the Hill sphere and creates a circle with  $R_H$ . Assuming the location of  $b$  is randomly picked from this circle for each flyby, the resultant radial distribution is linearly proportional to  $b$  (instead of being uniform). Therefore, the mean square of  $\Delta\theta$  is given by

$$\begin{aligned} \langle \Delta\theta^2 \rangle &= \frac{\int_{R_I}^{R_H} (\Delta\theta)^2 b db}{\int_{R_I}^{R_H} b db}, \\ &= \frac{8\mu_p^2 \ln(R_H/R_I)}{v_\infty^4 (R_H^2 - R_I^2)}, \\ &\approx \frac{8 \ln(R_H/R_I)}{R_H^2} \frac{\mu_p^2}{v_\infty^4}, \quad \text{if } R_I \ll R_H, \end{aligned} \quad (3.27)$$

where  $R_I$  is the impact radius, corresponding to the smallest  $b$  that would lead to a collision with the planet (Figure 3.9). If the planet’s gravity is neglected, the impact radius is the geometrical planetary radius  $R_p$ . The gravity well, however, bends

---

<sup>6</sup>For the critical value of  $v_\infty = \sqrt{2} - 1$ , this is equivalent to a Jupiter flyby further than  $\frac{1}{12}R_H$ , a Saturn flyby further than  $\frac{1}{25}R_H$ , or a Uranus/Neptune flyby further than about  $\frac{1}{100}R_H$ .

incoming velocity vectors towards the planet, causing  $R_I$  to be larger than  $R_p$ . This effect is also known as the ‘gravitational focusing’ in planetary formation theories (Safronov, 1972). The impact radius  $R_I$  is the product of the planet’s radius  $R_p$

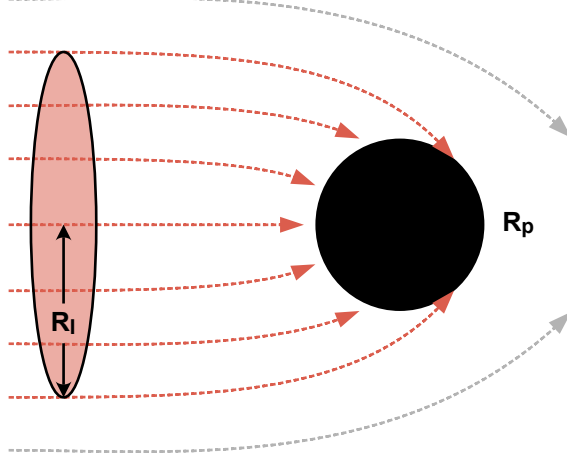


**Figure 3.9:** Gravitational focusing diagram. Due to its gravity, the planet would bend the incoming  $v_\infty$  towards itself. The impact radius  $R_I$  is defined as the smallest impact parameter  $b$  that would lead to a collision with the planet, which is larger than the planet’s physical radius  $R_p$ .

and the square root gravitational focusing enhancement  $\sqrt{\mathcal{F}_g}$  (Lissauer & de-Pater, 2013):

$$R_I = R_p \sqrt{\mathcal{F}_g} = R_p \sqrt{1 + \frac{v_{\text{escape}}^2}{v_\infty^2}} = R_p \sqrt{1 + \frac{2\mu_p}{v_\infty^2 R_p}}. \quad (3.28)$$

For giant planets in the Solar System,  $\sqrt{\mathcal{F}_g} \sim 10$  for  $v_\infty = \sqrt{2} - 1$ , therefore  $R_I$  can be approximated as

$$R_I \approx \frac{\sqrt{2\mu_p R_p}}{v_\infty}, \quad \text{if } R_I \gg R_p. \quad (3.29)$$

To estimate the timescale for scattering objects to reach the  $a^{-1.5}$  distribution, we recall the definition of relaxation time, which is commonly used in thermal conduction (Landau & Lifshitz, 2013)

$$t_R \sim \frac{l^2}{D_\theta}, \quad (3.30)$$

where  $l$  is the dimension of the system and  $D_\theta$  is the diffusion coefficient (similar to the  $D$  in Equation 3.2). The random walk in  $\theta$  is analogous to the conduction problem with the dimension  $l \sim (\pi - \theta_{\text{loss}})$  (Figure 3.6) and

$$D_\theta \sim \frac{\langle \Delta\theta^2 \rangle}{2\delta t}, \quad (3.31)$$

in which  $\delta t$  is the average time between two consecutive Hill sphere entrances. An order of magnitude estimate of  $\delta t$  for near-planet small-bodies (i.e.  $a \approx a_p = 1$ ) is

$$\begin{aligned} \delta t &\approx \underbrace{P_p}_{\text{Period of the planet}} \times \underbrace{\frac{1}{R_H}}_{\mathcal{M} \text{ factor}} \times \underbrace{\frac{1}{4R_H}}_{\omega \text{ factor}}, \\ &= \frac{P_p}{4R_H^2}. \end{aligned} \quad (3.32)$$

This equation is composed of three factors. The period factor  $P_p$  establishes the underlying timescale of the problem. The  $\mathcal{M}$  factor states that when the small body is on the planet's orbit ( $r = 1$  and  $z = 0$ ), the encounter probability is proportional to the planetary Hill radius  $R_H$ . The  $\omega$  factor arises for inclined orbits. It comes from the geometry constraint that for an orbit that is crossing ( $q < a_p$ ) and with inclination larger than the Hill radius factor  $i > i_H$ , the ascending and descending nodes cross the planet's orbit exactly 4 times during a precession of the small body's orbit. The scale  $i_H$  is defined simply as the angular height of the Hill sphere, which for our unit planetary semimajor axis

$$i_H = \frac{R_H}{1} = \sqrt[3]{\frac{m_p}{3M_\odot}}. \quad (3.33)$$

For Jupiter, Saturn, Uranus, and Neptune,  $i_H = 4^\circ, 2.6^\circ, 1.4^\circ, 1.5^\circ$ , respectively. In the case of  $i < i_H$ , close encounter probability with the planet will be greatly enhanced by a factor of  $1/R_H$ . However, except for the 2D case where the planet and particles are strictly co-planar, the scattering process itself will heat up the inclination distribution of small bodies (even though they have initially near co-planar orbits) up to  $i_H$  long before they reach the steady state. Therefore, the  $\omega$  factor plays a role in Equation 3.25 for the vast majority of the evolution, and the encounter prob-

ability is only temporarily boosted even if the particles and the planet are started on near co-planar orbits. The factor of this temporary encounter frequency boost varies from  $\sim 15$ – $60$  for Solar System giants. Therefore, I assume the average time between two encounters for near-planet orbits  $\delta t$  is unchanged (Equation 3.32), in order to continue the analytical derivation.

Combining Equations (3.27) and (3.32), one obtains

$$\frac{t_R}{P_p} \simeq \frac{(\pi - \theta_{\text{loss}})^2}{16 \ln(R_H/R_I)} \left( \frac{v_\infty^2}{\mu_p} \right)^2, \quad \text{if } v_\infty \geq \sqrt{2} - 1, \quad (3.34)$$

which is a function only weakly dependent on  $R_H$ , because the strong  $R_H^2$  terms in (3.27) and (3.32) cancel out.

For planets in our Solar System, the coefficient  $\ln(R_H/R_I) \approx 5$  (see Table 3.1), thus using (3.21),  $t_R$  can be rewritten as

$$t_R \simeq \frac{(\pi - \theta_{\text{loss}})^2}{80} (3 - \mathcal{T})^2 \left( \frac{m_p}{M_\odot} \right)^{-2} P_p, \quad \text{if } \mathcal{T} \leq \sqrt{8}. \quad (3.35)$$

**Table 3.1:** Relaxation time  $t_R$  for planets in the Solar System

Planet	$m_p/M_\odot$	$\ln(R_H/R_I)$	$t_R$
Mercury	$1.66 \times 10^{-7}$	4.5	$\sim 40$ Gyr
Venus	$2.45 \times 10^{-6}$	4.9	$\sim 400$ Myr
Earth	$3.00 \times 10^{-6}$	5.2	$\sim 400$ Myr
Mars	$3.23 \times 10^{-7}$	5.7	$\sim 60$ Gyr
Jupiter	$9.55 \times 10^{-4}$	4.2	$\sim 60$ kyr
Saturn	$2.86 \times 10^{-4}$	4.8	$\sim 1$ Myr
Uranus	$4.37 \times 10^{-5}$	5.9	$\sim 100$ Myr
Neptune	$5.15 \times 10^{-5}$	6.1	$\sim 200$ Myr

**Note.**  $t_R$  calculated for Solar System planets using Equation (3.34) assuming  $\mathcal{T} = \sqrt{8}$  (with respect to the target planet). The dimensionless coefficient  $\ln(R_H/R_I)$  is tabulated for the the relative velocity of  $v_\infty = \sqrt{2} - 1$ .

The  $t_R$  given in Table 3.1 is close to the diffusion timescale for near-planet orbits

in Figure 3.2, but instead of obtaining  $D$  via numerical simulation as Duncan et al. (1987) did, I derive an analytical solution for the diffusion coefficient. It is worth noting that the relaxation time  $t_R$  is inversely proportional to the planetary mass squared  $m_p^{-2}$ . Malyshkin & Tremaine (1999) show that the diffusion timescale in Yabushita (1980)'s solution also scales with  $m_p^{-2}$ , though they approach this problem from a different point of view. Using Equation (3.35), I calculate  $t_R$  for all Solar System planets in Table 3.1, assuming  $\mathcal{T} = \sqrt{8}$  and  $\theta_{\text{loss}} = 0$ . This  $t_R$  represents the shortest  $t_R$  among orbits with various  $\mathcal{T}$ , for the following reasons:

1. In the loosely-coupled ( $\mathcal{T} > \sqrt{8}$ ) case where the orbit may be able to spontaneously de-couple from the planet (see Figure 3.8), the time for orbits to reach the steady-state orbital distribution is longer than the  $t_R$  predicted by Equation (3.35), which will be illustrated numerically in Section 3.4 with numerical simulations. This can be understood through figure 1 in Duncan et al. (1987), where it demonstrates the average energy change per orbit decreases significantly as  $q$  rises above the planet's orbital distance.
2. In the closely-coupled case ( $\mathcal{T} < \sqrt{8}$ ), orbit decoupling does not occur. Equation (3.35) provides estimated timescales for scattering bodies in a wide range of orbital elements, whose dependence is compressed to a single variable  $\mathcal{T}$  (or  $v_\infty$ ).  $t_R$  is strongly influenced by  $v_\infty$  in two ways: Increasing  $v_\infty$  not only limits the  $\theta$  mobility (Equation 3.25), but also shortens the 'dimension' of the problem by limiting the accessible range of  $\theta$  (Figure 3.6). The net result of these two competing factors<sup>7</sup> can be evaluated through

$$\frac{t_R}{t_R|_{\mathcal{T}=\sqrt{8}}} \approx \left(1 - \frac{\arccos\left(\frac{\mathcal{T}-2}{2\sqrt{3-\mathcal{T}}}\right)}{\pi}\right)^2 \left(\frac{3-\mathcal{T}}{3-\sqrt{8}}\right)^2, \quad \text{if } \mathcal{T} \leq \sqrt{8}. \quad (3.36)$$

The value of the  $t_R$  scaling factor as a function of  $\mathcal{T}$  is plotted in Figure 3.10. Generally speaking, the Tisserand parameter  $\mathcal{T}$  decreases as  $i$  or  $e$  grows, extending the relaxation timescale as a result of a faster encounter velocity. This trend continues until the orbit hits the large- $a$  zone of  $\mathcal{T} < -1$ , where  $a = a_p$  orbits cannot exist

---

<sup>7</sup>The impact radius  $R_I$  is also affected by  $v_\infty$  as shown in Equation (3.29), but since  $R_I$  only appears in  $\ln(R_H/R_I)$ ,  $t_R$ 's  $v_\infty$  dependence through this term is weak.

(see Figure 3.7’s dark blue curve). Getting to very low values of  $\mathcal{T}$  requires low  $q$  or large  $i$ . To see this, set  $A(1 - e) = 1$  and send  $A \rightarrow \infty$  in Equation (1.17),  $\mathcal{T} \rightarrow 2\sqrt{2q}\cos i$ . Different ranges of  $\mathcal{T}$  dominantly (but not entirely) correspond to different  $i$ , from prograde, to polar, and to large-a retrograde orbits (Namouni & Morais, 2021). I will mainly focus on the implanted TNOs in Chapter 5 and 6, most of which lie within a limited range of  $\mathcal{T} \sim (2.5, 3.2)$ , for which  $t_R$  for Neptune is several hundred million years (Table 3.1).

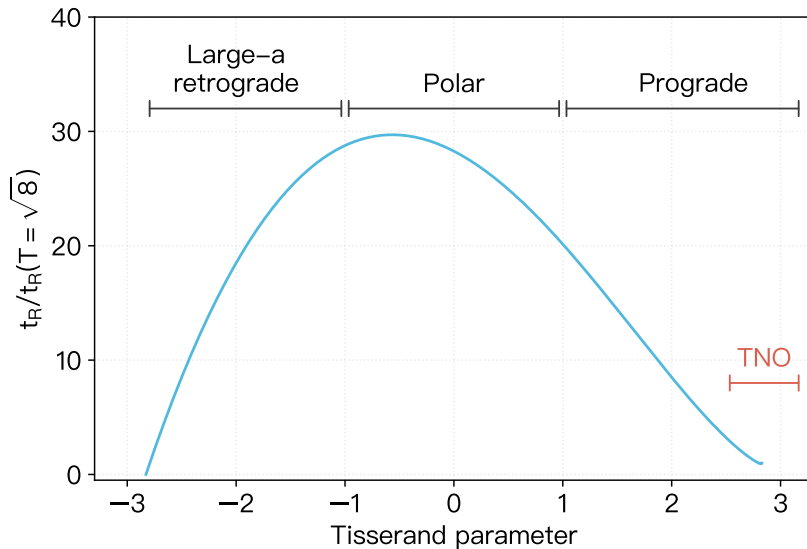


**Figure 3.10:** Relaxation time  $t_R$  (in the unit of  $t_R|_{\mathcal{T}=\sqrt{8}}$ , see Table 3.1) as a function of the Tisserand parameter in the range of  $-\sqrt{8} < \mathcal{T} < \sqrt{8}$  (closely-coupled case). To decrease  $\mathcal{T}$ ,  $i$  generally increases and thus the orbit changes from prograde, to polar ( $i \sim 90^\circ$ ), and to large-a retrograde (see Namouni & Morais 2021). Known ‘hot population’ TNOs normally have  $\mathcal{T} \sim (2.5, 3.2)$  so their relaxation timescales are several hundred million years.

### 3.4 Comparison with Numerical Simulations

To demonstrate the validity of the  $a^{-1.5}$  steady state (Equation 3.24) and the analytical equations for the relaxation time (Equation 3.35 and 3.36), I carry out several

numerical simulations with GLISSER, an extension of the GPU integrator GLISSE developed by Zhang & Gladman (2022) (also see Section A). It can follow thousands of test particles in parallel while handling their close encounters with planets. It is thus a perfect tool to study the time-varying distributions of particles scattered by planets. Appendix A details performance tests and Appendix A.1 shows the conservation of the Tisserand parameter by the integrator.

The first simulation contains a Neptune on a circular orbit at  $a_N = 30$  au and 10,000 test particles initialized with  $a_0 = 61$  au and  $\mathcal{T} = 2.8$ , which is a delta function in both  $a$  and  $\theta$  space. This corresponds to the closely-coupled case defined in Section 3.2, in which a loss cone of  $\theta_{\text{loss}} \approx 29^\circ$  (Equation 3.21) is opened. They are then integrated under the gravity of the Sun and Neptune, which is a CRTBP system where the Tisserand parameter is conserved (Section 1.1.3). The time evolution of test particle  $a$  and  $\theta$  distributions are illustrated in Figure 3.12.

Figure 3.12 confirms that the  $a^{-1.5}$  power law is indeed a steady state in the CRTBP system regardless of particle's initial conditions. However, a more practical numerical experiment would be to estimate the timescales for particles that are initially close to the planetary semimajor axis. This likely has a clearer cosmogenic implication as scattering objects we see in today's Kuiper Belt were thought to be planetesimals that were formed near giant planets or in the path of the Neptune's outward migration (i.e. they probably had initial  $a$  close to Neptune's  $a_N$  when there were first scattered). Additionally, in the patched-conic formalism, the scattering timescale can only be estimated for close-coupled orbits with  $\mathcal{T} < \sqrt{8}$  (Equation 3.35). It is thus important to verify whether the steady state for  $\mathcal{T} > \sqrt{8}$  orbits is also  $a^{-1.5}$ . If so, what are their scattering timescales?

I create another GLISSER simulations with 50,000 test particles with some value of the Tisserand parameter are initiated on orbits close to that of Neptune (and not in any neptunian MMRs). At each output, I fit the semimajor axis distribution with the functional form  $a^\alpha$  for  $a > 40$  au particles (see Figure 3.11). Figure 3.12 shows the time evolution of the power law index  $\alpha$  for  $\mathcal{T} = \sqrt{8}, 2.9$ , and 3, which represents the collective dynamical movement of the particle ensemble.

As shown in Figure 3.12, the  $\mathcal{T} = \sqrt{8}$  (blue) initial conditions have the shortest  $t_R$  of  $\simeq 200$  Myr, which is also the value estimated in Table 3.1. For  $\mathcal{T} = 2.9$  (orange),  $t_R$  is slightly longer than the critical case, as spontaneous orbital detachment at large

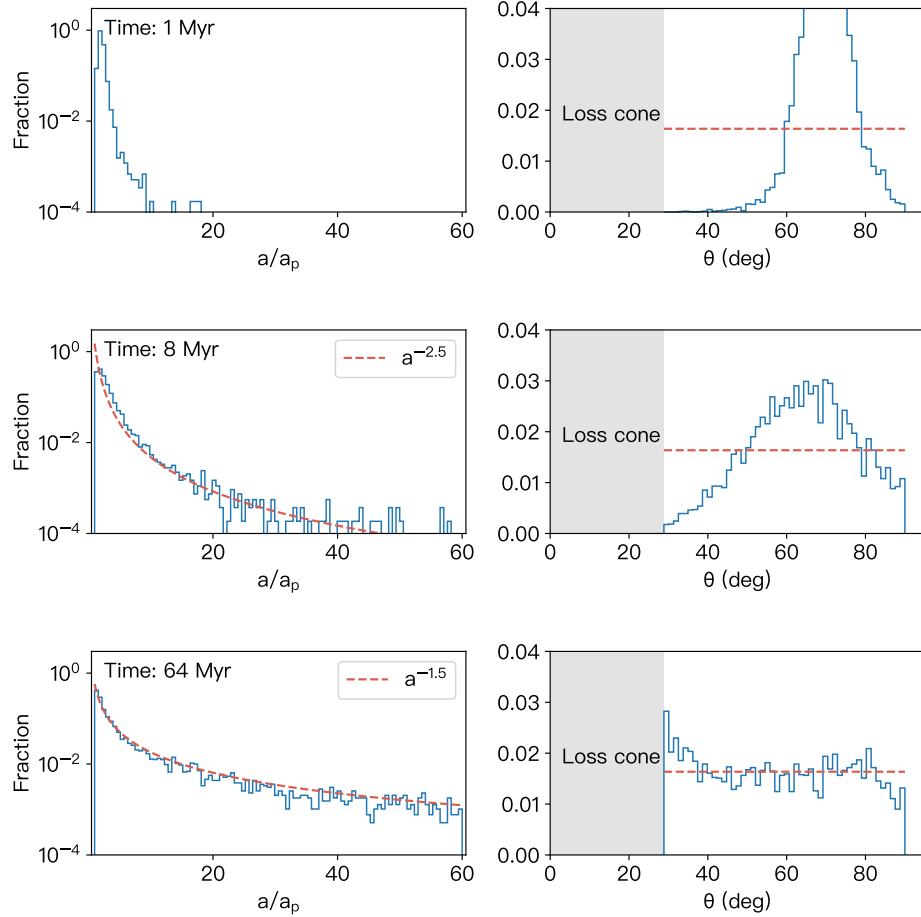


**Figure 3.11:** Three snapshots showing the development of  $a$  distributions (left panels) of 10,000 test particles (near co-planar with initial  $a_0 = 61$  au giving  $T = 2.8$  and  $\theta_0 \approx 70^\circ$ ) at 1 Myr, 8 Myr, and 64 Myr, respectively. They were integrated under the gravity of the Sun and a circular Neptune with  $a_p = 30$  au. Right panels show histograms for the angle  $\theta$ , where the uniform distribution in  $\theta$  corresponds to the  $a^{-1.5}$  power law in semimajor axis. The loss cone of  $\theta_{\text{loss}} \approx 29^\circ$  is denoted by the gray box, as this Tisserand parameter corresponds to the closely-couple case. The time for particles to asymptote to the  $a^{-1.5}$  steady state is shorter than Neptune's scattering timescale  $\sim 200$  Myr, because they were already started at  $a/a_p \approx 2$ .

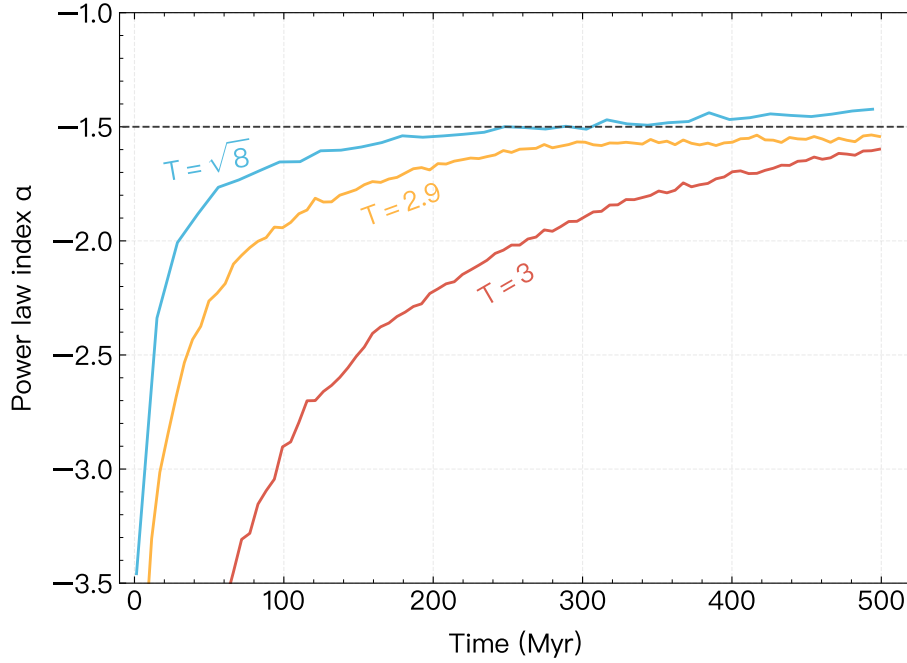


**Figure 3.12:** Time evolution of the  $a$  distribution power law index  $\alpha$  (also see Figure 3.11) for an external scattering disk of Neptune. These simulations all have a Neptune on a circular orbit of 30 au and 50,000 near co-planar particles initially outside Neptune, but with  $\mathcal{T} = \sqrt{8}$  (blue), 2.9 (orange), and 3 (red), respectively. In the loosely-coupled case,  $\mathcal{T} = \sqrt{8}$  particles have the shortest  $t_R \simeq 200$  Myr, matching in the analytically-computed Table 3.1.  $\mathcal{T} = 3$  represents test particles that are initialized near Neptune with  $e \simeq 0$ , in this case  $t_R \simeq 500$  Myr. The three curves also collectively demonstrate that  $a^{-1.5}$  (dashed line) is indeed the steady-state distribution of the scattering problem.

$a$  (see Figure 3.8) would reduce the impact of a flyby.  $\mathcal{T} = 3$  (red) corresponds to orbits that are initially near-planet, near-circular, and co-planar, which are often taken as initial conditions in scattering dynamics studies (e.g., Dones et al., 2004). At the end of the simulation, the  $\mathcal{T} = 3$  scattering disk is very close to the  $a^{-1.5}$  steady state, thus  $t_R \simeq 500$  Myr; it's also worth noting that this case passed through  $a^{-3.5}$  at  $\sim 60$  Myr and  $a^{-2.5}$  at  $\sim 150$  Myr. These values may have some linkage to the  $a^{-2.5}$  distribution in the observed implanted population, a topic which I will come back to in Chapter 6.

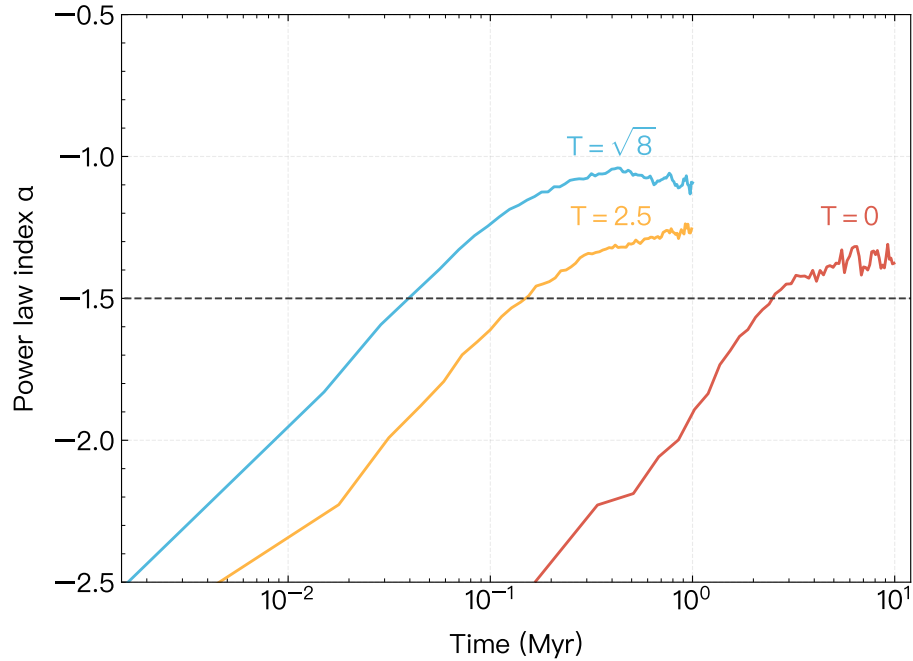


**Figure 3.13:** Same as Figure 3.12 but with Jupiter on a 5.2 au circular orbit and  $\mathcal{T} = \sqrt{8}$  (blue), 2.5 (orange), and 0 (red). The relaxation times for these three simulations are  $\sim 50$  kyr,  $\sim 150$  kyr, and  $\sim 2.5$  Myr, respectively.

Figure 3.13 shows another set of simulations, but with the very massive Jupiter ( $\approx 318 M_{\oplus}$ ) on a circular orbit of 5.2 au. Their initial Tisserand parameters are set as  $\mathcal{T} = \sqrt{8}$ , 2.5, and 0, respectively. In contrast to Neptune-scattering simulations, distributions of scattered objects by Jupiter do not cleanly asymptote to  $a^{-1.5}$  near

the end of the simulations<sup>8</sup>. This is probably due to small-number statistics caused by Jupiter's fast removal rate. The size of Jupiter's kicks are so large that several approximations above fail, and many particles enter the loss cone. At the end of the 1 Myr simulations for  $\mathcal{T} = \sqrt{8}$  and 2.5, only 2% and 7% particles are still present, respectively. The 10 Myr simulation for  $\mathcal{T} = 0$  has a much slower removal rate, with the particle survival rate of 74%, and is the closest to the  $a^{-1.5}$  value.

The relaxation time  $t_R$ , however, can still be measured as the time for  $\alpha = -1.5$  (dashed line) in Figure 3.13. The  $\mathcal{T} = \sqrt{8}$  critical case has  $t_R \simeq 60$  kyr, consistent with my analytical prediction (Table 3.1). The other two simulations are both closely-coupled cases, so their  $t_R$  can also be evaluated using Equation 3.36. The  $t_R$  scaling factors are  $\sim 3$  for  $\mathcal{T} = 2.5$  and  $\sim 30$  for  $\mathcal{T} = 0$  (see Figure 3.10), therefore, the computed relaxation times are  $\simeq 180$  kyr and  $\simeq 1.8$  Myr, in excellent agreement with numerical simulations. I have thus demonstrated the validity of Equations (3.35) and (3.36) for predicting the numerically-measured scattering timescale.

### 3.5 Discussion

Though derived from completely different perspectives, the  $a^{-1.5}$  steady state appears to be an universal distribution for the scattering and diffusion problem in comet dynamics. Based on the patched-conic model, I obtained analytical estimates for the diffusion coefficient  $D_\theta$  and the relaxation time  $t_R$ , for  $\mathcal{T} < \sqrt{8}$  closely-coupled orbits. I compared the scattering timescales with numerical simulations, demonstrating the validity of these equations. Here, I summarize the main points of my results, and their potential applications:

1. The relaxation timescale to the  $dN/da \propto a^{-1.5}$  is proportional to the planetary period  $P_p$  and inversely proportional to the planetary mass squared  $m_p^{-2}$ . This will shed light upon the scattering dynamics during planetary migration, when planetary semimajor axis (and potentially mass) is rapidly changing due to its interaction with planetesimals (see Section 4.3).
2. The scattering timescale's dependence on orbital elements can be mostly con-

---

<sup>8</sup>For Jupiter simulations, I measure  $\alpha$  for  $a > 10$  au objects.

densed down to the single Tisserand parameter  $\mathcal{T}$ , which affects the timescale because of the relation to the encounter velocity  $v_\infty$  (3.16).  $\mathcal{T} = \sqrt{8}$  represents the critical case in which the scattering timescale is the shortest. I thus address  $t_R|_{\mathcal{T}=\sqrt{8}}$  as the *typical timescale* for the scattering problem.

3. As the inclination  $i$  increases,  $v_\infty$  also increases. As a result, the scattering timescale for large- $i$  orbits is longer than typical timescale, which can be evaluated through Equation (3.36). Polar and retrograde orbits ( $i \gtrsim 90^\circ$ ) normally have scattering timescales 20–30 times longer than the typical timescale. This explains why retrograde TNOs generally have relatively long dynamical lifetimes, even comparable to the  $\sim 4$  Gyr Solar System age (e.g., Gladman et al., 2009; Chen et al., 2016). Understanding the scattering dynamics for retrograde orbits will shed light upon the formation of the peculiar retrograde small bodies, such as (528219) 2008 KV<sub>42</sub> (Gladman et al., 2009), (471325) 2011 KT<sub>19</sub> (Chen et al., 2016), and (514107) Ka‘epaoka‘awela (Wiegert et al., 2017; Greenstreet et al., 2020).
4. The timescale for most of the scattering TNOs (which have  $\mathcal{T} \approx 3$ ) is longer than the typical timescale and cannot be analytical measured with my method. This is because most of the scattering TNOs have  $q > 30$  au where the patched-conic approximation fails. By carrying out GLISSER simulations, I confirm that  $\sqrt{8} \leq T \leq 3$  particles all approach the  $a^{-1.5}$  steady state, with timescales 2–3× longer than the typical scattering timescale.

The fact that the current implanted Kuiper Belt can be acceptably fit with an  $a^{-2.5}$  power law (Petit et al., 2011; Beaudoin et al., 2023), one index steeper than the expected  $a^{-1.5}$ , may imply that the implantation process likely occurred *before* the scattering disk reached its steady state ( $\sim 500$  Myr from Figure 3.12 for  $\mathcal{T} = 3$ ). In the numerical simulation with  $\mathcal{T} = 3$  particles, the scattering disk obeyed  $a^{-2.5}$  at roughly 150 Myr after Neptune scattering began. If one assumes the implantation process itself (no matter what the mechanism lifted TNO  $q$  is) placed TNOs with equal efficiency in semimajor axis, then the implantation probably occurred around 150 Myr. If the implantation process was to be found to have placed them with, let’s say, efficiency  $\propto a$  (more objects lifted at larger  $a$  and less objects at lower  $a$ ), then the

implantation would have earlier, around 60 Myr, when the scattering disk was close to  $a^{-3.5}$ . It is also worth noting that this timing argument interpretation would be more complicated if primordial planetesimals coupled with Neptune tended to have a range of initial Tisserand parameters. Therefore, a more detailed study is needed to understand the relationship between Neptune's migration speed (or timescale) and the  $a$  distribution of the detached population.

In short, understanding the evolution of the ensemble of the scattering disk through the power law index  $\alpha$  provides a new way of diagnosing the timing of the implantation and its corresponding dynamical process. In Chapter 6, I will use these results to study the detachment of the scattering disk induced by an additional rogue planet, with the aim of constraining the possible dynamical path this planet may have taken.

## Chapter 4

# Introduction to the Early history of the Solar System

The origin of our planetary systems is a fundamental and complex scientific problem. One of the earliest idea related to this problem comes from the German philosopher Immanuel Kant, who proposed the Solar Nebula hypothesis in his book *Universal Natural History and Theory of the Heavens* (1755). It was later developed and refined by the French mathematician Pierre-Simon Laplace in 1796.

In the current consensus, the Solar System formed around 4.568 Gyr ago from the collapse of a dense giant molecular cloud. This cloud (i.e. the Solar Nebula) was composed of gas and dust and, as it collapsed, it began to spin and flatten into a disk-like shape (called a protoplanetary disk) due to the conservation of angular momentum. The dense core eventually became the Sun, while the dust and gas in the disk clump together to form planetesimals, which eventually become planets and other small bodies, such as moons, asteroids and Kuiper Belt objects, in the Solar System. This is the *planetesimal hypothesis* proposed in 1905 by American geologist Thomas Chrowder Chamberlin and astronomer Forest Ray Moulton. This hypothesis has since been supported by a wealth of scientific evidence. An excellent example of protoplanetary disks is the *Proplyds* image (Figure 4.1) captured by the Hubble Space Telescope (HST)'s wide field camera. These little blob-like structures are glowing protoplanetary disks found in the Orion Nebula. They are externally illuminated and photoevaporated by nearby stars and believed to be embryonic solar

systems that will eventually form planets.



**Figure 4.1:** Proplyds (glowing protoplanetary disks) in the Orion Nebula captured by the HST. This image shows the early stage of planetary system formation in a giant molecular cloud, where protoplanetary disks are externally photoevaporated by nearby bright stars. Photoevaporation could potentially explain the truncation of the protoplanetary disk that forms the Solar System (see Section 4.3.2).

This chapter will explore aspects of the formation and early history of the Solar System, with a focus on the dynamical process of giant planet migration and the resulting small-body orbital distributions. I will refer to the textbook *Fundamental Planetary Science* by Lissauer & de-Pater (2013) in this chapter.

## 4.1 Planesimals

Planetsimals are small, solid objects that are thought to have formed during the early stages of the development of our Solar System. They are believed to have been the precursors to the planets and other larger bodies that exist today. This term is also used in a more generic way to refer to small Solar System bodies – such as

asteroids and TNOs – which are in some sense unincorporated leftovers from the formation process.

Planetsimals are typically  $\lesssim 1000$  km in size and are composed of a variety of materials, including rock, ice, and metal. The chemical composition of a planetesimal will depend on the location it formed and its subsequent collisional histories. An important concept related to planetesimal chemical composition is the *frost line*, also known as the *snow line*. It is a boundary in the protoplanetary disk beyond which it is cold enough for a volatile compound (such as water, ammonia, or methane) to condense into solid icy grains. Inside a particular frost line, temperatures are too high for these volatiles to freeze, so they remain in a gaseous state and some eventually became part of the planetary atmospheres or escaped from the Solar System.

Each volatile substance has its own snow line depending on its condensation temperature. The snow line for water in our Solar System was likely at  $\approx 3$  au (Martin & Livio, 2012), resulting in the amalgamation of water-scarce rocky planetesimals that formed the terrestrial planets. It is also the line where comets become active. Beyond the snow line, large quantities of water-ice and other ices can condense in the protoplanetary disk, forming icy planetesimals like TNOs in the Kuiper Belt. The formation process from micrometer-sized dust particles to kilometer-sized planetesimals is an active branch of research in planetary formation (see recent review by Birnstiel et al. 2016), and *streaming instability* (Youdin & Shu, 2002; Johansen et al., 2007) is one of the new hypotheses that could explain the formation of planetesimals and match observational constraints.

Streaming instabilities are driven by differences in the motions of the gas and solid particles in the protoplanetary disk due to a global radial pressure gradient (Chiang & Goldreich, 1997). The differential speed causes gas drag onto the particles and the friction exerted from the particles back onto the gas accelerated the gas and diminished its difference from the Keplerian speed. In a simple disk this would result in a headwind that causes solid particles to spiral toward the star as they lose momentum to aerodynamics drag. If there is a small cluster of solid particles in gas, the local headwind is reduced so the inward drift rate of the cluster decreases. The slower drifting clusters are overtaken and joined by isolated particles, increasing the local density and further reducing radial drift. This positive feedback (i.e.

instability) eventually leads to exponential growth in the particle clumps and form planetesimals from self gravitation. (Weidenschilling, 1977; Birnstiel et al., 2016; Morbidelli & Nesvorný, 2020).



**Figure 4.2:** Composite image of the primordial Kuiper Belt object “Arrokoth” from New Horizons spacecraft data. This image shows it is a contact binary consisting of two lobes that have similar size and identical colors.

Numerical simulations of the streaming instability process (e.g., Johansen et al., 2015; Simon et al., 2016) show that planetesimals of a variety of sizes can be produced, but those that carry most of the final total mass are those of  $\sim$ 100 km in size. This corresponds to a ‘knee’ in the planetesimal size distribution, which can be found in OSSOS data (Kavelaars et al., 2021). Furthermore, Nesvorný et al. (2010) shows that the formation of binary planetesimals is the natural outcome of the gravitational collapse of clumps. These binaries are commonly found in the cold classical Kuiper Belt (Noll et al., 2008; Fraser et al., 2017; Noll et al., 2020), and one of them – (486958) Arrokoth – has even been closely imaged by the New Horizons spacecraft on 1 January 2019 (Figure 4.2).

## 4.2 Planet Formation

Planetesimals are important because they are thought to be the building blocks of planets. Once they reach  $\sim 1$  km in size, the primary factors controlling the growth of planetesimals into planets differ from those responsible for the accumulation of dust into planetesimals. Their orbits are then not significantly affected by interactions with gas in the disk, due to increasing mass-to-surface-area ratios for larger-sized planetesimals. Instead, the primary perturbations that affect their Keplerian orbits are mutual gravitational interactions and physical collisions (Lissauer & de Pater, 2013). As planetesimals collided and stuck together, they formed larger and larger objects, eventually creating the cores of planets (a.k.a protoplanets or planetary embryos). This process, known as planetary accretion, is believed to be how the terrestrial planets and the cores of giant planets formed. These cores can grow to be thousands of kilometers in size and vary from  $\sim 0.1 M_{\oplus}$  (e.g. Mercury and Mars) to  $\sim 10 M_{\oplus}$  (e.g., Jupiter and Saturn's cores with heavy elements, Guillot 1999) in mass. The dynamical process of planetesimals growing into planetary embryos are often divided into the following two steps (Armitage, 2020):

1. **Runaway growth**, in which a few large planetesimals grow very rapidly by accreting smaller objects in their vicinity.

This happens in the early stage of planetary accretion, where the mass of a protoplanet is small enough it cannot effectively heat up the orbital eccentricity or inclination of nearby planetesimals. The relative velocity dispersion in a circumsolar disk is given by

$$v_{\infty} \simeq \sqrt{e^2 + i^2} v_{\text{kep}}, \quad \text{if } e \approx 0 \text{ and } i \approx 0, \quad (4.1)$$

where  $v_{\text{kep}}$  is the Keplerian velocity. When the velocity dispersion among planetesimals is small ( $v_{\infty} \ll v_{\text{escape}}$ ), the gravitational focusing (described in Section 3.4) of the protoplanet is greatly enhanced, in other words,  $\mathcal{F}_g = 1 + (v_{\text{escape}}/v_{\infty})^2 \gg 1$ . As a result, the most massive protoplanet can very rapidly accrete materials in its vicinity. The growth rate of a runaway growth

is given by (Wetherill & Stewart, 1989; Kokubo & Ida, 1996):

$$\dot{M} \propto M^{4/3}, \quad (4.2)$$

which results in an exponential growth, with the largest objects growing much faster than the smaller ones.

2. **Oligarchic growth**, in which the growth of planet is more evenly distributed among protoplanets.

When planetary embryos dominate the stirring of the protoplanetary disk after reaching a critical mass about  $10^{22}$  kg (roughly the mass of Pluto, Wetherill & Stewart 1989; Ida & Makino 1993), the runaway growth would stall due to the heating up of planetesimal  $e$  and  $i$ . This leads to the onset of protoplanet-dominated stage, during which a small number of protoplanets with similar masses keep growing by more slowly sweeping up mass from the remaining large number of planetesimals that failed to become protoplanets. This phase is known as “oligarchic growth” in the sense that not one but several protoplanets dominate the planetesimal system. The growth rate during the oligarchic growth is given by (Kokubo & Ida, 1998)

$$\dot{M} \propto M^{2/3}. \quad (4.3)$$

By extrapolating oligarchic growth to the end of protoplanet accretion, the final mass or *isolation mass* of protoplanets can be obtained (Kokubo & Ida, 2000, 2002)

$$M_{\text{iso}} \simeq 0.16M_{\oplus} \left( \frac{b}{10R_H} \right)^{\frac{3}{2}} \left( \frac{\Sigma(a)}{10 \text{ g cm}^{-2}} \right)^{\frac{3}{2}} \left( \frac{a}{1 \text{ au}} \right)^3, \quad (4.4)$$

where  $b \simeq 10R_H$  is the orbital separation of protoplanets (Kokubo & Ida, 1998), and  $\Sigma(a)$  is the surface mass density of solids in the protoplanetary disk, with a typically-assumed value at 1 au being  $10 \text{ g cm}^{-2}$ . The end state of planetary accretion predicts closely-packed planetary embryos as massive as Mars at around 1 au, which is often used as initial conditions in numerical simulations that study the final stage of the terrestrial planet formation (e.g., O’Brien et al., 2006).

In the outer Solar System, planetary embryos are generally larger than those in

the terrestrial region (Equation 4.4). For example, Jupiter and Saturn are believed to have cores of  $\sim 10 M_{\oplus}$  (Guillot, 1999). When a planetary embryo reaches this mass, it is able to accumulate substantial amounts of gas from the surrounding protoplanetary disk (the average dust-to-gas ratio in protoplanetary disks is in the order of  $10^{-2}$ , as found in the interstellar medium (Birnstiel et al., 2010; Taki et al., 2016).) and undergo another runaway growth. This must have happened after the core had become sufficiently cool that the gas accretion can occur (a few million years, see Pollack et al. 1996; Lissauer et al. 2009), and prior to the removal of the hydrogen and helium in the disk by solar radiation ( $\lesssim 10$  Myr, Lissauer & Stevenson 2007; Lissauer & de-Pater 2013). This is known as the ‘core nucleated accretion model’ in the theory of giant planet formation (Safronov, 1972; Lissauer, 1993; Pollack et al., 1996).

## 4.3 Planetary Migration

Planetary migration refers to the process by which a planet changes its semimajor axis  $a$  over time due to interactions with the gas disk or planetesimals. The existence of hot Jupiters<sup>1</sup> in exoplanetary systems could be explained by substantial inward gas-driven migrations, though other explanations like planet-planet dynamical interactions and tides are also likely (Dawson & Johnson, 2018). There is also evidence for giant planet migrations in the Solar System (Nesvorný, 2018), which could potentially explain some puzzles in the small body distributions, including main-belt asteroids and TNOs.

### 4.3.1 Gas-Driven Migration

When abundant gases are still present in the protoplanetary disk, a planet can migrate towards the star as a consequence of angular momentum exchange between the disk and the planet. These are two types of disk-induced planetary migrations (Goldreich & Tremaine, 1980; Lin & Papaloizou, 1986; Lissauer & de-Pater, 2013; Armitage, 2020):

1. Type I migration in the gas happens when the planet’s mass is small enough

---

<sup>1</sup>Hot Jupiters are Jupiter-scale exoplanets on surprisingly close-in orbits, usually with  $a < 1$  au.

that it does not clear a gap around its orbit. For small bodies, the semimajor axis drift rate of type I migration is linearly proportional to the perturbing body's mass. But for planetary-sized bodies, the migration involves complicated nonlinear gravitational and fluid dynamics interactions and its rate may be very complicated to calculate. As a result of the planet interacting with strong spiral modes and the thermo and radiative state of the disc, both inward and outward migrations can occur and be relatively rapid (Kley et al., 2009; Michael et al., 2011).

2. **Type II migration** happens when the planet is able to perturb the disk so strongly that it clears an annular gap in the disk surrounding its orbit. The speed of this migration does not vary with planetary mass but depends on the disk's viscosity, unless the planetary mass is comparable to the mass of the local disk. When the planet's mass becomes similar to that of the protoplanetary disk, inertial effects become important, and the rate of migration slows (Lissauer & de-Pater, 2013).

The gas-driven migration of giant planets, especially Jupiter and Saturn, may relate to the formation of the terrestrial planets and the significant compositional differences across the main asteroid belt (see Section 1.3 for definition). The assembly of the Solar System terrestrial planets can be successfully modeled with all of the planetesimals initially confined to a narrow annulus between 0.7 to 1.0 au (Wetherill, 1986; Hansen, 2009). If too many planetesimals had existed beyond the orbit of Earth, many studies have shown (e.g., Raymond et al., 2006; O'Brien et al., 2006) the mass of a in-situ formed Mars would be too massive assuming a smoothly varying minimum-mass solar nebula<sup>2</sup>. This is also known as the ‘small Mars’ problem in planetary formation.

In addition to terrestrial planet formation, there are also problems with the mass, orbital distributions, and compositions of the main asteroid belt. The total mass of the main asteroid belt ( $\approx 3\%$  of Earth's moon) is 3 to 4 orders of magnitude

---

<sup>2</sup>The minimum-mass solar nebula is a protoplanetary disk that contains the minimum amount of solids necessary to build the eight planets of the solar system (Crida, 2009). The most famous version of the minimum-mass solar nebula was provided by Weidenschilling (1977) and Hayashi (1981), in which a lack of mass in the Mars and main asteroid belt region was observed in Weidenschilling (1977)'s figure 1.

less than would be expected from the minimum-mass solar nebula. Moreover, the orbits of most asteroids are more eccentric and inclined to the invariable plane of the Solar System, in contrast to the cold classical belt whose inclination profile is much more confined (Van-Laerhoven et al. 2019 and Chapter 2). There is also a mix between volatile-poor asteroids (mostly S types that formed closer to the Sun) and volatile-rich asteroids (mostly C types that formed farther away from the Sun) in the main asteroid belt. These two main asteroid classes have partially overlapping semimajor axis distributions, though C types outnumber S types beyond  $\sim 2.8$  au (Gradie & Tedesco, 1982). Recent compositional analyses on the asteroid (162173) Ryugu samples retrieved by the Japanese Hayabusa 2 mission suggest that the progenitor planetesimal of Ryugu could have formed in the outer Solar System reservoir and gotten implanted into the main belt at early stage of the Solar System (Yada et al., 2022; Nakamura et al., 2022b; Nakamura et al., 2022a; Paquet et al., 2022).

All these lines of evidence imply that there might have been large-scale stochastic evolutions of planetesimals in the inner Solar System. One hypothesis for explaining these features is the ‘Grand-Tack’ model proposed by Walsh et al. (2011), Raymond et al. (2014), and O’ Brien et al. (2014). In this model, Jupiter (initially formed around 3.5 au) has gone through both inward migration to the inner Solar System ( $\sim 1.5$  au) and then outward migration to its current location (5.2 au), leading to the truncation of the planetesimal disk that formed the terrestrial planets at 1 au and implantation of main belt asteroids from Jupiter scattering. Both the inward and outward migrations were gas-driven, but the outward migration would not activate until the subsequently rapidly inwardly migrating Saturn is caught in the 2:3 mean-motion resonance with Jupiter, after which the direction of type II migration is reversed for both giants (Masset & Snellgrove, 2001), sending them back to their current locations. A rapid inward migration of Saturn in a late oligarchic phase has potential advantages in a rogue-planet scenario (a topic briefly returned to in Chapter 6).

#### 4.3.2 Planetesimal-Driven Migration

In addition to torques from protoplanetary disks, planets can also migrate by scattering a large mass of planetesimals. Note that this process can continue after the

gas disk is dispersed (3–10 Myr) and thus is the only migration possible after the nebula’s removal. The large-scale scattering of planetesimals almost certainly happened in the past, supported by the existence of a massive Oort Cloud (see Section 1.3.3), the implanted Kuiper Belt (see Section 1.3.2) and the Late Heavy Bombardment (LHB)<sup>3</sup> supported by lunar rock samples from Apollo missions and crater histories on the Moon, Mars, and Mercury (Wetherill, 1975; Bottke & Norman, 2017).

The change of planet’s semimajor axis due to interactions with planetesimals can be simply modeled from the conservation of orbital energy:

$$\begin{aligned} E_{\text{planet},0} + E_{\text{planetesimal},0} &= E_{\text{planet},1} + E_{\text{planetesimal},1}, \\ -\frac{\mu_{\odot}m_p}{2a_{p,0}} - \frac{\mu_{\odot}m}{2a_0} &= -\frac{\mu_{\odot}m_p}{2a_{p,1}} - \frac{\mu_{\odot}m}{2a_1}, \\ \frac{1}{a_{p,1}} - \frac{1}{a_{p,0}} &= -\frac{m}{m_p} \left( \frac{1}{a_1} - \frac{1}{a_0} \right), \end{aligned} \quad (4.5)$$

where  $m_p$  and  $a_p$  denote the mass and semimajor axis of the planet, while  $m$  and  $a$  denote those of the planetesimal. As shown in Equation (4.5), any positive change in the planetesimal’s  $a$  (i.e.,  $1/a_1 - 1/a_0 < 0$ ) will also result in a negative change (scaled by their mass ratio  $m/m_p$ ) in planet’s  $a_p$ , vice versa. The maximum inward change in  $a_p$  occurs when the planetesimal is ejected ( $a_1 \rightarrow \infty$ ):

$$\Delta a_{p,\text{inward}} = \frac{m}{m_p} \frac{a_p^2}{a_0} \quad (4.6)$$

and the maximum outward change in  $a_p$  occurs when the planetesimal is scattered to a Sun-grazing orbit with  $Q = a_p$  and  $a_1 = a_p/2$ ,

$$\Delta a_{p,\text{outward}} = \frac{m}{m_p} \left( 2a_p - \frac{a_p^2}{a_0} \right). \quad (4.7)$$

---

<sup>3</sup>The Late Heavy Bombardment was a period of intense crater formation on the planets and moons of the solar system, particularly on Earth and the Moon. It is believed to have occurred between 4.1 and 3.8 Gyr ago. During this time, the Solar System was much more chaotic, with numerous large bodies colliding with each other and the inner planets. The LHB is thought to have played a major role in shaping the early solar system and in the evolution of life on Earth.

In the assumption that both the planet and planetesimal have similar initial orbits ( $a_p \simeq a_0$ ), the maximum inward/outward induced by one planetesimal have the same form:

$$\frac{\Delta a_p}{a_p} \simeq \frac{m}{m_p}, \quad (4.8)$$

thus the fractional change in planetary semimajor axis has the same magnitude of the planetesimal-planet mass ratio.

The planetesimal-driven migration dynamics is much more complex when several planets are interacting with a massive planetesimal disk, which is likely what happened in the past Solar System. One of the earliest numerical studies of giant planets interacting with a disk of planetesimals was carried out by Fernández & Ip (1984), in which the authors found the net effect of the planet-planetesimal angular momentum exchange is Saturn, Uranus, and Neptune migrating outward while Jupiter migrates sunward (their figure 3). The reason why Jupiter migrates in a different direction is that Jupiter is much more capable of ejecting planetesimals out of the system whereas the three less massive giants are more likely to ‘hand in’ planetesimals to Jupiter.

The timescale and radial range of the planetesimal-driven migration depend on the total mass and distributions of planetesimals (see Equation 4.8 and Hahn & Malhotra, 1999). Assuming a planetesimal disk of  $\sim 10 M_{\oplus}$ , the ejection of such a mass of planetesimals corresponds to an inward migration of Jupiter of a few tenths of an au, and an outward migration of Neptune of several au (Malhotra, 1993).

While the exact evolutionary history of a planetesimal-driven migration is stochastic, it is often approximated using a simple exponential model given by (Malhotra, 1993)

$$a(t) = a_f - \Delta a e^{-t/\tau}, \quad (4.9)$$

where  $a_f$  is the planet’s current semimajor axis,  $\Delta a = a_f - a_0$  is the migration distance, and  $\tau$  is the characteristic  $e$ -folding timescale of the migration.

In the outer Solar System, the outward migration history of Neptune has been extensively studied. This is because as the outermost known planet of the Solar System, the dynamical effect of Neptune migration is not only limited to the orbital range it had migrated through ( $\sim 20$ – $30$  au), but also extends to semimajor axis beyond 30 au due to its mean-motion resonances. Figure 4.3 is a schematic diagram

showing that as Neptune migrates outwards, its MMRs will also migrate at different speed. The farther a MMR is, the larger the distance (and faster) it will migrate.

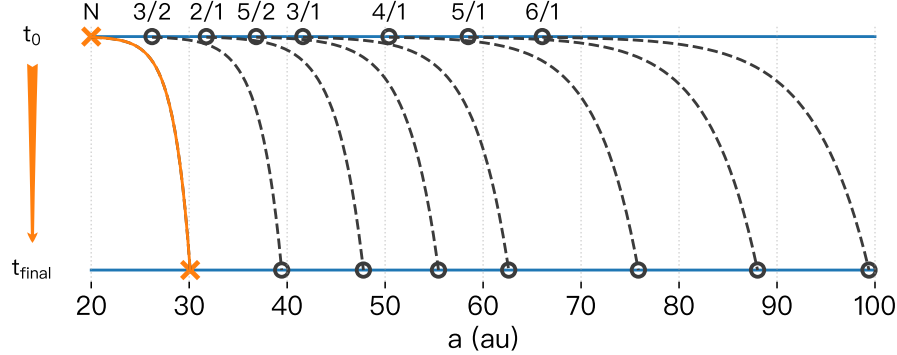


**Figure 4.3:** A schematic diagram showing the outward migrations of Neptune and its outer mean-motion resonances. The orange curve denote the exponential semimajor axis change of Neptune (modeled in Equation 4.9) from  $\sim 20$  au to its current location of 30.1 au. Dashed curves represent the resultant outward migration of its MMRs at different speed. Adapted from Malhotra (1995)'s figure 1.

Studies have attempted to constrain the migration history of Neptune by comparing migration models and TNO orbital distributions. Malhotra (1993) and Malhotra (1995) attempted to explain Pluto's peculiar orbit by resonant capture from an initially low- $e$  and low- $i$  orbits during Neptune's outward migration, but a Pluto-like inclination ( $\simeq 17^\circ$ ) is hard to produce by their simulations. Moreover, simulations show that Neptune's migration into a initially relatively cold Kuiper Belt is able to keep the cold classicals at low- $e$  and low- $i$  orbits, but still does not create the observed KBOs with inclinations above  $i \sim 15^\circ$  (Chiang et al., 2003; Hahn & Malhotra, 2005). In short, hot TNO populations do not seem to be created through in-situ stirring by neptunian MMRs, because 'resonant sweeping' does not account for their excited  $i$  distribution.

Instead, the hot population's excited inclination is most likely to have been created by Neptune scattering when Neptune migrated into a planetesimal disk (Gomes, 2003). The implantation rate of the hot population is  $\lesssim 1\%$  (Nesvorný, 2018), therefore a massive disk ( $\sim 10 M_\oplus$ ) outside Neptune is required to produce today's pop-

ulation. The primordial protoplanetary disk in which the Neptune has migrated through was mostly likely truncated at  $\sim 30\text{--}35$  au, because a continuous massive disk beyond 35 au would have led Neptune to keep migrating to  $a > 30$  au. In addition, to avoid producing Earth-mass or Mars-mass embryos originally outside the initial location of Neptune also requires the existence of a disk edge near 30 au (Gomes et al., 2004). The disk may have been truncated by photoevaporation or close-in stellar flybys if our Solar System formed within an embedded cluster (see Adams 2010, Gladman & Volk 2021, and Section 4.4).

Thanks to TNO surveys in the past two decades (e.g., Petit et al., 2011; Bannister et al., 2018), the details of Neptune's outward migration can be constrained. Nesvorný (2015a) shows that the TNO inclination constraint could be satisfied if the Neptune migration is slow ( $\tau \gtrsim 10$  Myr) and long-range ( $a_{N,0} \lesssim 25$  au). Detailed studies also show that Neptune's outward migration is not *smooth* but *grainy*, meaning that Neptune's orbit was constantly nudged by  $\Delta a \sim 10^{-3}$  au due to Pluto-scale planetesimal encounters during migration. This could avoid creating an excessively large 3:2 population (Nesvorný & Vokrouhlický, 2016; Lawler et al., 2019) and help populate both resonant and detached populations beyond 50 au (Nesvorný et al., 2016; Kaib & Sheppard, 2016). There is also evidence for an eccentric early migration of Neptune (Nesvorný, 2021), which could explain the  $q > 35$  au and  $i < 10^\circ$  TNOs with  $50 < a < 60$  au if Neptune's orbit was excited to  $e_N \simeq 0.1$  and subsequently damped to the current value of  $e_N = 0.01$ .

#### 4.3.3 Planetary Instability

Besides migration inside a gaseous or a planetesimal disk, planets are also able to suddenly drastically change their orbits by direct planet-planet interactions. Such a model is called an *instability* model because the rapid change is often triggered by breaking a temporarily-stable planetary configuration.

The best-known instability model of the Solar System is the *Nice model*, named after the Nice observatory in southern France where the model was initially conceived. It attempts to provide a large scenario for the currently observed planetary orbits, the present orbital distribution of the main-belt asteroids, the origin of Jupiter's Trojans, and the LHB which occurred  $\sim 700$  Myr after the planets formed.

The original Nice model, composed by Morbidelli et al. (2005), Tsiganis et al. (2005), and Gomes et al. (2005a), has four giant planets initially placed on compact quasi-circular and coplanar orbits, with the outermost ice giant having  $a < 20$  au. This configuration is metastable for several hundred million years, until Jupiter and Saturn ever crossed their 1:2 mutual mean-motion resonance due to planetesimal-driven migrations, triggering the planetary instability. The Solar System would be largely destabilized caused by the sudden jump in Jupiter and Saturn's eccentricities. As a result, Uranus and Neptune would get scattered outward to large- $a$  and  $e$  orbits, initiating a new wave of planet-planetesimal interaction in the outer disk (Tsiganis et al., 2005). This allows the two ice giants to migrate to their current locations while damping their eccentricities and inclinations. In addition, the instability also violently destabilized pre-existing Trojans and most of the Jupiter Trojans we see today were chaotically captured (Morbidelli et al., 2005). Jupiter and Saturn's temporary large- $e$  state also excited the primordial main asteroid belt and delivered them to the inner Solar System, which triggered the LHB (Gomes et al., 2005a).

Subsequent studies derived from the Nice model reveal its potential to 1) explain the capture of irregular satellites during planetary encounters, including Neptune's largest moon Triton (Nesvorný et al., 2007), 2) form an implanted Kuiper Belt (Levison et al., 2008) that is in agreement with some of the observations (Fraser et al., 2014; Pike et al., 2017a; Pike & Lawler, 2017) while 3) keeping the cold classical Kuiper Belt relatively unexcited (Batygin et al., 2011). It is also not inconsistent (but not fully consistent either) with the formation of the Oort Cloud (Brasser & Morbidelli, 2013).

The Nice model also faces several criticisms and challenges. The idea of an  $\approx 0.5$  Gyr metastable delay before dispersing the outer Solar System's massive primordial planetesimal is inconsistent with constrains on the Solar System's dynamical and collisional history (Nesvorný, 2018; Gladman & Volk, 2021; Benavidez et al., 2022). Moreover, the slow migration of Jupiter and Saturn past the 2:1 resonance, which is a defining feature of the original Nice model, is difficult to reconcile with the orbital distribution of the asteroid belt (Morbidelli et al., 2010) and constrains provided by terrestrial planets (Morbidelli et al., 2009; Brasser et al., 2009; Walsh & Morbidelli, 2011; Brasser et al., 2013). This has led to the proposal of the *five-planet*

*model*<sup>4</sup>, which involves a very short-lived additional ice giant that was eventually ejected by Jupiter (Thommes et al., 1999; Nesvorný, 2011; Nesvorný & Morbidelli, 2012; Brasser et al., 2013; Batygin et al., 2012) to address these challenges. In a ‘five-planet model’, the sudden jump in Neptune’s semimajor axis that occurs during the epoch of the ejection of the fifth ice giant could also account for the concentration of cold classicals near 44 au, known as the Kuiper Belt kernel (Petit et al., 2011; Nesvorný, 2015b), as well as a late excitation of Neptune’s eccentricity (Nesvorný et al., 2020; Nesvorný, 2021).

In summary, the planetary instability model represented by the Nice model is by far the most discussed Solar System model that provides proposed solutions for various puzzles in planetary formation and small body orbital distributions, including the main asteroid belt, Trojans, irregular satellites, and part of the Kuiper Belt. It would be fair to say that many of these solutions are ad-hoc tunings of the original scenarios. Additionally, it has great difficulties in explaining the *distant Kuiper Belt*, especially TNOs with high perihelia that are generally out of the reach of all known giant planets, even during an instability event. Starting from the next section, I will mostly focus on the formation hypotheses related to the distant Kuiper Belt.

#### 4.4 Stellar Environment

The birth environment of the Sun plays a vital role in the formation of the Solar System. Stars form in clusters of tens of stars to  $10^5$  stars. There is direct evidence that Sun was born in a moderate star-forming birth cluster (Adams, 2010):

1. The presence of short-lived radioactive species from meteorites could be produced in supernova explosions, which probably occurred when the Sun was in a birth cluster where the stellar density is high.
2. The protoplanetary disk was likely truncated at  $\sim 30$  au (see justifications in Section 4.3.3). This could be caused by either photoevaporation from the ultra-violet (UV) radiation or very close-in stellar flybys. Both processes would

---

<sup>4</sup>Although the rogue planet model I will study in the next two chapters also falls into the category of a ‘five-planet model’ in the literature, this term has been specifically used to address a Solar System model with an extra giant planet.

most likely happen if the Sun formed in a birth cluster of at least thousands of stars.

Another piece of evidence advocated by many researchers is the presence of distant detached objects, such as 2000 CR<sub>105</sub> (Gladman et al., 2002), Sedna (Brown et al., 2004), 2012 VP<sub>113</sub> (Trujillo & Sheppard, 2014), and Leleākūhonua (Sheppard et al., 2019). They all have very large semimajor axes, as well as very distant perihelia, too detached to be explained by any Solar System models with only the four giant planets. Table 4.1 shows the barycentric orbits of the 22 known TNOs with  $a > 200$  au and  $q > 38$  au. Recall there is huge bias against detecting orbits with increasing  $a$ ,  $q$ , and  $i$ .

Close-in stellar encounters when the Sun resided in a birth cluster has been discussed by several authors as an idea for their origin (Ida et al., 2000; Gladman et al., 2002; Morbidelli & Levison, 2004; Kenyon & Bromley, 2004; Brasser et al., 2012; Brasser & Schwamb, 2014). In this hypothesis, detached objects with extreme  $q$  are often called Inner Oort Cloud (ioc) objects, implying a belief they were created in a similar manner how the Oort Cloud was created. However, there are some stringent constraints and serious drawbacks related to the stellar encounter theory:

### 1. Flyby timing

Such stellar encounters creating ‘IOC objects’ must have occurred at the very early stage of planetary migrations and planetesimal scatterings ( $\lesssim 100$  Myr), in order to not hinder the subsequent formation of the more massive Oort Cloud (Morbidelli & Levison, 2004).

### 2. Flyby distance

The stellar flyby must also have pinpointed to a narrow annulus of the Solar System, with the closest encounter distance  $r_{\min} \lesssim 400$  au to create Sedna and  $r_{\min} \gtrsim 225$  au to preserve planetary orbits (Adams, 2010). Recently, Batygin & Brown (2021) also found that to maintain the unexcited structure of the cold classical Kuiper Belt, the upper bound of number density-weighted cluster residence time is  $\chi \lesssim 2 \times 10^4$  Myr pc<sup>-3</sup>, corresponding to the closest approach of  $r_{\min} \gtrsim 240$  au for a passing star within the Solar System’s birth cluster.

**Table 4.1:** barycentric orbital elements of TNO with  $a > 200$  au and  $q > 38$  au.

Name (Provisional designation)	$a$ (au)	$q$ (au)	$i$ ( $^{\circ}$ )
148209 (2000 CR <sub>105</sub> )	221.9	44.1	22.8
<b>90377 Sedna (2003 VB<sub>12</sub>)</b>	<b>506.4</b>	<b>76.2</b>	<b>11.9</b>
474640 Alicanto (2004 VN <sub>112</sub> )	328.2	47.3	25.5
2010 GB <sub>174</sub>	348.6	48.6	21.6
<b>2012 VP<sub>113</sub></b>	<b>262.0</b>	<b>80.5</b>	<b>24.1</b>
2013 FT <sub>28</sub>	291.7	43.5	17.4
2013 RA <sub>109</sub>	462.8	46.0	12.4
2013 SY <sub>99</sub>	732.9	50.0	4.2
2013 SL <sub>102</sub>	314.4	38.1	6.5
505478 (2013 UT <sub>15</sub> )	200.1	43.9	10.7
2014 SR <sub>349</sub>	298.6	47.5	18.0
2014 WB <sub>556</sub>	280.2	42.7	24.2
2015 GT <sub>50</sub>	311.2	38.4	8.8
2015 KG <sub>163</sub>	679.8	40.5	14.0
2015 RX <sub>245</sub>	423.5	45.6	12.1
<b>541132 Leleākūhonua (2015 TG<sub>387</sub>)</b>	<b>1089.6</b>	<b>65.0</b>	<b>11.7</b>
2016 SA <sub>59</sub>	244.9	39.1	21.5
2016 SD <sub>106</sub>	350.2	42.7	4.8
2018 VM <sub>35</sub>	289.4	44.5	8.5
2019 EU <sub>5</sub>	1220.9	46.8	18.2
2021 DK <sub>18</sub>	779.9	44.4	15.4
2021 RR <sub>205</sub>	990.9	55.5	7.6

**Note.** Three bolded TNOs are the three extremely detached Sednoids that have  $q > 60$  au. Data retrieved from JPL Small-Body Database ([https://ssd.jpl.nasa.gov/tools/sbdb\\_query.html](https://ssd.jpl.nasa.gov/tools/sbdb_query.html)) on January 3rd, 2023.

### 3. Inclination distribution

Numerical simulations that populate the IOC by passing stars generally create inclination profiles significantly hotter than the scattering disk, with a significant fraction of particles on even retrograde orbits (see, for example, figure 6 in Brasser & Schwamb 2014 and figure 3 in Batygin & Brown 2021). This is inconsistent with the inclination distribution of the 22 known distant high- $q$  TNOs (Table 4.1), whose mean ecliptic inclination is only  $\approx 15^{\circ}$ , consistent

with the inclination profile of the implanted population with the Gaussian width of  $\sim 15^\circ$  (Brown, 2001; Van-Laeerhoven et al., 2019). Assuming this population were really created by one close-in passing star, the direction of that particular stellar flyby must have also been a (low-probability) flyby at low inclination relative to the plane of the Solar System, in order to not heat their inclination distribution.

In conclusion, no stellar flyby model has successfully explained the  $a$ ,  $q$ , and  $i$  distributions of distant high- $q$  TNOs. The right timing, the small range of allowable approach distance and the right injection angle are all required to produce the observed distributions. These weaknesses of the birth cluster explanation are often glossed over and the argument that Sedna is an IOC object made by passing stars has often taken as a fact in literature (e.g. Pfalzner 2013; Portegies-Zwart et al. 2021)

Therefore, I will refrain from using the word ‘Inner Oort Cloud objects’ due to the lack of concrete evidence for their formation mechanisms. Instead, I adopt the term *Sednoids* (first coined by Bernstein 2004, but there is no accepted orbital element range) to address Sedna-like high- $q$  and large- $a$  TNOs. In the next chapter, I will focus on hypotheses that use an additional planet to explain puzzling features, including Sednoids, in the Solar System.

## 4.5 Additional Planets

The mathematical prediction of Neptune’s existence represents the only successful story of a new planetary discovery by dynamical evidence within the Solar System (Krajnović, 2016). Upon the discovery of Uranus by William Hershel, astronomers continued to keep track of Uranus’s location and computed ephemerides over time based on the then-known giant planets (e.g., Bouvard, 1824). Subsequent observations revealed a growing difference between the theoretical and the observed locations, which led French astronomer Urbain Le Verrier (Le-Verrier, 1846b,a) and British astronomer John Couch Adams (Adams, 1846) to propose an additional planet outside the orbit of Uranus. Le Verrier sent his results to Johann Gottfried Galle at the Berlin Observatory, who immediately began to search the suggested position in the night sky on 23 September with his student, Heinrich Louis d’Arrest. Neptune was discovered just after midnight, after less than an hour of searching and

less than 1 degree from the position Le Verrier had predicted.

After the successful discovery of Neptune, Le Verrier focused on the anomalous precession rate of Mercury's orbit, that could not be fully accounted for by known planets. In 1859, he proposed that an additional planet interior to Mercury (which he gave the name *Vulcan*) is responsible for imposing extra precession on Mercury. In the early 20th century, however, Einstein developed his theory of General Relativity (Einstein, 1916), which self-consistently resolved the Mercury precession problem. The need for Vulcan was thus alleviated.

#### 4.5.1 Still-Existing planets

Since the discovery of the Kuiper Belt (Jewitt & Luu, 1993), several hypotheses involving additional planets have been proposed to explain its orbital structures. The idea that Mars- or Earth-scale planets might have assembled beyond 50 au was inspected by Stern (1996), who hypothesized that the primordial disk was not truncated at  $\sim$ 50 au (their figure 5). Upon the discovery of the first detached TNO 2000 CR<sub>105</sub>, Gladman et al. (2002) argued that planetary-sized body that is still resident in the Kuiper Belt could in principle scatter this high- $q$  TNO to its current orbit. Brunini & Melita (2002) studied the effects of a Mars-sized planet with  $a \sim 60$  au and showed that the existence of such an object would produce a cliff at  $\sim$ 50 au. The still-present planetary-sized body in the Kuiper Belt was challenged by Morbidelli et al. (2002), who showed that planetary embryos never formed in the Kuiper Belt, otherwise at least one of the surviving embryos should have already been discovered by then Kuiper Belt surveys considering the 15-20% retention rate they calculated for the original embryos. Furthermore, the existence of an additional planetary mass inside 100 au would have excited the cold belt, which will be studied in Chapter 6.

The discovery of even more distant high- $q$  TNO Sedna (Brown et al., 2004) again lead to the creation of many hypotheses involving the presence of a distant planetary-mass objects. Gomes et al. (2006) proposed that Sednoids can be produced by a hypothetical Neptune or Jupiter-mass planet orbiting within the inner Oort Cloud. They also found that a very eccentric Earth-mass planet with  $q = 60$  au and low- $i$  could also produce Sedna-like orbits. Lykawka & Mukai (2008) carried out intensive numerical studies on the dynamical effects of a sub-Earth-mass planet

beyond  $a > 100$  au and proposed that to match several observational and dynamical constraints, the hypothetical planet would have  $0.3\text{--}0.7 M_{\oplus}$ , with  $a = 175\text{--}250$  au,  $q > 80$  au, and  $i = 20^{\circ}\text{--}40^{\circ}$ . They also concluded that the existence of 3:2, 2:1, and 5:2 resonant TNOs implies that any hypothetical resident distant planet must have an overall  $q > 80$  au, and used this to rule out *all* previous models suggesting resident planets with  $q \leq 70$  au (e.g. Brunini & Melita 2002; Melita & Williams 2003; Melita et al. 2004; Brown et al. 2004).

The enthusiasm for an unseen planet in the outer Solar System was re-motivated by the discovery of yet another TNO with  $q \sim 80$  au – 2012 VP<sub>113</sub> (Trujillo & Sheppard, 2014) – and the claims of (debated) *orbital clustering* (also called *orbital alignment*) for large- $a$  TNOs (Trujillo & Sheppard, 2014; Sheppard & Trujillo, 2016). Trujillo & Sheppard (2014) first proposed that the Kozai mechanism of an unseen planet at 210 au can explain the clustering of  $\omega$ . The ‘observed orbital alignment’ also prompted Batygin & Brown (2016a) to propose the so-called *Planet Nine* model, in which a distant eccentric planet with mass  $\gtrsim 10 M_{\oplus}$  imposes secular  $\Omega$  and  $\varpi$  cycles onto distant TNOs and creates the orbital clustering. A series of subsequent studies on Planet Nine (e.g. Batygin & Brown 2016b; Batygin & Morbidelli 2017; Millholland & Laughlin 2017; Becker et al. 2017; Khain et al. 2018; Cáceres & Gomes 2018; Batygin et al. 2019) have demonstrated that Planet Nine would impose the following dynamical effects onto the so-called ‘extreme’ TNOs (in their definition,  $a > 250$  au):

1. The apsidal confinement of extreme TNOs,
2. perihelion detachment of extreme TNOs,
3. clustering of the  $a \gtrsim 250$  au orbital planes, and
4. excitement of extreme TNO inclinations.

The reality of the distant TNO orbital clustering has been cast in doubt by outer Solar System surveys that account for the significant observational biases, such as OSSOS (Shankman et al., 2017) and the Dark Energy Survey (Bernardinelli et al., 2022). In particular, Napier et al. (2021) analyses the joint detection probability of the 14 distant TNOs discovered by OSSOS, DES, and Sheppard & Trujillo (2016),

in which they find the  $\Omega$  and  $\varpi$  distributions of detected TNOs are consistent with a uniform distribution and thus this sample provides no evidence for orbital clustering, upon which the Planet Nine hypothesis was built.

Other still-present planet models include a hypothetical distant planet ( $a \sim 665$  au) in resonance with the four extreme TNOs (Malhotra et al., 2016) and a close-in ( $a \lesssim 100$  au) Mars-mass planet to account for the so-called ‘curious warp’ in the Kuiper Belt’s mean plane (Volk & Malhotra, 2017), although a later independent analysis favors no such warp (Van-Laerhoven et al., 2019).

The gravitational effect of an unseen planet should be able to slightly perturb the trajectories of Solar System planets, and thus high-precision measurements of their positions by orbiting spacecraft provide important constraints to any still-existing planetary-mass models. Based on the INPOP19a planetary ephemerides (Fienga et al., 2019), the presence of a  $5 M_{\oplus}$  planet inside  $d \leq 500$  au and a  $10 M_{\oplus}$  planet inside  $d \leq 650$  au is ruled out (Fienga et al., 2020). In a study carried out by Gomes et al. (2022), the existence of a  $5 M_{\oplus}$  planet at  $d \leq 400$  au, an Earth-mass planet at  $d \leq 260$  au, and a Mars-mass planet at  $d \leq 120$  au is ruled out by data from *Juno*, *Cassini*, and Mars-orbiting spacecraft. This basically rules out over half of the already-reduced parameter space for the updated orbit of Planet Nine (with  $\approx 6 M_{\oplus}$  and  $a \approx 400$  au, Brown & Batygin 2021).

With the authenticity of the orbital clustering questioned and a large chunk of the parameter space ruled out, the Planet Nine hypothesis and other still-resident planet models seem less and less likely to be the explanation for structures in the outer Solar System.

#### 4.5.2 Rogue planets

The Solar System surprisingly lacks any ‘super-Earth’ planets (often defined as planets with radius between  $1R_{\oplus}$  to  $1.75R_{\oplus}$ ), which are the most common type of planets found in exoplanetary systems (Borucki et al., 2010). Moreover, given the fact that four  $\sim 10 M_{\oplus}$  giant planet cores (see Section 4.2) are present, and there must have been at least 2,000 Pluto-sized planetesimals to explain the formation of the Pluto-Charon binary (Stern, 1991), it is unnatural to believe that no planetary-scaled objects ever formed and temporarily existed in the early Solar System.

A hypothesis that posits the presence of temporarily present but eventually ejected planet(s) in the Solar System is commonly referred to as a ‘rogue planet model’. Ejected rogue planets<sup>5</sup> are natural results of planet–planet scattering in planet formation(Rasio & Ford, 1996; Weidenschilling & Marzari, 1996; Lin & Ida, 1997). It is estimated that most likely 90%–95% of giant planet systems must have undergone planet–planet scattering in their past (see Raymond & Morbidelli 2022 and references therein). Interstellar rogue planets are found in microlensing surveys; the discovered rogue planets have a wide range of masses, covering the range from Jupiter mass (Mróz et al., 2019) to Neptune mass (Mróz et al., 2018) to super-Earth mass (Mróz et al., 2019) and even Mars mass (Mróz et al., 2020).

Assuming one or more extra planetary-mass objects temporarily existed in our Solar System, their gravity could have left permanent marks on the orbital distribution of small bodies, especially TNOs in the outer Solar System. Petit et al. (1999) studied the effects of Jupiter-scattered rogues on the main asteroid belt and Neptune-scattered rogues on the primordial Kuiper Belt. In their simulations, the cold classical belt is completely destroyed by a Neptune-scattered Earth-mass rogue that is born in the Kuiper Belt and whose aphelion stays  $Q \lesssim 100$  au in their entire 100 Myr integration time. Morbidelli & Levison (2004) studied the rogue-planet scenario for the creation of Sedna and 2000 CR<sub>105</sub>. Their first simulation consisted of 10 half-Earth-mass embryos scattered out by Neptune. They also considered a non-scattering Earth-mass planet initially on an orbit similar to that postulated by Brunini & Melita (2002), with  $a \sim 60$  au,  $e = 0.2$ , and  $i = 6^\circ$ , and integrated it with low- $e$  and low- $i$  test particles between 60 and 90 au. Sedna was created in neither of their simulations. Morbidelli & Levison (2004) thus claimed that the rogue planet scenario cannot explain Sedna-like orbits, at least in the contexts they explored.

A more detailed study on the rogue planet theory was carried out by Gladman & Chan (2006), in which the authors run several simulations with Neptune-scattered rogues ranging from Mars mass to 2 Earth mass. Their simulations show that the rogue typically exist for  $\sim 100$  Myr before ejection, close to Neptune’s typical scattering timescale from Chapter 3. They demonstrated that orbits similar to Sedna can be produced by the rogue once its mass  $m_r \geq 1M_\oplus$ . The dynamical excitation produc-

---

<sup>5</sup>A rogue planet existing in the interstellar space is also termed a *free-floating planet* or an *interstellar planet*.

ing detached TNOs was found to be dominated by the most massive object. They also found detached TNOs produced by the rogue have maximum  $i$  as a declining function of  $a$ , in apparent contrast to stellar flyby models which generically produce large  $i$  for increasing small-body semimajor axes. The original Gladman & Chan (2006) model was compared against OSSOS detections in Lawler et al. (2018b), in which this specific rogue model overproduced  $a < 100$  au detached TNOs. Gladman & Volk (2021) illustrated an unpublished simulation (their figure 8) from the Gladman & Chan (2006) suite, demonstrating a  $2M_{\oplus}$  rogue with  $q$  near Uranus is also capable of creating orbital detachment from the scattering disk.

The rogue planet is a natural outcome of planet formation simulations and has the promising effect of producing Sedna-like detached TNOs in the distant Kuiper Belt. However, few extended studies since Gladman & Chan (2006) have been conducted to explore the rogue's dynamics or to check whether it fits into the updated TNO inventory. As Kavelaars et al. (2020) wrote in *The Trans-Neptunian Solar System*: “Precursor simulations like that of Gladman & Chan (2006) should be revisited in light of the new high- $q$  TNO discoveries to date”.

## 4.6 Important Metrics of an Outer Solar System Model

In this section, I will summarize the unsolved problems in the outer Solar System that are difficult to explain by current models of planetary formation and migration. Shedding light upon or even solving these problems is one of the main goals of this thesis, and I will also use them as metrics to evaluate the likelihood of a Solar System model, including the rogue planet model I will investigate in Chapter 5 and 6.

### 1. Distribution of detached objects

The  $a - q$  distributions of the detached objects is the most critical factor for the rogue planet simulation. The rogue should be able to form most of the discovered detached objects, including the three most-distant Sednoids (Table 4.1) with moderate inclinations.

### 2. Detached objects near resonances

My preliminary simulations (Fig. 1.8) show that a rogue can perturb TNOs from  $a=50-100$  au into neptunian resonances that are hard to populate by

planet migration (see figure 3 in Crompvoets et al., 2022). To my knowledge, this dynamical effect has never been discussed in literature. It is worth studying whether the rogue planet can provide some alternatives to planet migration (e.g. Nesvorný et al. 2016) for various populations.

### 3. Ratio of detached vs scattering

An important metric is the population ratio of the detached and the scattering components. Today's scattering population is estimated to be eroded down to only 1% of its primordial size (Duncan & Levison, 1997), while the detached population is almost unchanged after the rogue's ejection (Gladman & Chan, 2006).

Petit et al. (2011) estimated the number of  $D \geq 100$  km objects in the outer Kuiper belt ( $a$  beyond the 2:1 mean-motion resonance) is  $\sim 80,000$  non-resonant TNOs. These estimates are highly dependent on the assumed orbital distribution, and the population could be much larger if there are many high- $q$  objects. Lacking a consensus on the inventory of the detached population, UBC undergraduate student Matthew Beaudoin estimated the population of the detached Kuiper Belt (Beaudoin et al., 2023, submitted to PSJ) as  $(5 \pm 2) \times 10^4$  with  $H_r < 8.66$  ( $D > 100$  km for a 4% albedo). Part of this estimate is based on the detached orbital distributions produced by my rogue simulation in Section 5.

### 4. Stability of the cold classical Kuiper Belt

The cold classical Kuiper Belt must survive in its present state and not be disturbed by perturbing bodies like passing stars or rogues. In particular, the  $I_{\text{free}} < 4^\circ$  (see Chapter 2) cold classicals must not be heated to unacceptable degree.

In addition to these aspects used to judge the rogue planet theory, there are some other aspects that may have links to the formation of the outer Solar System and is worth looking at. Due to the uncertainty in some of the puzzles, these will *not* be used as metrics to judge the model:

#### 1. \*Ratio of distant resonant vs detached

Resonant population estimates (Gladman et al., 2012; Crompvoets et al., 2022) show that distant resonances (i.e. neptunian MMRs beyond 2:1) host large TNO populations, with some of the distant n:1 resonances comparable to the 3:2. The populated distant resonances contradict predictions from migration models, whereas more in line with an intrinsic resonance-sticking mechanism in the current scattering disk (Volk et al., 2018; Yu et al., 2018; Crompvoets et al., 2022). The rogue planet's effect on resonant TNOs is largely unknown. It is also unclear how adding a temporarily-present massive body will change the ratio of resonant vs detached in the distant Kuiper Belt.

## 2. \*Relations with Neptune outward migration

Recent outer Solar System surveys appear to establish that detached objects in proximity of a resonance are more likely to be found in the sunward side (i.e.  $a < a_{\text{res}}$ ), rather than just beyond. There is growing observational evidence for this (Lawler et al., 2019; Bernardinelli et al., 2022), and Neptune's grainy outward migration has been demonstrated to be able to create this asymmetry (Nesvorný et al., 2016; Kaib & Sheppard, 2016). It's worth investigating how Neptune's interaction with a temporarily-present planet would shape its migration path, which can be diagnosed through detailed orbital structures in the Kuiper Belt.

## 3. \*Perihelion gap

Trujillo & Sheppard (2014) and Kavelaars et al. (2020) pointed out for the range  $150 < a < 1000$  au, no objects have been discovered between  $50 < q < 75$  au, though detectability is actually easier than for the  $q$  of the two known higher- $q$  TNOs, Sedna and 2012 VP<sub>113</sub>. So far, the gap's presence is questionable and not statistically significant. If such a ' $q$ -gap' (see Figure 1.9) becomes more pronounced with further discoveries, a rogue planet scenario could be undermined due to fact that the  $q$  oscillations that the rogue uses to detach objects will fill the phase space up to the highest values of  $q$ . I have, however, noticed that the my preliminary simulation in Figure 1.8 shows an asymmetry in the  $a - q$  distribution, exhibiting a non-uniform density where at  $a \simeq 200-300$  au there are many more high- $q$  objects near  $q = 100$  au than

with  $q$  from 40-80 au, and thus perhaps there could be an explanation related to the large- $e$  nature of the rogue's orbit.

#### 4. \*The formation of the Oort Cloud

Planetesimals scattered out by Neptune and/or Uranus to  $a > 1000$  au will feel the gravity of galactic tidal field and random passing stars, which can raise their perihelia and send them into the Oort Cloud. Early simulations with only 4 giant planets predict a large scattering population today (Dones et al., 2004). The rogue planet, however, is likely to lift some scattering objects to the detached zone (at smaller  $a$  than the inner Oort Cloud), thus decreasing the size of the scattering population (see figure 2 of Lawler et al. 2017). The possible influences of the rogue in the formation of the Oort Cloud is still unknown.

To summarize, Table 4.2 compares existing outer Solar System formation hypotheses against confirmed observational constraints. In the next two chapters, I will concentrate on the metrics and problems above to understand the rogue's dynamics and constrain the possible pathway it might have taken until its ejection. More specifically, Chapter 5 will highlight the rogue's effects in the  $50 < a < 100$  au Kuiper Belt, while Chapter 5 will focus on the rogue's parameters and dynamical histories.

**Table 4.2:** Comparison between different outer Solar System formation hypotheses

	$a < 48$ au	$48 < a < 200$ au		$a > 200$ au		
	Cold belt	Detached	Resonant	Sednoids $a, q$	Sednoids $i$	Current clustering
<b>Grainy Migration</b>	✓	✓	?	✗	✗	✗
<b>Stellar Flyby (Birth Cluster)</b>	$r_{\min} \gtrsim 240$ au	?	?	$r_{\min} \lesssim 400$ au	near-planar flyby(?)	?
<b>Existing Planet (Planet Nine)</b>	?	?	?	✓	✗	all $q$
<b>Rogue Planet</b>	TBD	TBD	TBD	✓(TBD)	✓(TBD)	TBD

**Note.** ‘✓’ denotes a hypothesis that satisfies the constraint or produces this feature, ‘✗’ denotes a hypothesis that does not satisfy the constraint or produce this feature, and ‘?’ means unknown or no published studies. For grainy migration models, only the creation of  $a < 100$  au detached TNOs was demonstrated (Nesvorný et al., 2016). The two stellar flyby  $r_{\min}$  constraints come from Adams (2010) and Batygin et al. (2020), whereas the ‘near-planar flyby’ can make Sednoids that match their observed inclinations’ assumption is only postulated but never demonstrated. The rogue planet model here represents the preliminary study by Gladman & Chan (2006), and ‘TBD’ denotes aspects will be studied in Chapter 5 and 6; Declining inclinations with larger  $a$  were observed, but the statistics were poor. The orbital clustering of currently-discovered  $a > 200$  au TNOs, which is the motivator of the ‘Planet Nine’ hypothesis, is not supported by observational evidence (Shankman et al., 2017; Napier et al., 2021; Bernardinelli et al., 2022).

## Chapter 5

# A Rogue Planet Helps to Populate the Distant Kuiper Belt

The orbital distribution of transneptunian objects (TNOs) in the distant Kuiper Belt (with semimajor axes beyond the 2:1 resonance, roughly  $a = 50\text{--}100$  au) provides constraints on the dynamical history of the outer solar system. Recent studies show two striking features of this region:

1. a very large population of objects in distant mean-motion resonances with Neptune,
2. the existence of a substantial detached population (non-resonant objects largely decoupled from Neptune)

Neptune migration models are able to implant some resonant and detached objects during the planet migration era, but many fail to match a variety of aspects of the orbital distribution. In this work, we report simulations carried out using an improved version of the GPU-based code GLISSE, following 100,000 test particles per simulation in parallel while handling their planetary close encounters. We demonstrate for the first time that a 2 Earth-mass rogue planet temporarily present during

---

This chapter is based on the following published work: Y. Huang, B. Gladman, M. Beaudoin & K. Zhang, *A Rogue Planet Helps to Populate the Distant Kuiper Belt*. The Astrophysical Journal Letters **938**, L23 (2022)

planet formation can abundantly populate both the distant resonances and the detached populations, surprisingly even without planetary migration. We show how weak encounters with the rogue greatly increase the efficiency of filling the resonances, while also dislodging TNOs out of resonance once they reach high perihelia. The rogue’s secular gravitational influence simultaneously generates numerous detached objects observed at all semimajor axes. These results suggest that the early presence of additional planet(s) reproduces the observed TNO orbital structure in the distant Kuiper Belt.

## 5.1 Introduction

The heavily studied main Kuiper Belt has semimajor axes smaller than the 2:1 resonance at 48 au (often taken to be the outer boundary of the classical belt). Beyond the 2:1, the transneptunian region seems not as abundantly populated and is dominated by large-eccentricity ( $e$ ) transneptunian objects (TNOs) in the scattering (Trujillo et al., 2000; Lawler et al., 2018a), resonant (Gladman et al., 2012; Crompvoets et al., 2022), and detached (Gladman et al., 2008) populations. This apparent drop in TNO number is partly due to the observational bias that penalizes orbits with large- $a$ , large-perihelia ( $q$ ), and large-inclinations ( $i$ ). Deriving the intrinsic TNO orbital distribution at large semimajor axis requires well-characterized surveys that properly handle observation bias. Modern surveys like CFEPS (Petit et al., 2011), OSSOS (Bannister et al., 2018), and DES (Dark Energy Survey; Bernardinelli et al., 2022) all show evidence for an abundant population of  $a = 50\text{--}100$  au TNOs (referred to as ‘the distant belt’ here).

Studies that accounted for this bias (Gladman et al., 2012; Pike et al., 2015; Volk et al., 2018) all concluded that the distant resonances are heavily populated. The distant  $n:1$  resonances are particularly crowded, with populations comparable to the closer 3:2 (Crompvoets et al., 2022). Similar estimates indicate that the detached region hosts at least as many TNOs as the hot classical belt (Petit et al., 2011, Beaudoin et al. 2022, submitted to PSJ). All evidence points to an abundantly populated distant Kuiper Belt whose inventory should be greatly improved by LSST (Collaboration et al., 2009).

Neptune migration models have been proposed to create the distant resonant

and detached populations. Hahn & Malhotra (2005) simulated Neptune's smooth outward migration into both dynamically cold and heated disks; neither case populates the distant resonances as much as the 3:2 and 2:1. Gomes et al. (2008) realized detached objects can be created during Neptune's migration via Kozai  $q$  lifting. Grainy Neptune migrations, in which Neptune's  $a$  jumps due to planet encounters (Nesvorný et al., 2016; Kaib & Sheppard, 2016), are also able to capture some scattering particles into the distant resonances. Pike & Lawler (2017) bias a Nice model simulation from Brasser & Morbidelli (2013) (where Neptune undergoes a high- $e$  phase during outward migration) using the OSSOS survey simulator and conclude this model doesn't produce large-enough populations for many distant resonances. Crompvoets et al. (2022) suggest their recent resonant-population estimates disfavor all migration models, as they under-populate the  $n:1$  and  $n:2$  resonances; instead an underlying sticking of scattering TNOs to the resonances is preferred, although the efficiency is too low (Yu et al., 2018).

Perhaps effects other than migration are important. Passing stars, even in very dense initial stellar birth cluster environment, are ineffective perturbers inside 200 au (Brasser & Schwamb, 2014; Batygin et al., 2020). One way to create high- $q$  TNOs is via the presence of additional mass(es), whose secular gravitational effect elevates objects from the scattering into the detached population. The initial creation and scattering of now-gone planetary-scale objects in the outer solar system is reasonable (e.g., Stern, 1991; Chiang et al., 2006; Silsbee & Tremaine, 2018; Gladman & Volk, 2021). Gladman et al. (2002) postulated that additional planetary-mass bodies could account for large- $q$  detached objects like 2000 CR<sub>105</sub>. This evolved into the ‘Rogue Planet’ hypothesis (Gladman & Chan, 2006) in which an Earth-scale Neptune-crossing rogue planet (initially starting on a low eccentricity orbit) temporarily present in the early solar system creates detached TNOs, even as far out as Sedna; they showed that the perihelion-lifting effect is dominated by the single most-massive object, which shares the typical 100-Myr dynamical lifetime of Neptune-scattering bodies. Morbidelli & Levison (2004) explored several promising mechanism to explain the origin of Sednoids and concluded only the stellar-encounter scenarios produce the most satisfactory results. Gomes et al. (2006) demonstrated a distant planet orbiting within the inner Oort cloud is capable of raising the perihelia of scattering objects and place them on orbits similar to Sedna's. Lykawka

& Mukai (2008) also proposed a resident trans-Plutonian planet (with  $a = 100\text{--}175$  au,  $q > 80$  au, and  $0.3\text{--}0.7 M_{\oplus}$ ) to sculpt the Kuiper Belt and generate a substantial population of detached TNOs.

In the context of solar system studies, ‘rogue planets’ refers to planets born in the solar system that are scattered away from their formation location and could have left behind orbital structures caused by their temporary presence. We point out the same terminology is sometimes also applied to interstellar free-floating planets.

In light of the additional high- $q$  TNO discoveries in the last 15 years, we revisit the rogue planet hypothesis. We show that a rogue planet temporarily present on an eccentric orbit sufficiently populates both the resonant and detached populations in the  $a = 50\text{--}100$  au Kuiper Belt, even without any planetary migration.

## 5.2 Dynamics from the 4 Giant Planets

To quantify the dynamical effects in the distant Kuiper Belt induced by the four giant planets alone, we show a reference simulation with a synthetic young scattering disk. 100,000 test particles, starting from  $a=50$  au, were placed following a  $dN/da \propto a^{-2.5}$  distribution.<sup>1</sup>

A uniform  $q_0=33\text{--}37$  au distribution was used to cover the current values of scattering objects, but will allow us to post-facto explore the early scattering disk’s parameters integration by weighting the  $q_0$  values (Section 5.4). The initial inclination distribution follows  $\sin i$  times a gaussian of  $15^\circ$  width, the same distribution as the hot main Kuiper Belt objects (Brown, 2001; Petit et al., 2011). All phase angles ( $\Omega$ ,  $\omega$ , and  $M$ ) are random and orbital elements are always converted to the J2000 barycentric frame.

We integrated for 100 Myr, with 4 giant planets on their current orbits, using a regularized version of GLISSE (Zhang & Gladman, 2022). This modified integrator GLISSER can propagate  $\sim 10^5$  test particles on a GPU, while resolving close encounters with planets on multiple CPU cores using many SWIFT subroutine calls (Levison & Duncan, 1994). We have verified this integrator in several common test problems,

---

<sup>1</sup>We showed this with a simple Neptune scattering simulation in which initially low- $e$  and low- $i$  objects near Neptune followed an  $a^{-2.5}$  distribution at  $\sim 50$  Myr. This is steeper than the longer-term steady-state of  $dN/da \propto a^{-1.5}$ , predicted by a diffusion approximation (Yabushita, 1980) and validated by cometary dynamics simulations (Levison & Duncan, 1997).

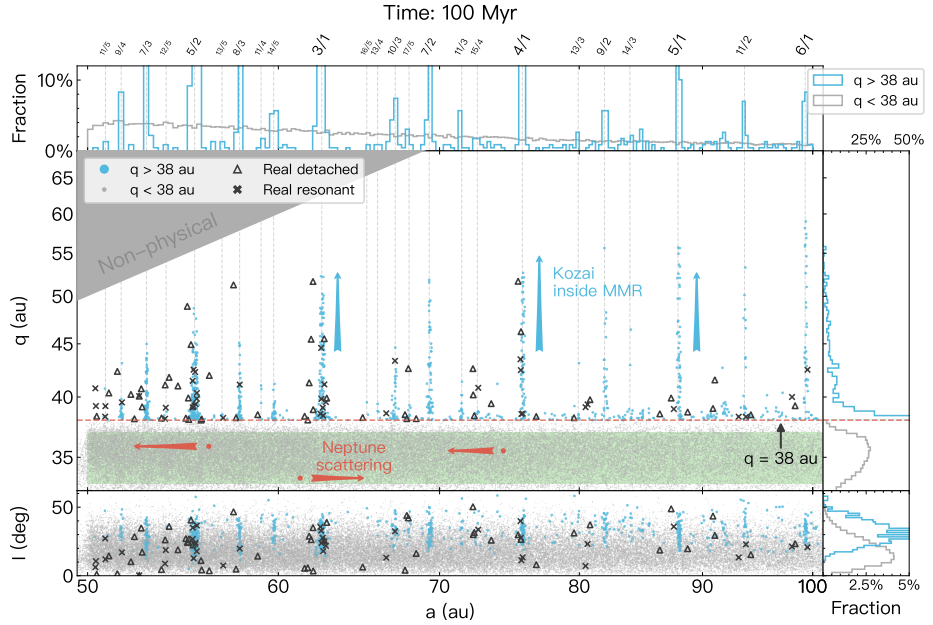


**Figure 5.1:**  $a$ ,  $q$ ,  $i$  distributions of TNOs at 100 Myr in the reference simulation (animated in the [online video](#)). The initial conditions have  $33 < q_0 < 37$  au (shaded green region). Arrows in the  $a$ ,  $q$  panel illustrate the two dominant dynamical effects in the scattering disk: horizontal Neptune scattering (red arrows) and vertical resonant  $q$  lifting (blue arrows). The three side panels show histograms for simulated  $q < 38$  au (gray) and  $q > 38$  au (blue) particles. At the simulation’s end, only  $\simeq 1\%$  of  $a = 50\text{--}100$  au particles have  $q > 38$  au, with the vast majority being resonant objects and almost none being detached objects. The superimposed real  $q > 38$  au detached objects (black triangles) show an apparent concentration near resonances (especially  $n:1$  and  $n:2$ , labelled at top).

confirming it correctly handles the resonant dynamics, secular dynamics and scattering dynamics. GLISSER provides final orbital distributions statistically identical to those simulated by other standard orbital integrators like MERCURY (Chambers, 1999) and SWIFT (Levison & Duncan, 1994).

The 100 Myr snapshot for the reference simulation’s movie is shown in Figure 5.1. We limit our comparisons to  $a = 50\text{--}100$  au because this region has a meaningful density of known  $q > 38$  au resonant and detached objects, making a compar-

ison feasible. With four giant planets, two dynamical processes dominate the scattering disk. At  $q < 38$  au, TNOs are steadily scattered due to their proximity at perihelion passages to Neptune's orbit; this produces horizontal movement (denoted by red particles and arrows in Figure 5.1 for a few examples) on the  $(a, q)$  plot as scattering TNOs random walk in  $a$  while approximately preserving  $q$ . At larger perihelia, where weaker Neptunian encounters less effectively change the TNO's orbital elements, the dominant dynamics occurs at Neptunian mean-motion resonances. The resonances allow evolution to higher- $q$  and higher- $i$  orbits via the Kozai-Lidov mechanism inside mean-motion resonances (Kozai, 1962; Gomes et al., 2008). The perihelion evolution (blue dots and arrows in Figure 5.1) is clearly stronger along  $n:1$  and  $n:2$  resonances. Unfortunately, the overall efficiency of the resonant  $q$ -lifting effect is low, with only  $\approx 1\%$  of  $a = 50$ –100 au objects reaching  $q > 38$  au in 100 Myr. Furthermore, we determined that almost every particle located in Figure 5.1's resonant spikes was *initially* within  $\pm 0.3$  au of the corresponding resonant center meaning they by chance started resonant rather than being delivered to it. This indicates that resonant sticking (a mechanism characterized by scattering objects evolving through intermittent temporary resonance captures, Lykawka & Mukai, 2007) is not the main source of the high- $q$  resonant TNOs. We will return to this in Section 5.3.

Compared to real TNOs in the same region (black triangles and crosses in Figure 5.1), this reference model produces some resonant objects but barely any detached objects, especially between the resonances at high  $q$ . This mismatch is unsurprising because Neptune with a largely unchanging orbit is extremely inefficient at detaching objects from the scattering disk (Gladman et al., 2002). Although resonance escape can (rarely) happen at high  $q$  without Neptune migration, Gomes et al. (2008, figure 10) conclude that Neptune migration is needed to break the reversibility. Therefore, grainy migration models (e.g., Nesvorný et al., 2016; Kaib & Sheppard, 2016) introduced moderate ( $\sim 0.1$  au) semimajor axis jumps to Neptune's migration history in order to detach objects from resonances by suddenly moving the resonance borders. Nesvorný et al. (2016) show how grainy Neptune migration results in greater resonance trapping and although they do not bias their numerical results to see if the orbital distribution matches known TNOs, their detached population agrees with the recent observational measurement (Beaudoin et al. 2022,

submitted).

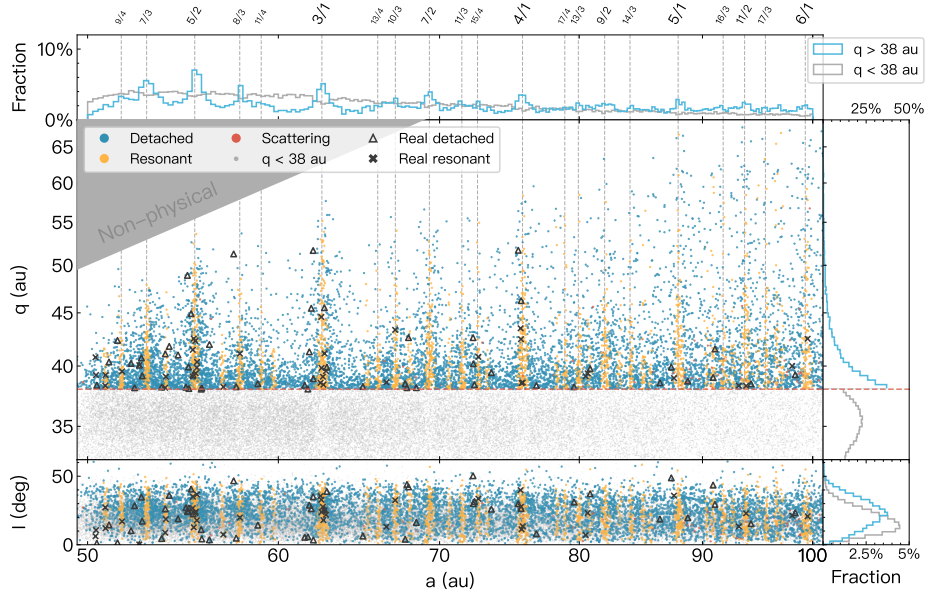


**Figure 5.2:**  $a$ ,  $q$ ,  $i$  distributions and histograms of test particles under 100-Myr gravitational influences of a  $2 M_{\oplus}$  rogue (initial  $a_r = 300$  au,  $q_r = 40$  au, and  $i_r = 20^\circ$ ) and the 4 giant planets. The [online animated version](#) shows the entire evolution. Particles are color-coded based on their constantly-evolving dynamical classes when they are above the red dashed line of  $q = 38$  au. With a rogue present, the resonant population (yellow) is now 3 times larger than in the reference simulation. The detached objects (blue) are created across all semimajor axes, with the high- $q$  ones concentrated near resonances (see the  $a$  histogram at the top). Depletions at strong resonances are visible in the  $q < 38$  au scattering disk (gray), due to the rogue boosting the efficiency of resonant  $q$  lifting.

### 5.3 Dynamical Effects Induced by the Rogue Planet

The letter presents a proof of concept that a temporarily present planet (called a *rogue*) can create high-perihelion objects distributed similarly to the observed Kuiper Belt, with sufficient efficiency to match observations and comparable to grainy mi-

gration simulations. We added a  $m_r = 2M_{\oplus}$  rogue with an initial  $a_r = 300$  au,  $q_r = 40$  au, and  $i_r = 20^\circ$  orbit to the simulation, and integrated it with the same 100,000 test particles to 100 Myr. The chosen rogue parameters (mass, semimajor axis, and dynamical lifetime) were inspired by the preliminary study of Gladman & Chan (2006) where the authors demonstrated such a rogue detaches objects from the scattering disk through secular  $q$  forcing, but they had insufficient statistics to examine the rogue’s role in populating distant resonances and detaching objects from these resonances (which we find is the major dynamical mechanism populating  $a = 50\text{--}100$  au). We set the rogue’s  $q_0=40$  au to produce weak  $a_r$  mobility over the simulation, as we’re concentrating on the new dynamics the rogue brings to the distant belt, rather than exploring the enormous parameter space of possible rogue histories. The TNO orbital evolution is displayed in Figure 5.2.

Each particle in Figure 5.2 is categorized into one of three dynamical classifications of detached (blue), resonant (orange), and scattering (red), using its 10-Myr dynamical history (Gladman et al., 2008) around a particular moment<sup>2</sup> in the animated version of Figure 5.2. We encourage the reader watch the movie on the journal website, which shows the constantly-evolving dynamical classes of each test particles. Only  $q > 38$  au particles are color-coded based on these classes; the  $q < 38$  au particles (gray) are less relevant to the problem we are exploring, as their distribution is largely set by initial conditions.

One striking difference in Figure 5.2 is that the rogue’s secular effect detaches TNOs directly from the scattering disk across all semimajor axes. This lifting is faster at larger  $a$ ; for TNOs with  $a \ll a_r$  and orbital period  $P$ , the order-of-magnitude  $q$  oscillation timescale  $P_{\text{sec}}$  induced by the rogue is given by (Gladman & Chan, 2006):

$$\frac{P_{\text{sec}}}{P} \sim \left( \frac{M_{\odot}}{m_r} \right) \left( \frac{a_r}{a} \right)^3 (1 - e_r^2)^{3/2}, \quad (5.1)$$

where  $e_r$  is the rogue’s eccentricity. For a  $2M_{\oplus}$  rogue with  $a_r \simeq 300$  au and  $e_r \simeq 0.87$ ,  $P_{\text{sec}}$  for  $a = 50\text{--}100$  au varies from  $\simeq 1.5$  Gyr to 500 Myr, longer than the  $\sim 100$  Myr dynamical lifetime of the rogue.

We detail a previously unreported dynamical effect that creates detached TNOs

---

<sup>2</sup>For example, the dynamical class at 100 Myr is based on the orbital history from 95–105 Myr. Classification was performed at each 0.14 Myr output interval (except for the first 5 Myr).

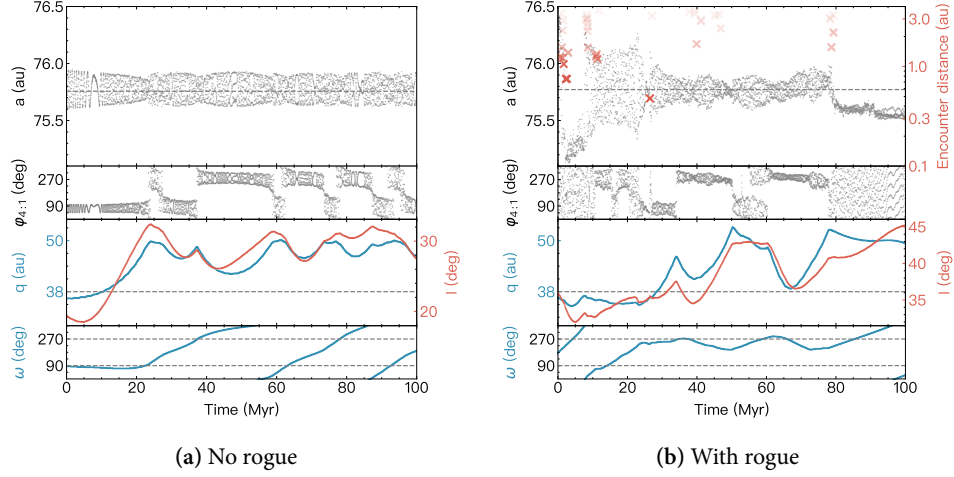


**Figure 5.3:** Dynamical evolutions of two particles initially near the 4:1 resonance from the reference simulation (left) and the rogue planet simulation (right). From top to bottom, the left axes of both plots are semimajor axis ( $a$ ), the 4:1 resonant angle ( $\varphi_{4:1}$ ), perihelion ( $q$ ), and argument of perihelion ( $\omega$ ). The right axes are proximity of rogue encounters (denoted by red ‘x’s) and inclination ( $I$ ). Without the rogue present, the Kozai mechanism (represented by  $\omega$  librating around  $90^\circ$  or  $270^\circ$ ) is able to raise resonant particle’s perihelion, but spontaneous decoupling from the resonance is highly unlikely. In comparison, the rogue helps build the detached population by both pushing the particle into the resonance and kicking it out at high  $q$ .

through a combination of Neptunian resonances and rogue encounters. We observe that weak encounters with the rogue are continuously nudging TNOs in semimajor axes, sometimes randomly pushing them into a nearby resonance from the scattering disk. Similarly, rogue encounters are capable of kicking objects out of the resonance; if this happens to occur at high perihelion after part of a Kozai cycle, it naturally forms detached objects near resonances, especially near those with strong  $q$  lifting effectiveness like  $n:1$  and  $n:2$ . Both the resonant ‘pushing in’ and ‘kicking out’ happen; our simulation shows the net effect is a  $3\times$  enhancement to the resonant population (compared to Figure 5.1’s reference simulation), in addition to the considerable quantity of detached TNOs formed around resonances. The power of

the rogue-aided  $q$  lifting is visible in the deficits of scattering objects (gray dots and upper histogram in Figure 5.2) at the resonant semimajor axes. Detached objects with  $a < 80$  au and  $q > 40$  au seem to concentrate near resonances, as do real detached TNOs (the movie illustrates these dynamics clearly). The resonance works as a sort of ‘water fountain’, constantly pumping the particles to higher  $q$ ; meanwhile the rogue supplies particles from the scattering disk, and ‘splashes’ them to nearby detached states along the resonances. Such fountain-like structures with a central resonant population and surrounding detached population are visible near strong resonances like 5:2, 3:1, and 4:1.

We selected a particle near the 4:1 from each of the two simulations and plot their evolutions (Figure 5.3). The reference simulation’s particle (Figure 5.3a) is *initially* inside the 4:1 resonance. It demonstrates a (rare)  $\sim 25$  Myr Kozai cycle, enabled by  $\omega$  remaining near  $90^\circ$  initially and diagnosed by strong  $e$  and  $i$  coupling; this lifts  $q$  from 37 au to 50 au and  $i$  from  $20^\circ$  to above  $30^\circ$ . Once Kozai stops ( $\omega$  circulates), the still-resonant particle’s critical angle jumps back and forth chaotically between the two asymmetrical libration centers (Morbidelli et al., 1995), with  $q$  and  $i$  remaining high. However, without additional disturbance (from a jumping Neptune or external rogue), it is almost impossible to spontaneously decouple from the resonance and thus become detached.

Figure 5.3b shows a case from the rogue scenario, but here the TNO is initially near but not inside the 4:1 resonance. Each red cross (top panel) marks a time and encounter distance with the rogue. These encounters nudge the particle’s  $a$ , thus changing its resonant dynamical behaviour. At  $\approx 10$  Myr, weak encounters move the particle into the 4:1, beginning  $\varphi$  libration around  $\sim 270^\circ$ . Interestingly, little  $q$  and  $i$  evolution occurs until a deep encounter pushes the TNO into a part of the resonant parameter space where Kozai activates. After several  $q$  and  $i$  oscillations from 25–80 Myr, additional encounters at  $\approx 2$  au distance kick the object out of the resonance, leaving  $q \approx 50$  au and  $i \approx 45^\circ$ , creating a detached TNO near the resonant border.

The juxtaposition of Figure 5.3’s two plots shows three dynamical effects the rogue induces via encounters:

1. randomly pushing nearby non-resonant scattering disk objects into the reso-

nance,

2. boosting the  $q$  lifting by supplying resonant particles into the parameter space where the Kozai cycle operates, and
3. randomly kicking resonant particles out and forming part of the detached population if this occurs at high perihelion.

Only a small fraction of the  $N$  scattering objects (that intersect rogue's orbit and are near the mutual node) will be affected per rogue orbit. Over the rogue's lifetime the entire scattering disk can have rogue encounters because of mutual precession of the rogue and TNO orbit. One can analytically estimate the accumulated encounter number  $N_{\text{enc}}$  closer than  $\beta$  Hill spheres<sup>3</sup> as, assuming a highly-eccentric planet with a large semimajor axis (derived in Appendix B.1)

$$\frac{N_{\text{enc}}}{N} \simeq 6 \beta^2 \left( \frac{T_r}{100 \text{ Myr}} \right) \left( \frac{m_r}{2M_{\oplus}} \right)^{\frac{2}{3}} \left( \frac{a_r}{300 \text{ au}} \right)^{-\frac{3}{2}}, \quad (5.2)$$

where  $N$  is the number of TNOs between the rogue perihelion and aphelion, and  $N_{\text{enc}}$  is the number of rogue encounters. For our simulations, the numerical integrator logged the  $\beta < 1$  encounters, recording  $\approx 5$  encounters per particle in 100 Myr, in excellent agreement.

Each encounter perturbs different TNO orbital elements; we focus on the rogue's effect on semimajor axes, as the random nudges in  $a$  are what determine resonance entrance and exit. In Appendix B.2, we estimate  $|\Delta a|$  for a typical rogue encounter at  $\beta R_H$  flyby distance as:

$$|\Delta a| \simeq \frac{0.1 \text{ au}}{\beta} \left( \frac{m_r}{2M_{\oplus}} \right)^{\frac{2}{3}} \left( \frac{a}{50 \text{ au}} \right). \quad (5.3)$$

For  $a = 50\text{--}100$  au, encounters at  $1 R_H$  induce  $|\Delta a| \simeq 0.1\text{--}0.2$  au for the TNO, approaching the  $\simeq \pm 0.5$  au width of the nearby resonances (Lan & Malhotra, 2019). This allows encounters to knock TNOs in and out of resonance or shift them inside the resonance, allowing activation of Kozai cycling. Deeper encounters induce

---

<sup>3</sup>Given the huge changes in the rogue's heliocentric distance, a time-varying Hill sphere  $r \sqrt[3]{m/3M}$  (where  $r$  is the solar distance when an encounter occurs) is used in both the numerical integrator and the analytical analysis.

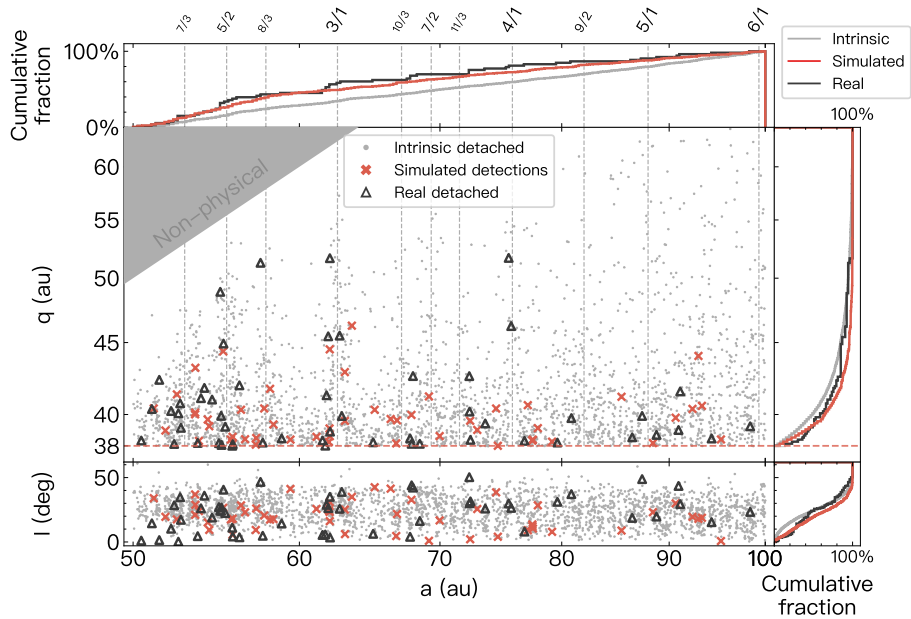


**Figure 5.4:**  $a, q, i$  distributions of the detached (gray dots), the simulated detections (red crosses), and the real  $q > 38$  au detached objects (black triangles). The intrinsic sample is built by the rogue and has been eroded to 4 Gyr (only particles with initial  $q_0 < 35$  au are included in this plot), on the basis of which the simulated detections are drawn using the OS-SOS survey simulator. A decent correspondence between the simulated and the red detached can be found on the three cumulative histograms; a valid proof that the rogue is capable of creating the observed TNO distributions.

ing larger  $\Delta a$  do exist (Figure 5.3b), but Equation (5.2) shows encounters become quadratically rarer with decreasing  $\beta$ . An average TNO suffers a passage no closer than  $0.4R_H$  for Figure 5.2’s rogue.

These encounters greatly increase how many TNOs end up in the high- $q$  region. We find the rogue’s 100 Myr presence raises 10% of the  $a=50-100$  au scattering disk objects to  $q > 38$  au, with 3% being resonant and 7% being detached. Compared to the reference simulation, this rogue scenario emplaces an order of magnitude more TNOs in the high- $q$  region. We also did a preliminary exploration of varying the rogue’s mass; two additional 100 Myr simulations show that  $0.5 M_\oplus$  or  $1 M_\oplus$

rogues still populate the high- $q$  region, but with lower efficiency (with 3.3% and 5.5%, respectively, of TNOs having  $q > 38$  au). Both the rogue’s time  $T_r$  intersecting the belt and its  $a_r$  and  $e_r$  evolution history (Eqs. 5.1 and 5.2) influences its sculpting of the distant Kuiper Belt’s structure.

## 5.4 Estimating Observation Bias

The real TNOs in Figure 5.2 are more concentrated to low- $a$  and low- $q$  than the distribution produced by the rogue. This is expected given observational bias which favors them. Observation biases differ from survey to survey, but the first-order effect for near-ecliptic surveys is that it penalizes large- $a$ , large- $q$ , and large- $i$  orbits.

To verify whether our numerically simulated TNO distribution is similar to the observed Kuiper Belt, we forward bias the numerical sample to compare it with the real objects. Lawler et al. (2018b) details how this forward biasing is done using a ‘survey simulator’. Biases for resonant objects are complex to simulate, as their perihelion passages are correlated to Neptune’s location, resulting in detection preferentially at specific longitudes relative to Neptune (Gladman et al., 2012). Lacking detailed pointing information for many past surveys, we do not compare to the resonant objects, instead focusing on  $q > 38$  au detached TNOs.

We first eroded the surviving test particles for 4 Gyr with only the four giant planets. That is, the rogue was assumed to be ejected after a typical dynamical lifetime of 100 Myr; in this case we manually removed it before the 4 Gyr integration. The dynamical classification algorithm was then repeated to remove resonant and scattering TNOs from the  $q > 38$  au sample, and the remaining detached TNOs are plotted in Figure 5.4 (gray dots). The uniform initial  $q_0$  distribution allowed us to weight the sample post-facto and we found obvious improvement in the match keeping only  $q_0 < 35$  au (see below). We superpose 53 real detached objects (black triangles); these TNOs were identified by Gladman & Volk (2021), consisting of the OSSOS detached (Bannister et al., 2018) and other TNOs with sufficiently good orbits. We utilized the OSSOS survey simulator to generate 689 simulated detections; a random 53 of them (the same as the real sample) are plotted (red crosses) to illustrate the biases. Cumulative  $a$ ,  $q$ , and  $i$  histograms for  $\sim 2800$  intrinsic (model) particles, the 689 simulated detections, and the 53 real objects are on Figure 5.4’s

side panels. Because detached TNOs from other surveys do not share the same detection biases<sup>4</sup> as OSSOS, this preliminary comparison is only approximate.

Figure 5.4’s cumulative distributions exhibit (perhaps surprisingly) similar trends between the simulated detections (red) and the real detached objects (black). When using all numerical initial conditions, the simulated  $a$  and  $q$  distributions have the general trend of the real detections, but restricting to  $q_0 < 35$  au produces an obvious improvement. We take this as evidence that much of the perihelion lifting began at an early stage when the scattering disk was still developing; Figure 3 of Gladman (2005) shows that in the first 50 Myr only  $q < 35$  au orbits are populated, only after  $\sim 1$  Gyr do scattering TNOs extend up to  $q = 37$ . The superiority of a more confined  $q_0$  distribution is verified in Beaudoin et al. (2022, submitted to PSJ), who more rigorously compares with only the OSSOS objects; they show that the  $q_0 < 35$  au detached TNO  $q$  distribution created by the  $2-M_{\oplus}$  rogue is non-rejectable, with Anderson-Darling probability of 32% (and is in fact the best model they studied).

## 5.5 Discussion

We demonstrate for the first time that a rogue planet present for  $\sim 100$  Myr during planet formation can abundantly create both the distant resonant and detached populations, even without any planetary migration. This is accomplished by the synergy of the Neptunian resonances (with the Kozai mechanism lifting perihelia) and weak rogue encounters (where the rogue supplies the resonance and detaches objects at high  $q$ ). Several points merit discussion.

**The Cold Classical Belt.** A potential concern regarding the temporary presence of Earth-scale planets is the possibility of dynamically heating the cold classical belt, which is often thought to be formed in-situ and unexcited for the age of the solar system. The observed limits on the  $e$  and  $i$  excitation are used to constrain Neptune’s dynamical history (Batygin et al., 2011; Dawson & Murray-Clay, 2012; Nesvorný & Vokrouhlický, 2016), including the absence of planets formed in the cold belt itself (Morbidelli et al., 2002). A rogue must have scattered to large  $a$  early, as even a few

---

<sup>4</sup>As an example, the Dark Energy Survey’s high-latitude coverage (Bernardinelli et al., 2022) strongly favors high- $i$  TNOs.

million-year residence with  $a_r \simeq 50$  au would excite the cold belt. Once the rogue reaches  $a$  of a few hundred au, the average time it stays in the classical belt drops by  $a^{3/2}$  (Equation 5.2), greatly reducing the cold-belt's excitation. We confirmed this with simple numerical simulation of just the cold classical belt, placing 10,000 objects with initial  $e_0 = 10^{-3}$  and  $i_{\text{free}} < 0.2^\circ$  (Huang et al., 2022b) from  $a_0 = 42$  au to 47 au and integrated with the same rogue in Section 5.3. Even though the rogue continuously crosses this cold belt<sup>5</sup> for 100 Myr, its gravity induces surprisingly little excitation: the vast majority of cold TNOs keep  $e < 0.05$  and  $i_{\text{free}} < 1^\circ$  (Figure 5.5). We conclude a large- $a$  rogue does not unacceptably excite the cold belt.

**Oort Cloud Building.** The period of the rogue's existence will coincide with the epoch in which the Oort cloud is created (Duncan et al., 1987; Dones et al., 2004; Portegies-Zwart et al., 2021). Although in principle one might worry that an Earth-scale rogue at 100 au could strongly interfere with the creation of the Oort cloud, Lawler et al. (2017) show that the presence of even a larger  $10 M_\oplus$  object in the 250–750 au range for the entire age of the Solar System lowers Oort cloud implantation efficiency by only a factor of  $\simeq 2$ . The efficiency of Oort cloud implantation and its mass are sufficiently uncertain (Portegies-Zwart et al., 2021) that there is no obvious problem with the temporary presence of a rogue like we envision.

**Sun's Birth Environment.** The rogue's highly-eccentric orbit of a few hundred au could be affected by close-in stellar flybys that could have happened in the Sun's birth environment. Arguments have been made that our Sun was likely born in a cluster of 1000–3000 stars/ $\text{pc}^3$ , based on extinct radionuclides and the assumption that extreme detached TNOs, represented by Sedna, needed to be produced in the birth cluster environment (Portegies-Zwart, 2009; Adams, 2010; Pfalzner, 2013). The question is how quickly the Sun exited this birth cluster. If Sun remained for a long time, there would be problems with retaining the Oort cloud (*e.g.*, Morbidelli & Levison, 2004; Nordlander et al., 2017). In addition, the recent study by Batygin et al. (2020) computes an upper bound of number density-weighted cluster residence of our Sun of  $2 \times 10^4$  Myr/ $\text{pc}^3$ , based on the unexcited inclination distribution of the cold classical belt; this implies that the Sun must have exited its birth cluster in less than  $\sim 15$  Myr, using their 1400 stars/ $\text{pc}^3$  estimate (Batygin & Brown, 2021). Similar early exit arguments are given by Brasser et al. (2006) and Pfalzner (2013),

---

<sup>5</sup>For this specific rogue, 50% of the 100 Myr has one mutual node inside the cold belt.

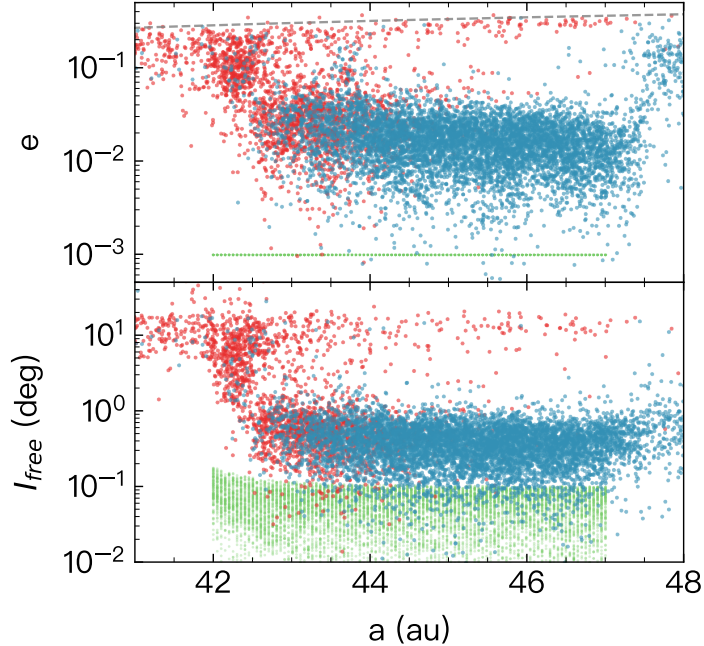


**Figure 5.5:** Orbital excitation of the cold classical Kuiper Belt, after 100 Myr of perturbation from the rogue with  $a$ ,  $q$ ,  $i$  of roughly 300 au, 40 au, and  $20^\circ$ . Green points mark initial conditions, and red/blue points show final values for particles that began with  $a_0$  smaller/larger than 43 au, respectively. From initial  $e_0 = 10^{-3}$  and  $i_{\text{free}} < 0.2^\circ$ , the surviving cold main belt with  $a_0 > 43$  au remains with low  $e$  and  $i$ . For  $a_0 < 43$  au secular resonances ( $g_8$  and  $s_8$ ) pump both  $e$  and  $i$  after which particles scatter to all values of  $a$  along the Neptune crossing line (gray dashed). Repeating the simulation using REBOUND (Rein & Liu, 2012) produces the same excitations. Thus, the rogue does not unacceptably excite the cold belt, whose TNOs currently have even higher values of  $e$  and  $i$ .

both of which suggest 5 Myr residence. The timescale for the rogue to reach several hundred au is comparable to this  $\sim 10$  Myr duration and we therefore think a 100 Myr survival timescale for the rogue is not problematic. Furthermore, the rogue's presence directly provides a way other than the Sun's birth cluster to explain Sednoids (Gladman & Chan, 2006), which would alleviate the “need to make Sedna

“with passing stars” constraint (figure 7 of Adams, 2010; Pfalzner, 2013; Brasser & Schwamb, 2014) in the Sun’s birth environment.

**An Existing Planet.** The natural 100 Myr ejection timescale for scattering rogues (Gladman & Chan, 2006) sets a typical timescale that we have seen produces the needed detached and resonant populations in the 50–100 au region. Instead of ejection, if the rogue’s perihelion was lifted (by an unspecified process) to very large  $q$ , it could remain in the outer solar system today and negligibly affect the 50–100 au region. Scenarios with a still-resident rogue (Sheppard & Trujillo, 2016; Batygin et al., 2019) presumably began with that planet on low- $q$  orbit for some period; that combination of  $T_r$ ,  $m_r$ , and  $a_r$  (Equation 5.2) while  $q_r < 100$  au could produce the same effects we study, before the mysterious  $q_r$  lift. But given that recent surveys (Shankman et al., 2017; Napier et al., 2021; Bernardinelli et al., 2022) do not support intrinsic clustering, we find the ‘now gone’ rogue scenario to be more natural.

**Neptune Migration.** It is generally believed that Neptune migrated outwards during the planet-formation and disk-dispersal epoch (reviewed by Nesvorný, 2018). The ‘grainy’ migration models are effective at creating detached TNOs when Neptune’s semimajor axis jumps (and thus so do all its resonances) due to encounters with dwarf planets; if the jumps become comparable to the resonance size ( $>0.1$  au, say), then some particles are suddenly no longer in resonance. A final phase of slow net-outward grainy migration results in an asymmetry of ‘stranded’ particles on the sunward side of the resonance (Kaib & Sheppard, 2016; Nesvorný et al., 2016). There is growing observational evidence for this (Lawler et al., 2019; Bernardinelli et al., 2022); after fixing an error in the Dark Energy Survey selection function (working with Bernardinelli, private communication 2022), we combined the  $q > 38$  au samples from these two studies and find that the binomial probability that the detached number just beyond each resonance is comparable to those on the sunward side remains  $<1\%$ .

Regarding detachment, we find the rogue planet scenario produces comparable numbers of detached TNOs. This is not too surprising, if one takes the view that the rogue produces ‘grainy’ TNO jumps while grainy migration jumps the resonances. In our case, Equation (5.3)’s  $\Delta a$  is set by the range of encounter distances and the rogue’s mass, while in grainy migration models there is an assumed mass spectrum of the bodies encountering Neptune (at a range of flyby distances). It is likely that

after the rogue's ejection there will still be moderately-massive scattering disk; during its erosion a final small outward Neptune migration will then occur. This would capture stranded TNOs on the high- $a$  side of the resonance and continue 'littering' TNOs on the sunward side, giving an outcome very similar to migration alone.

A unique outcome of our study is that we have rigorously compared the simulation's final orbital distribution to the known OSSOS TNOs, and find excellent agreement (Beaudoin et al. 2022, submitted to PSJ), yielding a population estimate of 40,000 detached TNOs with diameters  $>100$  km, a number identical to the Nesvorný et al. (2016) population estimate, who didn't have the information necessary for rigorous orbital comparison. Additionally, having a rogue during this period simultaneously allows the production of large- $q$  objects like Sedna (Gladman & Chan, 2006).

We expect that both processes operated in our early Solar System because it is natural that objects between Pluto and ice-giant scale existed during disk dispersal. The rogue's presence introduces another mechanism to produce many features seen in the distant Kuiper Belt. We believe that rogues and migration are both expected outcomes of the process of planet building; the uncertainties introduced into deriving parameters (such as the migration duration and mass spectrum of other bodies in the system) in future models which incorporate both seem unavoidable.

## Chapter 6

# Rogue Planet Parameters

In Chapter 5, I demonstrated that an Earth-mass rogue planet temporarily present in the early Solar System can help populate both the detached and resonant TNOs in the  $50 < a < 100$  au Kuiper Belt. The study on this very specific problem was prompted by the preliminary GLISSER simulation (Figure 1.8) with a fixed-orbit rogue, in which the new dynamical phenomenon was first discovered. In this Chapter, I will concentrate mainly on the secular  $q$  lifting dynamics the rogue will impose on distant TNOs, first investigated in Gladman & Chan (2006) with numerical simulations and hypothesized as a explanation for detached orbits. Specifically, in Section 6.1, I build up the analytical tools to estimate the strength and timescale of the secular forcing as a function of the rogue's mass and orbit. This is then used to derive the two critical constraints for a rogue-planet scenario, which are the creation of Sednoids and the preservation of an underheated cold classical Kuiper Belt. Section 6.2 shows my preliminary explorations on the rogue planet's possible dynamical route, and in Section 6.3 I numerically study the orbital distribution of the distant Kuiper Belt sculpted by a scattering planet. In Section 6.4, I further erode the most successful simulation in Section 6.3 to 4 Gyr, in order to simulate detections with the OSSOS survey simulator and compare the rogue planet model against real observations. In Section 6.5, I summarize the main results from the rogue planet model and its cosmogonic implication.

## 6.1 Dynamics Induced by an Distant Rogue Planet

The dynamical effects induced by a distant planet on TNOs can be divided into encounter and secular effects. In this section, I study both effects using analytical methods to constrain the parameters of the rogue planet.

### 6.1.1 Rogue Encounters

In Chapter 5, I discovered that weak encounters of the rogue assist both resonance capture and orbital detachment near resonances in the early scattering disk. As discussed in Section 4.5.2, the rogue planet is thought to be a temporarily-present planet with  $q_r$  near or inside the region of the giant planet (otherwise, it would likely have survived the age of the Solar System and be a resident planet). While traversing the early scattering disk, which helps populate resonant and detached TNOs, the rogue planet also inevitably crosses the cold classical belt and disturbs the residents within. Although Figure 5.5 shows that the rogue with  $a_r = 300$  au,  $q_r = 40$  au, and  $i_r = 20^\circ$  would not unacceptably heat the cold belt in 100 Myr, it is necessary to quantitatively estimate the cumulative effects induced by rogue encounters on a wide range of orbits.

As derived in Appendix B, the induced orbital element changes due to rogue encounters can be modeled as random walks, and the cumulative changes in  $a$ ,  $e$ , and  $i$  over the rogue's residence time  $T_r$  are given by:

$$\frac{|\Delta a|_c}{a} = 2|\Delta e|_c = 2|\Delta i|_c \simeq 0.005 \left( \frac{T_r}{100 \text{ Myr}} \right)^{\frac{1}{2}} \left( \frac{m_r}{2M_\oplus} \right) \left( \frac{a_r}{300 \text{ au}} \right)^{-\frac{3}{4}}, \quad (6.1)$$

where  $m_r$  and  $a_r$  are the planetary mass and semimajor axis.

The  $e$  and  $i$  excitations and semimajor axis mobility in the cold classical belt ( $a \simeq 45$  au) induced by recurring rogue encounters (neglecting its secular effects) are plotted in Figure 6.1. For the rogue parameters I used in Chapter 5 ( $T_r = 100$  Myr,  $m_r = 2M_\oplus$ , and  $a_r = 300$  au), the excitations of the cold belt are  $|\Delta e|_c \simeq 0.002$  and  $|\Delta i|_c \simeq 0.1^\circ$ , respectively. This explains why the  $e$  and  $i$  distributions are almost unaffected by the rogue in Figure 5.5. Though the  $e$  and  $i$  heating produced by weak encounters is negligible, this rogue, however, does nudge TNOs in semimajor axis by  $\sim 0.2$  au, which pushes some of them to nearby edges (i.e. the  $\nu_8$  and  $\nu_{18}$  secular

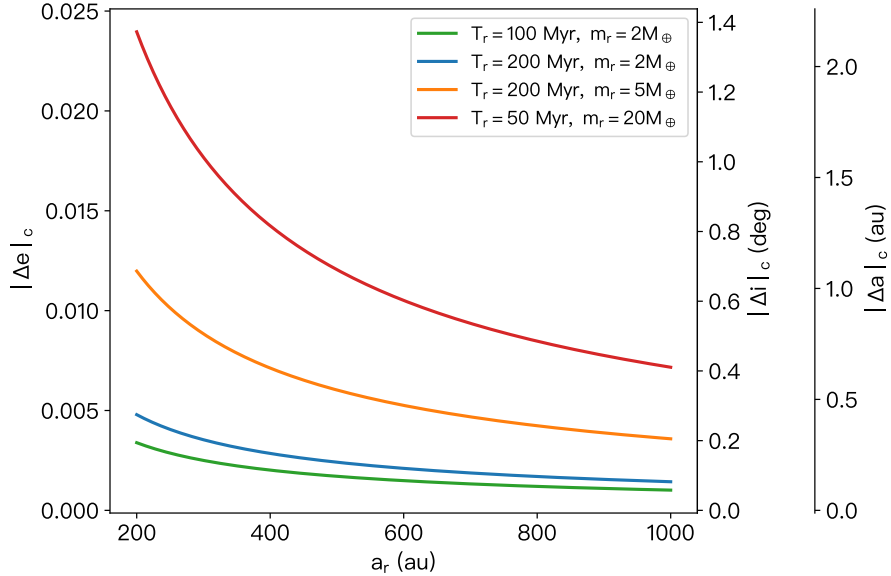


**Figure 6.1:** Cumulative  $\Delta a$ ,  $\Delta e$ , and  $\Delta i$  excitations of the cold classical belt ( $a \simeq 45$  au) under repeated rogue encounters. These estimates are based on Equations (B.19) and (B.20), assuming the rogue has a fixed orbit of  $a_r$  and was present for  $T_r$ , with its perihelion  $q_r$  always smaller than the inner edge of the Kuiper Belt (thus it traverses the belt during its presence). The four curves represent rogues with different parameters. Although none of them unacceptably heat the classical belt's  $e$  and  $i$  beyond the observed values, the most massive rogue with  $m_r = 20M_\oplus$  (comparable to that of an ice giant) can possibly mix the cold belt in semimajor axis due to the non-negligible  $\Delta a$  it induced (red curve).

resonances on the left, and 2:1 resonance on the right, see Figure 5.5). If the rogue planet is much more massive, say  $m_r = 20M_\oplus$  comparable to an ice giant, it will likely displace TNOs in the cold belt by  $\Delta a \simeq 1$  au if it survived 100 Myr. Whether this is an unacceptable level of cold belt perturbation is unclear; it is approaching what seems to be the maximum.

In conclusion, the cumulative dynamical heating caused by rogue encounters to the cold classical belt does not seem to be a problem. I will demonstrate in the next section that the rogue's secular heating provides a much more stringent constraint.

### 6.1.2 Secular Effect

The secular dynamics of a highly-eccentric planet in the distant Kuiper Belt has been intensively studied in the development of the Planet Nine hypothesis (Batygin & Brown, 2016a; Beust, 2016; Batygin & Morbidelli, 2017; Batygin et al., 2019). Here, I follow a similar methodology based on the Hamiltonian formalism (Section 1.1.2) to derive some analytical results for the rogue planet. Unlike the Planet Nine theory, which focuses primarily on the orbital clustering and high-inclination dynamics of distant TNOs, I will highlight the secular  $q$  raising effect (which is related to the apsidal alignment  $e - \Delta\varpi$  dynamics in Planet Nine discussions) brought by the rogue planet.

I start by writing down the instantaneous Hamiltonian between the test particle  $(a, e, \varpi)$  and the rogue planet  $(a_r, e_r, \varpi_r, m_r)$  in the framework of the planar restricted three-body problem (Morbidelli, 2002; Beust, 2016):

$$\mathcal{H}_{\text{planar}} = \underbrace{-\frac{\mu_\odot^2}{2\Lambda^2}}_{\text{Keplerian term}} - \underbrace{\mu_r \left( \frac{1}{|\mathbf{r} - \mathbf{r}'|} - \frac{\mathbf{r} \cdot \mathbf{r}'}{r'^3} \right)}_{\text{Disturbing function } \mathcal{R}}, \quad (6.2)$$

where  $\mu_\odot = GM_\odot$ .  $\mathbf{r}$  and  $\mathbf{r}'$  are the heliocentric radius of the test particle and of the rogue, respectively. The corresponding canonical variables related to  $\mathcal{H}_{\text{planar}}$  read (see Equation 1.14)

$$\begin{aligned} \Lambda &= \sqrt{\mu_\odot a}, & \lambda &= \mathcal{M} + \varpi, \\ \mathcal{P} &= \sqrt{\mu_\odot a} \left( 1 - \sqrt{1 - e^2} \right), & p &= -\varpi, \end{aligned} \quad (6.3)$$

Averaging  $\mathcal{H}_{\text{planar}}$  over the fast angles, one obtains

$$\overline{\mathcal{H}}_{\text{planar}} = -\frac{\mu_\odot^2}{2\Lambda^2} - \frac{\mu_r}{4\pi^2} \oint \oint \frac{1}{|\mathbf{r} - \mathbf{r}'|} d\lambda d\lambda', \quad (6.4)$$

where  $\overline{\mathcal{H}}_{\text{planar}}$ <sup>1</sup> is now independent of both longitudes  $\lambda$  and  $\lambda'$ , and the system is reduced to one degree of freedom (given  $\varpi_r$  is constant in the restricted problem). Therefore, the rate of change in semimajor axis is zero ( $\dot{a} = 0$ ), and the constant

---

<sup>1</sup>The  $\mathbf{r} \cdot \mathbf{r}'/r'^3$  term in  $\mathcal{H}_{\text{planar}}$  (the indirect term) is a non-inertial contribution resulting from pinning the reference frame to the central mass (Touma et al., 2009). The averaged indirect term over the planet's fast angle ( $\lambda'$ ) is zero (Morbidelli, 2002) and thus can be eliminated in Equation (6.4).

Keplerian term  $-\frac{\mu_\odot^2}{2\Lambda^2}$  can be removed from the secular Hamiltonian. The governing Hamiltonian attributed to the rogue planet is

$$\mathcal{H}_{\text{sec, rogue}} = -\frac{\mu_r}{4\pi^2} \oint \oint \frac{1}{|\mathbf{r} - \mathbf{r}'|} d\lambda d\lambda'. \quad (6.5)$$

In reality, both the TNO and the rogue planet are perturbed by the giant planets. The long-term evolution of objects can be understood using the secular perturbation theory (Murray & Dermott, 1999). If one ignores the orbital eccentricity and inclination of all the planets, to quadrupole order the Hamiltonian attributed to the four giants <sup>2</sup> is:

$$\mathcal{H}_{\text{GP}} = -\frac{1}{4} \frac{\mu_\odot}{a} (1 - e^2)^{-\frac{3}{2}} \sum_{i=5}^8 \frac{m_i a_i^2}{M_\odot a^2}, \quad (6.6)$$

where the index  $i$  denotes the  $i$ -th planet. The perturbation to the rogue has a similar form (replacing  $a$  and  $e$  in Equation 6.6 with  $a_r$  and  $e_r$ ). This Hamiltonian can be used to calculate the expected TNO precession rate ( $\dot{\varpi}$ ) when only considering the gravitational effects of the giant planets:

$$\begin{aligned} \dot{\varpi} &= -\frac{dp}{dt} = -\frac{\partial \mathcal{H}_{\text{GP}}}{\partial P}, \\ &= \frac{3}{4} \frac{n}{(1 - e^2)^2} \sum_{i=5}^8 \frac{m_i a_i^2}{M_\odot a^2}, \end{aligned} \quad (6.7)$$

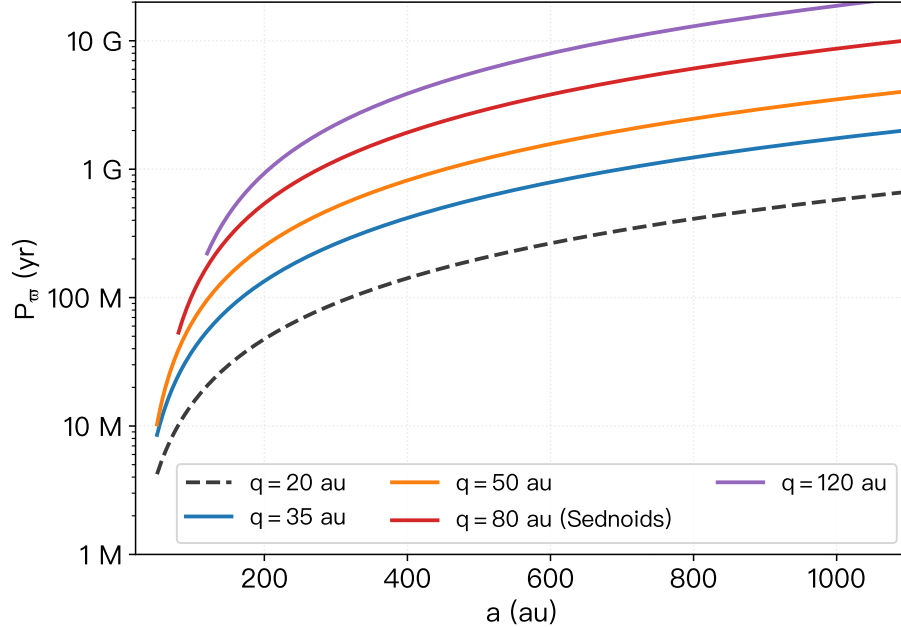
with the same expression giving the rogue's precession  $\dot{\varpi}_r$  with  $n_r, e_r$  and  $a_r$ .

Figure 6.2 shows the apsidal precession period ( $P_\varpi = 2\pi/\dot{\varpi}$ ) for rogues/TNOs on a wide range of orbits. For detached objects whose  $q$  ( $\gtrsim 35$  au) are a few au's away from Neptune,  $P_\varpi$  varies from  $\sim 10$  Myr to  $\sim$  Gyr (solid blue) over the 50–1000 au semimajor axis range. For  $a > 250$  au Sednoids with  $q \sim 80$  au, precession periods are so long ( $P_\varpi \sim 1$ –10 Gyr) that they only complete a few to no complete apsidal cycles for the age of the Solar System (see, for example, figure 7 in Sheppard et al. 2019 for direct integrations of Sednoids in the current Solar System).

In order to incorporate the perturbation of giant planets into the dynamical

---

<sup>2</sup>Terrestrial planets are not as massive and are too far away from the distant Kuiper belt to be considered.



**Figure 6.2:** Apsidal precession period  $P_{\varpi}$  as a function of  $a$  for rogue planets/TNOs with various perihelia. The calculation was done using Equation (6.7), assuming giant planets are all on circular and co-planar orbits. For  $q > 30$  au (solid curves), Equation (6.7) should accurately describe the apsidal precession of large- $e$  orbits. For  $q < 30$  au (dashed curves) where the orbit intersects with that of Neptune (or other giant planets), Equation (6.7) only serves as a reference since the object will get scattered in  $a$  and the precession rate is not constant.  $P_{\varpi}$  (and  $\dot{\varpi}$ ) can differ between objects with the same  $a$  by an order of magnitude depending on their perihelion.

model, one needs to first add the direct perturbation  $\mathcal{H}_{\text{GP}}$  into the secular Hamiltonian  $\mathcal{H}_{\text{sec}}$ :

$$\mathcal{H}_{\text{sec}, 0} = \mathcal{H}_{\text{GP}} + \mathcal{H}_{\text{sec, rogue}}, \quad (6.8)$$

where the Hamiltonian is implicitly time-dependent due to the apsidal precession of the rogue (i.e. non-constant  $\varpi_r$ ) in the double integral (6.4). I thus perform a canonical transformation with the generating function of the third kind

$$\mathcal{F}_3 = \mathcal{P}\varpi = \underbrace{\mathcal{P}}_{\text{old action}} (\varpi_r + \underbrace{\Delta\varpi}_{\text{new angle}}), \quad (6.9)$$

and the new autonomous secular Hamiltonian is given by

$$\begin{aligned} \mathcal{H}_{\text{sec}}(\Phi, \Delta\varpi) &= \mathcal{H}_{\text{sec}, 0} + \frac{\partial \mathcal{F}_3}{\partial t}, \\ &= -\frac{1}{4} \frac{\mu_{\odot}}{a} (1 - e^2)^{-\frac{3}{2}} \sum_{i=5}^8 \frac{m_i a_i^2}{M_{\odot} a^2} + \dot{\varpi}_r \sqrt{\mu_{\odot} a} \left( 1 - \sqrt{1 - e^2} \right) \\ &\quad - \frac{\mu_r}{4\pi^2} \oint \oint \frac{1}{|\mathbf{r} - \mathbf{r}'|} d\lambda d\lambda', \end{aligned} \quad (6.10)$$

where the corresponding new canonical variables are simply

$$\Phi = \sqrt{\mu_{\odot} a} \left( \sqrt{1 - e^2} - 1 \right), \quad \Delta\varpi = \varpi - \varpi_r, \quad (6.11)$$

where  $\Delta\varpi$  is the apsidal misalignment of the TNO and rogue.

Equation (6.10) is a one degree-of-freedom integrable system which describes the apsidal alignment dynamics (i.e. the  $e - \Delta\varpi$  coupling which is also the dynamics of  $q$  lifting) caused by an additional planet on a constantly precessing orbit. However, Equation (6.10) cannot be fully expressed with orbital elements in closed form due to the complexities of the integral. There are generally two ways of studying  $\mathcal{H}_{\text{sec}}$  in celestial mechanics: 1) analytical methods based on series expansion of the rogue's disturbing function, and 2) a semi-analytical method based on numerically averaging the Hamiltonian and visualizing the phase portraits. The first method can result in analytical estimates of the rogue's  $q$  lifting capability (such as the rate of lifting at various semimajor axis), but it only applies to rogue planets with small eccentricities due to the inevitable truncation in the series expansions. The second method works for arbitrary eccentricities, but analytical constraints are not easy to obtain from the averaged Hamiltonian.

The secular disturbing function for the coplanar three-body problem can be ex-

pressed as a infinite series (Murray & Dermott, 1999; Mardling, 2013):

$$\mathcal{R}_{\text{sec}} = \frac{\mu_r}{a_r} \sum_{m=0}^{\infty} \sum_{l=l_{\min}}^{l_{\max}} \zeta_m c_{lm}^2 \mathcal{M}_l \alpha^l X_0^{l,m}(e) X_0^{-(l+1),m}(e_r) \cos(m\Delta\varpi), \quad (6.12)$$

where  $\alpha$  is the semimajor axis ratio, and  $X_0^{l,m}(e)$  and  $X_0^{-(l+1),m}(e_r)$  are the Hansen coefficients for the secular dynamics. The dimensionless power-series coefficients  $\zeta$ ,  $c$ , and  $\mathcal{M}$  do not depend on the orbital elements, while  $X_0$  depends on  $e$ ; These functions are defined in Mardling (2013); I will not go into details.

Expanding to octopole order (i.e. 3rd order in  $\alpha$ ), the disturbing function (6.12) becomes

$$\mathcal{R}_{\text{sec, inner}} = \frac{\mu_r}{a_r} \left[ \underbrace{\frac{1}{4} \left( \frac{a}{a_r} \right)^2 \frac{1 + \frac{3}{2}e^2}{(1 - e_r^2)^{\frac{3}{2}}} - \frac{15}{16} \left( \frac{a}{a_r} \right)^3 \frac{ee_r(1 + \frac{3}{4}e^2)}{(1 - e_r^2)^{\frac{5}{2}}} \cos(\Delta\varpi)}_{h_{2,\text{inner}}} \right], \quad (6.13)$$

which is used for TNOs with semimajor axes smaller than the rogue's ( $a < a_r$ ), and

$$\mathcal{R}_{\text{sec, outer}} = \frac{\mu_r}{a_r} \left[ \underbrace{\frac{1}{4} \left( \frac{a_r}{a} \right)^3 \frac{1 + \frac{3}{2}e_r^2}{(1 - e^2)^{\frac{3}{2}}} - \frac{15}{16} \left( \frac{a_r}{a} \right)^4 \frac{e_r e(1 + \frac{3}{4}e_r^2)}{(1 - e^2)^{\frac{5}{2}}} \cos(\Delta\varpi)}_{h_{2,\text{outer}}} \right], \quad (6.14)$$

which is used for TNOs with semimajor axes larger than the rogue's ( $a > a_r$ ).

Replacing the last term of  $\mathcal{H}_{\text{sec}}$  with the expanded disturbing function:

$$\begin{aligned} \mathcal{H}_{\text{sec}} = & -\frac{1}{4} \frac{\mu_{\odot}}{a} (1 - e^2)^{-\frac{3}{2}} \sum_{i=5}^8 \frac{m_i a_i^2}{M_{\odot} a^2} + \dot{\varpi}_r \sqrt{\mu_{\odot} a} \left( 1 - \sqrt{1 - e^2} \right) \\ & + \frac{\mu_r}{a_r} (h_2 - h_3 \cos \Delta\varpi), \end{aligned} \quad (6.15)$$

where  $h_2$  and  $h_3$  are dimensionless and they are from either the inner or outer disturbing function. Apparently,  $\mathcal{H}_{\text{sec}}$  depends only the single angle  $\Delta\varpi$ , and thus is integrable and fully describes the  $e - \Delta\varpi$  dynamics or distant TNOs under the

influence of a co-planar rogue planet. An intuitive way to ‘visualize’ the dynamics described by Equation (6.15) is through a series of phase-space portraits, which are essentially contours of the governing Hamiltonian. For the purpose of my study, it is better to re-project the phase portraits to the  $q - \Delta\varpi$  space. I plot Figure 6.3 and Figure 6.4 to depict the  $q$ -lifting dynamics on a wide range of semimajor axes. The rogue planet used to make the two figures has  $m_r = 2M_{\oplus}$ ,  $a_r = 300$  au and  $q_r = 40$  au, which is the same one used in Chapter 5 to demonstrate its capability of populating distant resonances.

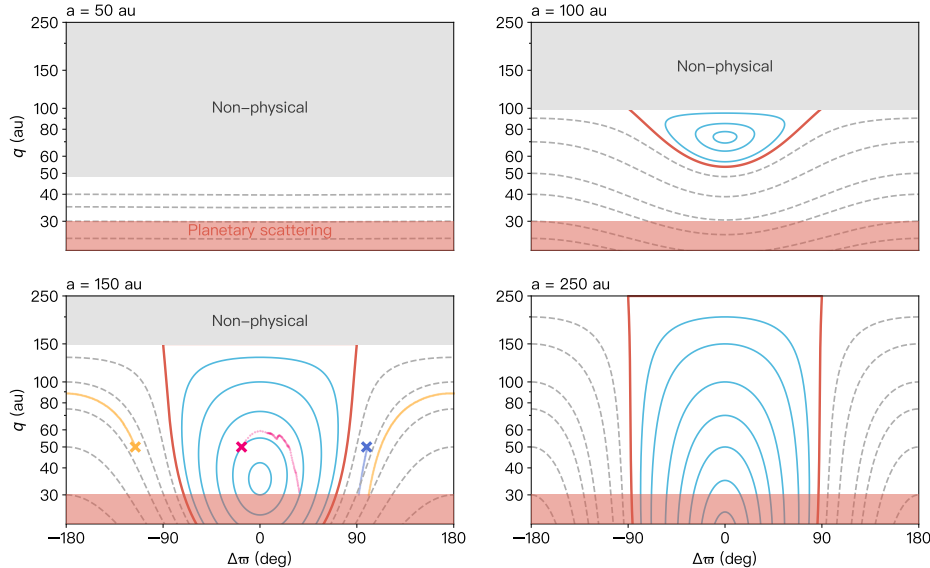


**Figure 6.3:** Four  $q - \Delta\varpi$  phase-space portraits for distant TNOs with the presence of a  $2M_{\oplus}$  planet on  $a_r = 300$  au and  $q_r = 40$  au orbit. Blue solid curves represent orbits that are apsidally confined with respect to the eccentric planet (i.e.  $\Delta\varpi$  libration), whereas dashed curves denote apsidal circulation. The bold red denotes separatrix that divides these two cases. Red shading  $q < 30$  au orbits which will be prone to scattering by Neptune, while gray shades represent non-physical orbits with  $q > a$ . Crosses and dots in the third panel shows the initial conditions and corresponding dynamical trajectories of numerically-integrated test particles under the same planet.

Figures 6.3 shows the  $q - \Delta\varpi$  coupling inside the rogue’s orbit ( $a < a_r$ ), corre-

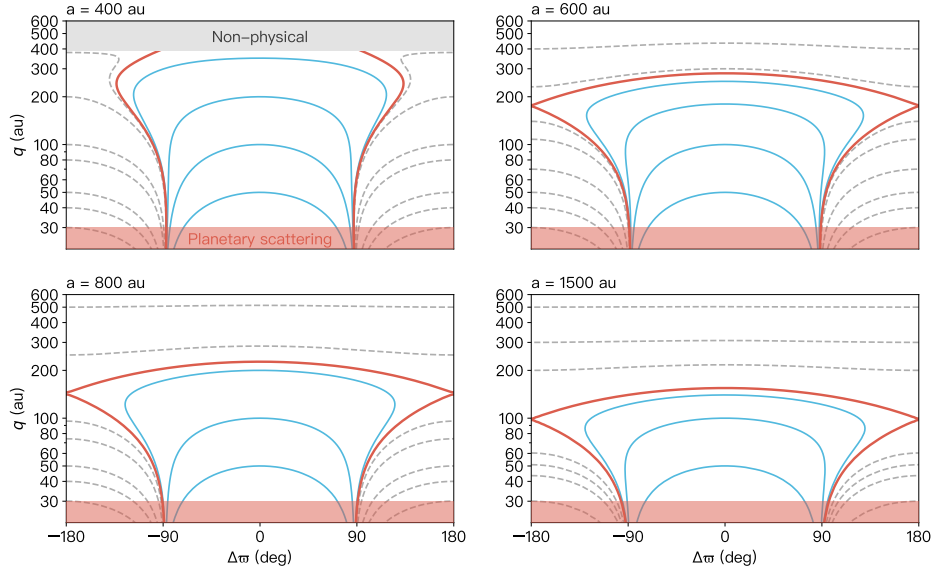


**Figure 6.4:** Same as Figure 6.3 but with TNOs outside the orbit of the rogue ( $a > a_r$ ).

sponding to the disturbing function of (6.13). As shown in the first panel, the rogue planet barely affects the  $a = 50$  au region, in which the Hamiltonian contours show apsidal precession (denoted by the circulation of  $\Delta\varpi$ ) with no significant  $q$  oscillation. By  $a = 100$  au, the rogue's presence is clearly visible in the phase portrait. It induces a  $\approx 20$  au  $q$  oscillation in the circulation zone (dashed curves) while creating a  $q - \varpi$  libration island centered on  $\Delta\varpi = 0^\circ$  (blue circles, surrounded by the red separatrix). The same dynamical phenomenon can also be seen in Batygin & Brown (2016a)'s figure 3, for different planet parameters. The libration region enlarges as  $a$  increases (panels 3 and 4), with the secular equilibrium point (the center of the blue circles with  $\Delta\varpi = 0$ ) sinking into the planetary scattering zone of  $q < 30$  au. At  $a = 250$  au, there is hardly any difference in the topology of the  $\Delta\varpi \sim 0^\circ$  and  $\Delta\varpi \sim 180^\circ$  regions, and the separatrix dividing the libration and circulation approaches two vertical lines at  $\Delta\varpi \approx \pm 90^\circ$ .

I also integrated three near co-planar test particles with  $a_0 = 150$  au and  $q_0 = 50$  au under the gravity of the same planet and superposed their dynamical trajectories on Figures 6.3's third phase portrait. Even though the rogue planet crosses the

orbits of the three particles and strictly speaking the series expansion method is no longer suitable, I argue that at several hundred au, the spatial volume becomes so large that rogue encounters are ineffective at perturbing particles (see Section 6.1.1). As a result, the phase portraits obtained through expanding the disturbing function given in (6.12) are still good approximations to the more complicated problem. This explains why the numerical trajectories basically follow the level curves in Figure 6.3.

Figures 6.4 shows the dynamics outside the rogue's orbit ( $a > a_r$ ), corresponding to the disturbing function of (6.14). Unlike the inner case, these phase portraits show no stable equilibrium point or libration zone in the plotted area. The separatrix for  $a = 600, 800$  and  $1500$  au connect the two unstable equilibrium point at  $\Delta\varpi = \pm 180^\circ$ , and also separates the circulation zone at very large perihelion. Although the planetary secular effect can always be felt at larger  $a$ , for this particular rogue, its  $q$ -lifting ability is limited to  $q \lesssim 200$  au for  $a \geq 800$  au.

The  $q - \Delta\varpi$  phase portraits are useful because they show the *maximum*  $q$ -raising ability by the additional massive body. That is, given enough time, what oscillations the planet secularly forces at various semimajor axes. What I focus on in this thesis, however, is an only temporarily-present planet that may also have migrated significantly in  $a$ , whose accumulated effect cannot be fully accounted for by static phase portraits. Therefore, it is more practical to estimate the instantaneous rate of change of  $q$  for a variety of rogue orbits.

I start by writing down the equation of motion for  $\Phi$ , using the closed-form secular Hamiltonian (6.15):

$$\begin{aligned} \frac{d\Phi}{dt} &= -\frac{\partial \mathcal{H}_{\text{sec}}}{\partial \Delta\varpi}, \\ &= -\frac{\mu_r}{a_r} h_3 \sin \Delta\varpi \end{aligned} \tag{6.16}$$

where  $h_3$  is the second dimensionless constant in Equation (6.13) or (6.14), depending on whether the particle is inside or outside the rogue. Using the definition of  $\Phi$

in (6.11) and the fact  $\dot{a} = 0$  in secular dynamics:

$$\begin{aligned}\frac{d\Phi}{dt} &= \frac{d\Phi}{de} \frac{de}{dt}, \\ &= -\sqrt{\mu_{\odot} a} \left( \frac{e}{(1-e^2)^{\frac{1}{2}}} \right) \frac{de}{dt},\end{aligned}\tag{6.17}$$

Equating (6.16) and (6.17), I obtain two formulas for the rate of  $e$  change:

$$\dot{e}|_{a < a_r} = \frac{m_r}{M_{\odot}} n \left( \frac{a}{a_r} \right)^4 \left[ \frac{15}{16} \left( 1 + \frac{3}{4} e^2 \right) (1 - e^2)^{\frac{1}{2}} \frac{e_r}{(1 - e_r^2)^{\frac{5}{2}}} \right] \sin \Delta \varpi,\tag{6.18}$$

and

$$\dot{e}|_{a > a_r} = \frac{m_r}{M_{\odot}} n \left( \frac{a_r}{a} \right)^3 \left[ \frac{15}{16} \frac{1}{(1 - e^2)^2} e_r \left( 1 + \frac{3}{4} e_r^2 \right) \right] \sin \Delta \varpi.\quad d\tag{6.19}$$

As the final step, I replace  $e$  with  $1 - q/a$  and  $\dot{e}$  with  $-\dot{q}/a$  to rewrite (6.18) and (6.19) as functions of  $a$  and  $q$ :

$$\dot{q} = -a |\dot{e}_{\max}| \sin \Delta \varpi = \dot{q}_{\max} \sin(-\Delta \varpi),\tag{6.20}$$

in which  $\dot{q}_{\max}$  is the amplitude and denotes the maximum  $q$  rate of change (for  $\Delta \varpi = -90^\circ$ ) and  $\dot{e}_{\max}$  is the amplitude of  $\dot{e}$ . Equation (6.20) shows that  $\dot{q}$  for different initial  $\Delta \varpi$  varies from  $-\dot{q}_{\max}$  to  $\dot{q}_{\max}$ , with the  $\Delta \varpi \simeq -90^\circ$  particles being lifted the fastest and forming the upper boundary in the  $a$ - $q$  space, as perihelia initially rise. This matches Fig. 6.3's behaviour.

I tested Equations (6.18) and (6.19) against N-body numerical integrations. What I find, however, is that both equations significantly overestimate the  $\dot{q}$  for high- $e$  objects. With the power series truncated to the octopole order, the expanded distribution functions (6.13 and 6.14) cannot accurately describe the dynamics in the limit of  $e \rightarrow 1$  and  $e_r \rightarrow 1$ . This can be also be understood from Equations (6.18) and (6.19) directly, where both expressions contain a  $1/(1 - e_{(r)}^2)$  singularity, resulting in an exploding  $\dot{e}$  at large  $e$  which does not reflect reality.

Instead of expanding the disturbing function to higher orders, which would dramatically increase the complexity of the problem, I experimented with a variety of

simplified model simulations with different planetary parameters (e.g. Figures 6.5 and 6.6) and summarize the following attributes related to the secular dynamics:

1. The maximum  $\dot{q}$  lifting happens near  $a = a_r$ .
2.  $\dot{q}$  is not a strong function of  $q$ , which means large- $e$  scattering TNOs are getting lifted in near constant rates regardless of their eccentricities.
3.  $\dot{q}$  is not a strong function of  $q_r$ , either. In other words, as long as the planet's perihelion is inside the semimajor range one is interested in (i.e.  $q_r < a$ ), the  $\dot{q}$  doesn't significantly depend on  $q_r$ .

With these properties in mind, I have found that a fairly close  $\dot{q}_{\max}$  approximation can be obtained by positing  $e = 0$  in Equation (6.19). This essentially erases the singularity in (6.19)'s denominator, and corresponds to the secular dynamics of circular and co-planar orbits:

$$\dot{q}_{\max} \simeq \frac{m_r}{M_{\odot}} n a \alpha^3 (e_r + \frac{3}{4} e_r^2), \quad (6.21)$$

where

$$\alpha = \begin{cases} \frac{a}{a_r}, & \text{if } a < a_r, \\ \frac{a_r}{a}, & \text{if } a > a_r, \end{cases} \quad (6.22)$$

which is the semimajor axis ratio between the inner and the outer bodies. Equation (6.21) is linear in  $m_r$ , with only weak dependence on  $q_r$ . This can be seen from the eccentricity factor:

$$e_r + \frac{3}{4} e_r^2 = \frac{7}{4} - \frac{5}{2} \frac{q_r}{a_r} + \frac{3}{4} \left( \frac{q_r}{a_r} \right)^2, \quad (6.23)$$

in which the leading factor is a constant that varies only by a factor of two for  $q_r/a_r < 0.4$ , and usually for rogue planets I consider  $q_r/a_r < 0.2$ .  $\dot{q}_{\max}$  is thus proportional to:

$$\dot{q}_{\max} \propto \begin{cases} m_r a_r^{-3} a^{2.5}, & \text{if } a < a_r, \\ m_r a_r^3 a^{-3.5}, & \text{if } a > a_r. \end{cases} \quad (6.24)$$

In the assumption that the initial scattering TNOs are distributed in  $a$  with a roughly constant  $q_0 \simeq 30\text{--}35$  au (see Section 3 for the scattering dynamics), one can describe the upper boundary of the small-body  $a$ - $q$  distribution as a function of  $a$  and  $t$ :

$$q(t) = q_0 + t \dot{q}_{\max}(a), \quad (6.25)$$

where  $t$  is the time during which a planet (on a roughly constant  $a_r$ ) imposes secular oscillation on scattering objects, and  $q_0$  is the initial perihelion for an un-detached scattering disk.

In Figures 6.5 and 6.6, I compare this approximate analytical solution to GLISSER simulations with a fixed rogue (see Section 6.3). More specifically, the first simulation is conducted with a 2 Earth-mass rogue with initial  $a_r = 400$  au and  $q_r = 50$  au, while the second one has with a 5 Earth-mass rogue with initial  $a_r = 800$  au and  $q_r = 60$  au. The initial conditions contain 50,000 initially low- $i$  test particles, uniformly distributed in semimajor axis, with  $q_0 = 32\text{--}35$  au. These test particles have randomly-chosen phase angles ( $\omega, \Omega$  and  $M$ ) and thus cover  $\Delta\varpi$  from  $-180^\circ$  to  $180^\circ$  with respect to the rogue's apsidal line. They were then integrated along with four giant planets and their respective rogue (orange cross) for 100 Myr.

As shown in Figures 6.5 and 6.6, both the interior ( $a < a_r$ ) and exterior ( $a > a_r$ ) boundaries (blue dashed curves) match the upper envelopes of the particle  $a$ - $q$  distributions (black dots) at various times. The interior envelope is close to  $q \propto a^{2.5}$ , while the exterior one is close to the  $q \propto a^{-3.5}$  analytical prediction (Equation 6.24). At certain distances (e.g.  $200 < a < 400$  au and  $900 < a < 1200$  au in Figure 6.6), the maximum  $q$  lifting rate is underestimated, but by less than a factor of 2. It is thus a reasonably good approximation to the secular dynamics induced by a highly-eccentric planet.

### 6.1.3 Analytical Constraints from the Making of Sednoids

In a rogue-planet scenario where the vast majority of high- $q$  TNOs were created by the temporarily-present secular forcing, constraints on the rogue's mass and residence time can be obtained from the requirement of making the three most detached TNOs: 2012 VP<sub>113</sub> ( $a = 262$  au,  $q = 81$  au,  $i = 24^\circ$  in barycentric elements), Sedna ( $a = 506$  au,  $q = 76$  au,  $i = 12^\circ$ ), and Leleākūhonua ( $a = 1090$

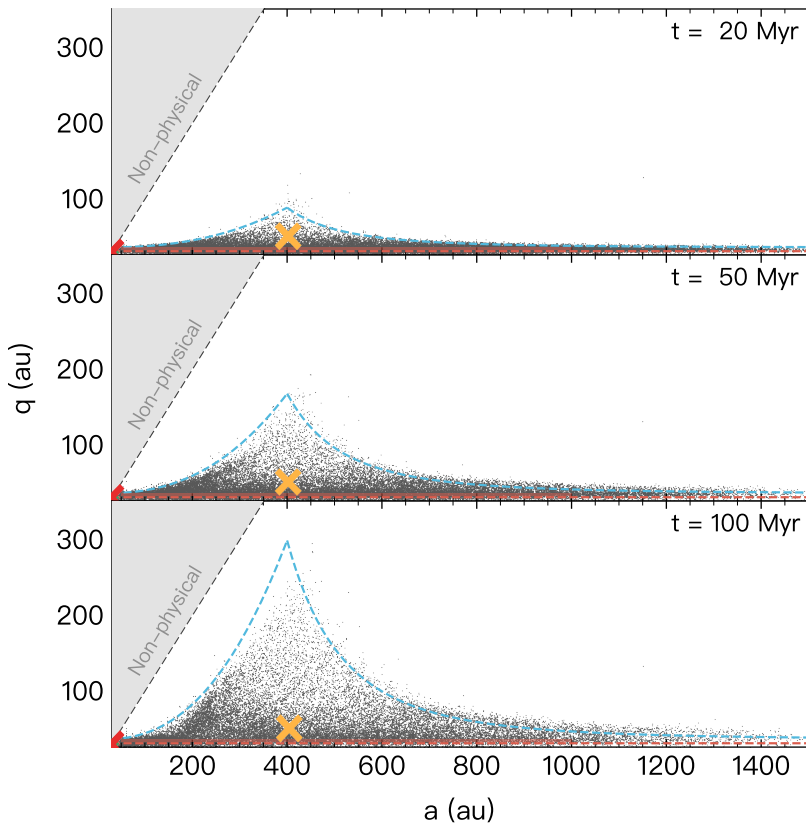


**Figure 6.5:** The three panels, from top to bottom, show the  $t = 20, 50$ , and  $100$  Myr  $a$ - $q$  distribution of simulated TNOs (black dots) under the influence of a  $m_r = 2M_{\oplus}$ ,  $a_r = 400$  au, and  $q_r = 50$  au planet (orange cross). Test particles are initially placed uniformly in a box of  $50 < a < 1000$  au and  $32 < q < 35$  au. The red dashed line denotes  $q = 30$  au which corresponds to strong Neptune scattering, whereas the left and right blue dashed curves are upper boundaries of the distribution, computed at different  $a$  and  $t$  using Equation (6.25) (see text for details). My analytical solution (6.21) provides a decent estimate to the maximum forced secular  $q$  lifting induced by the perturbing planet.

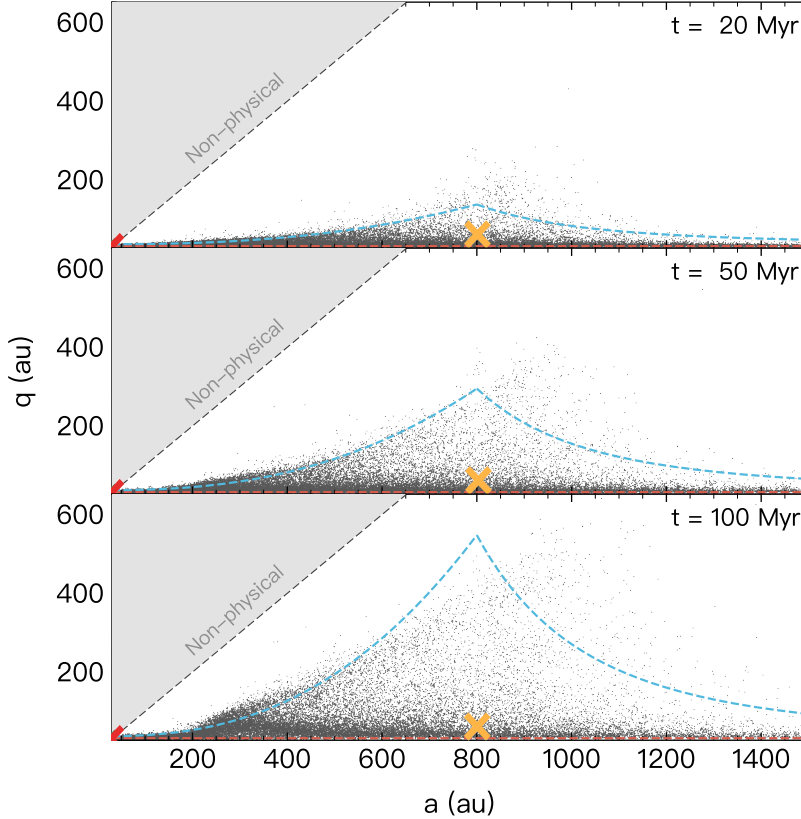


**Figure 6.6:** Same as Figure 6.5 but with a rogue planet with  $m_r = 5M_{\oplus}$ ,  $a_r = 800$  au, and  $q_r = 60$  au.

au,  $q = 65$  au,  $i = 12^\circ$ , collectively known as *Sednoids*; See also Table 4.1 for other high- $q$  TNOs.

In a rogue scenario, the innermost Sednoid – 2012 VP<sub>113</sub> – was likely lifted by an exterior rogue ( $a_r \gtrsim 250$  au). This is because million-year-scale presence of a planetary mass inside  $\sim 200$  au will rapidly detach the  $a = 50$ – $200$  au Kuiper Belt, creating an overabundant high- $q$  population in this  $a$  range that is more likely to be found than  $a > 200$  au detached objects (see Section 6.3.2 for details about this constraint). The outermost Sednoid – Leleākūhonua – was studied in Sheppard et al. (2019), who integrated Leleākūhonua’s orbit in a couple different physical ap-

proximations. They found this object is rather stable for the age of the Solar System, even in situations incorporating galactic tides and passing stars. The current galactic environment only induces a  $\sim 10$  au  $q$  oscillation (their figure 7), which cannot produce its  $q = 65$  au orbit from  $q_0 \sim 30$  au. In a rogue-planet scenario, Leleākūhonua was likely lifted when the rogue was inside its orbit ( $a_r \lesssim 1000$  au), because a scattering planet beyond  $\sim 1000$  au only exists for a short period of time ( $\lesssim 100$  Myr for Neptune-scattering and  $\lesssim 500$  kyr for Saturn-scattering, see Figure 3.2) before its ejection. The case for Sedna is more complicated. Its  $\approx 500$  au semimajor axis is a common value for a hypothetical scattering planet, so either the interior and exterior secular effects could have contributed to its high  $q$ .

To estimate the required timescale and planetary mass, I assume all of them were initially Neptune-scattered objects with  $q_0 \simeq 30$  au. Once they came close to their current  $a$  (which probably took 10–100 Myr), the rogue detached them from the scattering disk until the removal of the planet. The rogue planet is a scattering planet with constantly-changing  $a$  (otherwise it's a still-present planet model, *not* a rogue planet model) and, to the lowest order, I can pin down its parameters assuming it has fixed  $a_r$  and  $q_r$ . Rearranging Equation (6.25), I obtain

$$t_{\text{tno}} = \frac{q_{\text{tno}} - q_0}{\dot{q}_{\max}(a_{\text{tno}})}, \quad (6.26)$$

where  $t_{\text{tno}}$  is the least amount of time required to make a particular high- $q$  TNO from the scattering disk. The timescale for making 2012 VP<sub>113</sub> is

$$\begin{aligned} t_{\text{VP}_{113}} &\gtrsim \frac{50 \text{ au}}{\dot{q}_{\max}|_{a=250 \text{ au}}}, \\ &\gtrsim 12 \text{ Myr} \left( \frac{m_r}{2M_{\oplus}} \right)^{-1} \left( \frac{a_r}{250 \text{ au}} \right)^3, \quad \text{if } a_r > 250 \text{ au}. \end{aligned} \quad (6.27)$$

For Leleākūhonua

$$\begin{aligned} t_{\text{Leleā}} &\gtrsim \frac{35 \text{ au}}{\dot{q}_{\max}|_{a=1000 \text{ au}}}, \\ &\gtrsim 17 \text{ Myr} \left( \frac{m_r}{2M_{\oplus}} \right)^{-1} \left( \frac{a_r}{1000 \text{ au}} \right)^{-3}, \quad \text{if } a_r < 1000 \text{ au}, \end{aligned} \quad (6.28)$$

and for Sedna

$$t_{\text{Sedna}} \gtrsim \frac{45 \text{ au}}{\dot{q}_{\max}|_{a=500 \text{ au}}},$$

$$\gtrsim 15 \text{ Myr} \left( \frac{m_r}{2M_{\oplus}} \right)^{-1} \begin{cases} \left( \frac{a_r}{500 \text{ au}} \right)^3, & \text{if } a_r > 500 \text{ au}, \\ \left( \frac{a_r}{500 \text{ au}} \right)^{-3}, & \text{if } a_r < 500 \text{ au}. \end{cases} \quad (6.29)$$

Figure 6.7 shows these three timescales calculated for  $0.2 M_{\oplus}$  (Mars-scale),  $2 M_{\oplus}$  (Earth-scale), and  $20 M_{\oplus}$  (ice-giant-scale) rogues. The left panel displays the least amount of time required for making 2012 VP<sub>113</sub> (solid lines) and Leleākūhonua (dashed lines) at various  $a_r$ , while the right panel shows that for Sedna. Taking the  $2 M_{\oplus}$  rogue (orange curves) as an example, when the rogue has the semimajor axis of  $a_r = 500$  au, both the VP<sub>113</sub> and Leleākūhonua production timescales are close to  $\sim 100$  Myr, whereas the Sedna production timescale is only  $\lesssim 20$  Myr. In other words, the creation of Sedna is a less stringent constraint (at least for  $400 \lesssim a_r \lesssim 800$  au) compared to the production of VP<sub>113</sub> and Leleākūhonua. However, taking into account that Leleākūhonua (with  $a \simeq 1100$  au) may have been influenced by stellar flybys (Sheppard et al., 2019) or chaotic diffusion (Bannister et al., 2017) in the past, the constraint of making Leleākūhonua is thus ‘optional’ for a rogue-planet scenario.

#### 6.1.4 Analytical Constraints from the Cold Classical Belt

Another constraint can be obtained from the low dynamical excitation of the cold classical Kuiper Belt. Dawson & Murray-Clay (2012) point out in their figure 3 that the cold classicals between 42.5 and 44 au are confined to  $e < 0.05$ , while cold classicals between 44 and 45 are confined to  $e < 0.1$ . Cold classicals in these two regions are less eccentric than the survival limit of the current environment, which was used by Dawson & Murray-Clay (2012) to constrain the past evolution of Neptune’s eccentricity. Thus, I can constrain the *maximum* residence time of a rogue planet with Equation (6.21). To do this, I assume the maximum eccentricity

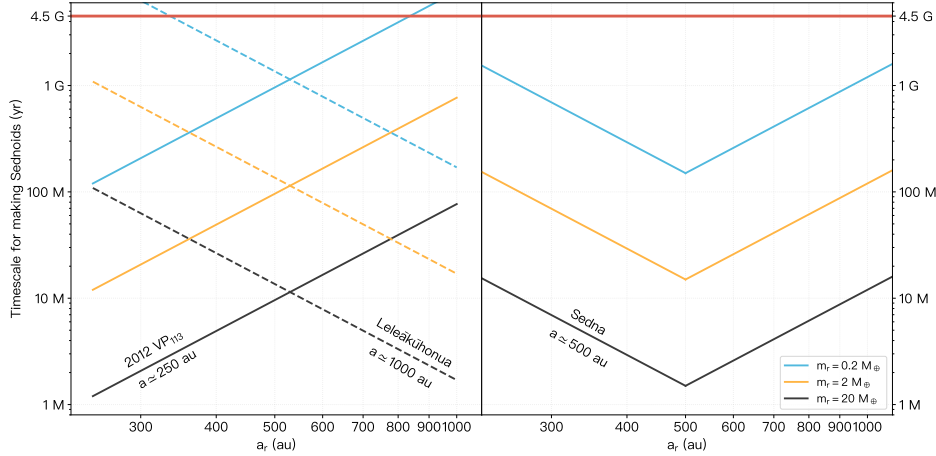


**Figure 6.7:** The least amount of time required for a rogue planet to make the three most-distant Sednoids: 2012 VP<sub>113</sub> (left panel, solid lines), Leleākūhonua (dashed lines), and Sedna (right panel). These timescales are computed using Equations (6.27) to (6.29). Notice that the timescale for making Sedna is generally shorter than those for the other two objects, which means it is a less strict constraint among the three.

heating at 44 au is  $e \lesssim 0.1$ , which corresponds to the maximum  $\Delta q \lesssim 4.4$  au:

$$t_{CC} \lesssim \frac{4.4 \text{ au}}{\dot{q}_{\max}|_{a=44 \text{ au}}},$$

$$\lesssim 9 \text{ Myr} \left( \frac{m_r}{2M_{\oplus}} \right)^{-1} \left( \frac{a_r}{100 \text{ au}} \right)^3 \left( e_r + \frac{3}{4} e_r^2 \right)^{-1}, \quad (6.30)$$

where I keep the eccentricity factor as its original form, due to the reason that at lower  $a_r$ ,  $e_r$  is no longer close to 1 and the rogue  $q_r$  will affect the secular dynamics. Figure 6.8 shows the maximum rogue presence time, as a function of  $a_r$ , that will not overheat the cold classicals (solid lines). In comparison, I also overlay Figure 6.7's minimum timescale for simultaneously producing Sedna and VP<sub>113</sub> in dashed lines, and the shaded regions between the two constraints give the allowable parameters for rogues with different masses.

All the constraints obtained so far assume the rogue planet is on an orbit with fixed  $a_r$  and  $q_r$ . This assumption is an over simplification, though it provides a

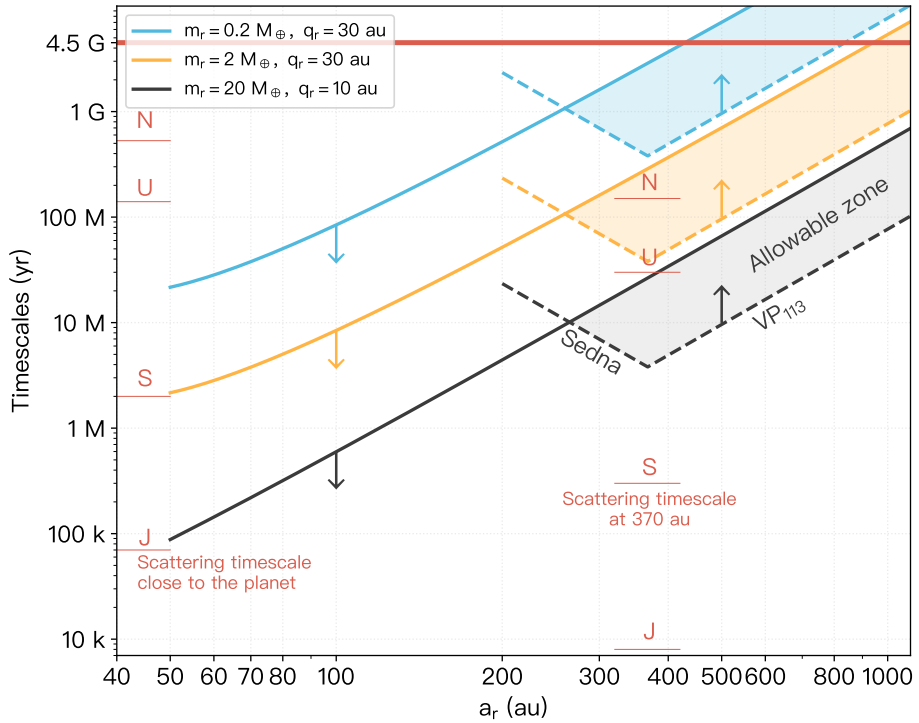


**Figure 6.8:** Solid lines show the maximum rogue presence time at various semimajor axis constrained by the underheated  $e < 0.1$  cold Kuiper Belt, computed with Equation 6.30. Dashed lines show the minimum timescales of making both Sedna and VP<sub>113</sub> in comparison, which is identical to Figure 6.7. The region confined by the two timescales define the allowable zone for the rogue’s  $a_r$  and the residence time corresponding to that semimajor axis. Thin red lines on the left mark the scattering timescales of Jupiter, Saturn, Uranus, and Neptune for initially near-planet objects, whose values are given in Figure 3.2. Those on the right are the same timescales but for  $a_r = 370$  au (the semimajor axis where the VP<sub>113</sub> and Sedna constraints cross) objects. Different colors represent rogues with different masses.

good estimate to the rogue's dynamics even if it is actually on a scattering orbit with constantly-changing semimajor axis. For a scattering planet coupled with other giant planets, the rate of  $a_r$  change and its dynamical lifetime depends on how strong the scattering effect is, which is related to the perihelion distance  $q_r$  and inclination  $i_r$ . In Chapter 3, I analytically derived the scattering timescale in a CRTBP model. Assuming that the rogue's mass is much smaller than its scatterer's mass (the dynamics of two similar-massed bodies scattering each other cannot be approximated by the diffusion approximation), the timescales for giant planets to scatter out the rogue are shown in Figure 3.2. These timescales are also marked in Figure 6.8 as thin red lines on the left side.

In Figure 6.8, a planet-scattered rogue must have its cold-belt constraint curve (solid curves) above the corresponding planet's scattering timescale (red lines) to generally not overheat the cold belt. As an example,  $m_r = 20M_{\oplus}$  rogue planet (black lines) will excite the cold belt in  $<1$  Myr if  $a_r < 100$  au, which is longer than Jupiter's but shorter than Saturn's scattering timescale. This is to say, a Jupiter-scattered ice giant probably would not have overheated the cold belt given its extremely short time scale to reach very large  $a$  (or ejection); this is consistent with Batygin et al. (2011)'s numerical result, where the authors showed that the ejection of the hypothetical 'fifth giant' would not overexcite the cold classical belt. A Saturn-coupled ice giant is not likely to satisfy this constraint because the  $\sim 2$  Myr scattering timescale is enough to heat the cold classicals to unacceptable degree. The result is that only Jupiter-scattered ice giants and Saturn-scattered 'Earths' and 'Mars' can meet such a constraint. Neptune and Uranus are too small to scatter even Mars-scaled objects out to large semimajor axis without overheating the Kuiper Belt; this is consistent with numerical simulations in Petit et al. (1999), where the authors demonstrate that a Neptune-scattered planetesimal of a Earth mass would completely destroy the cold belt. They also show that a Neptune-scattered planetesimal of mass  $0.1 M_{\oplus}$  would leave a significant number of TNOs in cold belt, but that surviving belt would have a significant fraction of the cold classicals with  $e > 0.1$ , which violates the current observational constraint (see figure 5 in Gladman & Volk 2021).

Once a rogue planet is scattered to a few hundred au, its secular effect of heating the cold belt is significantly reduced, whereas the  $q$ -lifting effect that form detached objects is greatly strengthened. The shaded 'allowable zone' in Figure 6.8 represents

where both the cold-belt constraint and the Sedna and VP<sub>113</sub> constraints <sup>3</sup> are satisfied. Taking the  $m_r = 20M_{\oplus}$  rogue as an example, the gray allowable zone defines the most-likely parameters for such a rogue when it is at large  $a_r$ ; and for this ice giant, the timescale varies from a few million years at  $a_r \sim 400$  au to several hundred million years at  $a_r \sim 1000$  au. This time must also be in agreement with the scattering timescale <sup>4</sup> of the corresponding scatterer, however. The required residence time for an ice giant at  $\sim 500$  au is roughly 2 Myr, an order-of-magnitude longer than the  $\sim 0.3$  Myr scattering timescale for a Saturn-scattered body at  $a_r \sim 400$  au (denoted by red thin lines on Figure 6.8's right side). It's evident from this figure that the most-likely workable combination is a Neptune-scattered Earth-scaled planet and an Uranus-scattered Earth-scaled planet is marginally acceptable.

Our analysis thus poses a seeming difficulty for the rogue planet scenario:

1. From the underheated  $e$  distribution of the cold classical belt, the rogue has to be scattered out by Jupiter if it's a ice giant, or by Saturn if it's a super Earth or Mars. A Neptune/Uranus-scattered planetary mass too slowly moves out to meet the constraint.
2. The rogue must be only coupled with Uranus or Neptune while at large semi-major axis, otherwise the timescale is not long enough to produce all Sednoids.

This conundrum, however, exists due to the assumption that, in the early Solar System, scattered objects stick to their respective scatterers and there is no transfer of scattering control from a gas-giant coupled orbit to an ice-giant coupled orbit. It is well understood that many initially Neptune/Uranus-scattered objects are able to penetrate the  $\lesssim 10$  au region and thus transfer scattering control to Saturn/Jupiter. In fact, that's how the Jupiter-Family Comets (JFC) are formed (Levison & Duncan, 1997; Kaib & Volk, 2022). The dynamics easily allow an initially Saturn-coupled, Earth-scaled planet to be scattered to several hundred au within a few million years,

---

<sup>3</sup>The Leleākūhonua constraint is not used in Figure 6.8 because it is considered an ‘optional’ constraint for the rogue planet model. See Section 6.1.4 for discussions.

<sup>4</sup>The scattering timescale in Figure 3.2 is computed for objects initially close to the planet, and Equation (3.9) shows that this timescale is proportional to  $a^{-0.5}$ , one can thus expect a factor of  $\sim 4\text{--}8$  decrease at several hundred au.

thus preserving the primordial Kuiper Belt on its way out. Its control would then need to be transferred to Uranus/Neptune (naturally or due to unexplored dynamical effects), initiating a much slower random walk (generally outward) in semimajor axis for the next few hundred million years, until its ejection.

In Section 6.2, I will perform numerous planetary simulations with an extra planetary mass to better understand and constrain possible production mechanisms of the rogue. Promising planetary histories will then be integrated with tens of thousands of scattering test particles in Section 6.3, in order to produce an orbital distribution model of the distant Kuiper Belt that can be compared against real TNO detections.

## 6.2 Planetary simulations with rogue planet(s)

The dynamical evolutional history of a now-lost planet has not been thoroughly studied. Numerical simulations of a model with 5 or 6 giant planets (e.g., Nesvorný, 2011; Nesvorný & Morbidelli, 2012; Batygin et al., 2012) often focused on the evolutions of extra planet(s) inside 30 au, while commonly ignoring their dynamical paths at larger semimajor axes (say,  $a > 100$  au). Silsbee & Tremaine (2018) conducted N-body simulations to understand the production and possible retention of distant planets from the source region of the giant planets. While the authors claimed the likelihood of the presence of one sub-Earth mass embryo in the outer Solar System, it should be noted that their simulations were limited to a small number of test particles (50 for each simulation) to examine perturbations to the Kuiper Belt, and the conservation of a cold classical belt was never demonstrated.

Therefore, it's necessary to carry out my own planetary simulations in order to provide more insight into the possible dynamical histories of a temporarily-present planet, with particular attention to its impact on the cold classical belt and the orbits of giant planets. To do this, I integrated several sets of initial planetary conditions with REBOUND's MERCURIUS package (Rein & Liu, 2012; Rein et al., 2019b). This package provides an optimized implementation of the original hybrid symplectic method of the MERCURY integrator (Chambers, 1999), which is capable of handling close encounters between planets.

### 6.2.1 Rogues Scattered by Neptune

To start with, I first explore the possibility of producing a feasible <sup>5</sup> rogue history with an initially Neptune-coupled  $m_r = 2M_{\oplus}$  planet. Two sets of REBOUND simulations were initialized with Jupiter, Saturn, and Uranus on their current orbits. Neptune starts on a near-circular orbit with  $a_{N,0} = 32$  au, and the rogue has initial  $a_{r,0} = 29.5$  au and  $q_{r,0} = 29$  au for the first set of simulations (Sim-N-1), and  $a_{r,0} = 34.5$  au and  $q_{r,0} = 34$  au for the second set (Sim-N-2). I initialized Neptune slightly outside its current orbits because given the rogue was predominantly scattered out by this gas giant, one would expect a net inward semimajor change due to the ejection of the massive body. The estimated magnitude of this change is given in Equation (4.8), in which a  $2 M_{\oplus}$  planet would likely result in  $\Delta a = 2M_{\oplus}/(17M_{\oplus}) \times 32 \simeq 4$  au.

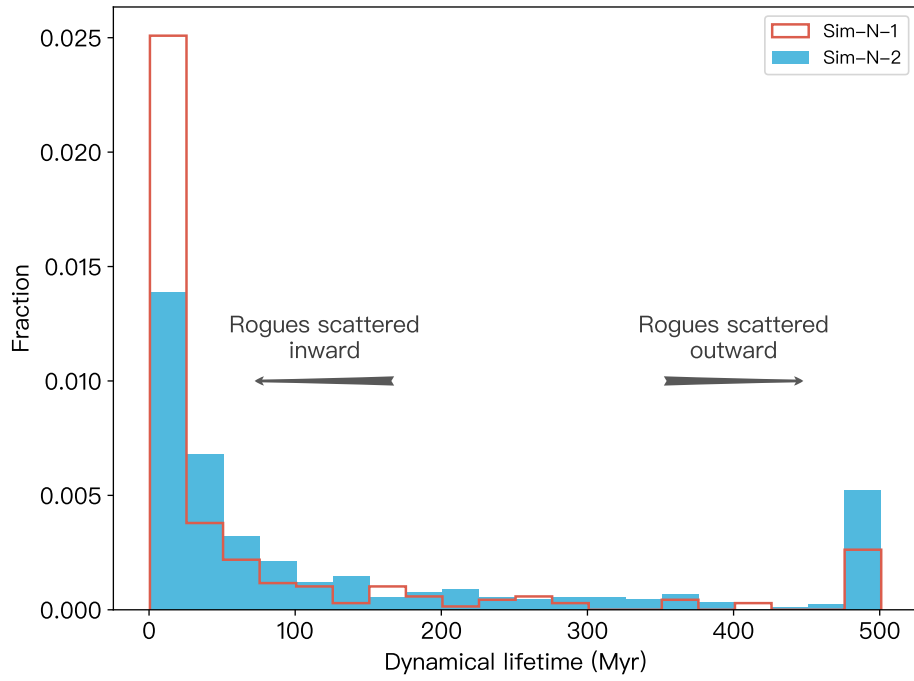
Each simulation set is composed of 360 simulations with randomized rogue phase angles, which, due to the strong chaos embedded in the system, leads to completely different evolutional histories. These simulations were integrated with the time step of 200 days, until the removal of the rogue or the maximum integration time of 500 Myr. The rogue is considered ‘ejected’ when it reaches the heliocentric distance of 3,000 au, a distance where torques from galactic tides are non-negligible (see Figure 3.2). The possibility of the retention of the rogue planet in the Oort Cloud is discussed in Section 6.5.

Figure 6.9 shows histograms of the rogue’s dynamical lifetimes in the two simulation sets. Both scenarios demonstrate relatively short rogue lifetimes, with the median being 10 Myr and 50 Myr, respectively. Only 20% of the runs in Sim-N-1 (blue bars in Figure 6.9) and 35% of those in Sim-N-2 (red lines) have rogues living longer than 100 Myr. Most of the rogues have survived much shorter than the single-planet scattering timescale of Neptune of several hundred million years, as a result of being randomly scattered inward and having perihelion coupled with more massive Saturn and Jupiter. Stronger gravitational scatterings by either of these two gas giants can then easily remove the rogue on the timescale  $\lesssim 10$  Myr.

Figure 6.10 demonstrates a rogue scattered into the Saturn-dominated region ( $q_r \sim 10$  au) as an example. It experienced strong gravitational scatterings as its

---

<sup>5</sup>A feasible rogue history is one that satisfies both the cold-belt constraint and the Sednoid constraint defined in Section 6.1.3.



**Figure 6.9:** Distribution of the rogue's dynamical lifetimes when initially coupled with Neptune. The two 360-simulation sets (Sim-N-1 and Sim-N-2) have the same initial conditions for giant planets (with Neptune at  $a_N = 32$  au), and a  $2M_{\oplus}$  rogue slightly inside of (Sim-N-1, blue bars) or outside of (Sim-N-2, red lines) Neptune. Simulations ran for 500 Myr. Most of the simulated rogues have dynamical lifetimes  $\lesssim 100$  Myr (80% and 65% for the two sets, respectively), with both histograms peaked at  $\lesssim 25$  Myr that correspond to rogues that got scattered inward by Neptune and then got rapidly ejected by Saturn/Jupiter (represented by the rogue history shown in Figure 6.10). Only a small portion of simulations have rogues that lived several hundred million years; examples of short-lived and long-lived rogues are displayed in Figures 6.10 and 6.11.

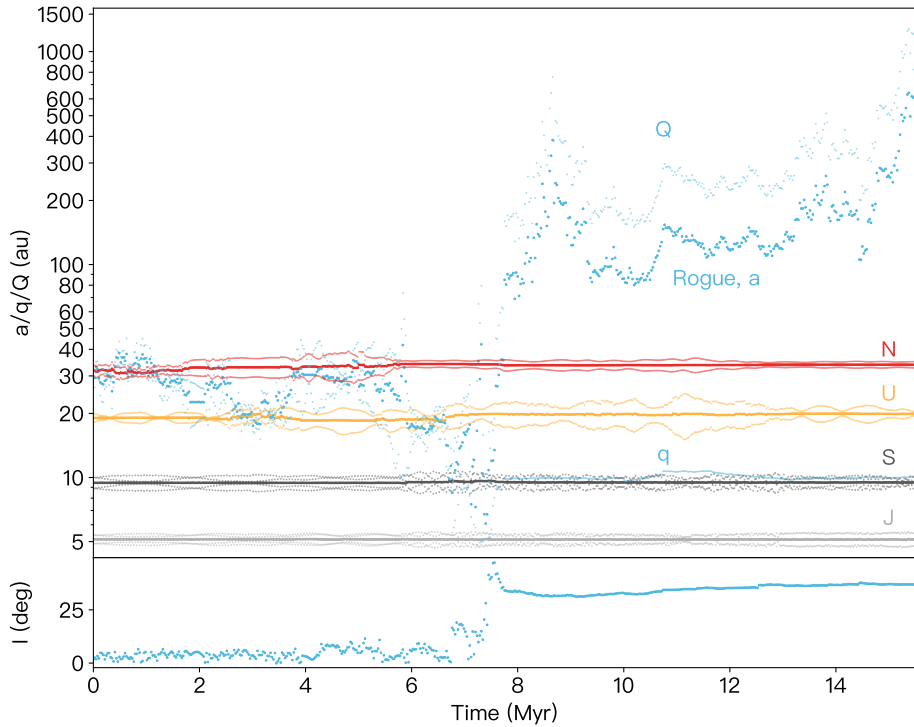


**Figure 6.10:** Planetary evolution histories of the four giant planets and a scattering rogue planet, initially placed inside the orbit of Neptune and scattered inward. The top panel shows the  $a$ ,  $q$  (perihelia), and  $Q$  (aphelia) evolutions of five planets (from top to bottom: the rogue, Neptune, Uranus, Saturn, and Jupiter), while the bottom panel shows the rogue's inclination. The rogue experienced Neptune and Uranus scatterings in the first 6 Myr, until it coupled with Saturn and temporarily with Jupiter near  $t = 7$  Myr. It then got scattered by Saturn, rapidly enlarging its semimajor axis for  $\simeq 8$  Myr until its ejection.

semimajor axis wandered between Neptune (red) and Uranus (orange) in the first 6 Myr, but a rapid subsequence of  $a$  jumps out to  $a$  of several hundred au did not occur until it was  $q$ -coupled with Saturn (black) and temporarily with Jupiter (gray). It then demonstrates frequent semimajor axis movement at large  $a$  due to strong Saturn coupling for the next 7 Myr, until its removal at  $a > 1500$  au. The reader may find this evolutional history surprising as this Saturn-coupled planet has survived longer than Saturn's typical scattering timescale of  $\sim 1$  Myr (Table 3.1). This is largely due to its moderately large inclination of  $\approx 30^\circ$  and  $T_S \approx 2.4$ , resulting in a factor of  $\approx 4$  longer scattering timescale as given by Equation 3.36. Even with the dynamical lifetime of  $\sim 10$  Myr, a  $2M_\oplus$  planet still cannot make Sednoids in time (Figure 6.8).

Compared to the Sim-N-1 group, rogues initialized outside Neptune's orbit (Sim-N-2 group) have a better chance of being scattered outward and generally survived longer (see blue bars in Figure 6.9). This can better be understood through Figure 6.12. The left panel shows the mean and minimum rogue perihelion distance ( $q_r$ ) of each simulation as a function of the rogue's dynamical lifetime. Almost all rogues ejected in  $< 100$  Myr have minimum  $q < 10$  au. Rogues that survived the entire 500 Myr integration tend to have minimum  $q_r$  above 10 au, with average  $q_r$  (denoted by dots) coupled with Neptune at  $\sim 30$  au. I find it also surprising that the vast majority of rogues (including the long-lived ones) have minimum  $q_r$  below 20 au, which implies that (temporary) Uranus coupling is prevalent in this type of dynamical evolution.

One example of a long-lived outward-scattering rogue is shown in Figure 6.11, in which the extra planet survives  $\gtrsim 150$  Myr. It first experiences  $\approx 25$  Myr scatterings among Neptune and Uranus, until a very proximate Neptune encounter swings its orbit to 100 au (denoted by the huge jump in the rogue's  $a$  history and the small discontinuity in Neptune's history in Figure 6.11's top panel). After that, the rogue keeps its  $q$  at  $\approx 30$  au and demonstrates the ordinary scattering-disk object behaviour of a random walk outward in  $a$  for  $\sim 100$  Myr until its ejection. There are patterns for the final orbit of Neptune depending on the rogue's dynamical lifetime, shown in Figure 6.12's right panel. Each dot denotes Neptune's  $a_{N,f}$  and  $e_{N,f}$  at the end of a simulation, color-coded by the rogue's lifetime (same as in the left panel). Shorter rogue lifetimes (red and orange) are strongly correlated with an increase in Neptune's  $a_N$  (caused by inward rogue scatterings which transfer control of the rogue to

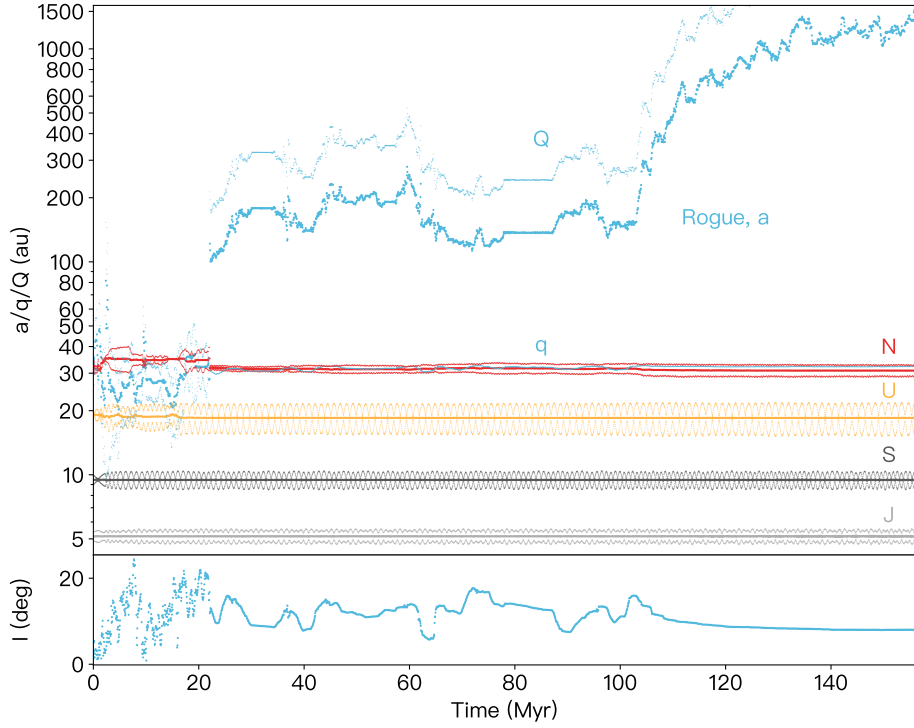


**Figure 6.11:** Same as Figure 6.10 but for a rogue planet initially placed outside the orbit of Neptune scattered outward. The rogue experienced strong interactions with Neptune and Uranus for the first 25 Myr, until a very close Neptune encounter ejected it to 100 au, after which the rogue is only coupled with Neptune for the next 130 Myr. Its  $a$  walks randomly with  $q$  just beyond 30 au. The rogue’s aphelion eventually reaches 3000 au.

the gas giants), whereas  $a_N$  decrements (by outward rogue scatterings) only occur for longer lifetime rogues (blue). In addition, because of gravitational interactions (with rogues and potentially other giant planets), at the end of the integrations, Neptune is more likely to be found with eccentricity higher than its initial value (denoted by the red cross in Figure 6.12) and much higher than its current value (denoted by the black cross)<sup>6</sup>.

---

<sup>6</sup>Although I started the integration with a  $e_N = 0.065$  Neptune, in the hope that the rogue could potentially circularize Neptune’s orbit to its modern value (which never works), rogue simulations

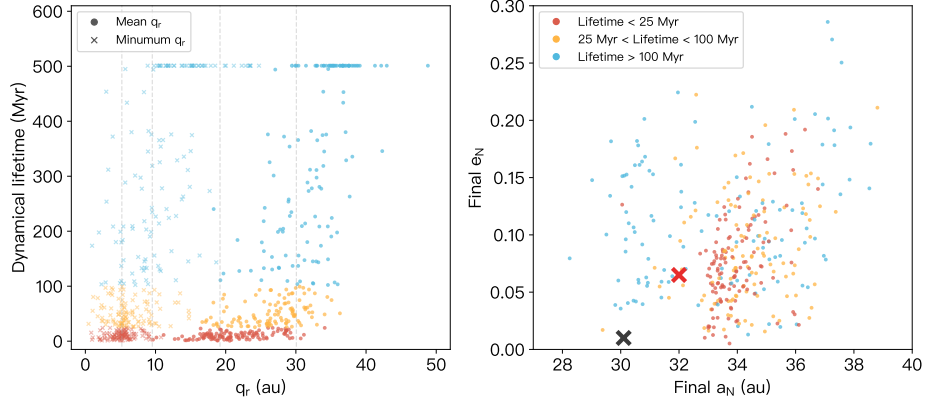


**Figure 6.12:** Dots in red, orange, and blue represent rogues with  $< 25$ ,  $< 100$ , and  $> 100$  Myr dynamical lifetimes, respectively. **Left panel:** Mean (dots) and minimum (crosses) perihelion distance ( $q_r$ ) of each planetary simulation (Sim-N-2) as a function of the rogue's dynamical lifetime. Locations of the four giant planets are denoted by gray dashed lines. **Right panel:** Final Neptune  $a_N$  and  $e_N$  at the end of each simulation (Sim-N-2). Red cross marks the initial Neptune orbit ( $a_{N,0} = 32$  au,  $e_{N,0} = 0.065$ ) used in simulations, whereas black cross denotes the real location of Neptune ( $a_N = 30.1$  au,  $e_N = 0.01$ ). This simulation ignore the dynamical damping of Neptune's eccentricity.

It is worth pointing out that the drastic semimajor axis change in Figure 6.11's rogue history (from 30 au to 100 au) is extremely rare for a Neptune-scattered body. After manually inspecting all evolutional histories, this is the only example displaying this level of  $a_r$  change caused by Neptune. Additionally, the short rogue presence time inside 100 au has the good attribute of potentially not overheating the cold classical belt. Thus, it is worth investigating whether or not such a 'lucky rogue' can keep the cold belt alive.

With GLISSE, I am able to understand the dynamical evolutions of thousands of test particles (which represent TNOs) under a certain planetary history. The methodology is summarized as follows: For a planetary evolution history considered worth studying (e.g., that of Figure 6.11), I reintegrated the exact same plan-

---

with a near-circular Neptune also tend to heat up its eccentricity to above the modern value.

etary initial conditions to generate a planetary lookup file that contains all planetary orbital elements at every lookup interval. The lookup file was then used as the planetary input to GLISSER, which then generates the Cartesian coordinates of each planet at every time step by interpolating the orbital elements (see Section 1.2.2 for details). GLISSER’s GPU algorithm can then compute the accelerations for test particles, and propagate them under the standard Wisdom-Holman MVS method (Wisdom & Holman, 1991) in parallel. Though the interpolation of planetary orbital elements brings extra errors to the integration, especially when the planet is fast evolving (such as being scattered or experiencing fast secular oscillation), I find when integrating with a reasonably large number of test particles and a relatively short lookup interval, the orbital distribution GLISSER produced is highly similar to those produced by a standard Solar System integrator, such as MERCURY (Chambers, 1999, see Figure 1.7 for comparison).

I used Figure 6.11’s planetary history as the input of a GLISSER integration. In this simulation, 3,000 test particles representing cold classicals were initialized from 40–50 au, with initial eccentricity  $e_0 < 0.001$  and inclination  $i_0 < 2^\circ$ <sup>7</sup>. They were integrated with the time step of 200 days until the ejection of the rogue planet at 157 Myr. Figure 6.13’s two panels show two orbital distribution snapshots at 27 Myr and at 157 Myr, respectively, in which green boxes on  $a - q$  and  $a - i$  panels roughly mark the allowable orbits for cold classicals.

The first snapshot was taken right after the rogue was scattered to  $\sim 100$  au, at which point the vast majority of initially cold objects had already been dislodged. This is presumably due to the gravities of both Neptune and the rogue. As shown in Figure 6.13, there was a period of several Myr when Neptune’s aphelion extended to 40 au, and the rogue’s aphelion transiently went as far as 100 au, because of their strong mutual interactions. The resultant secular forcing and gravitational scattering have overheated the cold belt, essentially expelling most primordial planetesimals out of the region. The heating and dislodging in the cold belt did not stop when the rogue jumped to 100 au and wandered between 100 to 200 au for the next 80 Myr. The second snapshot of Figure 6.13 shows that the rogue’s presence at  $a_r \approx 100\text{--}200$  au essentially cleared the cold belt, with only  $\approx 10$  (0.3%) particles

---

<sup>7</sup>Although a better way to initialize the cold belt is doing it on the free inclination space, I here generated their initial  $i_0$  with respect to the ecliptic for simplicity.

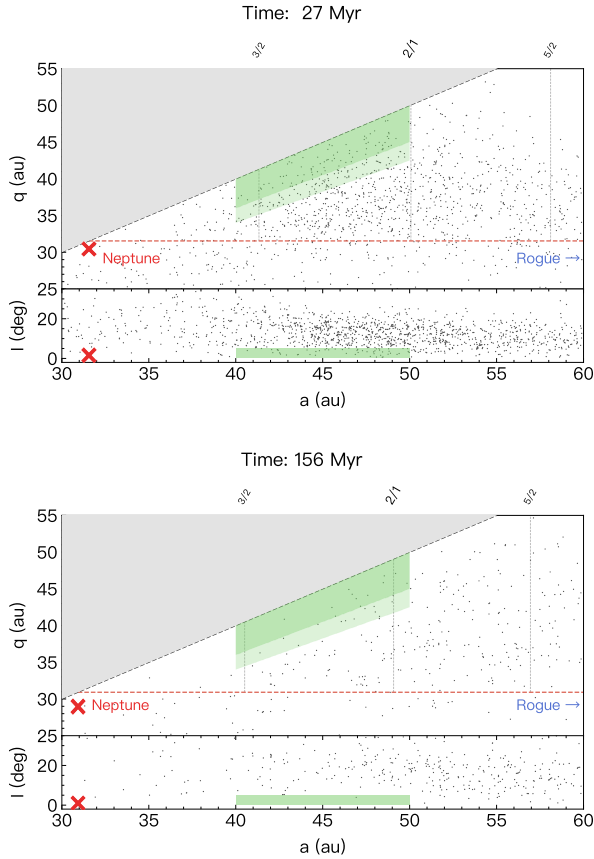


**Figure 6.13:** GLISSER simulation snapshots showing the destruction of the cold classical belt by a Neptune-scattered rogue. The two green regions on the  $a - q$  panel represent  $e < 0.1$  (dark shaded) and  $e < 0.15$  (light shaded), respectively, while the rectangular box on the  $a - i$  panel represents  $i < 5^\circ$ . They indicate the rough boundaries for cold classics. The red cross marks the elements of Neptune, whereas the rogue's location is beyond the plotted region (denoted by the blue right arrow). The red dashed line indicates where  $q = a_N$ . **Top:** The orbital distribution at 27 Myr, right after the rogue was scattered to  $\sim 100$  au. The vast majority of initially cold particles have been significantly heated in  $e$  and  $i$ . **Bottom:** The orbital distribution at the end of the 157 Myr, by which time the cold classical belt has been completely destroyed.

still present at  $e < 0.1$  (dark shaded green in the  $a - q$  panel) and a single particle at  $i < 5^\circ$  (shaded green in the  $a - i$  panel).

Even with such a ‘hand-picked’ rogue history where the planet’s presence at  $30 < a_r < 100$  au was intentionally avoided, a stable cold belt was not preserved. In other words, it is extremely unlikely that a Earth-mass planet had been scattered out by a Neptune with  $a_{N,0} \simeq 30$  au and traversed the primordial cold planetesimal belt without overheating or even destroying it. This conclusion is in agreement with numerical simulations carried out by Petit et al. (1999).

### 6.2.2 Rogues Scattered by Saturn

In the previous section, I have demonstrated that a Neptune-scattered Earth-scaled planet normally has two fates. It either gets scattered inward and coupled with Saturn/Jupiter, in which case its presence time at several hundred au is too short to detach Sednoids, or it wandered outward under mainly Neptune’s gravity, for a duration long enough that the cold classical belt would likely be overheated. In addition, Neptune’s interaction with this extra planet is also likely to heat up its own eccentricity (Figure 6.12), and additional dynamical friction (such as Neptune migrating through a planetesimal disk, see Section 4.3.2) is needed to account for its current low eccentricity.

This prompts us to consider an alternative route for the rogue planet. If the rogue cannot be scattered to large  $a$  by Neptune (and presumably not by Uranus either because of the similar scattering timescale as Neptune, see Table 3.1), can it first be scattered out by Saturn, and, when it reaches  $a$  of several hundred au, be coupled only with Neptune/Uranus and thus have enough time ( $\sim 100$  Myr) to produce Sednoids as we see today? This ‘perihelion transfer’ from a higher-mass planet, which scatters more intensely, to a lower-mass planet is not often seen in numerical simulations of test particles. Therefore, it is worth exploring whether a rogue rapidly scattered out by Saturn and then coupled with Uranus/Neptune could be produced through planet-planet interactions.

I thus created two sets of planetary simulations with four giant planets on their current orbits and two  $2M_\oplus$  rogues near Saturn. The goal is to see how often rogue-rogue interactions could decouple one of the rogues from Saturn. The first simula-

tion set (Sim-S-1) has the two planets on initially near-circular ( $e_{r,0} = 0$ ) orbits with  $a_{r,0} = 14$  au and 16 au (between Saturn and Uranus), while the second set (Sim-S-2) has them on  $e_{r,0} = 0.1$  orbits with  $a_{r,0} = 8$  au and 9 au (one inside and one outside the orbit of Saturn). Both set contains 360 independent simulations with randomized rogue phase angles. They were integrated until the ejection of either of the two rogue planets, and at the end of each simulation, orbital elements of the remaining rogue were recorded.

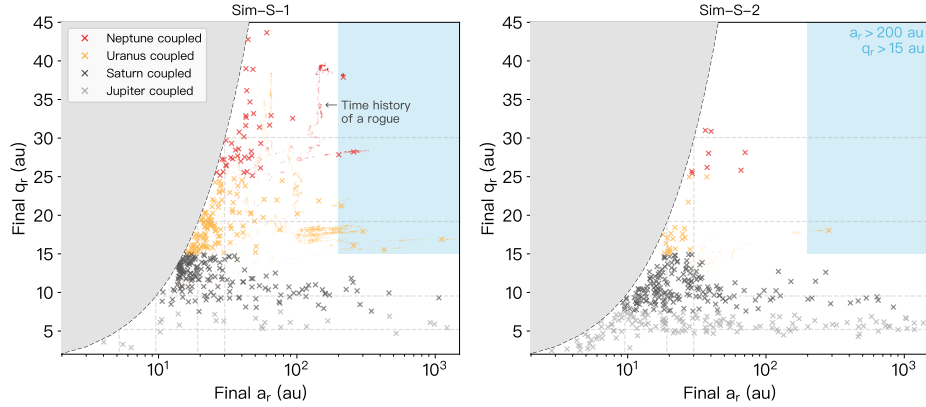


**Figure 6.14:** Final  $a_r$  and  $q_r$  of the remaining rogue planet when the other one was ejected in two  $2M_\oplus$  rogue simulations (left panel for Sim-S-1 and right panel for Sim-S-2). The rogues are color coded based on their final  $q_r$ , indicating the giant planet they coupled with at the end of the integration. The blue box represents  $a_r > 200$  au and  $q_r > 15$  au, which are the potentially desireable parameters to begin the stage of Sednoids creation. For a few rogues that ended up in the blue region, time histories of their orbits are also plotted with red or orange dots. The four horizontal and vertical dashed lines mark the semimajor axes and perihelia of the giant planets.

The median ejection times for the first of the two rogue planets are 2 Myr and 0.3 Myr for Sim-S-1 and Sim-S-2, respectively. Figure 6.14 displays the  $a_r - q_r$  location of the remaining rogue planet when the other one was ejected (left panel for Sim-S-1 and right panel for Sim-S-2). At the end of simulations, only 8/360 (2%) and 1/360 (0.3%) rogues ended up in the  $a_r > 200$  au and  $q_r > 15$  au (blue box), which I consider the desireable ‘starting’ region for a  $2M_\oplus$  planet to later produce

Sednoids. Figure 6.14 also shows the  $a_r - q_r$  evolutional histories of those rogues (dots in corresponding colors) that eventually made it to the blue box. It is clear that for these planets, the  $a$  raising from the giant-planet region to 200 au is due to Uranus and Neptune scatterings, as the rogue perihelia are not coupled with Saturn (denoted by orange and red crosses with  $q_r > 15$  au) for most of the time. The desireable detachment from Saturn or Jupiter scattering (denoted by gray crosses) does not seem to occur at large semimajor axes. Visually speaking, there is no direct path for the black and gray crosses to reach the blue region at  $a > 100$  au in Figure 6.14.

The planetary histories corresponding to the rightmost red cross in the left panel of Figure 6.14 is plotted in Figure 6.15, while that corresponding to the rightmost orange cross the right panel is plotted in Figure 6.16. As shown in Figure 6.15, the rapid  $a$  growth (< 10 Myr) of Rogue 1 is not mainly induced by Saturn scattering but (very rare) Neptune and Uranus scatterings, as several remarkable jumps in Rogue 1's  $a_r$  are all associated with sudden semimajor axis drops in Uranus (at  $\approx 1.1$  Myr) and Neptune (at  $\approx 1.9$  Myr and  $\approx 2.3$  Myr); these fast and large  $a_r$  changes rarely occur when the planet's perihelion is above 15 au. Figure 6.16 demonstrates the history of two rogues in one of the Sim-S-2 set. Both planets have their  $q_r$  between Uranus and Saturn for 8 Myr, until a Uranus scattering leads to a significant  $a$  jump in Rogue 1 and a set of Saturn encounters boost Rogue 2 in the next  $\approx 3$  Myr. Both the jump and the beginning of Saturn coupling occur at the same time and it is unclear if they are dynamically related. Again, the 8-Myr presence of Rogue 1 at  $a_r \approx 40$  au would almost certainly overheat the cold classical belt beyond its observed state (see Figure 6.8).

Both Figure 6.15 and Figure 6.16 demonstrate that the interaction of the two Earth-mass planets does not create perihelion decoupling. The speculated spontaneous ‘perihelion transfer’ of the rogue planet from Saturn to Uranus/Neptune is unlikely to occur at  $\sim 100$  au semimajor axis, in models where the giant planets are initially on their current orbits and not migrating. This is likely because the volume of space is simply so large that rogue-rogue encounters are too unlikely. Therefore, I conclude that the production of a large- $a$  Saturn-decoupled planet is a low-probability event in pure N-body planetary simulations.

However, two important factors that were not modeled in the simulation sets are

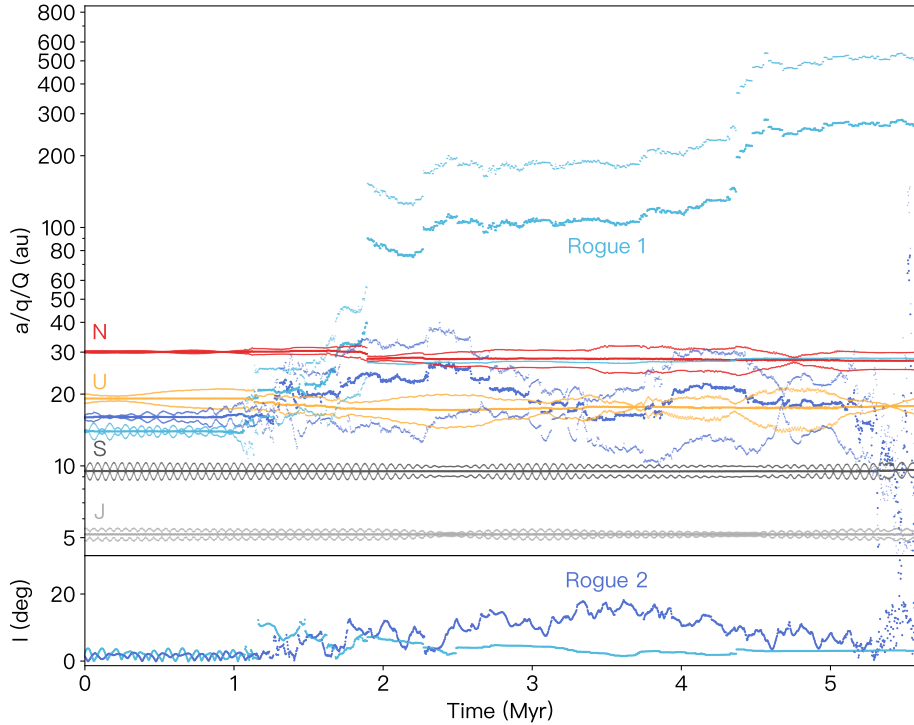


**Figure 6.15:** Planetary evolution histories of the four giant planets and two scattering rogue planets, initially placed at  $a_{r,0} = 14$  and 16 au (Sim-S-1). At the end of the simulation, the remaining planet (light blue, Rogue 1)'s end location corresponds to the rightmost red cross in Figure 6.14's left panel. Despite being started near Saturn, Rogue 1's rapid  $a$  growth is mostly related to scatterings at  $15 < q_r < 30$  au, not associated with Saturn's gravity. Rogue 2 experienced chaotic movement between Saturn and Neptune for 5 Myr until it coupled with Jupiter, leading to its ejection.

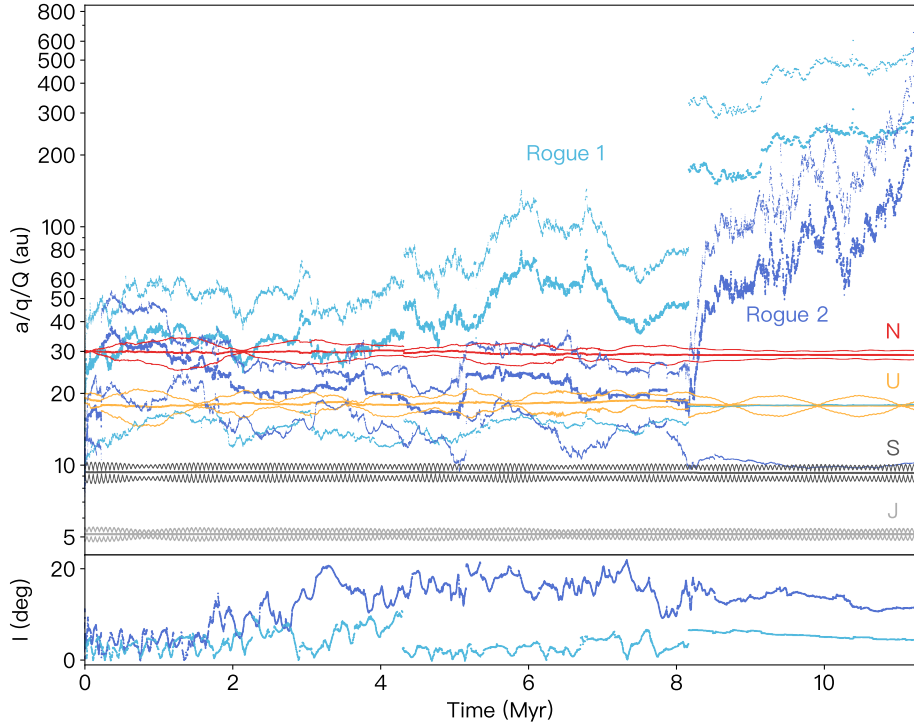


**Figure 6.16:** Same as Figure 6.15 but the two planets were initialized at  $a_{r,0} = 8$  and 9 au (Sim-S-2). The remaining Rogue 1’s end location corresponds to the rightmost orange cross in Figure 6.14’s right panel. At the end of Rogue 2’s ejection, Rogue 1 reached  $a_r > 200$  au and  $q_r \sim 20$  au, but its 8-Myr presence at  $a_r \approx 40$  au would likely overexcite the cold classical belt (see Figure 6.8).

the migration of giant planets and planetary instability. Due to gravitational interactions with the gas disk, giant planets can rapidly migrate several au in timescale of a million year (Goldreich & Tremaine, 1980; Lin & Papaloizou, 1986; Lissauer & de-Pater, 2013; Armitage, 2020). Subsequently, scattering of an outer *planetesimal* disk would also result in 5–10 au outward migration in Neptune and Uranus semimajor axes, with a timescale between  $\sim 10$  to  $\sim 100$  Myr (e.g., Nesvorný, 2018). Moreover, planetary instability models (for example, the ‘Nice model’ proposed by Morbidelli et al., 2005; Tsiganis et al., 2005; Gomes et al., 2005a) have provided so-

lutions for various puzzles, including the current location of giant planets, the Late Heavy Bombardment (LHB), and small body orbital distributions in the inner Solar System. It is very unclear that how planetary instability and migration would affect the production of the rogue planet, and investigating this topic would require a deep understanding of the planet-gas disk interactions and a thorough numerical exploration in the instability and migration. Therefore, I only present preliminary planetary simulations, as further exploration is beyond the scope of my thesis. Nevertheless, I speculate on a few scenarios that may have the potential to address the timescale difficulty. They are:

1. The rogue got scattered out very quickly and subsequent inward migration of giant planets led to Saturn decoupling.
2. The rogue got scattered out very quickly and subsequent interaction with the gaseous protoplanetary disk (or the outer planetesimal disk) raised its perihelion to near Uranus/Neptune. As far as I'm aware, the dynamical interaction between a protoplanet disk with an early scattered large- $a$  and large- $e$  planet (presumably with aphelion beyond the outer edge of the disk) is not studied in literature<sup>8</sup>.
3. The rogue is a natural product of planetary-instability models when extra Earth-mass cores are considered. In the original Nice model (Tsiganis et al., 2005), Uranus and Neptune were initially formed within 18 au and got scattered outward (mainly by Saturn), which further triggered subsequent migration in the planetesimal disk. So far, only additional ice giant(s) have been simulated in instability models (Thommes et al., 1999; Nesvorný, 2011; Nesvorný & Morbidelli, 2012; Batygin et al., 2012). It is unclear whether a Saturn-decoupled large- $a$  planet can be produced in planetary-instability models.

Hence, it would be worthwhile to investigate in future studies whether the rogue planet is consistent with any of the above scenarios or any other plausible scenarios. In the next section, I will shift my focus from the creation of the rogue onto the

---

<sup>8</sup>However, Kretke et al. (2012) investigated the dynamical evolutions of TNOs inside the protosolar nebula to constrain its size.

dynamical sculpting of the distant Kuiper Belt by this additional planet. Instead of integrating test particles with a rogue history from its birth in the planet-formation region to its ejection, I assume the rogue is already at large  $a$ , with  $q$  coupled to Uranus or Neptune and generally scattered outward. This allows me to explore the desireable rogue parameters at large- $a$ , which can be used in planetary formation simulations to further assess the probability of making such a planet.

### 6.3 GLISSER Simulations with a Rogue Planet

In Section 6.1, I established with analytically-computed constraints that the rogue planet capable of making Sednoids would most probably be a super Earth coupled with Uranus or Saturn (see Figure 6.8). However, these constraints were obtained assuming the rogue has a fixed orbit, as opposed to a more realistic scenario where it experiences planetary scatterings and random walks in semimajor axis. The dynamical effect of a rogue with time-varying  $a_r$  can be better understood through large-scale numerical simulations, in which test particles feel gravitational pulls from both the giant planets and the wandering rogue planet.

#### 6.3.1 Reference Simulations

Before showing results from my rogue planet simulations, it is important to have in mind what the four giants can already do. For example, in Chapter 5, I demonstrated the rogue’s role in populating  $a = 50\text{--}100$  au resonances and the detached TNOs by comparing the reference simulation (with just the giant planets) and a rogue planet simulation. Figure 5.1 only displays orbital distributions from 50 to 100 au. To help the reader understand what the current Solar System can do to the larger- $a$  region, I illustrate the same reference simulation to  $a = 1500$  au in Figure 6.17.

Test particles in the high- $q$  region (defined as  $q > 38$  au in this work) are highlighted in blue. Below  $a < 200$  au, Kozai mechanisms inside neptunian mean-motion resonances (Gomes et al., 2005b) play significant roles in lifting TNO perihelia, which is studied in Chapter 5. Beyond 200 au, neptunian resonances do not seem to effectively detach TNOs from the scattering disk, and the 22 TNOs with  $a > 200$  au and  $q > 38$  au (listed in Table 4.1 and marked with dark red crosses in Figure 6.17) require an emplacement mechanism.

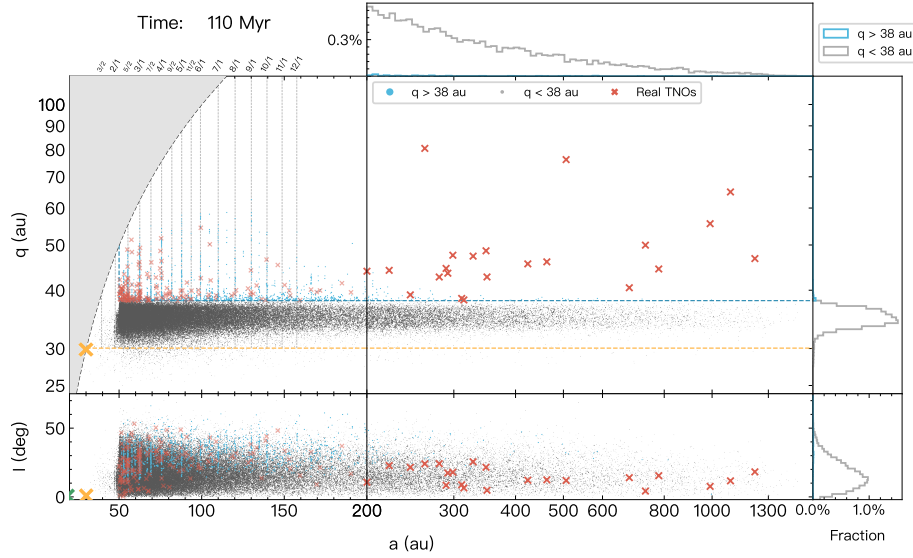


**Figure 6.17:** Same  $a$ ,  $q$ ,  $i$  orbital distributions as in Figure 5.1 but replotted in a larger  $a$  range.  $q < 38$  au and  $q > 38$  au particles are color coded in black and blue, respectively. All detected  $q > 38$  au TNOs are marked by red crosses, whereas Neptune is marked by the orange cross. The orange and blue dashed lines indicate  $q = a_N$  and  $q = 38$  au, respectively, and major neptunian n:1 and n:2 resonances are denoted by vertical dashed lines. The three side panels show the  $a$  (top),  $q$  (upper right), and  $i$  (lower right) histograms for  $a > 200$  au particles, with blue and gray lines corresponding to the low- $q$  and high- $q$  subsamples. The percentage represents the number of test particles in each bin as a fraction of the total remaining particles. This simulation contains 50,000 initial test particles.

It should be pointed out that the GLISSER simulation producing Figure 6.17 had a synthetic early scattering disk with particles uniformly distributed in  $q$  from 33 to 38 au (for details of this simulation, see Chapter 5). This is a rather simplified model, as I have shown in Chapter 3 that particles with higher initial perihelia would experience weaker Neptune scatterings. In addition, there are dynamical arguments that Neptune probably migrated  $\sim 20$  au to its current location at 30 au (Malhotra, 1993; Nesvorný, 2015a; Nesvorný et al., 2016; Nesvorný, 2018, 2021), and the

early scattering disk was likely formed as a result of continuous gravitational scatterings in the outer planetesimal disk as Neptune's orbit expanded. Consequently, the synthetic scattering disk with presumed (though still reasonable)  $a$ ,  $q$ , and  $i$  distributions is no longer suitable if one attempts to explore the rogue-planet scenario in the context of Neptune and Uranus migration. This is to say, to better capture the constant-changing nature of an early scattering disk, one needs to perform a ‘primordial’ simulation with Neptune migrating through an initial near-circular and co-planar planetesimal disk, with heliocentric distance  $< 33$  au.

With the additional REBOUNDX package (Tamayo et al., 2019), I can directly add migration forces to a REBOUND simulation to induce exponential migration from an initial  $a_0$  to a final  $a_f$  (see Section 4.3 for details). The migration of Neptune<sup>9</sup> can be modeled as a two-stage eccentric migration with  $\tau_1 = 30$  Myr and  $\tau_2 = 100$  Myr; this set of parameters is found to be better at recreating observed inclination profile of implanted TNOs (Nesvorný, 2015a), and have been thoroughly investigated in ‘grainy migration’ models (Nesvorný & Vokrouhlický, 2016; Nesvorný et al., 2016; Kaib & Sheppard, 2016; Nesvorný, 2018). I note in passing that an early eccentric stage of Neptune (with  $e_N \sim 0.1$ ) can better produce the low- $e$  and low- $i$  orbits at 50–60 au (Nesvorný, 2021).

Figure 6.18 shows a dynamical history of the four giant planets in a two-stage eccentric migration model that I produced. Uranus and Neptune were started at  $a_{U,0} = 15.4$  au and  $a_{N,0} = 24$  au, respectively. In the fast migration stage, Neptune migrated with  $\tau_1 = 30$  Myr, until a sudden eccentricity boost at 15 Myr prolonged the e-folding timescale to  $\tau_2 = 100$  Myr (Nesvorný & Morbidelli, 2012; Nesvorný & Vokrouhlický, 2016). Similar increments in Neptune’s eccentricity are often seen in migration simulations when Uranus and Neptune cross their mutual 2:1 mean-motion resonance<sup>10</sup>. Subsequent Neptune-planetesimal interaction in the disk can further damp its eccentricity and inclination to current values. Nesvorný (2021) pointed out that Neptune’s eccentricity boost can also be caused by the ejection of a fifth ice giant.

The planetary history displayed in Figure 6.18 was input to GLISSE to demon-

---

<sup>9</sup>The planetesimal-driven migrations for Saturn and Jupiter are small enough (of order a tenth of an au) to be disregarded in the modeling.

<sup>10</sup>Specially, among 200 independent simulations, 17% have  $e_N > 0.05$  and 5% have  $e_N > 0.1$ .

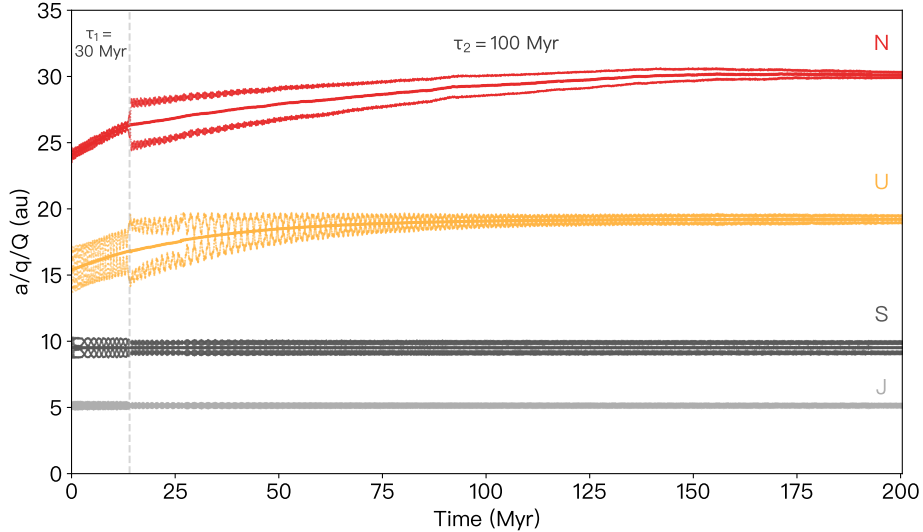


**Figure 6.18:** Dynamical history of the four giant planets in a two-stage eccentric migration simulation. Uranus and Neptune were initially at  $a_{U,0} = 15.4$  au and  $a_{N,0} = 24$  au, respectively. The migration e-folding timescales are  $\tau_1 = 30$  Myr for the first 15 Myr and  $\tau_2 = 100$  Myr for the rest of the simulation. The sudden growth in Neptune’s eccentricity (denoted by the vertical dashed line and probably caused by the mutual 2:1 resonance between Uranus and Neptune) is often seen in rogue planet simulations.

strate the effect of Neptune’s migration on the small body population. The initial planetesimal disk (that may have driven Neptune and Uranus migration) contains 50,000 massless particles uniformly distributed from  $a_0 = 24.5$  to 33 au (for the outer edge of the disk, see Section 4.3.2) with  $e_0 < 0.1$  and  $i_0 < 5^\circ$ . Another 2,000 particles (with  $42 < a_0 < 47$  au,  $e_0 < 0.01$ , and  $i_0 < 0.5^\circ$ ) representing the unexcited primordial cold belt are also included. The  $a, q, i$  orbital snapshot at 200 Myr is plotted in Figure 6.19, with black dots denoting final locations of the main planetesimal disk and orange dots the same for the initial cold belt.

This reference migration simulation is largely consistent with previous findings:  
1) The cold classical belt was (as expected) heated by the sweeping of the 2:1 resonance, with some cold classicals even removed from their birth region. Neverthe-

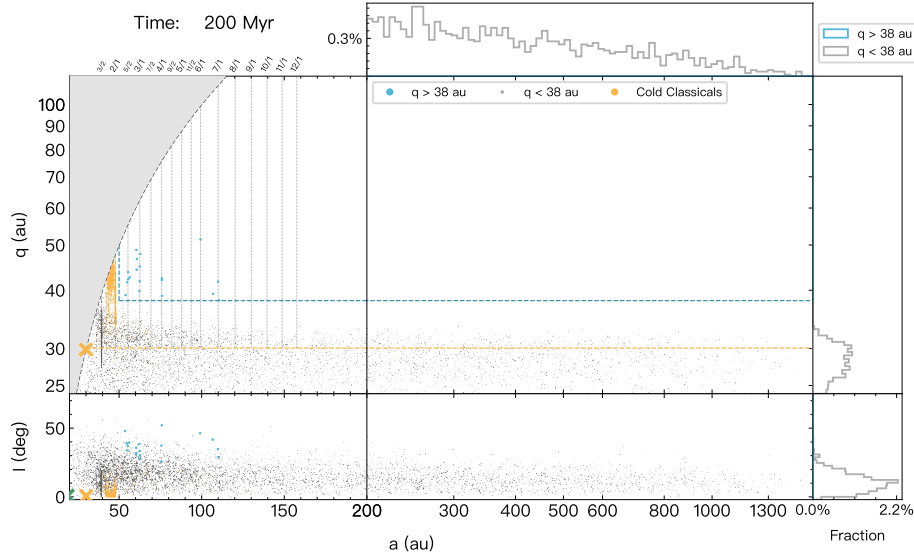


**Figure 6.19:**  $a$ ,  $q$ ,  $i$  distributions at 200 Myr of the reference migration simulation, corresponding to the planetary history shown in Figure 6.18. Black and orange dots represent particles from the massive planetesimal disk initialized inside 33 au and those from the cold classical belt, respectively. This shows that Neptune's migration (along with its resonances) is capable of explaining some detached TNOs inside  $\sim 100$  au, but does not create any orbital detachment at  $a > 200$  au (similar to Figure 6.17's result).

less, nearly half (971/2000) of the cold-belt particles still remain unheated (defined as  $e < 0.15$  and  $i < 5^\circ$ ) at the end of the simulation. 2) The slow migration of Neptune can account for the observed  $\sim 15^\circ$  inclination width in the implanted TNOs. 3) Some detached or high- $q$  resonant objects are created within  $\sim 100$  au through the Kozai mechanism inside Neptune MMRs <sup>11</sup>. 4)  $a > 200$  au particles are not found in  $q > 35$  au. Simply put, the primordial migration simulation produces an early scattering disk with  $q$  more closely attached to Neptune's orbit, and detached

<sup>11</sup>In my reference migration simulation, the implantation efficiency for  $50 < a < 100$  au and  $q > 34$  au TNOs is  $84/50000 \approx 1.7 \times 10^{-3}$ , close to the  $2 \times 10^{-3}$  efficiency estimate in Nesvorný et al. (2016). This level of implantation efficiency is probably needed to account for the number estimation of detached objects in Beaudoin et al. (2023).

objects are not made at several hundred au. Therefore, there is a compelling reason to incorporate additional perturbers, such as the rogue planet, to explain the observed distant Kuiper Belt.

### 6.3.2 Uranus-coupled Distant Rogue Planet

To begin with, I explore the possibility that the rogue planet (at large semimajor axis) was dominantly coupled with Uranus as it scattered. The first planetary simulation has migrating Uranus and Neptune, and a  $1M_{\oplus}$  rogue initialized at  $a_{r,0} = 100$  au,  $q_{r,0} = 14$  au, and  $i_{r,0} = 20^{\circ}$  (Sim-U-Mig-1). The rogue was assumed to not experience planetesimal-driven migration; at  $\sim 100$  au, the close encounter frequency with planetesimals becomes so rare that it barely affects the rogue planet's orbit. The planetary history generated by this set of initial conditions <sup>12</sup> is shown in Figure 6.20, and the corresponding GLISSER simulation (with 400,000 particles in a planetesimal disk outside the initial orbit of Neptune from  $a_0 = 24\text{--}30$  au) is plotted in Figure 6.21.

This specific  $1M_{\oplus}$  rogue spent the first  $\sim 60$  Myr between  $a_r = 100$  au to 200 au and the rest  $\sim 60$  Myr at  $a_r > 200$  au before ejection at  $t \approx 120$  Myr. The secular effect during the first  $\sim 60$ -Myr presence is evident in Figure 6.21, where low- $i$  detached TNOs are abundantly created below  $a < 200$  au, outnumbering the high- $i$  detached in the same orbital range. This is presumably not in agreement with the real detached TNO detections from  $75 < a < 150$  au, most of which have  $i \gtrsim 20^{\circ}$  despite the fact that low- $i$  objects are easier to find when taking observational biases into account. This implies that  $\sim 60$  Myr presence of the rogue planet at  $a_r < 200$  au would likely result in an orbital distribution that does not match the observed one, and distant rogues started at even larger semimajor ( $a_r \gtrsim 200\text{--}400$  au) seem more desireable.

Furthermore, Figure 6.21 also demonstrates the difficulty of producing TNOs with  $q > 60$  au perihelia by this Uranus-coupled planet. The three Sednoids and the two  $a > 1000$  au high- $q$  TNOs are not generated from this simulation, presumably

---

<sup>12</sup>Even when started at  $a_r$  of 100 au, the rogue still has a reasonable chance to be scattered inward, in which case the cold belt will likely be destroyed. Therefore, with the cold-classical constraint in mind, I manually selected planetary histories of outward scattering rogues and only integrated those cases with test particles.

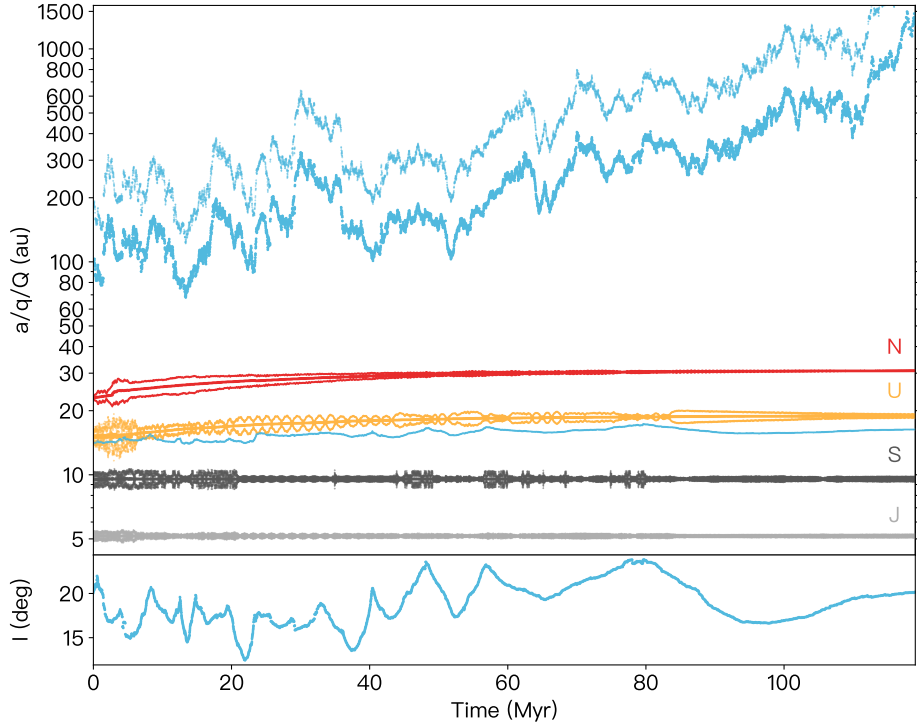


**Figure 6.20:** Planetary history of the first Uranus-coupled rogue planet simulation (Sim-U-Mig-1). The test particle simulation related to this history is shown in Figure 6.21.

due to the competing effect of Uranus and Neptune on the rogue’s secular dynamics. Upon close inspection of the orbital evolutions of  $q_0 \simeq 15$  au rogues, I find almost all of them have constant longitudes of perihelia  $\varpi_r$ . This would likely suppress its  $q$ -lifting ability (see Equation 6.10) due to faster differential precessions between TNOs and the rogue. However, the inclination distribution of the  $a > 200$  au detached TNOs seems in line with the known TNOs, and an  $i \sim 20^\circ$  scattering planet does not significantly alter the inclination structure of distant objects (compared to the scattering disk in the same  $a$  range).

In light of the constraint of not overproducing the  $a = 75\text{--}200$  au low- $i$  detached, I carried out another set of simulations (Sim-U-Mig-2) with a  $2M_\oplus$  rogue initialized at  $a_{r,0} = 400$  au,  $q_{r,0} = 15$  au, and  $i_{r,0} = 25^\circ$ . The exit condition of each

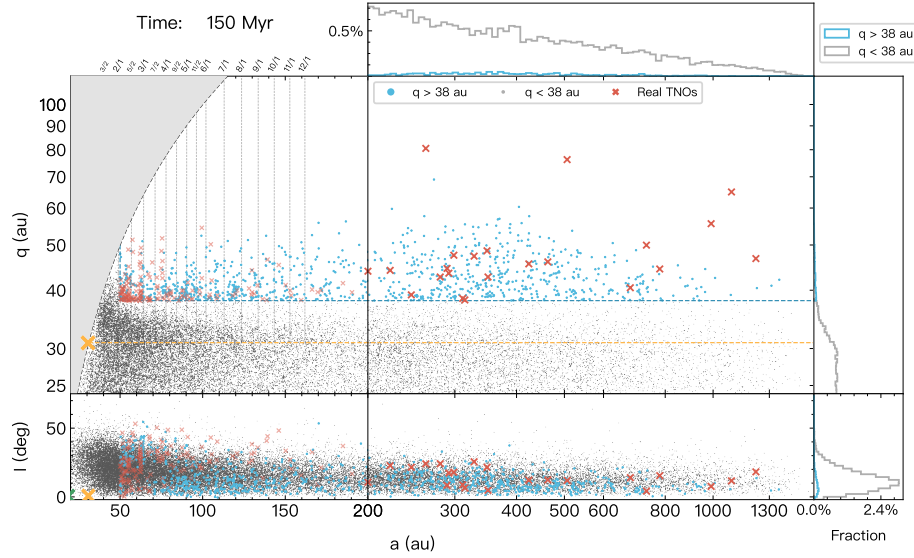


**Figure 6.21:** Same as Figure 6.19, but for the  $a$ ,  $q$ ,  $i$  distributions at 150 Myr of Sim-U-Mig-1, corresponding to the planetary history in Figure 6.20. This simulation contains 400,000 initial test particles.

simulation is either 1) the rogue's ejection at  $a = 1500$  au, or 2)  $>5$  Myr cumulative presence time within  $a_r < 200$  au. 200 simulations were integrated, and the median survival time of the rogue is merely  $\sim 20$  Myr due to the larger  $a_{r,0}$ . I plot the history of the rogue with the longest survival time of 110 Myr (99% percentile) in Figure 6.22, and the corresponding particle simulation in Figure 6.23. Note that this GLISSER simulation only contains 50,000 particles, nearly an order of magnitude lower than the particle number in Figure 6.21. This decision was mainly made for the trade-off between statistics and efficiency: A 50,000-particle GLISSER simulation normally finishes in a day, and a 500,000-particle simulation takes about a week. Though with poorer statistics, a 50,000-particle simulation allows me to 'take a peek' at the general distribution related to a particular rogue history without spending too much time and computing resources. If a simulation is deemed to be promising, I then re-execute it with an order of magnitude more particles to get a model with better statistics.

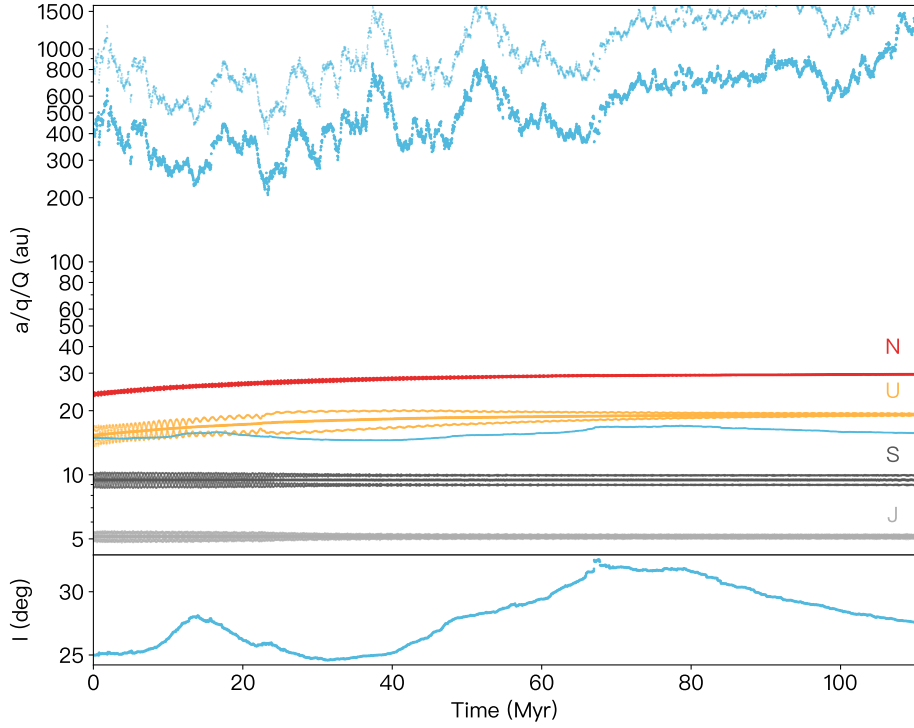


**Figure 6.22:** Planetary history of the second Uranus-coupled rogue planet simulation (Sim-U-Mig-2). The test particle simulation related to this history is shown in Figure 6.23.

As shown in Figure 6.23, this rogue planet (though with a relatively longer presence time compared to other Uranus-coupled planets in the same set) still has trouble creating the  $q > 60$  au Sednoids. Moreover, due to the rogue's higher inclination ( $25\text{--}35^\circ$ ), the inclination profile of large- $a$  detached is more heated than in Sim-U-Mig-2, with a small fraction reaching  $i > 50^\circ$ . In the  $a < 200$  au region, nearly no detached particles are created, in major contrast to both the reference migration simulation (Figure 6.19) and Sim-U-Mig-1 (Figure 6.23). Statistically, the  $50 < a < 100$  au and  $q > 35$  au implantation efficiency for this simulation is  $\sim 5 \times 10^{-4}$ , four times lower than the  $\sim 2 \times 10^{-3}$  efficiency in the reference simulation and the  $\sim 3 \times 10^{-3}$  efficiency in Sim-U-Mig-1. The reasons are as follows:

1. Compared to the planetary histories in the reference simulation and Sim-U-

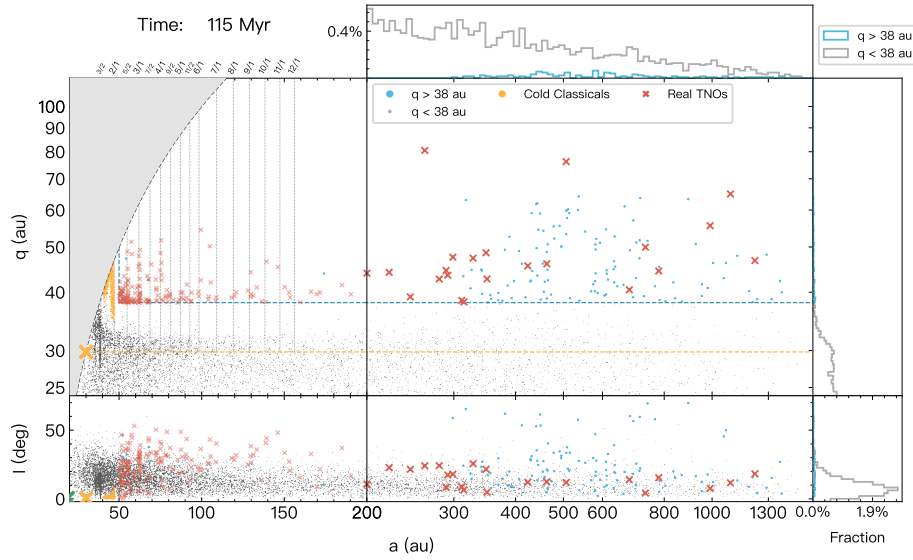


**Figure 6.23:**  $a, q, i$  distributions at 115 Myr of Sim-U-Mig-2, corresponding to the planetary history in Figure 6.22. This simulation contains 50,000 initial test particles.

Mig-1, Sim-U-Mig-2 doesn't have a eccentric migration phase of Neptune (Figure 6.22). A temporary eccentric phase is likely an important component of Neptune migration, which helps populate the low- $i$  detached objects within  $a < 60$  au (Nesvorný, 2021). As stated above, the rogue planet unlikely stayed around  $a \sim 100$  au for longer than 10 Myr, otherwise it would overproduce low- $i$  detached TNOs with  $75 < a < 200$  au (Figure 6.21) and potentially heat the classical belt. Consequently, the rogue is probably not the cause for  $a < 60$  au low- $i$  detached TNOs, and the eccentric Neptune migration would still be needed.

2. Chapter 5 demonstrated the rogue's capability of helping populate the resonant and detached objects in  $50 < a < 100$  au. However, the synthetic scattering disk used in Chapter 5 has a relatively wide initial  $q$  distribution from 33 au to 37 au, and the rogue collaborates with neptunian resonances more effectively if the early scattering disk already consists of objects with

$q \sim 35$  au. Eccentric Neptune migration is able to satisfy this constraint.

3. Eccentric Neptune migration is a natural outcome of gravitational interactions between Uranus and Neptune, and is compatible with the presence of a third scattering planet. Both planetary simulations related to Figure 6.18 and Figure 6.20 have Neptune started at zero eccentricity, and the temporary eccentric phases are directly caused by the gravitational interactions between the three planets <sup>13</sup>.

In addition to the two simulations shown in Figures 6.21 and 6.23, I also carried out one more run with a different rogue history ( $2M_{\oplus}$  Uranus-coupled). The three most distant Sednoids are still not created. Therefore, I conclude through numerical simulations that Uranus-coupled ( $q \sim 15$  au) Earth-mass planets have difficulty sufficiently detaching TNOs from the scattering disk, presumably due to its fast-changing semimajor axis and relatively short dynamical lifetime.

### 6.3.3 Neptune-coupled Distant Rogue Planet

Objects with  $q$  near 30 au generally survive longer than those with  $q$  near 15 au. While in my analytical estimates, Neptune and Uranus on their current orbits should have similar scattering timescales (see Table 3.1), in reality objects coupled with Uranus also traverse Neptune's orbit, shortening the timescale of scattering. In (Duncan et al., 1987), the numerically-measured diffusion timescale for  $q \sim 15$  au is an order of magnitude shorter than that for  $q \sim 30$  au, which explains why few simulations in Sim-U-Mig-2 have rogues that survived  $>100$  Myr.

I thus created two simulations to explore the general dynamics imposed by a Neptune-scattered rogue planet. This first set of planetary simulations (Sim-N-Mig-1) has a  $2M_{\oplus}$  rogue initialized at  $a_{r,0} = 400$  au,  $q_{r,0} = 33$  au, and  $i_{r,0} = 10^\circ$ , while the second simulation set (Sim-N-Mig-2) has  $a_{r,0} = 400$  au,  $q_{r,0} = 32$  au, and  $i_{r,0} = 15^\circ$ . The exit condition is the same as in Sim-U-Mig-2. The median rogue survival times are 160 Myr and 200 Myr for the two simulations, significantly longer than Uranus-coupled rogues and in line with the analytical estimate. Two

---

<sup>13</sup>Although Figure 6.18 only shows the history of the four giants, the corresponding planetary run actually has a rogue planet interacting with Neptune (but not plotted or included in the test particle simulation of Figure 6.19).

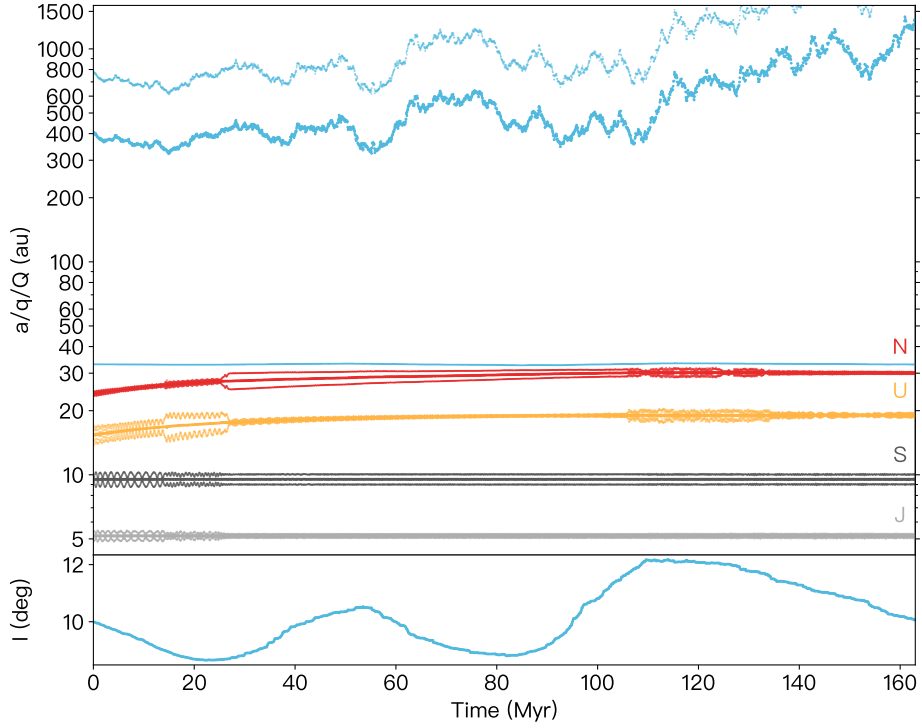


**Figure 6.24:** Planetary history of the first Neptune-coupled rogue planet simulation (Sim-N-Mig-1). The test particle simulation related to this history is shown in Figure 6.25.

selected planetary histories (which are typical evolutions in both sets) are plotted in Figures 6.24 and 6.26. They were further integrated along with 50,000 test particles (shown in Figures 6.25 and 6.27) to understand the resultant dynamical sculpting in the distant Kuiper Belt.

Figure 6.24 shows a rogue first wandering at  $a_r \sim 400$  au for 100 Myr, and beyond 600 au for the rest of the simulation. Neptune's eccentricity jumped to  $e_N \sim 0.07$  at 25 Myr and was then damped to its current value due to dynamical frictions in the planetesimal disk. The timescales of the eccentricity damping and the inclination damping (though the latter is not as important) are set to be the same as the e-folding time of the migration (Nesvorný, 2018). The history plotted in Figure 6.26 demonstrates very similar evolutional behaviours, with the rogue

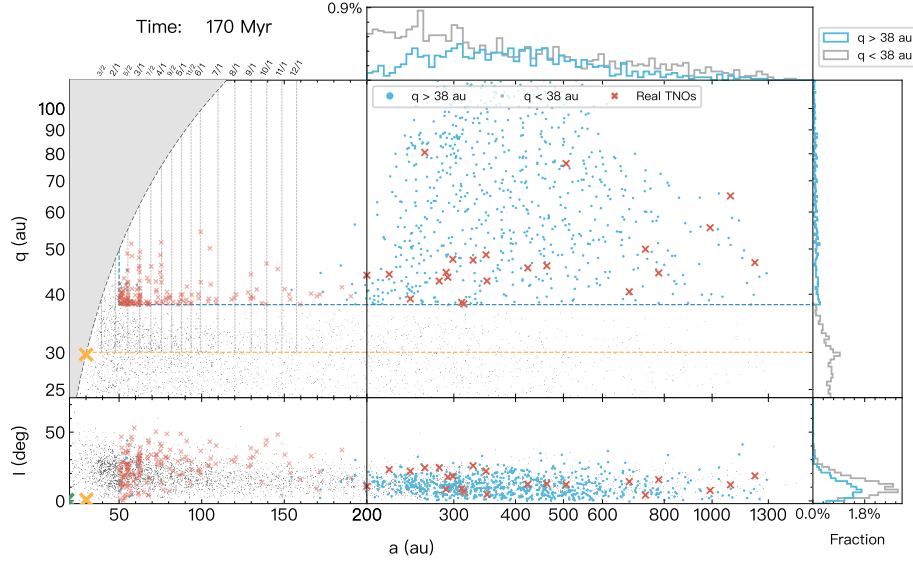


**Figure 6.25:**  $a, q, i$  distributions at 170 Myr of Sim-N-Mig-1, corresponding to the planetary history in Figure 6.24. This simulation contains 50,000 initial test particles.

hovering between 400 au to 100 au for near 200 Myr and Neptune having an early eccentric state during its migration.

The TNO orbital distributions sculpted by the two rogues (with different dynamical histories) also look strikingly similar. Both Figure 6.25 and Figure 6.27 have a prominent detached population beyond  $\sim 200$  au, covering all orbits of the observed  $a > 200$  au detached objects. In the  $75 < a < 200$  au region, few low- $i$  detached TNOs are created, due to the rogue's non-presence inside 200 au. Although it seems that the simulated distribution doesn't have enough  $q > 38$  au objects within 200 au, this is likely due to the small particle number (50,000) I used in these two simulations. For a dynamical process that has the implantation effectively as low as  $\sim 2 \times 10^{-3}$  (Nesvorný et al., 2016), at least an order of magnitude more particles are needed to create a distribution that can be compared against detections.

Furthermore, both simulations demonstrate an inclination profile of distant objects in line with observations. The rogue-lifted TNOs largely preserve their incli-

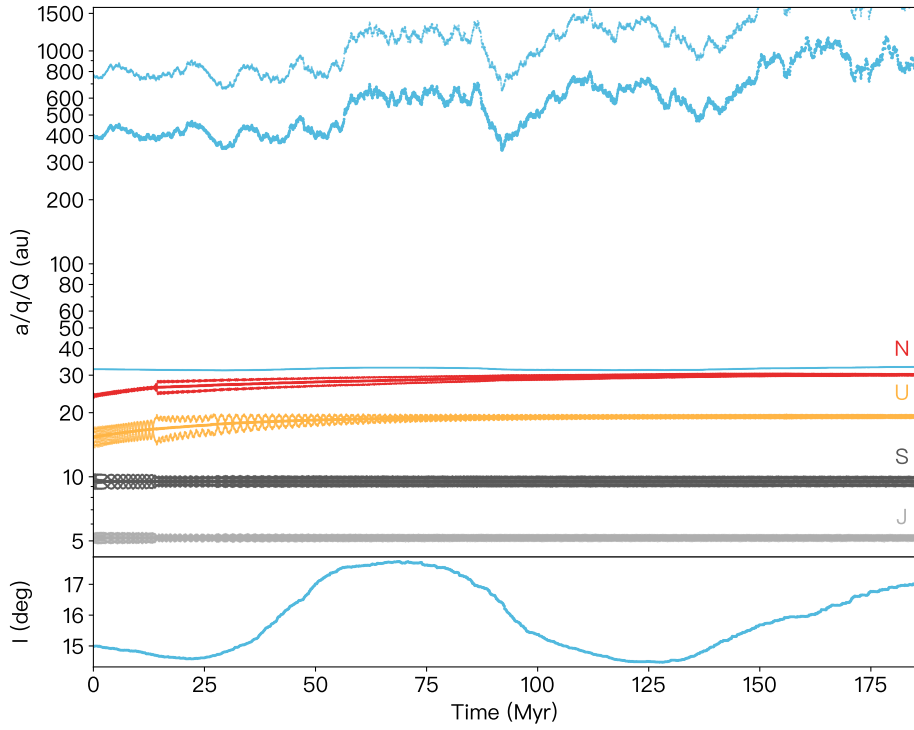


**Figure 6.26:** Planetary history of the second Neptune-coupled rogue planet simulation (Sim-N-Mig-2). The test particle simulation related to this history is shown in Figure 6.25.

nation structure (blue histograms in the lower right panel) as in the scattering disk (gray histograms). However, Figure 6.23 shows that if the rogue’s average  $i$  exceeds  $25^\circ$ , more inclined TNOs will be produced at large semimajor axis, which will presumably violate the observational constraint.

To summarize, a Neptune-scattered distant planet, if started at  $\sim 400$  au and  $i < 25^\circ$ , is very promising at creating all the discovered large- $a$  detached TNOs, while not overproducing low- $i$  detached TNOs at  $a \sim 100$  au. Alternatively stated, this situation would mean a rogue that gets to large  $a$  quickly. The same simulation shown in Figure 6.27 will thus be reintegrated with a larger number particles, in order to be compared against observations.

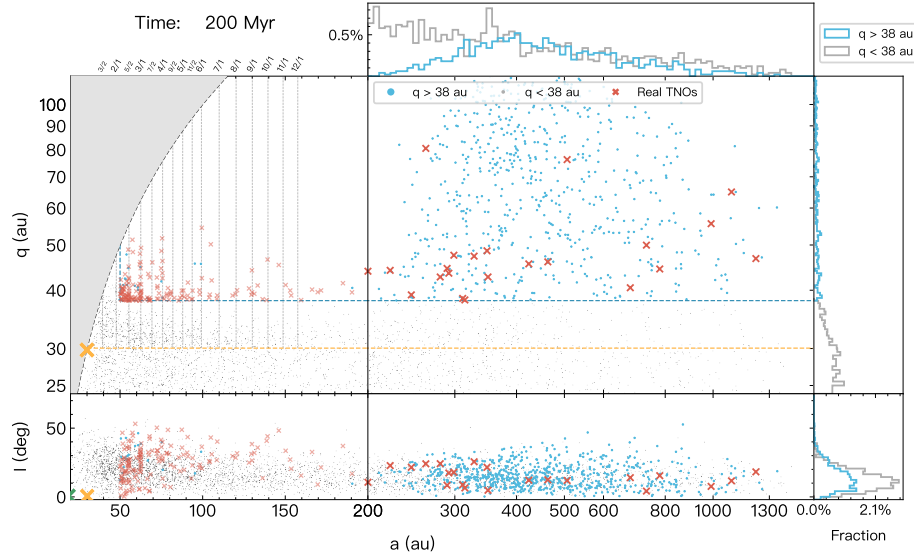


**Figure 6.27:**  $a$ ,  $q$ ,  $i$  distributions at 200 Myr of Sim-N-Mig-2, corresponding to the planetary history in Figure 6.26. This simulation contains 50,000 initial test particles.

## 6.4 The Rogue Planet Model

The most promising distant TNO orbital distribution (Figure 6.27) from my preliminary experiments in Section 6.3 is produced by the Neptune-scattered rogue planet shown in Figure 6.26. To further study this distribution with better statistics and compare it against observations, I re-performed the GLISSER simulation with the same planetary history and 500,000 (an order of magnitude more) particles representing the massive planetesimal disk ( $25.5 < a < 33$  au). I also added 2,000 near-circular and co-planar particles initialized in the cold belt ( $42 < a < 47$  au). The test particle simulation was first integrated to 180 Myr (similar to the one in Figure 6.27) with the presence of the additional planet, and further eroded to 4 Gyr to obtain a present-day distribution.

At the end of the 4 Gyr simulation, 10,561/500,000 (2%) of the outer-disk particles and 1,139/2,000 (57%) of the initially cold-belt particles remain in the Solar System. I carried out another 10-Myr long integration for all the remaining ones to

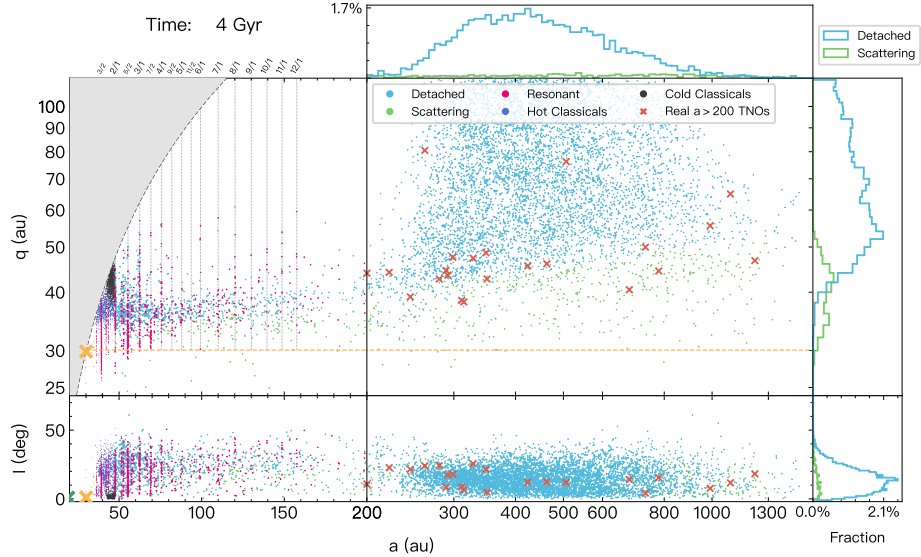


**Figure 6.28:**  $a$ ,  $q$ ,  $i$  distributions sculpted by the rogue planet in Figure 6.24 for  $\sim 200$  Myr and further eroded to 4 Gyr. Particles are color-coded based on their dynamical classes at the end of the integration, with blue representing the detached, green the scattering, pink the resonant, dark blue the hot classicals, black the hot classicals. The three side panels show corresponding histograms for  $a > 200$  au scattering (green) and detached (blue) particles. The  $a > 200$  au high- $q$  TNOs are denoted by red crosses. See Table 6.1 for the implantation fractions for each population.

categorize them based on their dynamical classes (see Section 1.3.1 and Gladman et al. 2008; Gladman & Volk 2021). The final snapshot of the all surviving particles, color-coded according to their dynamical classes, is plotted in Figure 6.28. I also record the implantation efficiency for the detached, resonant, scattering, and hot classicals, as well as the retention fraction for cold classicals, in Table 6.1. In the last three rows of this table, I give the ratios of the detached to other hot populations in three different semimajor axis ranges. These rates and ratios will be used to judge the credibility of the rogue planet model based on metrics introduced in Section 4.6.

The rogue planet model creates a detached orbital distribution (blue dots) that essentially covers *all* discovered detached TNOs from  $a = 48$  au to  $\sim 1000$  au (for

**Table 6.1:** Implantation (or retention) fractions for each TNO population in the rogue planet model (Figure 6.28) and their relative ratios

	$a \leq 48$ au	$48 < a < 200$ au	$a \geq 200$ au	Total
<b>Detached</b>	—	$1.6 \times 10^{-3}$	$1.2 \times 10^{-2}$	$1.3 \times 10^{-2}$
<b>Resonant</b>	$3.6 \times 10^{-3}$	$1 \times 10^{-3}$	—	$4.6 \times 10^{-3}$
<b>Scattering</b>	$2.6 \times 10^{-5}$	$3.3 \times 10^{-4}$	$1 \times 10^{-3}$	$1.3 \times 10^{-3}$
<b>Hot Classicals</b>	$1.8 \times 10^{-3}$	—	—	$1.8 \times 10^{-3}$
<b>Cold Classicals</b>	0.55	$2 \times 10^{-2}$	$5 \times 10^{-4}$	0.57
Det / Res	—	1.6	—	2.8
Det / Sca	—	4.8	12	10
Det / Hot	(0.9)	—	—	7.2

**Note.** Implantation fractions (the number of particles that ended up in each population divided by the total number of initial particles) for each implanted population (detached, resonant, scattering, and hot classicals), and the retention fraction for cold classicals. The last three rows show the ratios of detached/resonant, detached/scattering, and detached/hot classicals at each  $a$  range. Note that the first Det/Hot ratio is actually the ratio of  $48 < a < 200$  au detached to the hot classicals. See text below for more discussion.

better clarity, real objects with  $a < 200$  au are not plotted in Figure 6.28, but the reader can find them in Figure 6.17). Because different dynamical mechanisms contributed to their formation, I will further divide detached TNOs into two subgroups: those with  $a = 48\text{--}200$  au and those beyond  $a > 200$  au.

#### 6.4.1 Detached Objects with $a = 48\text{--}200$ au

In  $48 < a < 100$  au, TNOs are mainly detached by Neptune migration and resonances. The rogue planet acts as an assisting perturber in the process, helping replenish resonances from the early scattering disk and kicking TNOs out of the resonance at high- $q$  (see Chapter 5). Most of the detached TNOs formed in this region concentrate on a band of  $34 < q < 38$  au, whereas the high- $q$  ones ( $q > 38$  au) are more likely to be discovered on the sunward side of strong neptunian resonances. This distribution looks strikingly similar to those produced by grainy migration models (e.g., Nesvorný et al., 2016; Kaib & Sheppard, 2016). However, I didn't

manually model the graininess of Neptune's migration as a result of scattering of Pluto-mass planetesimals, as in Nesvorný et al. (2016). The rogue planet by itself is a natural cause for the grainy migration, as the rogue-Neptune mutual interaction naturally jiggle Neptune's orbit. In addition, the rogue's weak encounters in the scattering disk can also be treated as adding graininess to TNO orbits.

One evident difference between the distributions in Figure 5.2 (in which Neptune's orbit is fixed) and in Figure 6.28 (in which Neptune migrates) is that when the rogue acts as the only perturbation, detached TNOs drop out symmetrically around neptunian resonances at high- $q$ , forming fountain-like structures in the  $a - q$  space. This does not reflect the  $a - q$  distribution of detected high- $q$  TNOs, because they are mostly concentrated at the sunward side (i.e.  $a < a_{\text{res}}$ ) of neptunian n:1 or n:2 resonances (Lawler et al., 2019; Bernardinelli et al., 2022). The only known way of creating this asymmetry is through outward Neptune migration (Nesvorný et al., 2016; Kaib & Sheppard, 2016). In scenarios where both the migration and the rogue planet are considered, the asymmetry can also be produced if the duration of the rogue's presence is not significantly longer than the time for Neptune to reach its current location. This is because even the rogue detaches TNOs symmetrically, subsequent resonance sweeping can still pickup the  $a > a_{\text{res}}$  TNOs when the resonance slowly moves outward. Furthermore, as the rogue planet wanders outward, its TNO encounter rate drops as  $a_r^{-3/2}$  (Equation B.7); an  $a_r = 800$  au rogue would only have one third of an  $a_r = 400$  au rogue's encounter rate. The rogue planet's extreme large- $a$  presence normally occurs near the end of its  $\sim 200$  Myr lifetime, at which point Neptune had basically migrated to its current location (see Figure 6.26). This could explain why the  $48 < a < 100$  au high- $q$  detached are still preferentially distributed on the resonance sunward sides (Figure 6.28), despite the  $\sim 200$ -Myr presence of the rogue.

In  $100 < a < 200$  au, the detached TNO's concentration around resonances is not evident. Nevertheless, the more heated  $i$  distribution (compared to the green scattering TNOs) suggests that the  $q$  lifting is still mainly induced by the resonance-related Kozai mechanism (Gomes et al., 2005b). The rogue planet also likely contributed to the  $q$  lifting, but the apparent lack of low- $i$  detached objects in this region (which is purposely designed by choosing a rogue history that is absent in  $100 < a < 200$  au, in order to satisfy the observational constraint) shows that it is

not the main factor. In addition, this rogue planet model also creates non-negligible populations of distant resonances beyond  $a > 100$  au, which will be further discussed in Section 6.4.2.

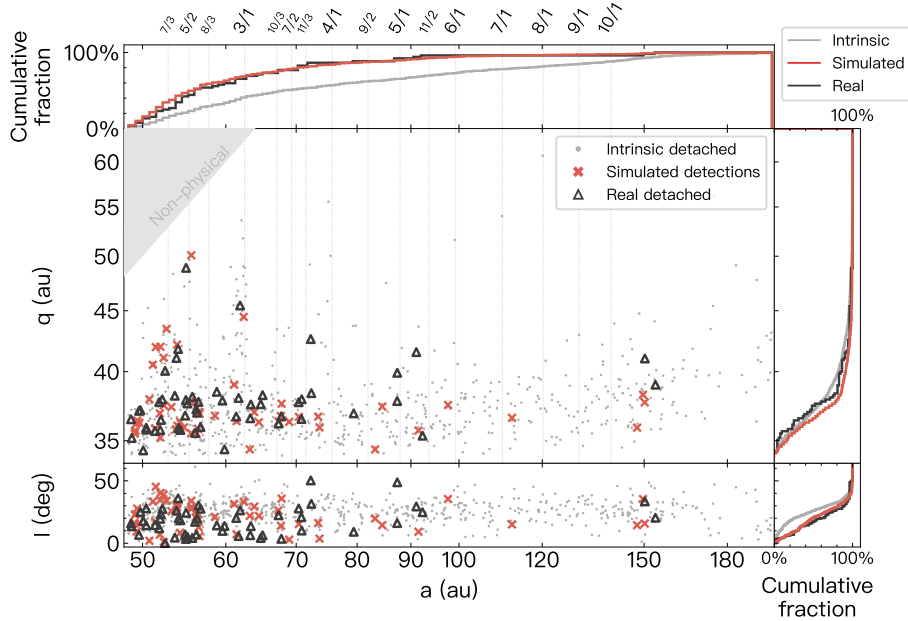


**Figure 6.29:**  $a$ ,  $q$ ,  $i$  distributions of the intrinsic detached based on the rogue planet model (gray dots), the simulated detections using the OSSOS survey simulator (red crosses), and the real detached objects discovered by OSSOS (black triangles). The superimposed simulated detections are of the same size as the OSSOS sample (52 objects), whereas the cumulative distributions are plotted with a larger sample size. Other information is the same as Figure 5.4.

Similar to what I have done in Section 5.4, I also estimated the observation bias by forward-biasing the  $48 < a < 200$  au detached population using the OSSOS survey simulator (Lawler et al., 2018b). The orbital distributions of the intrinsic model (gray dots), the simulated detections (red crosses), and all the OSSOS-discovered detached (black triangles) in this  $a$  range are plotted in Figure 6.29. The three side panels show the cumulative histograms for the  $a$  (top),  $q$  (upper right), and  $i$  (low

right) distributions<sup>14</sup>. Note that this figure is intended to provide a comparison of general trends in distribution, not a statistical comparison.

On Figure 6.29’s  $a$  and  $i$  panels, the cumulative fractions of the simulation detections (red) have very similar trends with the real OSSOS detections (black), even if the intrinsic  $a$  and  $i$  distributions are quite different. One can see that a TNO survey like OSSOS would preferentially detect objects at lower  $a$ ,  $q$ , and  $i$ . In terms of the  $q$  distribution, this rogue planet history results in fractionally more objects at lower  $q$  and less objects at higher  $q$ , although the  $q \approx 38$  au ‘knee’ can be spotted in both the simulated and real distributions. These distributions are both sensitive to Neptune’s migration history and the rogue planet history. For example, the e-folding timescale, the graininess (Nesvorný et al., 2016), as well as the presumed eccentric migration of Neptune (Nesvorný, 2021) should all collectively affect the  $q$  distribution of the implanted detached TNOs in Figure 6.28. I also uncovered the previously-unknown role of the rogue planet in helping populate this region (see Chapter 5.3), bringing broader perspective of how to model ‘graininess’ in Neptune migration.

From Table 6.1, the implantation efficiency for the detached TNOs in  $48 < a < 200$  au is  $1.6 \times 10^{-3}$ . When limited to  $50 < a < 100$  au (the same range used in Nesvorný et al. 2016), the efficiency is  $1.1 \times 10^{-3}$ , roughly a factor of two lower than Nesvorný et al. (2016)’s grainy migration simulation. When using the slightly wider range of  $48 < a < 250$  au used by Beaudoin et al. (2023), the implantation efficiency is  $1.8 \times 10^{-3}$ . By de-biasing a parametric detached population model and my preliminary rogue planet model in Chapter 5 with the OSSOS survey simulator (Lawler et al., 2018b), Beaudoin et al. (2023) proposed an estimate of  $N(H_r < 8.66) = (5 \pm 2) \times 10^4$  detached objects in  $48 < a < 250$  au with 95% confidence. Using the  $\sim 7 \times 10^{-7}$  Trojan capture efficiency (Nesvorný et al., 2013) and the fact that there are 13 Jupiter Trojans with  $H_r < 8.66$ , one can estimate the origin planetesimal disk should have contained  $\sim 2 \times 10^7$  bodies with diameter  $D > 100$  km<sup>15</sup> (Nesvorný et al., 2016). Based on this, this rogue planet model pro-

---

<sup>14</sup>Only particles and simulated detections with  $q > 34$  au are shown in Figure 6.29, because the detached TNOs discovered by OSSOS start from  $q = 34$  au.

<sup>15</sup> $H_r < 8.66$  magnitude corresponds to  $D > 100$  km assuming a 4% albedo. This  $\sim 2 \times 10^7$  gets used a bit later.

vides  $\sim$ 36,000 objects with  $H_r < 8.66$  in the  $48 < a < 250$  au detached population, consistent with Beaudoin et al. (2023)'s population estimate calibrated against the OSSOS survey (Bannister et al., 2018).

#### 6.4.2 Other Implanted Populations within $a < 200$ au

When compared against other distant resonances (which is one of the metrics in Section 4.6), the  $48 < a < 200$  au detached population outnumbers the distant resonant population by a ratio of  $\simeq 1.6$  (Table 6.1). Recently, Crompvoets et al. (2022) estimated the distant resonances beyond 2:1 should contain  $110,000^{+240,000}_{-82,000}$  objects with  $H_r < 8.66$  in total, resulting in a fairly uncertain observed det/res ratio of order unity. The rogue planet model is therefore consistent with the distant resonance estimate, but favors an  $a < 200$  au detached population larger than distant resonances combined. It is worth mentioning that rogue planet models are the only known models bringing the ratio within the observational constraint (including the preliminary model studied in Chapter 5.4, which gives a det/res ratio of 2.3). Two grainy migration models in (Nesvorný et al., 2016) give 8 or 11 for the ratio of  $50 < a < 100$  au detached to the total n:1 resonance population in that range. It is also worth highlighting that this rogue planet also creates non-negligible populations in distant resonances beyond  $a > 100$  au, including the 8:1 (Bernardinelli et al., 2022) and 9:1 (Volk et al., 2018). This apparent improvement compared to just grainy migration models can be explained by the rogue's assisting effect of populating distant resonances regardless of their semimajor axis (Chapter 5). In contrast, resonant capture during neptune migration preferentially favors captures into close-in resonances like the 3:2, whereas distant resonances are weaker or faster moving (illustrated in Figure 4.3), resulting in less efficient population.

Turning to the present-day scattering sub-population, the detached/scattering ratio for this simulation in the  $48 < a < 200$  au range is  $\simeq 5$ . This is larger than the ratio of  $1.5 \pm 0.7$  obtained by combining Lawler et al. (2018a)'s scattering estimate with Beaudoin et al. (2023)'s detached estimate. If one uses the earlier Petit et al. (2011)'s estimate of  $\simeq 5,000^{+5,000}_{-3,000}$  scattering disk objects with  $H_r < 8.66$ , the ratio would be 10 with a factor of 2 uncertainty, consistent with the 5 resulted from this rogue planet simulation. The det/sca ratio of  $\simeq 4$  in Nesvorný et al. (2016) is the

closest.

The final component of the implanted population is the hot classicals, which were essentially formed in the same way (dropouts from the sweeping 2:1 resonance) and period of time as the  $a < 200$  au detached. They were historically labeled as a different dynamical group because they coincidentally overlap with the cold classical belt. Using the  $1.8 \times 10^{-3}$  implantation efficiency for hot classicals (Table 6.1) and the same  $2 \times 10^7$  for disk TNOs, I obtain 36,000 objects with  $H_r < 8.66$ . This is in agreement with Petit et al. (2011)'s hot belt estimate of  $35,000^{+8000}_{-7000} D > 100$  km objects. The  $a < 200$  au detached population thus has a comparable size with the entire hot classical belt.

The only obvious inconsistency of Figure 6.28 with the observed Kuiper Belt that this rogue history produces is an overpopulated 3:2 resonance. The 3:2 implantation frequency is  $3 \times 10^{-3}$  in my model, resulting in a population of  $60,000^{+6000}_{-5000} H_r < 8.66$  objects. This is *not* compatible with the population estimates of  $13,000^{+6000}_{-5000}$  in Gladman et al. (2012) and  $10,000^{+3600}_{-3000}$  in Volk et al. (2016). Nesvorný (2015a) pointed this out as the *resonance overpopulation problem*<sup>16</sup>, which was also noted in many previous dynamical studies on Kuiper Belt formation (e.g., Hahn & Malhotra, 2005; Levison et al., 2008). Nesvorný & Vokrouhlický (2016) studied the capture into the 3:2 in a variety of smooth and grainy migration models, where their table 1 shows the current 3:2 population is highly sensitive to migration details. Again, it is within my expectation that implanted populations closer to Neptune is more sensitive to the migration than the rogue planet history.

As mentioned at the beginning of Chapter 3, CFEPS found the entirety of the implanted population from 40 au to 100 au can be fit with a continuous  $dN/da \propto a^{-2.5}$  power law (Petit et al., 2011, their figure 8). Beaudoin et al. (2023) measured the  $a$  distribution of the detached sample from the OSSOS survey, concluding it follows  $a^{-2.5}$  all the way to at least  $\sim 200$  au. I have demonstrated in Chapter 3 that a semimajor axis power law naturally results from the scattering dynamics. Though the long-term steady state of a scattering disk is  $a^{-1.5}$ , a transient  $a^{-2.5}$  distribution does temporarily appear in numerical experiments prior to the scattering disk reaching the steady state (Figure 3.12). It is therefore worth investigating the  $a$  distribution of the implanted population from the rogue planet model. Apparently,

---

<sup>16</sup>In contrast to the underpopulation of resonances with  $a > 50$  au.

the  $a > 200$  au detached population does not follow any power law due to the secular sculpting from the rogue planet (see Figure 6.28 and the next subsection). I thus plot the  $a$  histogram of the implanted population (resonant + detached) from 40 au to 200 au in Figure 6.30. The 3:2 resonance at  $\sim 39$  au is not included due to overpopulation.

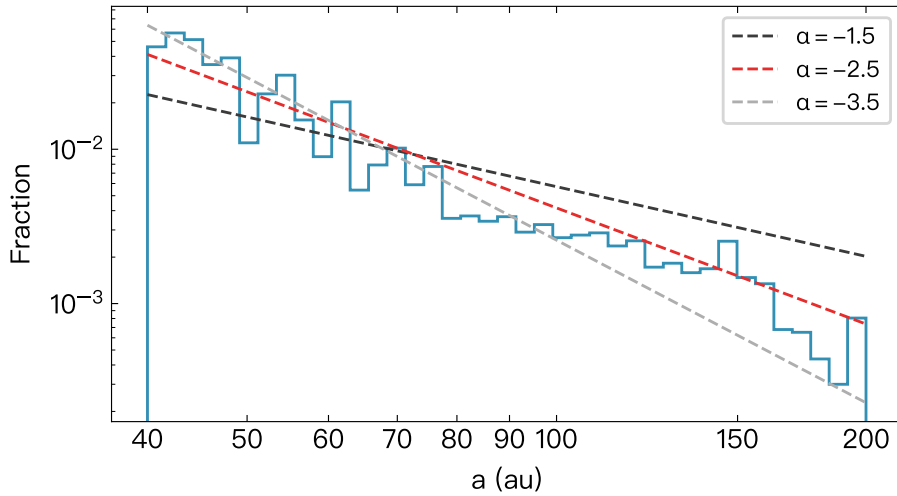


**Figure 6.30:**  $a$  histogram of the implanted population from 40 au to 200 au (excluded scattering and the 3:2 resonance in Figure 6.28’s case). Three dashed lines denote reference power laws with  $a^\alpha$ , where  $\alpha$  is -1.5 (black), -2.5 (red), and -3.5 (gray), respectively. This plot demonstrates that the  $a$  distribution of the implanted population is close to a continuous  $a^{-2.5}$  power law.

Figure 6.30 shows that the rogue planet model also results in a roughly  $a^{-2.5}$  power law<sup>17</sup> in the  $40 < a < 200$  au implanted Kuiper Belt, explaining why in Figure 6.29, the real detached match the simulated detections so well in the  $a$  histogram. The fact that this distribution is steeper than the steady state of the scattering disk may put new constraints on Neptune’s migration timescale, as well the dynamical history of the rogue planet:

1. Numerical experiments confirm that a  $a^{-3.5}$  temporary state can be reached

---

<sup>17</sup>I fit this distribution with the functional form of  $a^\alpha$  and confirm the best fit is  $\alpha = -2.87$ .

at  $\sim 60$  Myr, and  $a^{-2.5}$  can be reached at  $\sim 150$  Myr (see Figure 3.12), assuming initial particles have  $\mathcal{T} \approx 3$  corresponding to a near-circular and co-planar planetesimal disk just outside the migrating Neptune. The dynamical implantation within 200 au is mainly caused by the sweeping of neptunian resonances in the scattering disk (though rogue encounters helped in the process, it's not the main factor). Therefore, the implantation efficiency across different semimajor axes is highly dependent on the underlying scattering distribution. I assess, to achieve the observed  $a^{-2.5}$  distribution, Neptune migration probably had not ended in  $\lesssim 50$  Myr after Neptune started interacting with the planetesimal disk. A steeper power law would otherwise be observed assuming a faster Neptune migration.

2. The rogue planet's secular  $\dot{q}$  effect, which scales as  $a^{2.5}$  according to Equation (6.24) assuming  $a < a_r$ , is naturally incompatible with a decaying power law in  $a$ . It is also shown in Figure 6.28 that the detached distribution beyond  $a > 200$  au does not follow a power law distribution, due to the rogue's  $> 100$  Myr presence beyond  $a_r \sim 400$  au. Therefore, as more large- $a$  objects to be discovered by future surveys like LSST (Collaboration et al., 2021), it will also likely reveal where the  $a^{-2.5}$  distribution of the implanted population ends (presumably near  $\sim 200$  au as the innermost Sednoid, 2012 VP<sub>113</sub>, is at  $a \sim 250$  au). This will provide a valuable constraint to the rogue's dynamical history.

In a short summary, up to  $a = 200$  au, the rogue planet model presented in Figure 6.28 and Table 6.1 is largely in agreement with observational constrains from various dynamical groups, with the only exception being an overpopulated 3:2 resonance. The observed  $a^{-2.5}$  power law in the implanted population can be reproduced in the rogue planet model, and the semimajor axis distribution of the implanted Kuiper Belt is a key to constrain both the migration timescale of Neptune and the dynamical history of the rogue.

#### 6.4.3 Detached Objects with $a > 200$ au, the ‘Iceberg’ Population

In these rogue planet models, the orbital distribution beyond 200 au looks completely different from that below 200 au. As shown in Figure 6.28's side panels, the

rogue-raised large- $a$  TNOs have a peak near  $a \sim 400$  au. Because the  $q$ -lifting rate for distant TNOs is the fastest near  $a = a_r$  (Equation 6.21), it makes sense that the semimajor axis where most of the detached objects formed is close to where the planet had spent most of its time ( $400 < a_r < 600$  au, see Figure 6.26).

The detached TNOs also cover a wide range of  $q$ , from  $\sim 40$  au all the way to  $\sim 200$  au, with a peak near  $q = 50$  au. Compared to distribution right after the removal of the rogue planet (Figure 6.27), the  $q < 50$  au objects (including the enormous scattering population initially created by the rogue, see Figure 6.27) had experienced significant dynamical erosion over the age of the Solar System, due to chaotic diffusion induced by overlapping neptunian resonances in the distant Kuiper Belt (Batygin et al., 2021, and private communications with Sam Hadden (2023)). There is thus no practical need to check whether an  $a > 200$  au TNO is in any resonance with Neptune, because 1) neptunian resonances at this distance cannot help lift perihelion and are irrelevant to the formation of the detached objects (see reference simulations in Figures 6.17 and 6.19), and 2) resonant states are chaotic in the scattering disk because of the overlap. This is *not* to say, however, that none of the TNOs from this gigantic population are in resonance with Neptune. In fact, Volk & Malhotra (2022) explored the phase-space structures of resonances for  $a > 150$  au and  $q > 38$  au TNOs, where they found that almost all distant TNOs are very close to (or even inside of) high-order neptunian resonances. Nevertheless, distant resonances beyond  $a > 200$  au have never been shown to help detach TNOs from the scattering disk. They are thus not considered in my dynamical classification algorithm.

For the sake of simplicity, I designate the entire  $200 < a < 1500$  au range of TNOs (including both the detached and scattering) as the *iceberg* population because 1) they are presumably made of icy bodies, 2) they were all likely formed as a result of the synergy of Neptune scattering and the rogue's secular forcing, and 3) their triangular shape in the  $a - q$  plot resembles an iceberg (see Figure 6.31 for its full range). I did not adopt the commonly-used term of Inner Oort Cloud objects, because there is no model (that matches orbital distributions in  $a$ ,  $q$ , and  $i$  and is compared against observations) showing that they were formed from galactic tides or stellar flybys (see Section 4.4), nor are  $a < 1500$  au objects dominated by the current galactic tides.

The observation bias against detection of iceberg objects is huge, and the currently discovered residents were resulted from various surveys over the course of the last two decades. For example, Sedna was resulted from an all-sky survey based on the Palomar Observatory in California, which was designed to discover the rare bright (large) objects in the Kuiper Belt (Brown et al., 2004). 2012 VP<sub>113</sub> was discovered using the Dark Energy Camera (DECam) at the Cerro Tololo Inter-American Observatory in northern Chile (Trujillo & Sheppard, 2014). The entire OSSOS survey (whose fields mainly follow the invariable plane, Bannister et al. 2018) only discovered one  $a > 200$  au detached TNOs – 505478 (2013 UT<sub>15</sub>) – while the Dark Energy Survey (DES, whose larger sky coverage preferentially looked at the high-latitude southern sky, Bernardinelli et al. 2022) added three more distant detached objects – 2013 RA<sub>109</sub>, 2014 WB<sub>556</sub>, and 2016 SA<sub>59</sub> – to the detected sample (see Table 4.1).

These and the other surveys which provided the  $a > 200$  au sample had different pointing strategies and magnitude limits, making it extremely difficult to estimate the observation bias for each iceberg object. Therefore, instead of forward biasing the intrinsic model and comparing the resultant distribution with only the OSSOS sample (which is impossible because there is only one detection), I simply assume all iceberg TNOs share the same detection bias as the OSSOS survey. The comparison result is shown in Figure 6.31. It is worth noting that this is far from a rigorous comparison, but rather a rough estimate of the bias with limited tools.

Roughly, the observationally biased simulated detections (red curves and crossed) in Figure 6.31 show the same trends as the  $a$ ,  $q$ , and  $i$  distributions of the 22 real discoveries. Compared to the real TNOs (black curves and triangles), the synthetic detections have a smaller fraction of the objects at larger semimajor axis, implying this rogue planet in Figure 6.26 underpopulated the  $a > 500$  au region. Perhaps all that is needed is the rogue spend more time near  $a \approx 1000$  au. Alternatively, this could be explained by unmodeled effects that could have helped populate the extremely large semimajor axes, including galactic tides and passing stars. Though close-in passing stars are not thought to fully account for the formation of the Sednoids (because of the excited inclination distribution it would have produced, see Section 4.4), the cumulative effects of galactic tides and normal passing stars in 4 Gyr can still help lift the perihelia of some extremely large- $a$  TNOs (see figure 9 in

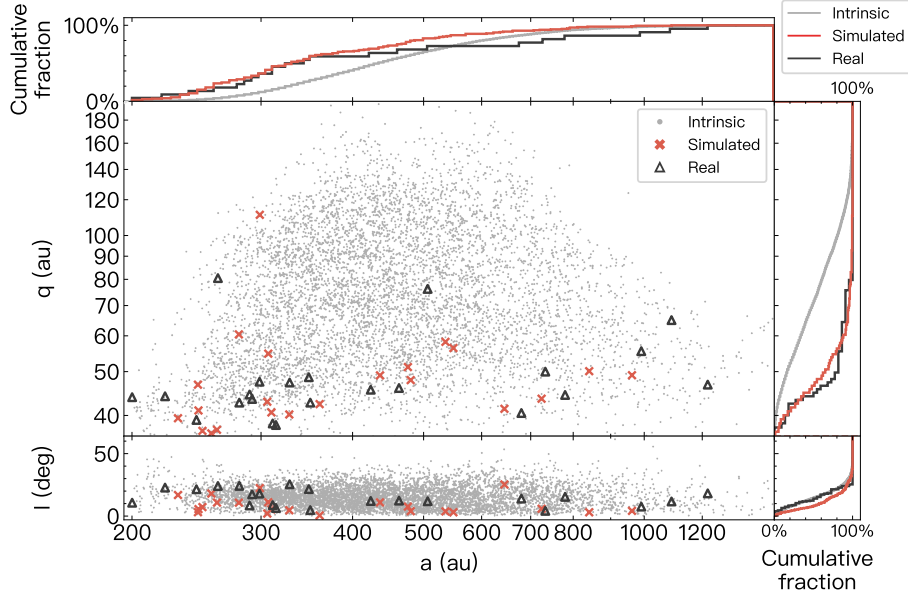


**Figure 6.31:**  $a$ ,  $q$ ,  $i$  distributions of the intrinsic ‘iceberg’ population (gray dots), the simulated detections using the OSSOS survey simulator (red crosses), and the currently-detected TNOs in this region (black triangles). The superimposed simulated detections are of the same size as the discovered TNOs (22 objects), whereas the cumulative distributions are plotted with a larger sample size. Note that this is not a rigorous comparison but a preliminary estimate of the observation bias.

Kaib & Volk 2022). Moreover, my planetary simulation removes the rogue planet once it reaches  $a = 1500$  au, which limited the duration of its presence at very large semimajor axis. Therefore, future rogue planet simulations should fully account for the effects of galactic tides and passing stars, as well as the rogue planet’s behaviour under these effects while at thousands of au.

Surprisingly, the inclination profile of real TNOs (black curve in lowest right panel of Figure 6.31) look almost identical to the intrinsic model (gray curves), whereas the simulated distribution contains a greater fraction of low- $i$  orbits. This is not concerning, as the survey simulator was built upon ecliptic surveys like CFEPS and OSSOS and thus the simulator greatly favors low- $i$  detections. In fact, these

$a > 200$  au TNOs were discovered by a variety of surveys, including high-latitude surveys like the DES and all-sky surveys that revealed Sedna, and thus the real detection bias against large- $i$  orbits is certainly weaker than what the OSSOS simulator predicts. Therefore, I argue that the intrinsic inclination distribution given by the rogue planet model may be close to the real profile, and the lack of large- $i$  orbits in the iceberg strongly favors a moderately-inclined ( $\sim 15^\circ$ ) rogue planet scenario over other explanations that would result in a heated  $i$ . The latter includes theories like Planet 9 (Batygin & Brown, 2016b; Batygin et al., 2019), and the hypothesis that Sedna was formed by stellar encounters when the Sun was in its birth cluster (Morbidelli & Levison, 2004; Kenyon & Bromley, 2004; Brasser & Schwamb, 2014).

The intrinsic  $q$  distribution of the iceberg is close to a uniform distribution from  $\sim 40$  au to  $\sim 120$  au, but both the simulated detections and the real TNOs greatly favor low- $q$  because of the strong observation bias against discovering high- $q$  orbits. Although the biased match of the  $q$  distribution is pleasing, a detail is that the simulated distribution (containing 169 samples) does not have a strong knee shape at  $q \sim 50$  au as the real one. It is unclear whether this feature is caused by an underlying inhomogeneous  $q$  distribution or small-number statistics. Related to this, Trujillo & Sheppard (2014) and Kavelaars et al. (2020) pointed out for the range  $150 < a < 1000$  au, no objects have been discovered between  $50 < q < 75$  au. Although the recently-discovered 2021 RR<sub>205</sub> at  $a = 990$  au and  $q = 55$  au (Table 4.1) will further limit this range down to  $55 < q < 75$  au, this so-called ‘ $q$  gap’ in the large- $a$  population piqued questions about its interpretation: is it just a statistical fluke or does it imply some unknown dynamical formation mechanisms? So far, no published dynamical models (including the rogue planet model I present in this thesis) can create a complete  $q$  gap in the intrinsic distribution.

Because the  $q$  gap’s presence is questionable, I’m interested in whether some sort of  $q$  gap also appears in my simulated detections of the same sample size. My simulated detections contain 169 objects (which apparently have no gap in the  $q$  distribution, see the upper right panel in Figure 6.31) and I experiment by randomly drawing 22 simulated detections from this sample. I then measure the maximum ‘ $q$  gap’ within  $a = 1000$  au for each experiment. Among 20 experiments I ran, 12/20 (60%) experiments have a  $q$  gap  $> 10$  au, and 4/20 (20%) have a  $q$  gap  $> 20$  au. One example of the randomly-generated  $q$  gap is demonstrated in Figure 6.31 with

red crosses. This shows that a ‘ $q$  gap’ can be easily created by sparsely sampling an underlying uniform distribution in  $q$ , and the one currently observed in the large- $a$  Kuiper Belt is plausibly just a statistical fluke. Moreover, if the  $q$  gap proves to be real, my preliminary rogue-planet simulation in Figure 1.8 shows an asymmetry in the  $a - q$  distribution, exhibiting a non-uniform density at  $a \simeq 200$  au. This is perhaps a mechanism to create a ‘ $q$  depression’ if it really exists.

Using the implantation efficiency in Table 6.1 and the estimate that there were initially  $\sim 2 \times 10^7 D > 100$  km object in the outer planetesimal disk, one obtains an  $a > 200$  au population of  $\sim 250,000$  objects with  $H_r < 8.66$ . Assuming the initial planetesimal disk has  $M_{\text{disk}} \simeq 20M_{\oplus}$  (Nesvorný, 2018), the iceberg should currently contain  $\sim 0.25M_{\oplus}$  of material. Given there are only 22 discovered iceberg TNOs with the dimmest being 2015 GT<sub>50</sub> with the H magnitude of 8.5, I estimate only  $\sim 0.01\%$  of the population have been discovered so far, truly the ‘tip of the iceberg’. The iceberg population thus represents the largest component of the Kuiper Belt and future surveys like LSST (Collaboration et al., 2021) should help find more of its residents.

Last but not least, given the existence of Pluto in the resonant population and Eris in the  $a < 200$  au detached population, Table 6.1 implies that  $\simeq 5$  Pluto-sized objects should currently reside in the iceberg. Given the  $\simeq 1.2 \times 10^{-2}$  implantation efficiency of the iceberg, the largest body in the iceberg would be at the scale where there were  $\approx 100$  bodies in the massive planetesimal disk, which would be between Pluto and Mars scale depending on how steep the H magnitude distribution is.

#### 6.4.4 Stability of the Cold Classical Belt

The non-excitation of the cold classical belt is used in Sections 6.1 and 6.2 to constrain the early evolution of the rogue planet and the duration of its presence at several hundred au. Figure 6.8 demonstrates that for a  $2M_{\oplus}$  rogue to overheat the cold classical belt, it needs to resides at 400 au for  $\gtrsim 500$  Myr or at 500 au for  $\gtrsim 1$  Gyr. This is much longer than typical lifetimes of rogue planets. Consequently, the cold classical belt is unlikely to be overheated by the rogue planet.

In addition to 500,000 outer-disk particles, the rogue planet model in Figure 6.28 also contained 2,000 initial cold belt particles from  $a = 42$  to 47 au. The final orbital

distributions of the surviving  $\sim 1,100$  particles are plotted in Figure 6.32.

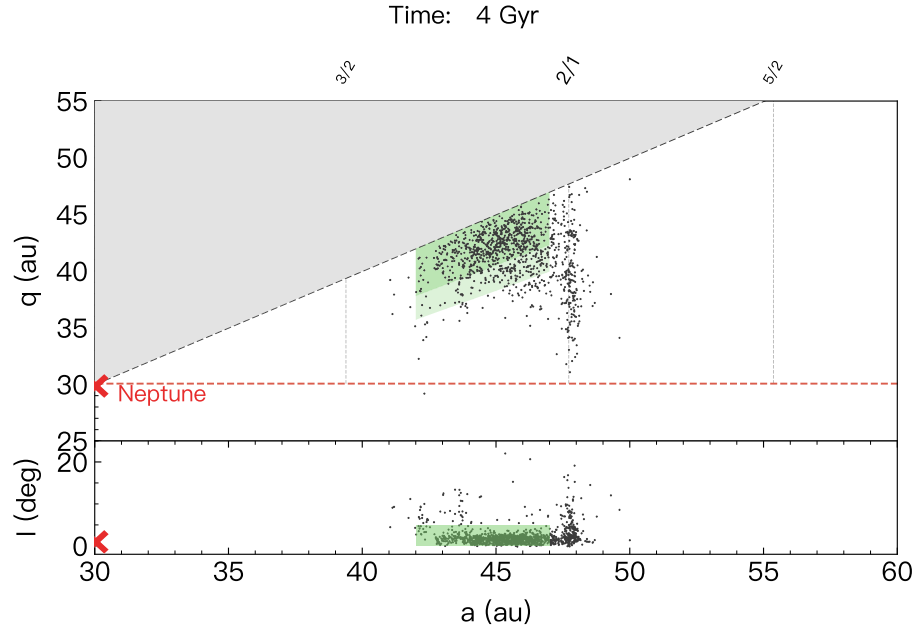


**Figure 6.32:** The preservation of an underheated cold classical belt in the rogue planet model. Other information is the same as Figure 6.13.

The clearing of  $a < 42.5$  au particles is mainly due to the  $\nu_8$  secular resonance (see Figure 2.3). The biggest disturber of the cold belt, however, is not the rogue planet but the outward-sweeping 2:1 resonance during Neptune migration, which starts at  $\approx 38$  au assuming  $a_{N,0} = 24$  au. The 2:1 resonance is able to heat the cold belt, keeping most  $e < 0.1$  (with  $e \approx 0.15$  for some beyond 45 au), while keeping their inclinations mostly untouched. This is consistent with previous simulations by Hahn & Malhotra (2005), in which they show in their figure 2 that the 2:1 resonance is ineffective at heating cold classicals inclinations. Even though the cold belt was initialized within 47 au, there are still a reasonable number of particles ending up with  $a > 47$  au, due to resonant sweeping. At 4 Gyr, the retention fraction of the cold belt is 55% (Table 6.1), with 8% eventually being captured into the 2:1 resonance.

Figure 6.32 corroborates that neither encounters (estimated in Figure 6.1) nor the secular effect (estimated in Figure 6.8) from this particular rogue planet has

visible effects on the cold classical belt. Rogue planet models are thus compatible with the stability of the cold belt.

#### 6.4.5 Orbital Clustering

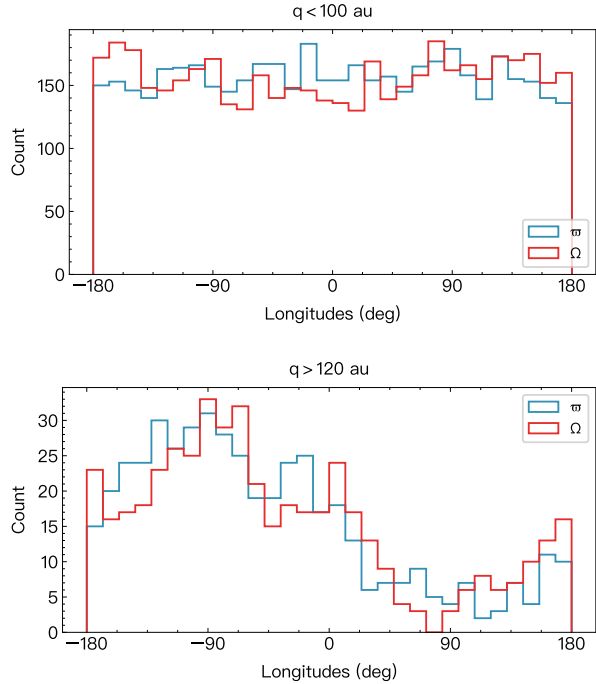


**Figure 6.33:** Distributions of  $\varpi$  and  $\Omega$  at 4 Gyr for iceberg TNOs. The top panel shows that  $q < 100$  au TNOs are randomized in phase angles, whereas  $q > 120$  au TNOs in the bottom panel display a  $\varpi$  concentration near  $-90^\circ$ . The longitude they cluster at does not matter, as that depends on the initial apsidal line of the rogue planet, a random parameter in numerical simulations. This plot shows that  $q > 120$  TNOs (if they truly exist) should still possess the primordial apsidal clustering, as their precession periods  $P_{\varpi}$  are generally longer than the age of the Solar System (see Figure 6.2).

Claims of so-called ‘clustering’ of orbital angles in  $a > 200$  au TNOs have been used to advocate for a still-existing planet in the outer Solar System (Trujillo & Sheppard, 2014; Batygin & Brown, 2016a; Batygin et al., 2019). The credibility of the

intrinsic clustering is called into doubt by well-characterized surveys (Shankman et al., 2017; Bernardinelli et al., 2022). Napier et al. (2021) shows that the joint detection probability of the 14 distant TNOs discovered by OSSOS, DES, and Sheppard & Trujillo (2016) is consistent with an intrinsically uniform distribution. There is thus no need for a currently resident planet.

While present, the rogue planet induces similar TNO dynamics as the hypothetical Planet Nine. The perihelion lifting of distant TNOs is closely related to their apsidal directions with respect to the planet (i.e. the angle  $\Delta\varpi$  in Equation 6.20). As a result, all of the secularly-raised iceberg TNOs should have similar range of  $\Delta\varpi$  when they were first formed. In addition, because the rogue planet is not rapidly precessing,<sup>18</sup>  $a > 200$  au high- $q$  TNOs should have displayed orbital clustering when they were initially detached from the scattering disk.

Subsequent apsidal precessions caused by the giant planets, however, would essentially randomize their phase angles, given that TNOs on different orbits have unequal precession rates. As shown in Figure 6.2, the apsidal precession periods  $P_{\varpi}$  for  $a > 200$  au and  $q < 80$  au orbits vary from several hundred million years to longer than the age of the Solar System, one might thus expect that a primordial orbital clustering in  $\varpi$  would be fully randomized at  $\sim 4$  Gyr. The top panel in Figure 6.33 demonstrates the final distributions of angles  $\varpi$  and  $\Omega$  for  $q < 100$  au iceberg TNOs, in which uniform distributions in both  $\varpi$  and  $\Omega$  are displayed. For TNOs with higher perihelia, the time for the apsidal line to go through one cycle becomes longer than the age of the Solar System (see the purple curve in Figure 6.2). This is to say, there is not enough time for the giant planets to fully randomize their phase angles if some sort of primordial orbital clustering was generated. Figure 6.33's bottom panel shows that  $q > 120$  au TNOs still possess clustering in  $\varpi$  and  $\Omega$ , preserved from the rogue's effects from  $\sim 4$  Gyr ago. This poses an interesting question to future outer Solar System surveys: will TNOs with  $q > 120$  au have clustered orbits in phase angles? If so, one would expect the majority of such detections to be clustered on the sky around a certain right ascension, because their longitudes of perihelion are close to each other.

Last but not least, I also realized that Sedna-like orbits generally have apsidal

---

<sup>18</sup>For example, the rogue in Figure 6.26 has an average apsidal precession rate of  $\dot{\varpi}_r = 0.6^\circ/\text{Myr}$ , so it only precessed  $\sim 100^\circ$  in its entire  $\sim 100$  Myr lifetime.

precession periods in the order of billion years. If they really were produced by the same dynamical process and possessed similar initial  $\varpi$ , by ‘rewinding’ their current longitudes of perihelion back to  $\sim 4$  Gyr ago using Equation 6.7, one should be able to directly see the primordial  $\varpi$  clustering (similar to what is done to identify asteroid families, Nesvorný et al. 2002).

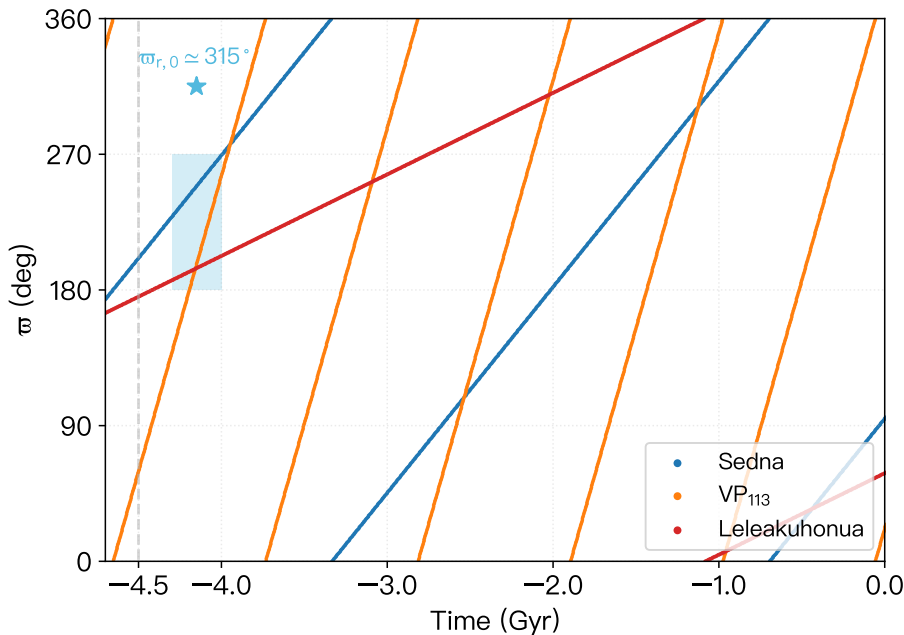


**Figure 6.34:** Rewinding the longitudes of perihelion ( $\varpi$ ) of three Sednoids back to 4 Gyr ago appears to show primordial orbital clustering. The three adopted TNOs (Sedna, 2012 VP<sub>113</sub>, and Leleākūhonua) all have apsidal precession periods ( $P_{\varpi}$ ) of the order  $\sim 1$  Gyr and nearly-fixed orbits with little  $a$  and  $q$  mobility (see dynamical classifications in Figure 6.28). This plot implies that they were likely all detached 4.3 – 4.0 Gyr ago (blue box) by the same dynamical process that also created the primordial  $\varpi$  clustering. If the orbital detachment was caused by a rogue planet, it would have initial  $\varpi_{r,0} \simeq 315^\circ$ , because the maximum  $q$  raising occurs at  $\Delta\varpi = -90^\circ$ .

As shown in Figure 6.34, I calculated their longitudes of perihelion  $\varpi$  of the three Sednoids around 4 Gyr ago by assuming constant precession rates as given

in Equation 6.7<sup>19</sup>. Surprisingly, their  $\varpi$  all come close to  $\varpi \simeq 180^\circ\text{--}270^\circ$  as the time rewinds to 4.3 – 4.0 Gyr ago (denoted by the blue box), right at the beginning of the Solar System. The chance of this just being a coincidence is estimated to be  $0.25^3 \simeq 1.6\%$ , though with post-facto reasoning. Therefore, this simple calculation provides potential evidence for the primordial apsidal clustering in the iceberg population, consistent with the rogue planet origin. Specifically, given that fact that the maximum perihelion detachment occurs at  $\Delta\varpi = \varpi - \varpi_r = -90^\circ$  (Equation 6.24), the rogue planet would have been at  $\varpi_{r,0} \simeq 315^\circ$  when it was first scattered to several hundred au, thus picking out a preferential direction.

## 6.5 Discussion

I demonstrate that the rogue planet scenario is a viable solution to various puzzles in the outer Solar System. Rogue planet models seem to be the only known models that can simultaneously explain the implantation of hot classicals, distant resonant and detached, as well as the gigantic iceberg population that contains the three most distant Sednoids. This is accomplished through the synergy of the rogue planet and a slow eccentric Neptune migration. The rogue planet model presented in this thesis has been compared against the real TNOs using the OSSOS survey simulator. It is largely in line with the orbital distributions of detected TNOs, and satisfies observational constraints provided by various outer Solar System surveys. Here, I summarize the main results from the rogue planet model and its implication.

**Working seamlessly with Neptune's grainy migration.** Neptune's grainy migration is still considered the main dynamical mechanism that populates the  $a < 200$  au Kuiper Belt. I show that rogue planet can be seen as one of the causes for the migration graininess, not only because it constantly nudges Neptune's orbit at perihelion passages, but it also disturbs the  $a < 200$  au Kuiper Belt through flybys, enhancing both the resonant capture efficiency and the detachment efficiency around resonances (see also Chapter 5). It is noteworthy the rogue planet model is the only model that produces enough TNOs in distant resonances.

---

<sup>19</sup>Other iceberg TNOs either have precession rates that are too fast (so their lines cross the primordial clustering anyways) or experience dynamical diffusion over the age of the Solar System (so their  $\varpi$  evolutions cannot be determined due to chaotic semimajor axis movement).

**Producing the iceberg population which explains the formation of Sednoids.** A rogue’s  $\sim 200$  Myr presence at several hundred au naturally create an enormous detached population which I call the *iceberg*. The resulting  $a$ ,  $q$ , and  $i$  distributions produced by a scattering rogue planet are largely consistent with observations (Figure 6.7). I estimate this population to host  $\sim 250,000$  objects with diameter  $D > 100$  km, totalling  $\sim 0.25M_{\oplus}$  in mass. The currently-discovered 22 TNOs consist of 0.01% of the entire population, only representing the ‘tip of the iceberg’. The suggested ‘ $q$  gap’ by Trujillo & Sheppard (2014) and Kavelaars et al. (2020) is easily reproduced with a small number of synthetic detections from the rogue planet, and thus is plausibly just a statistical fluke that will disappear with additional discoveries.

The production of the iceberg 4 Gyr ago is closely related to the rogue’s secular dynamics, which would have induced a primordial apsidal clustering. For TNOs with  $q < 100$  au, the longitudes of perihelion ( $\varpi$ ) are fully randomized by subsequent fast and differential precession rates. The precessions for  $q > 120$  au objects, however, are too slow to homogenize  $\varpi$ , so the primordial orbital clustering could persist to this day. Additionally, I compute the  $\varpi$  evolutions for the three most distant TNOs with  $q > 55$  au, concluding they indeed had nearly aligned apsidal lines  $\sim 4$  Gyr ago. This provides another potential perspective to verify the rogue planet hypothesis, and future outer Solar System surveys should provide a larger sample to study the primordial orbital clustering in the iceberg.

**Keeping the cold classical belt alive.** Although the rogue continuously transverses the cold classical belt, both my analytical estimates and numerical studies demonstrate the stability of the cold classical belt in the presence of this rogue planet. In this picture, the biggest perturber of the cold belt is still the 2:1 resonance that likely swept through the whole belt during migration.

**Oort Cloud building.** In Section 5.5, I argued that the building of the Oort Cloud is unlikely to be impeded by the presence of a temporary rogue planet, as previous numerical studies by Lawler et al. (2017) show that even a  $10 M_{\oplus}$  rogue that existed for 4 Gyr would lower Oort cloud implantation efficiency by only a factor of  $\simeq 2$ . The rogue planet can build an iceberg of  $0.25M_{\oplus}$  at  $200 < a < 1500$  au, which is nearly an order-of-magnitude smaller than the estimated  $1.3 \pm 0.9M_{\oplus}$  mass of the outer Oort Cloud (Boe et al., 2019). Moreover, the yet undiscovered inner Oort Cloud is likely 1-2 times more massive than the outer Oort Cloud (Dones et al.,

2004; Kaib & Volk, 2022). Therefore, the early lifting of a quarter of an Earth’s mass from the scattering disk should not hinder the formation of the Oort Cloud (inner + outer), which is thought to contain cometary bodies with a total mass equal to several times that of Earth.

A Neptune-scattered planet, like all the other early scattering disk objects, has a small probability of being trapped in the Oort Cloud, rather than ejection. Dones et al. (2004) estimated the Oort Cloud trapping efficiency is  $\sim 5\%$ , while Brasser & Morbidelli (2013) shows a moderately higher efficiency of  $\sim 7\%$ . This suggests there is at least  $\sim 5\%$  chance that the  $2M_{\oplus}$  planet still resides in the Oort Cloud. Alternatively, the biggest Oort Cloud body would be, on average, at the scale where there were  $\approx 20$  bodies in the massive disk, which would be roughly Mars scale.

**Potential falsifications of the rogue planet hypothesis.** The rogue planet model presented here is based on our current understanding of the Solar System. It is noteworthy that the model can account for various TNO populations without fine tuning of the rogue planet’s parameters. While the rogue planet’s specific history is inherently chaotic due to planetary scatterings, simulations of small body dynamics consistently yield certain outcomes, including the insertion of many objects in distant resonances, the creation of detached objects near resonances with  $a < 200$  au, and the production of an ‘iceberg’ beyond  $a > 200$  au. As a scientific hypothesis, falsifiability is an essential component. In the case of the scattering rogue planet model, future discoveries that may fundamentally contradict the type of rogue histories I discussed include: 1) a large fraction of high- $i$  and even retrograde sednoids, 2) a low- $e$  and low- $i$  primordial belt beyond 100 au, and 3) objects with  $q > 120$  au (if discovered) that do not exhibit orbital clustering. Future TNO surveys like LSST (Collaboration et al., 2021), CLASSY (Fraser et al., 2022), DEEP (Trujillo et al., 2022), and TAOS II (Huang et al., 2021) are expected to uncover more TNOs in the outer Solar System. These surveys may either support or refute the rogue planet hypothesis.

#### Comparison between outer Solar System formation hypotheses.

In Table 4.2, I compared different outer Solar System formation hypotheses against confirmed observational constraints, including the original rogue planet proposed by Gladman & Chan (2006). I updated the information for the rogue planet model in Table 6.2 based on the new results in Chapter 5 and 6.

**Table 6.2:** Comparison between different outer Solar System formation hypotheses

	$a < 48$ au	$48 < a < 200$ au		$a > 200$ au			
	Cold belt	Detached	Resonant	Sednoids $a, q$	Sednoids $i$	Current clustering	Primordial clustering
<b>Grainy Migration Only</b>	✓	✓	?	✗	✗	✗	✗
<b>Stellar Flyby (Birth Cluster)</b>	$r_{\min} \gtrsim 240$ au	?	?	$r_{\min} \lesssim 400$ au	near-planar flyby(?)	?	?
<b>Existing Planet (Planet Nine)</b>	?	?	?	✓	✗	all $q$	N.A.
<b>Rogue Planet + Grainy Migration</b>	✓	✓	✓	✓	✓	$q > 120$ au	✓

**Note.** Same as Table 4.2 but with the rogue planet model thoroughly inspected. The additional ‘Primordial clustering’ is a new testable constraint that comes out of Section 6.4.5. A rogue planet model with some outward Neptune migration is a very promising model that could explain the implantation of the observable hot Kuiper Belt.

## Chapter 7

# Future Work

This thesis provides new insights into transneptunian dynamics in the main Kuiper Belt, the scattering disk, and under the influence of a rogue planet, offering new avenues for future research. There are still many questions that remain unanswered and opportunities for further exploration. In this chapter, I will outline future directions for research closely related to this thesis, including areas for improvement in the current study and new opportunities that have arisen from the results this work has provided.

1. Chapter 2 presents a reliable method to accurately compute free inclinations for all non-resonant TNOs. Previous TNOs surveys, lacking a consensus on where the mean plane of the Kuiper Belt is, chose to either follow the ecliptic plane (e.g., the Deep Ecliptic Survey, Elliot et al. 2005) or the invariable plane of the Solar System (e.g., CFEPS, Elliot et al. 2005, and OSSOS, Bannister et al. 2018). This study confirms that there is not a ‘universal plane’ for the main belt, as objects with different orbital elements each have their respective forcing centers.

After finishing this paper, I joined the ongoing Classical and Large-a Distant Solar SYstem (CLASSY) TNO surveys (Fraser et al., 2022) and did some extra work on computing the ‘averaged forcing plane’ for existing main-belt TNOs. The averaged plane, which, in theory, has the maximum number of main-belt TNOs orbit, has  $i = 1.76^\circ$  and  $\Omega = 89^\circ$ , slightly different from

the invariable plane of  $i = 1.58^\circ$  and  $\Omega = 108^\circ$ . This average plane has been adopted by the CLASSY team to polish the pointing strategies and maximum the TNO detection rate. It will be interesting to see whether this plane will indeed reveal more main-belt TNOs compared to previous surveys. In addition, using this plane should allow the survey to detect more objects with free inclinations  $< 1^\circ$  (previous surveys were unsensitive to them because of their pointings). The current distribution of the cold belt's free inclination has a peak between  $1\text{--}2^\circ$  (see Figure 2.3), and CLASSY will likely reveal whether a larger population of  $I_{\text{free}} < 1^\circ$  cold classicals exists in the Kuiper Belt.

2. Chapter 3 provides an intuitive understanding to the  $a^{-1.5}$  steady state of a planet-scattering debris disk. The scattering timescale estimate (3.34) can be applied to not only the Solar System's Kuiper Belt, but also exoplanetary systems with observed disk disks (e.g., Fomalhaut, MacGregor et al. 2017,  $\beta$  Picoris, Wahhaj et al. 2003, and AU Microscopii, Fitzgerald et al. 2007 ). Gladman & Volk (2021) show in their figure 9 that the Solar System's Kuiper Belt is visually similar to the Fomalhaut debris disk from the perspective of an external observer. As another example, the outer part of AU Microscopii's debris disk is best fit by a surface density of  $\Sigma(r) \propto r^{-2.5}$  from 32–300 au (Fitzgerald et al., 2007), corresponding to the steady-state  $a^{-1.5}$  number density in semimajor axis. There is thus a constraint on the minimum mass of the needed scatterer. My result provides a novel perspective to understand the radial profile of debris disks if the vast majority of particles have crossing orbits with (possibly unseen) planets.
3. Chapters 5 and 6 presented the rogue planet hypothesis to explain orbital distributions of Kuiper Belt TNOs. The enormous *iceberg* it produced beyond 200 au is particularly interesting, as it indicates that future Solar System surveys like LSST (Collaboration et al., 2021), CLASSY (Fraser et al., 2022), DEEP (Trujillo et al., 2022), and TAOS II (Huang et al., 2021) might find TNOs in this region. It is thus of great importance to study 1) whether these TNOs are consistent with the ‘primordial orbital clustering’ proposed in Section 6.4.5, 2) whether objects with perihelia higher than Sedna and 2012 VP<sub>113</sub> will be discovered, and if so, 3) whether any current orbital clustering

will be confirmed for TNOs with  $q > 120$  au. I will work with the LSST and the CLASSY teams to model the expectations. Additionally, the primordial clustering in the four most distant TNOs was only demonstrated in a preliminary way, with apsidal precession rates computed using the first-order analytical theory. I intend to verify this potentially interesting phenomenon with more accurate numerical simulations, which may require incorporating the galactic tide.

4. The rogue planet model in Section 6.4 was constructed assuming a  $2M_{\oplus}$  planet was quickly scattered out to several hundred au and then decoupled from Saturn. In Section 6.2, I did limited exploration on the emplacement of such a planet. However, it is still unclear what the most likely dynamical mechanism for emplacing such a distant rogue is. Possible scenarios that could address this problem include planetary migration, the rogue's interaction with the gaseous protoplanetary disk, and planetary instability (see the end of Section 6.2). It would also be interesting to study whether an additional short-lived ( $\sim 10$  Myr) ice giant ( $10\text{--}20 M_{\oplus}$ ), or a long-lived ( $\sim 1$  Gyr) Mars-scale planet, at large  $a$  could create Sednoids; the scattering timescale constraints shown in Figure 6.8 seem to disfavor such scenarios.
5. I only focused on the scenario with one extra planet in this thesis, because Gladman & Chan (2006) demonstrated that the secular lifting is largely induced by the most massive planet. However, assuming more Earth-mass cores existed in the early Solar System, the exact dynamical sculpting induced by multiple rogues will differ somewhat from what a single rogue planet was able to do. A detailed investigation of multiple extra planets is potentially interesting in understanding the early formation and evolution of the Solar System.
6. The rogue planet explanation for the outer Solar System also provides a bigger picture for future free-floating planet (i.e., interstellar rogue planet) surveys and exoplanet direct-imaging surveys. Free-floating planets with masses ranging from that of Mars to gas giants are discovered in microlensing surveys (see Mróz et al. 2019, 2018, 2020). The Nancy Grace Roman Space Telescope

is expected to detect  $\sim$ 250 free-floating planets, including  $\sim$ 60 planets with sub-Earth masses (Johnson et al., 2020). The direct imaging method detects large- $a$  exoplanets through their thermal emission. It was initially thought that the object designated “Fomalhaut b” was a rogue planet on a highly eccentric orbit (Kalas et al., 2013) but the inability to detect the planet in the infrared has led many workers to prefer that the observed moving structure is a dispersing dust cloud from the disruption of a large comet in the system (Lawler et al., 2015; Gáspár & Rieke, 2020), rather than a planet. Future discovery of large- $a$  exoplanets on highly-eccentric orbits could provide direct observational evidence for the presented rogue planet hypothesis.

# Bibliography

- Adams, E. R., Gulbis, A. A. S., Elliot, J. L., Benecchi, S. D., Buie, M. W., Trilling, D. E. & Wasserman, L. H. (2014). *The Astronomical Journal* **148**, 55 (page [37](#)).
- Adams, F. C. (2010). *Annual Review of Astronomy and Astrophysics* **48**, 47 (pages [100](#), [102](#), [103](#), [114](#), [129](#), [131](#)).
- Adams, J. C. (1846). *Monthly Notices of the Royal Astronomical Society* **7**, 149 (pages [23](#), [105](#)).
- Armitage, P. J. (2020). *Astrophysics of Planet Formation* (2nd ed.) Cambridge: Cambridge University Press (pages [92](#), [94](#), [168](#)).
- Baguet, D., Morbidelli, A. & Petit, J.-M. (2019). *Icarus* **334**, 99 (page [52](#)).
- Bannister, M. T., Gladman, B. J., Kavelaars, J. J., Petit, J.-M., Volk, K., Chen, Y.-T., Andersen, M., Gwyn, S. D. J., Schwamb, M. E., Ashton, E., Benecchi, S. D., Cabral, N., Dawson, R. I., Delsanti, A., Fraser, W. C., Granvik, M., Greenstreet, S., Guilbert-Lepoutre, A., Ip, W.-H., Jakubik, M., Jones, R. L., Kaib, N. A., Lacerda, P., Laerhoven, C. V., Lawler, S., Lehner, M. J., Lin, H. W., Lykawka, P. S., Marsset, M., Murray-Clay, R., Pike, R. E., Rousselot, P., Shankman, C., Thirouin, A., Vernazza, P. & Wang, S.-Y. (2018). *The Astrophysical Journal Supplement Series* **236**, 18 (pages [26](#), [37](#), [38](#), [100](#), [116](#), [127](#), [190](#), [195](#), [207](#)).
- Bannister, M. T., Shankman, C., Volk, K., Chen, Y. T., Kaib, N., Gladman, B. J., Jakubik, M., Kavelaars, J. J., Fraser, W. C., Schwamb, M. E., Petit, J.-M., Wang, S.-Y., Gwyn, S. D. J., Andersen, M. & Pike, R. E. (2017). *The Astronomical Journal* **153**, 0 (page [150](#)).
- Batygin, K., Adams, F. C., Batygin, Y. K. & Petigura, E. A. (2020). *The Astronomical Journal* **159**, 101 (pages [114](#), [117](#), [129](#)).

- Batygin, K., Adams, F. C., Brown, M. E. & Becker, J. C. (2019). *Physics Reports*, 1 (pages 52, 107, 131, 136, 197, 200).
- Batygin, K. & Brown, M. E. (2016a). *The Astronomical Journal* 151, 22 (pages 107, 136, 142, 200).
- (2016b). *The Astrophysical Journal Letters* 833, L3 (pages 107, 197).
  - (2021). *The Astrophysical Journal Letters* 910, L20 (pages 103, 104, 129).
- Batygin, K., Brown, M. E. & Betts, H. (2012). *The Astrophysical Journal Letters* 744 (pages 102, 155, 169).
- Batygin, K., Brown, M. E. & Fraser, W. C. (2011). *The Astrophysical Journal* 738, 13 (pages 52, 101, 128, 153).
- Batygin, K., Mardling, R. A. & Nesvorný, D. (2021). *The Astrophysical Journal* 920, 148 (page 194).
- Batygin, K. & Morbidelli, A. (2017). *The Astronomical Journal* 154, 229 (pages 107, 136).
- Beaudoin, M., Gladman, B., Huang, Y., Bannister, M., Kavelaars, J., Petit, J.-M. & Volk, K. (2023). *submitted to PSJ* (pages 58, 86, 111, 174, 189–191).
- Beaugé, C. (1994). *Celestial Mechanics and Dynamical Astronomy* 60, 225 (page 11).
- Becker, J. C., Adams, F. C., Khain, T., Hamilton, S. J. & Gerdes, D. (2017). *The Astronomical Journal* 154, 61 (page 107).
- Benavidez, P. G., Campo Bagatin, A., Curry, J., Álvarez-Candal, Á. & Vincent, J.-B. (2022). *Monthly Notices of the Royal Astronomical Society* 514, 4876 (page 101).
- Bernardinelli, P. H., Bernstein, G. M., Sako, M., Yanny, B., Aguena, M., Allam, S., Andrade-Oliveira, F., Bertin, E., Brooks, D., Buckley-Geer, E., Burke, D. L., Rosell, A. C., Kind, M. C., Carretero, J., Conselice, C., Costanzi, M., Costa, L. N. d., Vicente, J. D., Desai, S., Diehl, H. T., Dietrich, J. P., Doel, P., Eckert, K., Everett, S., Ferrero, I., Flaugher, B., Fosalba, P., Frieman, J., García-Bellido, J., Gerdes, D. W., Gruen, D., Gruendl, R. A., Gschwend, J., Hinton, S. R., Hollowood, D. L., Honscheid, K., James, D. J., Kent, S., Kuehn, K., Kuropatkin, N., Lahav, O., Maia, M. A. G., March, M., Menanteau, F., Miquel, R., Morgan, R., Myles, J., Ogando, R. L. C., Palmese, A., Paz-Chinchón, F., Pieres, A., Malagón, A. A. P., Romer, A. K., Roodman, A.,

- Sanchez, E., Scarpine, V., Schubnell, M., Serrano, S., Sevilla-Noarbe, I., Smith, M., Soares-Santos, M., Suchyta, E., Swanson, M. E. C., Tarle, G., To, C., Varga, T. N. & Walker, A. R. (2022). *The Astrophysical Journal Supplement Series* **258**, 41 (pages [26](#), [37](#), [107](#), [112](#), [114](#), [116](#), [128](#), [131](#), [187](#), [190](#), [195](#), [201](#)).
- Bernstein, G. M., Trilling, D. E., Allen, R. L., Brown, M. E., Holman, M. & Malhotra, R. (2004). *The Astronomical Journal* **128**, 1364 (pages [35](#), [36](#), [53](#)).
- Bernstein, G. (2004). *Exploring the Solar System with Wide-Field Imaging from Space*. Berkeley, CA (page [105](#)).
- Beust, H. (2016). *Astronomy & Astrophysics* **590**, L2 (page [136](#)).
- Birnstiel, T., Dullemond, C. P. & Brauer, F. (2010). *Astronomy & Astrophysics* **513**, A79 (page [94](#)).
- Birnstiel, T., Fang, M. & Johansen, A. (2016). *Space Science Reviews* **205**, 41 (pages [90](#), [91](#)).
- Boe, B., Jedicke, R., Meech, K. J., Wiegert, P., Weryk, R. J., Chambers, K., Denneau, L., Kaiser, N., Kudritzki, R.-P., Magnier, E., Wainscoat, R. & Waters, C. (2019). *Icarus* **333**, 252 (page [204](#)).
- Borucki, W. J., Koch, D., Basri, G., Batalha, N., Brown, T., Caldwell, D., Caldwell, J., Christensen-Dalsgaard, J., Cochran, W. D., DeVore, E., Dunham, E. W., Dupree, A. K., III, T. N. G., Geary, J. C., Gilliland, R., Gould, A., Howell, S. B., Jenkins, J. M., Kondo, Y., Latham, D. W., Marcy, G. W., Meibom, S., Kjeldsen, H., Lissauer, J. J., Monet, D. G., Morrison, D., Sasselov, D., Tarter, J., Boss, A., Brownlee, D., Owen, T., Buzasi, D., Charbonneau, D., Doyle, L., Fortney, J., Ford, E. B., Holman, M. J., Seager, S., Steffen, J. H., Welsh, W. F., Rowe, J., Anderson, H., Buchhave, L., Ciardi, D., Walkowicz, L., Sherry, W., Horch, E., Isaacson, H., Everett, M. E., Fischer, D., Torres, G., Johnson, J. A., Endl, M., MacQueen, P., Bryson, S. T., Dotson, J., Haas, M., Kolodziejczak, J., Cleve, J. V., Chandrasekaran, H., Twicken, J. D., Quintana, E. V., Clarke, B. D., Allen, C., Li, J., Wu, H., Tenenbaum, P., Verner, E., Bruhwiler, F., Barnes, J. & Prsa, A. (2010). *Science* **327**, 977 (page [108](#)).
- Bottke, W. F., Durda, D. D., Nesvorný, D., Jedicke, R., Morbidelli, A., Vokrouhlický, D. & Levison, H. (2005). *Icarus* **175**, 111 (page [24](#)).
- Bottke, W. F., Morbidelli, A., Jedicke, R., Petit, J.-M., Levison, H. F., Michel, P. & Metcalfe, T. S. (2002). *Icarus* **156**, 399 (page [25](#)).

- Bottke, W. F. & Norman, M. D. (2017). *Annual Review of Earth and Planetary Sciences* **45**, 619 (page 97).
- Bouvard, A. (1824). *Astronomische Nachrichten* **2**, 441 (page 105).
- Brasser, R., Duncan, M. & Levison, H. (2006). *Icarus* **184**, 59 (page 129).
- Brasser, R., Duncan, M., Levison, H., Schwamb, M. & Brown, M. (2012). *Icarus* **217**, 1 (page 103).
- Brasser, R. & Morbidelli, A. (2013). *Icarus* **225**, 40 (pages 101, 117, 205).
- Brasser, R., Morbidelli, A., Gomes, R., Tsiganis, K. & Levison, H. F. (2009). *Astronomy & Astrophysics* **507**, 1053 (page 101).
- Brasser, R. & Schwamb, M. E. (2014). *Monthly Notices of the Royal Astronomical Society* **446**, 3788 (pages 103, 104, 117, 131, 197).
- Brasser, R., Walsh, K. J. & Nesvorný, D. (2013). *Monthly Notices of the Royal Astronomical Society* **433**, 3417 (pages 101, 102).
- Brouwer, D. & Clemence, G. M. (1961). *Methods of Celestial Mechanics* (page 12).
- Brouwer, D. & Woerkm, A. J. J. v. (1950). *The Secular Variations of the Orbital Elements of the Principal Planets*. Vol. 13. Astronomical papers prepared for the use of the American ephemeris and nautical almanac. U.S. Government Printing Office (pages 14, 46).
- Brown, M. E., Trujillo, C. A. & Rabinowitz, D. L. (2005). *The Astrophysical Journal Letters* **635**, L97 (page 23).
- Brown, M. E. (2001). *The Astronomical Journal* **121**, 2804 (pages 35, 53, 105, 118).
- Brown, M. E. & Batygin, K. (2021). *The Astronomical Journal* **162**, 219 (page 108).
- Brown, M. E. & Pan, M. (2004). *The Astronomical Journal* **127**, 2418 (page 37).
- Brown, M. E., Trujillo, C. & Rabinowitz, D. (2004). *The Astrophysical Journal* **617**, 645 (pages 29, 103, 106, 107, 195).
- Brož, M. & Vokrouhlický, D. (2008). *Monthly Notices of the Royal Astronomical Society* **390**, 715 (page 25).
- Brunini, A. & Melita, M. D. (1998). *Icarus* **135**, 408 (page 31).

- Brunini, A. & Melita, M. (2002). *Icarus* **160**, 32 (pages [106](#), [107](#), [109](#)).
- Burns, J. A., Gladman, B. J. & Greenberg, R. J. (2022). *Unpublished Celestial Mechanics Book* (pages [2](#), [68](#), [247](#)).
- Cáceres, J. & Gomes, R. (2018). *The Astronomical Journal* **156**, 157 (page [107](#)).
- Chambers, J. E. (1999). *Monthly Notices of the Royal Astronomical Society* **304**, 793 (pages [17](#), [119](#), [155](#), [162](#), [240](#)).
- Chen, Y. T., Lin, H. W., Ip, W. H., Chen, W. P., Lin, H. W., Holman, M. J., Payne, M. J., Fraser, W. C., Lacerda, P., Wing-Huen, I. P., Kudritzki, R.-P., Jedicke, R., Wainscoat, R. J., Tonry, J. L., Magnier, E. A., Waters, C., Kaiser, N., Wang, S.-Y. & Lehner, M. (2016). *The Astrophysical Journal Letters* **827**, L24 (page [86](#)).
- Chiang, E. I. & Goldreich, P. (1997). *The Astrophysical Journal* **490**, 368 (page [90](#)).
- Chiang, E. I., Jordan, A. B., Millis, R. L., Buie, M. W., Wasserman, L. H., Elliot, J. L., Kern, S. D., Trilling, D. E., Meech, K. J. & Wagner, R. M. (2003). *The Astronomical Journal* **126**, 430 (page [99](#)).
- Chiang, E., Lithwick, Y., Murray-Clay, R., Buie, M., Grundy, W. & Holman, M. (2006). *A Brief History of Transneptunian Space*. Ed. by B. Reipurth & D. Jewi. Protostars and Planets V. Tucson: University of Arizona Press (page [117](#)).
- Chiang, E. & Choi, H. (2008). *The Astronomical Journal* **136**, 350 (pages [37](#), [41](#), [43](#)).
- Collaboration, T. L. S. S. S., Jones, R. L., Chesley, S. R., Connolly, A. J., Harris, A. W., Ivezić, Z., Knezević, Z., Kubica, J., Milani, A. & Trilling, D. E. (2009). *Earth, Moon, and Planets* **105**, 101 (page [116](#)).
- Collaboration, V. C. R. O. L. S. S. S., Jones, R. L., Bannister, M. T., Bolin, B. T., Chandler, C. O., Chesley, S. R., Eggel, S., Greenstreet, S., Holt, T. R., Hsieh, H. H., Ivezić, Z., Juric, M., Kelley, M. S. P., Knight, M. M., Malhotra, R., Oldroyd, W. J., Sarid, G., Schwamb, M. E., Snodgrass, C., Solontoi, M. & Trilling, D. E. (2021). *Bulletin of the AAS* **53** (pages [26](#), [193](#), [198](#), [205](#), [208](#)).
- Connors, M., Wiegert, P. & Veillet, C. (2011). *Nature* **475**, 481 (page [32](#)).
- Crida, A. (2009). *The Astrophysical Journal* **698**, 606 (page [95](#)).

- Crompvoets, B. L., Lawler, S. M., Volk, K., Chen, Y.-T., Gladman, B., Peltier, L.,  
 Alexandersen, M., Bannister, M. T., Gwyn, S., Kavelaars, J. J. & Petit, J.-M.  
 (2022). *The Planetary Science Journal* **3**, 113 (pages [111](#), [112](#), [116](#), [117](#), [190](#)).
- Ćuk, M., Hamilton, D. P. & Holman, M. J. (2012). *Monthly Notices of the Royal Astronomical Society* **426**, 3051 (page [31](#)).
- Dawson, R. I. & Johnson, J. A. (2018). *Annual Review of Astronomy and Astrophysics* **56**, 175 (page [94](#)).
- Dawson, R. I. & Murray-Clay, R. (2012). *The Astrophysical Journal* **750**, 43  
 (pages [36](#), [52](#), [128](#), [150](#)).
- Delsanti, A. & Jewitt, D. (2006). *Solar System Update: The Solar System Beyond The Planets*. Springer Praxis Books. Berlin: Springer (page [29](#)).
- Dones, L., Weissman, P., Levison, H. & Duncan, M. (2004). *Oort Cloud Formation and Dynamics*. Ed. by M. C. Festou, H. U. Keller & H. A. Weaver. Comet II. Tucson: The University of Arizona Press (pages [28](#), [84](#), [113](#), [129](#), [204](#), [205](#)).
- Doressoundiram, A. (2003). *Earth, Moon, and Planets* **92**, 131 (page [36](#)).
- Doressoundiram, A., Peixinho, N., Bergh, C. d., Fornasier, S., Thébault, P.,  
 Barucci, M. A. & Veillet, C. (2002). *The Astronomical Journal* **124**, 2279  
 (page [36](#)).
- Duncan, M., Quinn, T. & Tremaine, S. (1987). *The Astronomical Journal* **94**, 1330  
 (pages [30](#), [59](#), [62](#), [63](#), [79](#), [129](#), [180](#)).
- Duncan, M. J. & Levison, H. F. (1997). *Science* **276**, 1670 (pages [28](#), [111](#)).
- Duncan, M. J., Levison, H. F. & Lee, M. H. (1998). *The Astronomical Journal* **116**, 2067 (page [17](#)).
- Edgeworth, K. E. (1949). *Monthly Notices of the Royal Astronomical Society* **109**, 600 (page [26](#)).
- Einstein, A. (1916). (Page [106](#)).
- Elliot, J. L., Kern, S. D., Clancy, K. B., Gulbis, A. A. S., Millis, R. L., Buie, M. W.,  
 Wasserman, L. H., Chiang, E. I., Jordan, A. B., Trilling, D. E. & Meech, K. J.  
 (2005). *The Astronomical Journal* **129**, 1117 (pages [26](#), [35](#), [37](#), [207](#)).

- Emel'yanenko, V. V., Asher, D. J. & Bailey, M. E. (2003). *Monthly Notices of the Royal Astronomical Society* **338**, 443 (page [29](#)).
- Evans, N. W. & Tabachnik, S. A. (2002). *Monthly Notices of the Royal Astronomical Society* **333**, L1 (page [31](#)).
- Evans, N. W. & Tabachnik, S. (1999). *Nature* **399**, 41 (pages [31](#), [32](#)).
- Fernandez, J. A. (1981). *Astronomy & Astrophysics* **96**, 26 (pages [29](#), [62](#)).
- Fernández, J. & Ip, W.-H. (1984). *Icarus* **58**, 109 (page [98](#)).
- Fernández-Valenzuela, E., Pinilla-Alonso, N., Stansberry, J., Emery, J. P., Perkins, W., Laerhoven, C. V., Gladman, B. J., Fraser, W., Cruikshank, D., Lellouch, E., Müller, T. G., Grundy, W. M., Trilling, D., Fernandez, Y. & Ore, C. D. (2021). *The Planetary Science Journal* **2**, 10 (page [36](#)).
- Fienga, A., Deram, P., Viswanathan, V., Ruscio, A. D., Bernus, L., Durante, D., Gastineau, M. & Laskar, J. (2019). *Notes Scientifiques et Techniques de l'Institut de Mécanique Céleste* **109** (page [108](#)).
- Fienga, A., Ruscio, A. D., Bernus, L., Deram, P., Durante, D., Laskar, J. & Iess, L. (2020). *Astronomy & Astrophysics* **640**, A6 (page [108](#)).
- Fitzgerald, M. P., Kalas, P. G., Duchêne, G., Pinte, C. & Graham, J. R. (2007). *The Astrophysical Journal* **670**, 536 (page [208](#)).
- Fraser, W. C., Bannister, M. T., Pike, R. E., Marsset, M., Schwamb, M. E., Kavelaars, J. J., Lacerda, P., Nesvorný, D., Volk, K., Delsanti, A., Benecchi, S., Lehner, M. J., Noll, K., Gladman, B., Petit, J.-M., Gwyn, S., Chen, Y.-T., Wang, S.-Y., Andersen, M., Burdullis, T., Sheppard, S. & Trujillo, C. (2017). *Nature Astronomy* **1**, 0088 (page [91](#)).
- Fraser, W. C., Brown, M. E., Morbidelli, A., Parker, A. & Batygin, K. (2014). *The Astrophysical Journal* **782**, 100 (pages [36](#), [101](#)).
- Fraser, W. C., Brown, M. E. & Schwamb, M. E. (2010). *Icarus* **210**, 944 (page [35](#)).
- Fraser, W., Lawler, S., Ashton, E., Chen, Y.-T., Huang, Y., Gladman, B., Kavelaars, J., Petit, J.-M., Peltier, L., Pike, R., Andersen, M., Hestroffer, D., Noyelles, B., Chang, C.-K., Wang, S.-Y., Connolly, A., Kalmbach, B., Eduardo, M., Juric, M. & Gwyn, S. (2022). AAS/Division for Planetary Sciences Meeting Abstracts **54**, 414.01 (pages [205](#), [207](#), [208](#)).

- Froeschle, C. & Morbidelli, A. (1994). *Symposium - International Astronomical Union* **160**, 189 (page 44).
- Gáspár, A. & Rieke, G. H. (2020). *Proceedings of the National Academy of Sciences* **117**, 9712 (page 210).
- Gladman, B. & Chan, C. (2006). *The Astrophysical Journal* **643**, L135 (pages viii, 109–111, 114, 117, 122, 130–133, 205, 209).
- Gladman, B. & Duncan, M. (1990). *The Astronomical Journal* **100**, 1680 (page 31).
- Gladman, B., Holman, M., Grav, T., Kavelaars, J., Nicholson, P., Aksnes, K. & Petit, J.-M. (2002). *Icarus* **157**, 269 (pages viii, 28, 29, 103, 106, 117, 120).
- Gladman, B., Kavelaars, J., Petit, J. .-.-M., Ashby, M. L. N., Parker, J., Coffey, J., Jones, R. L., Rousselot, P. & Mousis, O. (2009). *The Astrophysical Journal* **697**, L91 (page 86).
- Gladman, B., Lawler, S. M., Petit, J. M., Kavelaars, J., Jones, R. L., Parker, J. W., Laerhoven, C. V., Nicholson, P., Rousselot, P., Bieryla, A. & Ashby, M. L. N. (2012). *The Astronomical Journal* **144**, 23 (pages 52, 112, 116, 127, 191).
- Gladman, B. (2005). *Science* **307**, 71 (page 128).
- Gladman, B. J., Migliorini, F., Morbidelli, A., Zappalà, V., Michel, P., Cellino, A., Froeschlé, C., Levison, H. F., Bailey, M. & Duncan, M. (1997). *Science* **277**, 197 (page 25).
- Gladman, B., Marsden, B. G. & Vanlaerhoven, C. (2008). *Nomenclature in the Outer Solar System*. Ed. by M. A. Barucci, H. Boehnhardt, D. P. Cruikshank & A. Morbidelli. Vol. 43. The Solar System Beyond Neptune. Tucson: University of Arizona Press (pages 26, 29, 39, 116, 122, 185).
- Gladman, B. & Volk, K. (2021). *Annual Review of Astronomy and Astrophysics* **59**, 203 (pages 27, 35, 36, 38, 39, 43, 100, 101, 110, 117, 127, 153, 185, 208).
- Goldreich, P. & Tremaine, S. (1980). *The Astrophysical Journal* **241**, 425 (pages 94, 168).
- Gomes, D. C. H., Murray, Z., Gomes, R. C. H., Holman, M. J. & Bernstein, G. M. (2022). *arXiv* (page 108).
- Gomes, R. S., Fernández, J. A., Gallardo, T. & Brunini, A. (2008). *The Scattered Disk: Origins, Dynamics, and End States*. Ed. by M. A. Barucci, H. Boehnhardt,

- D. P. Cruikshank & A. Morbidelli. The Solar System Beyond Neptune. Tucson: University of Arizona Press (pages 117, 120).
- Gomes, R., Levison, H. F., Tsiganis, K. & Morbidelli, A. (2005a). *Nature* **435**, 466 (pages 101, 168).
- Gomes, R. S. (2003). *Icarus* **161**, 404 (page 99).
- Gomes, R. S., Gallardo, T., Fernández, J. A. & Brunini, A. (2005b). *Celestial Mechanics and Dynamical Astronomy* **91**, 109 (pages 170, 187).
- Gomes, R. S., Matese, J. J. & Lissauer, J. J. (2006). *Icarus* **184**, 589 (pages 106, 117).
- Gomes, R. S., Morbidelli, A. & Levison, H. F. (2004). *Icarus* **170**, 492 (page 100).
- Gradie, J. & Tedesco, E. (1982). *Science* **216**, 1405 (page 96).
- Granvik, M., Morbidelli, A., Jedicke, R., Bolin, B., Bottke, W. F., Beshore, E., Vokrouhlický, D., Nesvorný, D. & Michel, P. (2018). *Icarus* **312**, 181 (page 25).
- Greenstreet, S. (2020). *Monthly Notices of the Royal Astronomical Society: Letters* (page 25).
- Greenstreet, S., Gladman, B. & Ngo, H. (2020). *The Astronomical Journal* **160**, 0 (pages 32, 86).
- Greenstreet, S., Ngo, H. & Gladman, B. (2012). *Icarus* **217**, 355 (page 25).
- Guillot, T. (1999). *Planetary and Space Science* **47**, 1183 (pages 92, 94).
- Hahn, J. M. & Malhotra, R. (1999). *The Astronomical Journal* **117**, 3041 (page 98).
- Hahn, J. M. & Malhotra, R. (2005). *The Astronomical Journal* **130**, 2392 (pages 99, 117, 191, 199).
- Hansen, B. M. S. (2009). *The Astrophysical Journal* **703**, 1131 (page 95).
- Hayashi, C. (1981). *Progress of Theoretical Physics Supplement* **70**, 35 (page 95).
- Henrard, J. (1990). *Celestial Mechanics and Dynamical Astronomy* **49**, 43 (page 44).
- Hill, G. W. (1878). *American Journal of Mathematics* **1**, 129 (page 66).
- Hills, J. G. (1981). *The Astronomical Journal* **86**, 1730 (page 30).
- Holman, M. J. (1997). *Nature* **387**, 785 (page 31).

- Holman, M. J. & Wisdom, J. (1993). *The Astronomical Journal* **105**, 1987 (page [31](#)).
- Horner, J., Evans, N. W. & Bailey, M. E. (2004). *arXiv* (page [25](#)).
- Huang, C.-K., Lehner, M. J., Contreras, A. P. G., Castro-Chacón, J. H., Chen, W.-P., Alcock, C., Alvarez-Santana, F. I., Cook, K. H., Geary, J. C., Peña, C. A. G., Hernández-Águila, J. B., Hernández-Valencia, B., Karr, J., Kavelaars, J. J., Norton, T., Nuñez, J. M., Ochoa, D., Reyes-Ruiz, M., Sánchez, E., Silva, J. S., Szentgyorgyi, A., Wang, S.-Y., Yen, W.-L. & Zhang, Z.-W. (2021). *Publications of the Astronomical Society of the Pacific* **133**, 034503 (pages [205](#), [208](#)).
- Huang, Y. & Gladman, B. (2020). *Monthly Notices of the Royal Astronomical Society* **500**, 1151 (page [31](#)).
- Huang, Y., Gladman, B., Beaudoin, M. & Zhang, K. (2022a). *The Astrophysical Journal Letters* **938**, L23 (page [23](#)).
- Huang, Y., Gladman, B. & Volk, K. (2022b). *The Astrophysical Journal Supplement Series* **259**, 54 (page [129](#)).
- Huang, Y., Li, M., Li, J. & Gong, S. (2018). *The Astronomical Journal* **155**, 262 (page [4](#)).
- Ida, S., Larwood, J. & Burkert, A. (2000). *The Astrophysical Journal* **528**, 351 (page [103](#)).
- Ida, S. & Makino, J. (1993). *Icarus* **106**, 210 (page [93](#)).
- Jewitt, D. (2009). *The Astronomical Journal* **137**, 4296 (page [25](#)).
- Jewitt, D. & Luu, J. (1993). *Nature* **362**, 730 (pages [26](#), [106](#)).
- Johansen, A., Low, M.-M. M., Lacerda, P. & Bizzarro, M. (2015). *Science Advances* **1**, e1500109 (page [91](#)).
- Johansen, A., Oishi, J. S., Low, M.-M. M., Klahr, H., Henning, T. & Youdin, A. (2007). *Nature* **448**, 1022 (page [90](#)).
- Johnson, S. A., Penny, M., Gaudi, B. S., Kerins, E., Rattenbury, N. J., Robin, A. C., Novati, S. C. & Henderson, C. B. (2020). *The Astronomical Journal* **160**, 123 (page [210](#)).
- Jones, R., Gladman, B., Petit, J.-M., Rousselot, P., Mousis, O., Kavelaars, J., Bagatin, A. C., Bernabeu, G., Benavidez, P., Parker, J., Nicholson, P.,

- Holman, M., Grav, T., Doressoundiram, A., Veillet, C., Scholl, H. & Mars, G. (2006). *Icarus* **185**, 508 (pages [26](#), [37](#)).
- Kaib, N. A. & Sheppard, S. S. (2016). *The Astronomical Journal* **152**, 133 (pages [100](#), [112](#), [117](#), [120](#), [131](#), [172](#), [186](#), [187](#)).
- Kaib, N. A. & Volk, K. (2022). *arXiv* (pages [154](#), [196](#), [205](#)).
- Kalas, P., Graham, J. R., Fitzgerald, M. P. & Clampin, M. (2013). *The Astrophysical Journal* **775**, 56 (page [210](#)).
- Kavelaars, J. J., Petit, J.-M., Gladman, B., Bannister, M. T., Alexandersen, M., Chen, Y.-T., Gwyn, S. D. J. & Volk, K. (2021). *The Astrophysical Journal Letters* **920**, L28 (pages [28](#), [35](#), [37](#), [91](#)).
- Kavelaars, J., Lawler, S. M., Bannister, M. T. & Shankman, C. (2020). *Perspectives on the distribution of orbits of distant Trans-Neptunian objects*. Vol. astro-ph.EP. The Trans-Neptunian Solar System. Elsevier (pages [110](#), [112](#), [197](#), [204](#)).
- Kenyon, S. J. & Bromley, B. C. (2004). *Nature* **432**, 598 (pages [103](#), [197](#)).
- Khain, T., Becker, J. C., Adams, F. C., Gerdes, D. W., Hamilton, S. J., Franson, K., Zullo, L., Sako, M., Napier, K., Lin, H. W., Markwardt, L., Bernardinelli, P., Abbott, T. M. C., Abdalla, F. B., Annis, J., Avila, S., Bertin, E., Brooks, D., Rosell, A. C., Kind, M. C., Carretero, J., Cunha, C. E., Costa, L. N. d., Davis, C., Vicente, J. D., Desai, S., Diehl, H. T., Doel, P., Eifler, T. F., Flaugher, B., Frieman, J., García-Bellido, J., Gruen, D., Gruendl, R. A., Gutierrez, G., Hartley, W. G., Hollowood, D. L., Honscheid, K., James, D. J., Krause, E., Kuehn, K., Kuropatkin, N., Lahav, O., Maia, M. A. G., Menanteau, F., Miquel, R., Nord, B., Ogando, R. L. C., Plazas, A. A., Romer, A. K., Sanchez, E., Scarpine, V., Schindler, R., Schubnell, M., Sevilla-Noarbe, I., Smith, M., Soares-Santos, M., Sobreira, F., Suchyta, E., Swanson, M. E. C., Tarle, G., Vikram, V., Walker, A. R., Wester, W., Zhang, Y. & Collaboration, D. (2018). *The Astronomical Journal* **156**, 273 (page [107](#)).
- Khain, T., Becker, J. C., Lin, H. W., Gerdes, D. W., Adams, F. C., Bernardinelli, P., Bernstein, G. M., Franson, K., Markwardt, L., Hamilton, S., Napier, K., Sako, M., Abbott, T. M. C., Avila, S., Bertin, E., Brooks, D., Buckley-Geer, E., Burke, D. L., Rosell, A. C., Kind, M. C., Carretero, J., Costa, L. N. d., Vicente, J. D., Desai, S., Diehl, H. T., Doel, P., Flaugher, B., Frieman, J., García-Bellido, J., Gaztanaga, E., Gruen, D., Gruendl, R. A., Gschwend, J., Gutierrez, G., Hollowood, D. L., Honscheid, K., James, D. J., Kuropatkin, N.,

- Maia, M. A. G., Marshall, J. L., Menanteau, F., Miller, C. J., Miquel, R., Plazas, A. A., Sanchez, E., Scarpine, V., Schubnell, M., Sevilla-Noarbe, I., Smith, M., Sobreira, F., Suchyta, E., Swanson, M. E. C., Tarle, G., Walker, A. R., Wester, W. & Collaboration, T. D. E. S. (2020). *The Astronomical Journal* **159**, 133 (page 39).
- Kley, W., Bitsch, B. & Klahr, H. (2009). *Astronomy & Astrophysics* **506**, 971 (page 95).
- Knežević, Z., Milani, A., Farinella, P., Froeschle, C. & Froeschle, C. (1991). *Icarus* **93**, 316 (page 49).
- Kokubo, E. & Ida, S. (1996). *Icarus* **123**, 180 (page 93).
- (1998). *Icarus* **131**, 171 (page 93).
  - (2000). *Icarus* **143**, 15 (page 93).
  - (2002). *The Astrophysical Journal* **581**, 666 (page 93).
- Kozai, Y. (1962). *The Astronomical Journal* **67**, 579 (page 120).
- Krajnović, D. (2016). *Astronomy & Geophysics* **57**, 5.28 (pages 23, 105).
- Kretke, K. A., Levison, H. F., Buie, M. W. & Morbidelli, A. (2012). *The Astronomical Journal* **143**, 91 (page 169).
- Kuiper, G. P. (1951). *Proceedings of the National Academy of Sciences* **37**, 1 (page 26).
- Lan, L. & Malhotra, R. (2019). *Celestial Mechanics and Dynamical Astronomy* **131**, 39 (page 125).
- Landau, L. D. & Lifshitz, E. M. (2013). *Fluid Mechanics: Landau and Lifshitz: Course of Theoretical Physics*. Vol. 6. Elsevier (page 76).
- Lawler, S. M., Greenstreet, S. & Gladman, B. (2015). *The Astrophysical Journal Letters* **802**, L20 (page 210).
- Lawler, S. M., Pike, R. E., Kaib, N., Andersen, M., Bannister, M. T., Chen, Y. .-. T., Gladman, B., Gwyn, S., Kavelaars, J. J., Petit, J. .-. M. & Volk, K. (2019). *The Astronomical Journal* **157**, 253 (pages 100, 112, 131, 187).
- Lawler, S. M., Shankman, C., Kaib, N., Bannister, M. T., Gladman, B. & Kavelaars, J. J. (2017). *The Astronomical Journal* **153**, 33 (pages 113, 129, 204).

- Lawler, S. M., Shankman, C., Kavelaars, J. J., Alexandersen, M., Bannister, M. T., Chen, Y.-T., Gladman, B., Fraser, W. C., Gwyn, S., Kaib, N., Petit, J. -M. & Volk, K. (2018a). *The Astronomical Journal* 155, 197 (pages 116, 190).
- Lawler, S. M., Kavelaars, J. J., Alexandersen, M., Bannister, M. T., Gladman, B., Petit, J.-M. & Shankman, C. (2018b). *Frontiers in Astronomy and Space Sciences* 5, 14 (pages viii, ix, 110, 127, 188, 189).
- Levison (1996). *Comet Taxonomy*. Vol. 107. Astronomical Society of the Pacific Conference Series (page 10).
- Levison, H. F. & Duncan, M. J. (1994). *Icarus* 108, 18 (pages 17, 29, 118, 119, 238).
- Levison, H. F. & Duncan, M. J. (1997). *Icarus* 127, 13 (pages vii, 69, 118, 154).
- Levison, H. F., Morbidelli, A., VanLaerhoven, C., Gomes, R. & Tsiganis, K. (2008). *Icarus* 196, 258 (pages 101, 191).
- Levison, H. F., Shoemaker, E. M. & Shoemaker, C. S. (1997). *Nature* 385, 42 (page 25).
- Levison, H. F. & Stern, S. A. (2001). *The Astronomical Journal* 121, 1730 (page 35).
- Lin, D. N. C. & Ida, S. (1997). *The Astrophysical Journal* 477, 781 (page 109).
- Lin, D. N. C. & Papaloizou, J. (1986). *The Astrophysical Journal* 309, 846 (pages 94, 168).
- Lissauer, J. J. (1993). *Annual Review of Astronomy and Astrophysics* 31, 129 (page 94).
- Lissauer, J. J., Hubickyj, O., D'Angelo, G. & Bodenheimer, P. (2009). *Icarus* 199, 338 (page 94).
- Lissauer, J. J. & de-Pater, I. (2013). *Fundamental Planetary Science* (pages 76, 89, 92, 94, 95, 168).
- Lissauer, J. J. & Stevenson, D. J. (2007). "Formation of Giant Planets". Protostars and Planets V, p. 591 (page 94).
- Lowell, P. (1915). *Memoir on a Trans-Neptunian Planet*. Memoirs of the Lowell Observatory. T.P. Nichols (page 23).
- Lykawka, P. S. & Mukai, T. (2008). *The Astronomical Journal* 135, 1161 (pages 106, 117).

- Lykawka, P. S. & Mukai, T. (2007). *Icarus* **192**, 238 (pages 28, 120).
- MacGregor, M. A., Matrà, L., Kalas, P., Wilner, D. J., Pan, M., Kennedy, G. M., Wyatt, M. C., Duchene, G., Hughes, A. M., Rieke, G. H., Clampin, M., Fitzgerald, M. P., Graham, J. R., Holland, W. S., Panić, O., Shannon, A. & Su, K. (2017). *The Astrophysical Journal* **842**, 8 (page 208).
- Malhotra, R. (1995). *The Astronomical Journal* **110**, 420 (pages 28, 99).
- Malhotra, R. (1993). *Nature* **365**, 819 (pages 98, 99, 171).
- Malhotra, R., Volk, K. & Wang, X. (2016). *The Astrophysical Journal Letters* **824**, L22 (page 108).
- Malyshkin, L. & Tremaine, S. (1999). *Icarus* **141**, 341 (pages 28, 61, 62, 79).
- Mardling, R. A. (2013). *Monthly Notices of the Royal Astronomical Society* **435**, 2187 (pages 12, 140).
- Markwardt, L., Gerdes, D. W., Malhotra, R., Becker, J. C., Hamilton, S. J. & Adams, F. C. (2020). *Monthly Notices of the Royal Astronomical Society* **492**, 6105 (page 32).
- Martin, R. G. & Livio, M. (2012). *Monthly Notices of the Royal Astronomical Society: Letters* **425**, L6 (page 90).
- Masset, F. & Snellgrove, M. (2001). *Monthly Notices of the Royal Astronomical Society* **320**, L55 (page 96).
- Melita, M. & Williams, I. P. (2003). *Earth, Moon, and Planets* **92**, 447 (page 107).
- Melita, M., Williams, I., Collander-Brown, S. J. & Fitzsimmons, A. (2004). *Icarus* **171**, 516 (page 107).
- Michael, S., Durisen, R. H. & Boley, A. C. (2011). *The Astrophysical Journal Letters* **737**, L42 (page 95).
- Michel, P. & Froeschlé, C. (1997). *Icarus* **128**, 230 (page 44).
- Millholland, S. & Laughlin, G. (2017). *The Astronomical Journal* **153**, 91 (page 107).
- Morais, H. & Namouni, F. (2017). *Nature* **543**, 635 (page 25).
- Morais, M. (2002). *Icarus* **160**, 1 (page 32).

- Morbidelli, A., Brasser, R., Tsiganis, K., Gomes, R. & Levison, H. F. (2009). *Astronomy & Astrophysics* **507**, 1041 (page 101).
- Morbidelli, A., Brown, M. & Levison, H. (2003). *Earth, Moon, and Planets* **92**, 1 (page 28).
- Morbidelli, A., Jacob, C. & Petit, J.-M. (2002). *Icarus* **157**, 241 (pages 106, 128).
- Morbidelli, A., Levison, H. F., Tsiganis, K. & Gomes, R. (2005). *Nature* **435**, 462 (pages 101, 168).
- Morbidelli, A., Thomas, F. & Moons, M. (1995). *Icarus* **118**, 322 (page 124).
- Morbidelli, A. (2002). *Modern Celestial Mechanics: Aspects of Solar System Dynamics*. CRC Press (pages 2, 6, 44, 49, 136).
- Morbidelli, A., Brasser, R., Gomes, R., Levison, H. F. & Tsiganis, K. (2010). *The Astronomical Journal* **140**, 1391 (page 101).
- Morbidelli, A. & Henrard, J. (1991). *Celestial Mechanics and Dynamical Astronomy* **51**, 131 (page 44).
- Morbidelli, A. & Levison, H. F. (2004). *The Astronomical Journal* **128**, 2564 (pages 103, 109, 117, 129, 197).
- Morbidelli, A. & Nesvorný, D. (2020). *Kuiper belt: Formation and evolution. The Trans-Neptunian Solar System* (page 91).
- Mróz, P., Poleski, R., Gould, A., Udalski, A., Sumi, T., Szymański, M. K., Soszyński, I., Pietrukowicz, P., Kozłowski, S., Skowron, J., Ulaczyk, K., Albrow, M. D., Chung, S.-J., Han, C., Hwang, K.-H., Jung, Y. K., Kim, H.-W., Ryu, Y.-H., Shin, I.-G., Shvartzvald, Y., Yee, J. C., Zang, W., Cha, S.-M., Kim, D.-J., Kim, S.-L., Lee, C.-U., Lee, D.-J., Lee, Y., Park, B.-G. & Pogge, R. W. (2020). *The Astrophysical Journal Letters* **903**, L11 (pages 109, 209).
- Mróz, P., Ryu, Y. .-.H., Skowron, J., Udalski, A., Gould, A., Szymański, M. K., Soszyński, I., Poleski, R., Pietrukowicz, P., Kozłowski, S., Pawlak, M., Ulaczyk, K., Collaboration, T. O., Albrow, M. D., Chung, S. .-.J., Jung, Y. K., Han, C., Hwang, K. .-.H., Shin, I. .-.G., Yee, J. C., Zhu, W., Cha, S. .-.M., Kim, D. .-.J., Kim, H. .-.W., Kim, S. .-.L., Lee, C. .-.U., Lee, D. .-.J., Lee, Y., Park, B. .-.G., Pogge, R. W. & Collaboration, T. K. (2018). *The Astronomical Journal* **155**, 121 (pages 109, 209).

- Mróz, P., Udalski, A., Bennett, D. P., Ryu, Y.-H., Sumi, T., Shvartzvald, Y., Skowron, J., Poleski, R., Pietrukowicz, P., Kozłowski, S., Szymański, M. K., Wyrzykowski, Ł., Soszyński, I., Ulaczyk, K., Rybicki, K., Iwanek, P., Albrow, M. D., Chung, S.-J., Gould, A., Han, C., Hwang, K.-H., Jung, Y. K., Shin, I.-G., Yee, J. C., Zang, W., Cha, S.-M., Kim, D.-J., Kim, H.-W., Kim, S.-L., Lee, C.-U., Lee, D.-J., Lee, Y., Park, B.-G., Pogge, R. W., Abe, F., Barry, R., Bhattacharya, A., Bond, I. A., Donachie, M., Fukui, A., Hirao, Y., Itow, Y., Kawasaki, K., Kondo, I., Koshimoto, N., Li, M. C. A., Matsubara, Y., Muraki, Y., Miyazaki, S., Nagakane, M., Ranc, C., Rattenbury, N. J., Suematsu, H., Sullivan, D. J., Suzuki, D., Tristram, P. J., Yonehara, A., Maoz, D., Kaspi, S. & Friedmann, M. (2019). *Astronomy & Astrophysics* **622**, A201 (pages [109](#), [209](#)).
- Müller, T., Lellouch, E. & Fornasier, S. (2020). *The Trans-Neptunian Solar System*, 153 (page [36](#)).
- Murray, C. D. & Dermott, S. F. (1999). *Solar System Dynamics*. Cambridge University Press (pages [2](#), [6](#), [12](#), [36](#), [43](#), [137](#), [140](#)).
- Nakamura, E., KOBAYASHI, K., TANAKA, R., KUNIHIRO, T., KITAGAWA, H., POTISZIL, C., OTA, T., SAKAGUCHI, C., YAMANAKA, M., RATNAYAKE, D. M., TRIPATHI, H., KUMAR, R., AVRAMESCU, M.-L., TSUCHIDA, H., YACHI, Y., MIURA, H., ABE, M., FUKAI, R., FURUYA, S., HATAKEDA, K., HAYASHI, T., HITOMI, Y., KUMAGAI, K., MIYAZAKI, A., NAKATO, A., NISHIMURA, M., OKADA, T., SOEJIMA, H., SUGITA, S., SUZUKI, A., USUI, T., YADA, T., YAMAMOTO, D., YOGATA, K., YOSHITAKE, M., ARAKAWA, M., FUJII, A., HAYAKAWA, M., HIRATA, N., HIRATA, N., HONDA, R., HONDA, C., HOSODA, S., IIJIMA, Y.-i., IKEDA, H., ISHIGURO, M., ISHIHARA, Y., IWATA, T., KAWAHARA, K., KIKUCHI, S., KITAZATO, K., MATSUMOTO, K., MATSUOKA, M., MICHIKAMI, T., MIMASU, Y., MIURA, A., MOROTA, T., NAKAZAWA, S., NAMIKI, N., NODA, H., NOGUCHI, R., OGAWA, N., OGAWA, K., OKAMOTO, C., ONO, G., OZAKI, M., SAIKI, T., SAKATANI, N., SAWADA, H., SENSHU, H., SHIMAKI, Y., SHIRAI, K., TAKEI, Y., TAKEUCHI, H., TANAKA, S., TATSUMI, E., TERUI, F., TSUKIZAKI, R., WADA, K., YAMADA, M., YAMADA, T., YAMAMOTO, Y., YANO, H., YOKOTA, Y., YOSHIHARA, K., YOSHIKAWA, M., YOSHIKAWA, K., FUJIMOTO, M., WATANABE, S.-i. & TSUDA, Y. (2022a). *Proceedings of the Japan Academy, Series B* **98**, 227 (page [96](#)).

Nakamura, T., Matsumoto, M., Amano, K., Enokido, Y., Zolensky, M. E.,  
Mikouchi, T., Genda, H., Tanaka, S., Zolotov, M. Y., Kurosawa, K., Wakita, S.,  
Hyodo, R., Nagano, H., Nakashima, D., Takahashi, Y., Fujioka, Y., Kikuiri, M.,  
Kagawa, E., Matsuoka, M., Brearley, A. J., Tsuchiyama, A., Uesugi, M.,  
Matsuno, J., Kimura, Y., Sato, M., Milliken, R. E., Tatsumi, E., Sugita, S.,  
Hiroi, T., Kitazato, K., Brownlee, D., Joswiak, D. J., Takahashi, M.,  
Ninomiya, K., Takahashi, T., Osawa, T., Terada, K., Brenker, F. E.,  
Tkalcec, B. J., Vincze, L., Brunetto, R., Aléon-Toppani, A., Chan, Q. H. S.,  
Roskosz, M., Viennet, J. .-.C., Beck, P., Alp, E. E., Michikami, T., Nagaashi, Y.,  
Tsuji, T., Ino, Y., Martinez, J., Han, J., Dolocan, A., Bodnar, R. J., Tanaka, M.,  
Yoshida, H., Sugiyama, K., King, A. J., Fukushi, K., Suga, H., Yamashita, S.,  
Kawai, T., Inoue, K., Nakato, A., Noguchi, T., Vilas, F., Hendrix, A. R.,  
Jaramillo-Correa, C., Domingue, D. L., Dominguez, G., Gainsforth, Z.,  
Engrand, C., Duprat, J., Russell, S. S., Bonato, E., Ma, C., Kawamoto, T.,  
Wada, T., Watanabe, S., Endo, R., Enju, S., Riu, L., Rubino, S., Tack, P.,  
Takeshita, S., Takeichi, Y., Takeuchi, A., Takigawa, A., Takir, D., Tanigaki, T.,  
Taniguchi, A., Tsukamoto, K., Yagi, T., Yamada, S., Yamamoto, K.,  
Yamashita, Y., Yasutake, M., Uesugi, K., Umegaki, I., Chiu, I., Ishizaki, T.,  
Okumura, S., Palomba, E., Pilorget, C., Potin, S. M., Alasli, A., Anada, S.,  
Araki, Y., Sakatani, N., Schultz, C., Sekizawa, O., Sitzman, S. D., Sugiura, K.,  
Sun, M., Dartois, E., Pauw, E. D., Dionnet, Z., Djouadi, Z., Falkenberg, G.,  
Fujita, R., Fukuma, T., Gearba, I. R., Hagiya, K., Hu, M. Y., Kato, T.,  
Kawamura, T., Kimura, M., Kubo, M. K., Langenhorst, F., Lantz, C., Lavina, B.,  
Lindner, M., Zhao, J., Vekemans, B., Baklouti, D., Bazi, B., Borondics, F.,  
Nagasawa, S., Nishiyama, G., Nitta, K., Mathurin, J., Matsumoto, T.,  
Mitsukawa, I., Miura, H., Miyake, A., Miyake, Y., Yurimoto, H., Okazaki, R.,  
Yabuta, H., Naraoka, H., Sakamoto, K., Tachibana, S., Connolly, H. C.,  
Lauretta, D. S., Yoshitake, M., Yoshikawa, M., Yoshikawa, K., Yoshihara, K.,  
Yokota, Y., Yogata, K., Yano, H., Yamamoto, Y., Yamamoto, D., Yamada, M.,  
Yamada, T., Yada, T., Wada, K., Usui, T., Tsukizaki, R., Terui, F., Takeuchi, H.,  
Takei, Y., Iwamae, A., Soejima, H., Shirai, K., Shimaki, Y., Senshu, H.,  
Sawada, H., Saiki, T., Ozaki, M., Ono, G., Okada, T., Ogawa, N., Ogawa, K.,  
Noguchi, R., Noda, H., Nishimura, M., Namiki, N., Nakazawa, S., Morota, T.,  
Miyazaki, A., Miura, A., Mimasu, Y., Matsumoto, K., Kumagai, K.,  
Kouyama, T., Kikuchi, S., Kawahara, K., Kameda, S., Iwata, T., Ishihara, Y.,  
Ishiguro, M., Ikeda, H., Hosoda, S., Honda, R., Honda, C., Hitomi, Y.,  
Hirata, N., Hirata, N., Hayashi, T., Hayakawa, M., Hatakeyama, K., Furuya, S.,  
Fukai, R., Fujii, A., Cho, Y., Arakawa, M., Abe, M., Watanabe, S. & Tsuda, Y.  
(2022b). *Science*, eabn8671 (page 96).

Namouni, F. & Morais, M. H. M. (2021). *Monthly Notices of the Royal Astronomical Society* **510**, 276 (page [80](#)).

Napier, K. J., Gerdes, D. W., Lin, H. W., Hamilton, S. J., Bernstein, G. M., Bernardinelli, P. H., Abbott, T. M. C., Aguena, M., Annis, J., Avila, S., Bacon, D., Bertin, E., Brooks, D., Burke, D. L., Rosell, A. C., Kind, M. C., Carretero, J., Costanzi, M., Costa, L. N. d., Vicente, J. D., Diehl, H. T., Doel, P., Everett, S., Ferrero, I., Fosalba, P., García-Bellido, J., Gruen, D., Gruendl, R. A., Gutierrez, G., Hollowood, D. L., Honscheid, K., Hoyle, B., James, D. J., Kent, S., Kuehn, K., Kuropatkin, N., Maia, M. A. G., Menanteau, F., Miquel, R., Morgan, R., Palmese, A., Paz-Chinchón, F., Plazas, A. A., Sanchez, E., Scarpine, V., Serrano, S., Sevilla-Noarbe, I., Smith, M., Suchyta, E., Swanson, M. E. C., To, C., Walker, A. R. & Wilkinson, R. D. (2021). *The Planetary Science Journal* **2**, 59 (pages [107](#), [114](#), [131](#), [201](#)).

Nesvorný, D., Thomas, F., Ferraz-Mello, S. & Morbidelli, A. (2002). *Celestial Mechanics and Dynamical Astronomy* **82**, 323 (page [202](#)).

Nesvorný, D. (2011). *The Astrophysical Journal Letters* **742**, L22 (pages [102](#), [155](#), [169](#)).

- (2015a). *The Astronomical Journal* **150**, 73 (pages [100](#), [171](#), [172](#), [191](#)).
- (2015b). *The Astronomical Journal* **150**, 68 (page [102](#)).
- (2018). *Annual Review of Astronomy and Astrophysics* **56**, 137 (pages [20](#), [52](#), [94](#), [99](#), [101](#), [131](#), [168](#), [171](#), [172](#), [181](#), [198](#)).
- (2021). *The Astrophysical Journal Letters* **908**, L47 (pages [100](#), [102](#), [171](#), [172](#), [179](#), [189](#)).

Nesvorný, D. & Morbidelli, A. (2012). *The Astronomical Journal* **144**, 117 (pages [102](#), [155](#), [169](#), [172](#)).

Nesvorný, D. & Vokrouhlický, D. (2016). *The Astrophysical Journal* **825**, 94 (pages [100](#), [128](#), [172](#), [191](#)).

Nesvorný, D., Vokrouhlický, D., Andersen, M., Bannister, M. T., Buchanan, L. E., Chen, Y.-T., Gladman, B. J., Gwyn, S. D. J., Kavelaars, J. J., Petit, J.-M., Schwamb, M. E. & Volk, K. (2020). *The Astronomical Journal* **160**, 46 (page [102](#)).

- Nesvorný, D., Vokrouhlický, D. & Morbidelli, A. (2007). *The Astronomical Journal* **133**, 1962 (page 101).
- (2013). *The Astrophysical Journal* **768**, 45 (page 189).
- Nesvorný, D., Vokrouhlický, D. & Roig, F. (2016). *The Astrophysical Journal* **827**, L35 (pages 100, 111, 112, 114, 117, 120, 131, 132, 171, 172, 174, 182, 186, 187, 189, 190).
- Nesvorný, D., Youdin, A. N. & Richardson, D. C. (2010). *The Astronomical Journal* **140**, 785 (page 91).
- Noll, K. S., Grundy, W. M., Nesvorný, D. & Thirouin, A. (2020). *Trans-Neptunian binaries (2018)*. The Trans-Neptunian Solar System (pages 35, 91).
- Noll, K. S., Grundy, W. M., Stephens, D. C., Levison, H. F. & Kern, S. D. (2008). *Icarus* **194**, 758 (page 91).
- Nordlander, T., Rickman, H. & Gustafsson, B. (2017). *Astronomy & Astrophysics* **603**, A112 (page 129).
- O'Brien, D. P., Morbidelli, A. & Levison, H. F. (2006). *Icarus* **184**, 39 (pages 93, 95).
- O'Brien, D. P., Walsh, K. J., Morbidelli, A., Raymond, S. N. & Mandell, A. M. (2014). *Icarus* **239**, 74 (page 96).
- Oort, J. H. (1950). *Bulletin of the Astronomical Institutes of the Netherlands* **11**, 91 (page 30).
- Paquet, M., Moynier, F., Yokoyama, T., Dai, W., Hu, Y., Abe, Y., Aléon, J., Alexander, C. M. O., Amari, S., Amelin, Y., Bajo, K.-i., Bizzarro, M., Bouvier, A., Carlson, R. W., Chaussidon, M., Choi, B.-G., Dauphas, N., Davis, A. M., Rocco, T. D., Fujiya, W., Fukai, R., Gautam, I., Haba, M. K., Hibiya, Y., Hidaka, H., Homma, H., Hoppe, P., Huss, G. R., Ichida, K., Iizuka, T., Ireland, T. R., Ishikawa, A., Ito, M., Itoh, S., Kawasaki, N., Kita, N. T., Kitajima, K., Kleine, T., Komatani, S., Krot, A. N., Liu, M.-C., Masuda, Y., McKeegan, K. D., Morita, M., Motomura, K., Nakai, I., Nagashima, K., Nesvorný, D., Nguyen, A. N., Nittler, L., Onose, M., Pack, A., Park, C., Piani, L., Qin, L., Russell, S. S., Sakamoto, N., Schönbaechler, M., Tafla, L., Tang, H., Terada, K., Terada, Y., Usui, T., Wada, S., Wadhwa, M., Walker, R. J., Yamashita, K., Yin, Q.-Z., Yoneda, S., Young, E. D., Yui, H., Zhang, A.-C., Nakamura, T., Naraoka, H., Noguchi, T., Okazaki, R., Sakamoto, K., Yabuta, H., Abe, M., Miyazaki, A., Nakato, A., Nishimura, M.,

- Okada, T., Yada, T., Yogata, K., Nakazawa, S., Saiki, T., Tanaka, S., Terui, F., Tsuda, Y., Watanabe, S.-i., Yoshikawa, M., Tachibana, S. & Yurimoto, H. (2022). *Nature Astronomy*, 1 (page 96).
- Peixinho, N., Lacerda, P. & Jewitt, D. (2008). *The Astronomical Journal* 136, 1837 (page 36).
- Petit, J. M., Kavelaars, J. J., Gladman, B. J., Jones, R. L., Parker, J. W., Laerhoven, C. V., Nicholson, P., Mars, G., Rousselot, P., Mousis, O., Marsden, B., Bieryla, A., Taylor, M., Ashby, M. L. N., Benavidez, P., Bagatin, A. C. & Bernabeu, G. (2011). *The Astronomical Journal* 142, 131 (pages vii, 35, 36, 58, 86, 100, 102, 111, 116, 118, 190, 191).
- Petit, J.-M., Morbidelli, A. & Valsecchi, G. B. (1999). *Icarus* 141, 367 (pages 109, 153, 164).
- Pfalzner, S. (2013). *Astronomy & Astrophysics* 549, A82 (pages 105, 129, 131).
- Pike, R. E., Kavelaars, J. J., Petit, J. M., Gladman, B. J., Alexandersen, M., Volk, K. & Shankman, C. J. (2015). *The Astronomical Journal* 149, 202 (page 116).
- Pike, R. E. & Lawler, S. M. (2017). *The Astronomical Journal* 154, 171 (pages 101, 117).
- Pike, R. E., Lawler, S., Brasser, R., Shankman, C. J., Alexandersen, M. & Kavelaars, J. J. (2017a). *The Astronomical Journal* 153, 127 (page 101).
- Pike, R. E., Fraser, W. C., Schwamb, M. E., Kavelaars, J. J., Marsset, M., Bannister, M. T., Lehner, M. J., Wang, S.-Y., Alexandersen, M., Chen, Y.-T., Gladman, B. J., Gwyn, S., Petit, J.-M. & Volk, K. (2017b). *The Astronomical Journal* 154, 101 (page 36).
- Pitjeva, E. V. & Pitjev, N. P. (2018). *Astronomy Letters* 44, 554 (page 24).
- Pollack, J. B., Hubickyj, O., Bodenheimer, P., Lissauer, J. J., Podolak, M. & Greenzweig, Y. (1996). *Icarus* 124, 62 (page 94).
- Portegies-Zwart, S. F. (2009). *The Astrophysical Journal* 696, L13 (page 129).
- Portegies-Zwart, S., Torres, S., Cai, M. X. & Brown, A. G. A. (2021). *Astronomy & Astrophysics* 652, A144 (pages 30, 105, 129).
- Rasio, F. A. & Ford, E. B. (1996). *Science* 274, 954 (page 109).

- Raymond, S. N., Kokubo, E., Morbidelli, A., Morishima, R. & Walsh, K. J. (2014). *Protostars and Planets VI*, 595 (page 96).
- Raymond, S. N. & Morbidelli, A. (2022). *Astrophysics and Space Science Library*, 3 (page 109).
- Raymond, S. N., Quinn, T. & Lunine, J. I. (2006). *Icarus* 183, 265 (page 95).
- Rein, H. & Liu, S.-F. (2012). *Astronomy & Astrophysics* 537, A128 (pages ix, 17, 39, 130, 155).
- Rein, H., Brown, G. & Tamayo, D. (2019a). *Monthly Notices of the Royal Astronomical Society* 490, 5122 (page 18).
- Rein, H., Hernandez, D. M., Tamayo, D., Brown, G., Eckels, E., Holmes, E., Lau, M., Leblanc, R. & Silburt, A. (2019b). *Monthly Notices of the Royal Astronomical Society* 485, 5490 (pages 18, 155).
- Rein, H. & Spiegel, D. S. (2014). *Monthly Notices of the Royal Astronomical Society* 446, 1424 (pages 17, 39).
- Rein, H. & Tamayo, D. (2015). *Monthly Notices of the Royal Astronomical Society* 452, 376 (pages 17, 39).
- Safronov, V. S. (1972). *Evolution of the protoplanetary cloud and formation of the earth and planets*. Jerusalem (Isreal): Israel Program for Scientific Translations (pages 76, 94).
- Sarid, G., Volk, K., Steckloff, J. K., Harris, W., Womack, M. & Woodney, L. M. (2019). *The Astrophysical Journal Letters* 883, L25 (page 25).
- Schwamb, M. E., Fraser, W. C., Bannister, M. T., Marsset, M., Pike, R. E., Kavelaars, J. J., Benecchi, S. D., Lehner, M. J., Wang, S.-Y., Thirouin, A., Delsanti, A., Peixinho, N., Volk, K., Alexandersen, M., Chen, Y.-T., Gladman, B., Gwyn, S. D. J. & Petit, J.-M. (2019). *The Astrophysical Journal Supplement Series* 243, 12 (page 36).
- Shankman, C., Kavelaars, J. J., Bannister, M. T., Gladman, B. J., Lawler, S. M., Chen, Y.-T., Jakubik, M., Kaib, N., Alexandersen, M., Gwyn, S. D. J., Petit, J.-M. & Volk, K. (2017). *The Astronomical Journal* 154, 50 (pages 107, 114, 131, 201).
- Sheppard, S. S. & Trujillo, C. (2016). *The Astronomical Journal* 152, 221 (pages 107, 131, 201).

- Sheppard, S. S., Trujillo, C. A., Tholen, D. J. & Kaib, N. (2019). *The Astronomical Journal* 157, 139 (pages 103, 137, 148, 150).
- Silsbee, K. & Tremaine, S. (2018). *The Astronomical Journal* 155, 75 (pages 117, 155).
- Simon, J. B., Armitage, P. J., Li, R. & Youdin, A. N. (2016). *The Astrophysical Journal* 822, 55 (page 91).
- Smullen, R. A. & Volk, K. (2020). *Monthly Notices of the Royal Astronomical Society* 497, 1391 (page 39).
- Steffl, A., Cunningham, N., Shinn, A., Durda, D. & Stern, S. (2013). *Icarus* 223, 48 (page 32).
- Stern, S. A., Weaver, H. A., Spencer, J. R., Olkin, C. B., Gladstone, G. R., Grundy, W. M., Moore, J. M., Cruikshank, D. P., Elliott, H. A., McKinnon, W. B., Parker, J. W., Verbiscer, A. J., Young, L. A., Aguilar, D. A., Albers, J. M., Andert, T., Andrews, J. P., Bagenal, F., Banks, M. E., Bauer, B. A., Bauman, J. A., Bechtold, K. E., Beddingfield, C. B., Behrooz, N., Beisser, K. B., Benecchi, S. D., Bernardoni, E., Beyer, R. A., Bhaskaran, S., Bierson, C. J., Binzel, R. P., Birath, E. M., Bird, M. K., Boone, D. R., Bowman, A. F., Bray, V. J., Britt, D. T., Brown, L. E., Buckley, M. R., Buie, M. W., Buratti, B. J., Burke, L. M., Bushman, S. S., Carcich, B., Chaikin, A. L., Chavez, C. L., Cheng, A. F., Colwell, E. J., Conard, S. J., Conner, M. P., Conrad, C. A., Cook, J. C., Cooper, S. B., Custodio, O. S., Ore, C. M. D., Deboy, C. C., Dharmavaram, P., Dhingra, R. D., Dunn, G. F., Earle, A. M., Egan, A. F., Eisig, J., El-Maarry, M. R., Engelbrecht, C., Enke, B. L., Ercol, C. J., Fattig, E. D., Ferrell, C. L., Finley, T. J., Firer, J., Fischetti, J., Folkner, W. M., Fosbury, M. N., Fountain, G. H., Freeze, J. M., Gabasova, L., Glaze, L. S., Green, J. L., Griffith, G. A., Guo, Y., Hahn, M., Hals, D. W., Hamilton, D. P., Hamilton, S. A., Hanley, J. J., Harch, A., Harmon, K. A., Hart, H. M., Hayes, J., Hersman, C. B., Hill, M. E., Hill, T. A., Hofgartner, J. D., Holdridge, M. E., Horányi, M., Hosadurga, A., Howard, A. D., Howett, C. J. A., Jaskulek, S. E., Jennings, D. E., Jensen, J. R., Jones, M. R., Kang, H. K., Katz, D. J., Kaufmann, D. E., Kavelaars, J. J., Keane, J. T., Keleher, G. P., Kinczyk, M., Kochte, M. C., Kollmann, P., Krimigis, S. M., Kruizinga, G. L., Kusnierzewicz, D. Y., Lahr, M. S., Lauer, T. R., Lawrence, G. B., Lee, J. E., Lessac-Chenen, E. J., Linscott, I. R., Lisse, C. M., Lunsford, A. W., Mages, D. M., Mallder, V. A., Martin, N. P., May, B. H., McComas, D. J., McNuttJr., R. L., Mehoke, D. S., Mehoke, T. S., Nelson, D. S., Nguyen, H. D.,

Núñez, J. I., Ocampo, A. C., Owen, W. M., Oxton, G. K., Parker, A. H., Pätzold, M., Pelgrift, J. Y., Pelletier, F. J., Pineau, J. P., Piquette, M. R., Porter, S. B., Protopapa, S., Quirico, E., Redfern, J. A., Regiec, A. L., Reitsema, H. J., Reuter, D. C., Richardson, D. C., Riedel, J. E., Ritterbush, M. A., Robbins, S. J., Rodgers, D. J., Rogers, G. D., Rose, D. M., Rosendall, P. E., Runyon, K. D., Ryschkewitsch, M. G., Saina, M. M., Salinas, M. J., Schenk, P. M., Scherrer, J. R., Schlei, W. R., Schmitt, B., Schultz, D. J., Schurr, D. C., Scipioni, F., Sepan, R. L., Shelton, R. G., Showalter, M. R., Simon, M., Singer, K. N., Stahlheber, E. W., Stanbridge, D. R., Stansberry, J. A., Steffl, A. J., Strobel, D. F., Stothoff, M. M., Stryk, T., Stuart, J. R., Summers, M. E., Tapley, M. B., Taylor, A., Taylor, H. W., Tedford, R. M., Throop, H. B., Turner, L. S., Umurhan, O. M., Eck, J. V., Velez, D., Versteeg, M. H., Vincent, M. A., Webbert, R. W., Weidner, S. E., WeigleII, G. E., Wendel, J. R., White, O. L., Whittenburg, K. E., Williams, B. G., Williams, K. E., Williams, S. P., Winters, H. L., Zangari, A. M. & Zurbuchen, T. H. (2019). *Science* **364**, eaaw9771 (page [38](#)).

Stern, S. A. (1996). *The Astronomical Journal* **112**, 1203 (page [106](#)).

Stern, S. (1991). *Icarus* **90**, 271 (pages [108](#), [117](#)).

Stoer, J. & Bulirsch, R. (1980). *Introduction to Numerical Analysis*. New York: Springer (pages [16](#), [17](#)).

Szebehely, V. & Jefferys, W. H. (1968). *American Journal of Physics* **36**, 375 (page [10](#)).

Tabachnik, S. A. & Evans, N. W. (2000). *Monthly Notices of the Royal Astronomical Society* **319**, 63 (page [31](#)).

Taki, T., Fujimoto, M. & Ida, S. (2016). *Astronomy & Astrophysics* **591**, A86 (page [94](#)).

Tamayo, D., Rein, H., Shi, P. & Hernandez, D. M. (2019). *Monthly Notices of the Royal Astronomical Society* **491**, 2885 (pages [ix](#), [172](#)).

Thommes, E. W., Duncan, M. J. & Levison, H. F. (1999). *Nature* **402**, 635 (pages [102](#), [169](#)).

Tombaugh, C. W. (1946). *Leaflet of the Astronomical Society of the Pacific* **5**, 73 (page [23](#)).

- Touma, J. R., Tremaine, S. & Kazandjian, M. V. (2009). *Monthly Notices of the Royal Astronomical Society* **394**, 1085 (page 136).
- Trujillo, C. A. & Brown, M. E. (2002). *The Astrophysical Journal* **566**, L125 (page 36).
- Trujillo, C. A., Jewitt, D. C. & Luu, J. X. (2000). *The Astrophysical Journal* **529**, L103 (pages 28, 116).
- Trujillo, C. A. & Sheppard, S. S. (2014). *Nature* **507**, 471 (pages 103, 107, 112, 195, 197, 200, 204).
- Trujillo, C., Trilling, D., Chandler, C., Fuentes, C., Gerdes, D., Strauss, R., Lin, H.-W., Markwardt, L., Napier, K., Oldroyd, W., Sheppard, S., Adams, F., Bernardinelli, P., Holman, M., Juric, M., McNeill, A., Mommert, M., Payne, M., Ragozzine, D., Rivkin, A., Schlichting, H., Simpson, A. & Smotherman, H. (2022). AAS/Division for Planetary Sciences Meeting Abstracts **54**, 501.01 (pages 205, 208).
- Tsiganis, K., Gomes, R., Morbidelli, A. & Levison, H. F. (2005). *Nature* **435**, 459 (pages 101, 168, 169).
- Van-Laerhoven, C., Gladman, B., Volk, K., Kavelaars, J. J., Petit, J.-M., Bannister, M. T., Alexandersen, M., Chen, Y.-T. & Gwyn, S. D. J. (2019). *The Astronomical Journal* **158**, 49 (pages 36, 50, 53, 96, 105, 108).
- Le-Verrier, U. (1846a). *Astronomische Nachrichten* **25**, 85 (pages 23, 105).
- (1846b). *Astronomische Nachrichten* **25**, 65 (pages 23, 105).
- Vinogradova, T. A. & Chernetenko, Y. A. (2015). *Solar System Research* **49**, 391 (page 25).
- Vokrouhlický, D., Farinella, P. & Bottke, W. F. (2000). *Icarus* **148**, 147 (page 32).
- Volk, K. & Malhotra, R. (2008). *The Astrophysical Journal* **687**, 714 (page 28).
- (2017). *The Astronomical Journal* **154**, 62 (pages 52, 108).
- (2022). *The Astrophysical Journal* **937**, 119 (pages 11, 194).
- Volk, K., Murray-Clay, R. A., Gladman, B. J., Lawler, S. M., Yu, T. Y. M., Alexandersen, M., Bannister, M. T., Chen, Y. T., Dawson, R. I., Greenstreet, S.,

- Gwyn, S. D. J., Kavelaars, J. J., Lin, H. W., Lykawka, P. S. & Petit, J.-M. (2018). *The Astronomical Journal* 155, 260 (pages 112, 116, 190).
- Volk, K., Murray-Clay, R., Gladman, B., Lawler, S., Bannister, M. T., Kavelaars, J. J., Petit, J.-M., Gwyn, S., Alexandersen, M., Chen, Y. T., Lykawka, P. S., Ip, W. & Lin, H. W. (2016). *The Astronomical Journal* 152, 23 (page 191).
- Wahhaj, Z., Koerner, D. W., Ressler, M. E., Werner, M. W., Backman, D. E. & Sargent, A. I. (2003). *The Astrophysical Journal Letters* 584, L27 (page 208).
- Walsh, K. J. & Morbidelli, A. (2011). *Astronomy & Astrophysics* 526, A126 (page 101).
- Walsh, K. J., Morbidelli, A., Raymond, S. N., O'Brien, D. P. & Mandell, A. M. (2011). *Nature*, 1 (page 96).
- Weidenschilling, S. J. (1977). *Astrophysics and Space Science* 51, 153 (pages 91, 95).
- Weidenschilling, S. J. (1978). *Icarus* 35, 99 (page 32).
- Weidenschilling, S. J. & Marzari, F. (1996). *Nature* 384, 619 (page 109).
- Weissman, P. R. (1990). *Nature* 344, 825 (page 30).
- Wetherill, G. W. (1975). “Late heavy bombardment of the moon and terrestrial planets”. Vol. 2. Lunar Science Conference. New York: Pergamon Press, Inc., p. 1539 (page 97).
- (1986). “Accumulation of the terrestrial planets and implications concerning lunar origin”. *Origin of the Moon*, p. 519 (page 95).
- Wetherill, G. & Stewart, G. R. (1989). *Icarus* 77, 330 (page 93).
- Wiegert, P., Connors, M. & Veillet, C. (2017). *Nature* 543, 687 (page 86).
- Williams, J. G. (1969). “Secular Perturbations in the Solar System”. PhD thesis. University of California, Los Angeles (page 44).
- Wisdom, J. (2016). *Monthly Notices of the Royal Astronomical Society* 464, 2350 (page 18).
- Wisdom, J. & Holman, M. (1991). *The Astronomical Journal* 102, 1528 (pages 17, 162).
- Yabushita, S. (1980). *Astronomy & Astrophysics* (pages vii, 59–61, 79, 118).

Yada, T., Abe, M., Okada, T., Nakato, A., Yogata, K., Miyazaki, A., Hatakeyama, K., Kumagai, K., Nishimura, M., Hitomi, Y., Soejima, H., Yoshitake, M., Iwamae, A., Furuya, S., Uesugi, M., Karouji, Y., Usui, T., Hayashi, T., Yamamoto, D., Fukai, R., Sugita, S., Cho, Y., Yumoto, K., Yabe, Y., Bibring, J.-P., Pilorget, C., Hamm, V., Brunetto, R., Riu, L., Lourit, L., Loizeau, D., Lequertier, G., Moussi-Soffys, A., Tachibana, S., Sawada, H., Okazaki, R., Takano, Y., Sakamoto, K., Miura, Y. N., Yano, H., Ireland, T. R., Yamada, T., Fujimoto, M., Kitazato, K., Namiki, N., Arakawa, M., Hirata, N., Yurimoto, H., Nakamura, T., Noguchi, T., Yabuta, H., Naraoka, H., Ito, M., Nakamura, E., Uesugi, K., Kobayashi, K., Michikami, T., Kikuchi, H., Hirata, N., Ishihara, Y., Matsumoto, K., Noda, H., Noguchi, R., Shimaki, Y., Shirai, K., Ogawa, K., Wada, K., Senshu, H., Yamamoto, Y., Morota, T., Honda, R., Honda, C., Yokota, Y., Matsuoka, M., Sakatani, N., Tatsumi, E., Miura, A., Yamada, M., Fujii, A., Hirose, C., Hosoda, S., Ikeda, H., Iwata, T., Kikuchi, S., Mimasu, Y., Mori, O., Ogawa, N., Ono, G., Shimada, T., Soldini, S., Takahashi, T., Takei, Y., Takeuchi, H., Tsukizaki, R., Yoshikawa, K., Terui, F., Nakazawa, S., Tanaka, S., Saiki, T., Yoshikawa, M., Watanabe, S.-i. & Tsuda, Y. (2022). *Nature Astronomy* **6**, 214 (page [96](#)).

Ye, Q., Masci, F. J., Ip, W. H., Prince, T. A., Helou, G., Farnocchia, D., Bellm, E. C., Dekany, R., Graham, M. J., Kulkarni, S. R., Kupfer, T., Mahabal, A., Ngeow, C.-C., Reiley, D. J. & Soumagnac, M. T. (2020). *The Astronomical Journal* **159**, 70 (page [32](#)).

Youdin, A. N. & Shu, F. H. (2002). *The Astrophysical Journal* **580**, 494 (page [90](#)).

Yu, T. Y. M., Murray-Clay, R. & Volk, K. (2018). *The Astronomical Journal* **156**, 33 (pages [112](#), [117](#)).

Zhang, K. & Gladman, B. J. (2022). *New Astronomy* **90**, 101659 (pages [vi](#), [16](#), [18](#), [31](#), [81](#), [118](#)).

Zhou, L., Xu, Y.-B., Zhou, L.-Y., Dvorak, R. & Li, J. (2019). *Astronomy & Astrophysics* **622**, A97 (page [32](#)).

## Appendix A

# GLISSER Validation of Performance

### A.1 Validation of the GLISSER Integrator

Precise validation of numerical celestial mechanics codes is difficult because exact solutions to the problem exist only as special cases. Usually, there are some conserved integrals (e.g. energy) in the system, and test particles could have wildly-wrong orbits if the total system energy is negligibly perturbed. To validate simulations resulted from the GLISSER integrator, I first verified the conservation of the Jacobi constant  $C_J$  in a CRTBP system (Section 1.1.3) by carrying out a 1000-yr integration with a circular Earth at  $a = 1$  au and a test particle initialized on a crossing orbit with  $a_0 = 1.1$  au,  $e_0 = 0.12$ , and  $i_0 = 3^\circ$ ; this gives the particle the Jacobi constant of  $C_J \approx 2.99$ . This simulation has the time step of 10 days ( $P_{\text{orb}}/\Delta t \approx 0.027$ ) and the time block size of 100 time steps. The time evolutions of its  $a$  and  $q$ , and the fractional changes of both the Jacobi constant and the Tisserand parameter are plotted in Figure A.1.

As shown in Figure A.1, the Jacobi constant (and the Tisserand parameter) is conserved to the order of  $<5 \times 10^{-6}$  for the majority of the integration (middle panel). Relative-large variations in energy ( $\sim 1 \times 10^{-4}$ ) only occur when the particle is having encounters with the planet (bottom panel). I also halved the time step to 5 days and re-run the same initial condition and confirm that the Jacobi constant will be conserved to  $\sim 2 \times 10^{-6}$  (if ignoring those spikes), nearly a factor of 4 smaller than the previous simulation with a doubled time step. This is consist with the  $\mathcal{O}(\Delta t^2)$

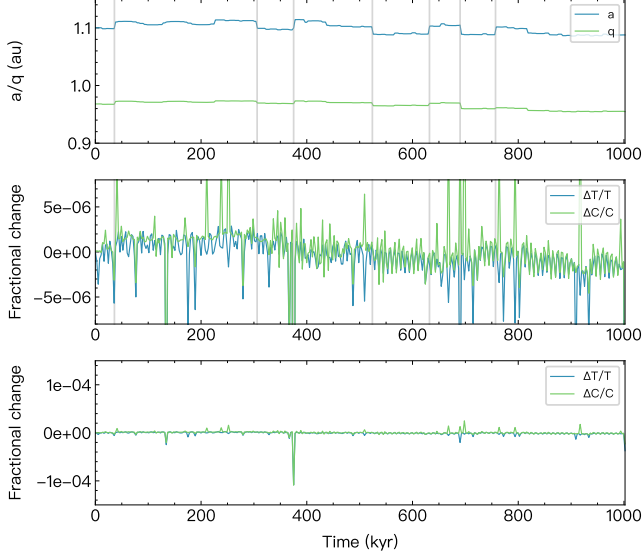


**Figure A.1:** A GLISSER simulation with an Earth-scattered particle showing the conservation of the Jacobi constant and the Tisserand parameter for 1000 yr. The top panel shows the time histories of  $a$  and  $q$ , the middle panel shows the fractional changes of  $\mathcal{C}_J$  and  $\mathcal{T}$ , and the bottom panel is a re-plot of the middle panel but with a larger range. Dark lines mark  $> 3$  Hill-sphere encounters recorded by the integrator.

numerical error of a second-order integrator.

Furthermore, I carried out another simulation with a Neptune-scattered particle (with  $a_0 = 31.4$  au,  $e_0 = 0.4$ , and  $i_0 = 1^\circ$  giving  $\mathcal{T} \approx 2.75$ ) to show the conservation of the Tisserand parameter for 500 Myr (Figure A.2). This simulation has the time step of 200 days ( $P_{\text{orb}}/\Delta t \approx 0.003$ ) and the time block size of 250 time steps. Figure A.2 demonstrates the Tisserand parameter is conserved to the order of  $< 1 \times 10^{-4}$  in this long-term GLISSER simulation. Considering the integrator intrinsically interpolates planetary locations (the planetary history file is stored in single-precision float numbers with the precision of  $\sim 1 \times 10^{-6}$ ) to speed up the close encounter algorithm, this level of conservation is within expectation.

I also directly compared the orbital evolutions of resonant particles integrated by SWIFT (Levison & Duncan, 1994) and GLISSER, shown in Figures A.3 and A.4. Note that this is a rather challenging test as GLISSER interpolates planetary orbits

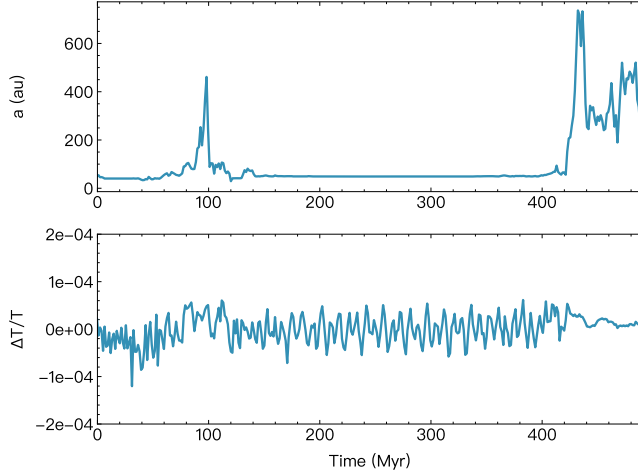


**Figure A.2:** A GLISSER simulation with an Neptune-scattered particle showing the conservation of the Tisserand parameter for 100 kyr.

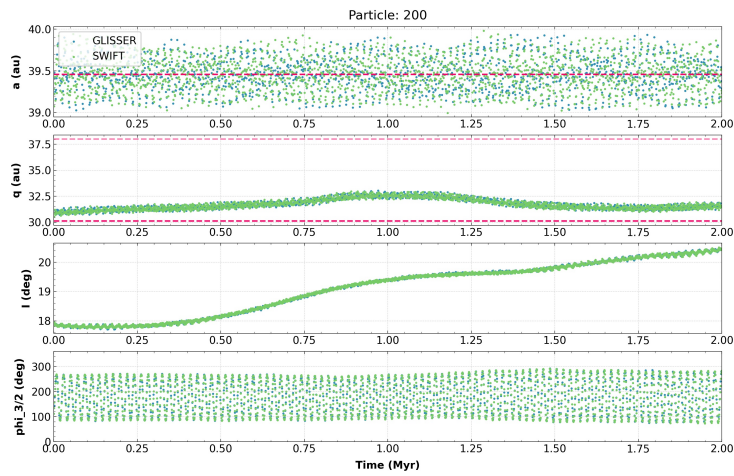


**Figure A.3:** Comparison between GLISSER and SWIFT simulations for a 3:2 resonant TNO with Neptune. The four panels show time histories of  $a$ ,  $q$ ,  $i$ , and the resonant angle, from top to bottom.

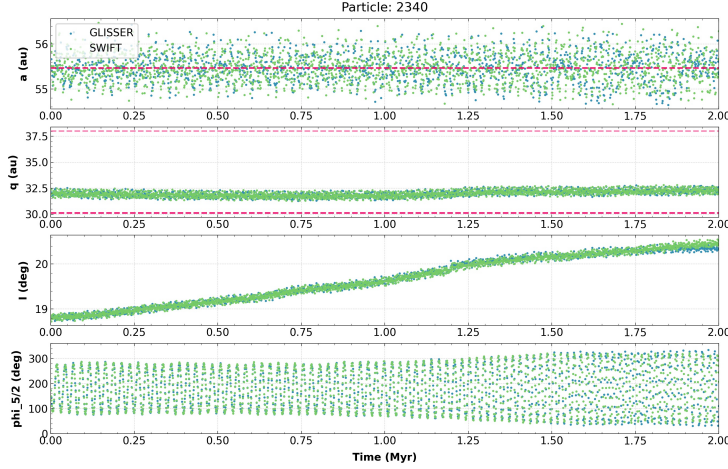


**Figure A.4:** Same as Figure A.3 but for the 5:2 resonance.

between time chunks. However, these two examples demonstrate that GLISSER is a reliable integrator that produces very similar evolutional histories produced by SWIFT, a heavily-tested N-body integrator in the industry.

In addition to these two validation, I also compared GLISSER against the MERCURY integrator (Chambers, 1999) by running the  $q$ -raising simulation that demonstrates the rogue’s secular effect. Figure 1.7 shows show very similar orbital distributions produced by the two integrators. Therefore, I conclude GLISSER is a reliable GPU integrator that can correctly resolve close encounters and produce both resonant and secular dynamics.

## A.2 Efficiency Comparison Between GLISSER and Other Integrators

An enormous advantage of GLISSER over other CPU integrators (SWIFT or MERCURY) is that it can handle far more test particles with almost no speed penalty, as long as the particle count is less than the ‘chunk size’ (similar to the number of “threads”) that a certain GPU can handle simultaneously; for example, one can integrate 14,000 particles using GLISSER on a K20 GPU in the same amount of time

as 1000. Once the number of particles exceeds the GPU chunk size, the execution time would double, as the GPU has to handle two batches of test particles in serial sequence. Different GPUs have different clock speed and chunk size, which together dominantly determine the overall efficiency of a GPU card in this application.

A merit comparison between MERCURY and GLISSER is shown in Table A.1, where the K20 is about ten years old, the V100 is released in 2017, and the RTX 3070 is a gaming GPU (not optimal for scientific calculation) released in 2020. When the particle number is small, GLISSER is about an order of magnitude faster than MERCURY. But that's not even the full power of GLISSER. Rows 7-11 in Table A.1 show GLISSER loaded with large amount of particles is  $60\text{-}260\times$  faster than MERCURY.

Additionally, GLISSER's efficiency also depends on number of the used CPU cores. When the close encounter frequency is so high that one CPU core is not enough to resolve all encounters in time, GLISSER will automatically split the SWIFT jobs for available CPU cores to speedup the integration. This explains why in Table A.1, V100(s/12) is slightly faster than V100(s/8).

**Table A.1:** Comparison between SWIFT, MERCURY, and GLISSER on different machines

#	Integrator	GPU (CPU cores)	Particles	Integration Time (Myr)	Compute Time (hr)	Merit
1	SWIFT	CPU only (1)	1000	30	27.0	1.1
2	MERCURY	CPU only (1)	1000	100	44.0	2.7
3	GLISSER	K20 (1)	1000	100	4.4	22.7
4	GLISSER	V100 (o/1)	1000	100	3.0	33.3
5	GLISSER	V100 (s/1)	1000	100	2.6	38.5
6	GLISSER	RTX 3070 (1)	1000	1	0.1	9.1
7	GLISSER	K20 (8)	80000	100	21.9	365.3
8	GLISSER	V100 (o/8)	80000	100	12.2	655.7
9	GLISSER	V100 (s/8)	80000	100	11.8	678.0
10	GLISSER	V100 (s/12)	80000	100	11.4	701.8
11	GLISSER	RTX 3070 (6)	80000	1	0.5	170.0

**Note.** The merit (higher is better) is in the unit of kiloparticles  $\times$  Myr / (computation hours). ‘o’ stands for ‘opio’ which is a machine in Brett Gladman’s laboratory, and ‘s’ stands for ‘sockeye’ which is the high-performance computing platform at UBC.

## Appendix B

# Dynamical Effects of Rogue Encounters

In this appendix, I estimate the encounter effect induced by a rogue planet, in the assumption that the dominant effect brought by the planet is through encounters not the secular. This only holds when the rogue's semimajor axis is much larger than the small body's ( $a_r \gg a$ ). The derived equations are used in Chapters 5 and 6.

### B.1 Encounter Frequency from a Highly-Eccentric Planet

To estimate the number of close encounters occurring in the scattering disk during the rogue's presence, I assume a rogue planet of the mass  $m_r$  is orbiting the Sun on an eccentric orbit with the semimajor axis of  $a_r$ , the perihelion of  $q_r$ , and a dynamical life time of  $T_r$ . I also assume a swarm of TNOs with the same  $a$ ,  $e$ , and  $i$ , but various orbital orientations (thus random  $\omega$ ,  $\Omega$ , and  $M$ ), which roughly forms an partial spherical shell of small bodies. When an eccentric planet crosses the shell, its orbital plane basically slices an annulus of TNOs from perihelion  $q = a(1 - e)$  to aphelion  $Q = a(1 + e)$ . If the rogue's perihelion  $q_r$  is inside the annulus inner edge of  $\sim 35$  au (which is often the case for a more realistic rogue coupled with giant planets), for each rogue orbit, it will go through the annulus twice with the typical crossing velocity  $v_{\text{cross}}$  roughly being the rogue's velocity at the annulus' average distance ( $a$ ).

Using the vis-viva equation:

$$v_{\text{cross}} = \sqrt{\mu} \sqrt{\frac{2}{a} - \frac{1}{a_r}}, \quad (\text{B.1})$$

where  $\mu = GM_{\odot}$  is the gravitational parameter. The crossing time  $t_{\text{cross}}$ , which is defined as the time the rogue spends in the annulus per orbit, is roughly

$$t_{\text{cross}} \approx \frac{2(Q - q)}{v_{\text{cross}}} = \frac{4ae}{v_{\text{cross}}}. \quad (\text{B.2})$$

The accumulated crossing time  $T_{\text{cross}}$  throughout the rogue's dynamical lifetime is thus

$$\begin{aligned} \frac{T_{\text{cross}}}{T_r} &= \frac{t_{\text{cross}}}{P_r} \\ &= \frac{4ae}{\sqrt{\mu} \sqrt{\frac{2}{a} - \frac{1}{a_r}}} \times \frac{\sqrt{\mu}}{2\pi a_r^{\frac{3}{2}}} \\ &= \frac{2e}{\pi} \left( \frac{a}{a_r} \right) \left( 2 \frac{a_r}{a} - 1 \right)^{-\frac{1}{2}}. \end{aligned} \quad (\text{B.3})$$

In the assumption that  $a_r \gg a$ , Equation (B.3)'s last term can be expanded around 0, leaving the leading term of  $\sqrt{\frac{a}{a_r}}/\sqrt{2}$ . Thus I have

$$\frac{T_{\text{cross}}}{T_r} \approx \frac{\sqrt{2}e}{\pi} \left( \frac{a}{a_r} \right)^{\frac{3}{2}}, \quad (\text{B.4})$$

which gives the ratio of the total rogue encounter time to its lifetime.

Next, let's estimate the rogue's encounter volume. Since the rogue has an extremely eccentric orbit, its Hill sphere varies significantly along the orbit, which should thus not be calculated using the rogue's semimajor axis. Instead, one knows all the encounters occur in the annulus, thus the average hill radius of the rogue should be set by its average encounter distance, which to the lowest order is approximately the semimajor axis of the small bodies

$$\bar{R}_H \approx a \left( \frac{m_r}{3M_{\odot}} \right)^{\frac{1}{3}}, \quad (\text{B.5})$$

For weak encounters whose proximity is larger than the Hill radius, the ‘effective radius’ is still proportional to  $\left(\frac{m_r}{M_\odot}\right)^{\frac{1}{3}}$ . Thus, without loss of generality, one can use  $\beta\bar{R}_H$  as the ‘encounter domain’. The number of encounters per orbit can be obtained using Equation 3.32

$$\frac{n_{\text{enc}}}{N} \simeq 4 \left( \frac{\beta\bar{R}_H}{a} \right)^2 \simeq \beta^2 \left( \frac{m_r}{M_\odot} \right)^{\frac{2}{3}}. \quad (\text{B.6})$$

The cumulative encounter frequency (i.e. the average number of encounters for each particle) over the rogue’s dynamical lifetime  $T_r$  is thus

$$\begin{aligned} \frac{N_{\text{enc}}}{N} &= \frac{n_{\text{enc}}}{N} \times \frac{T_r}{P_r} \\ &\simeq \beta^2 \left( \frac{T_r}{1 \text{ yr}} \right) \left( \frac{m_r}{M_\odot} \right)^{\frac{2}{3}} \left( \frac{a_r}{1 \text{ au}} \right)^{-\frac{3}{2}}, \\ &\simeq 6 \beta^2 \left( \frac{T_r}{100 \text{ Myr}} \right) \left( \frac{m_r}{2M_\oplus} \right)^{\frac{2}{3}} \left( \frac{a_r}{300 \text{ au}} \right)^{-\frac{3}{2}}. \end{aligned} \quad (\text{B.7})$$

Note that this is independent of ‘ $a$ ’ as long as  $a_r \gg a$

## B.2 Orbital Element Changes Due to Rogue Encounters

To estimate the magnitude of the induced orbital element changes ( $\Delta a$ ,  $\Delta e$ , and  $\Delta i$ ) for a certain rogue flyby, I start by writing down the vis-viva equation for a TNO at the heliocentric distance of  $r$ :

$$v = \sqrt{\mu} \sqrt{\frac{2}{r} - \frac{1}{a}}, \quad (\text{B.8})$$

where  $\mu = GM_\odot$  and  $v$  is the TNO’s heliocentric speed. Before and after a rogue encounter, the distance  $r$  remains almost unchanged, whereas a small change in  $v$ ’s magnitude due to the flyby will result in a change in its orbital elements. Differentiating both sides of Equation (B.8) gives

$$\Delta v = \frac{\mu}{2v} \frac{1}{a^2} \Delta a. \quad (\text{B.9})$$

I demonstrated in Section 3, that in a hyperbolic flyby, the relative velocity ( $\mathbf{v}_\infty$ ) between the TNO's heliocentric velocity vector ( $\mathbf{v}$ ) and the rogue's ( $\mathbf{v}_r$ ) will change its orientation by  $\Delta\theta$  while maintaining the magnitude before and after the encounter. Recall that when the impact parameter  $b$  is large,  $\Delta\theta$  can be approximated as (see also Equation 3.26)

$$\Delta\theta \approx \frac{2\mu_r}{b v_\infty^2}, \quad (\text{B.10})$$

where  $\mu_r = Gm_r$ ,  $m_r$  is the mass of the rogue, and  $b$  is the impact parameter. Considering  $\mathbf{v} = \mathbf{v}_r + \mathbf{v}_\infty$ , their magnitudes are given by (see Figure 3.3):

$$v^2 = v_r^2 + v_\infty^2 + 2v_r v_\infty \cos\theta, \quad (\text{B.11})$$

where  $\theta$  is the angle between  $\mathbf{v}_r$  and  $\mathbf{v}_\infty$ . As illustrated in the hyperbolic flyby model, the planetary encounter can only change  $\mathbf{v}$  by rotating  $\mathbf{v}_\infty$ 's orientation (in other words, alter  $\theta$  in Equation (B.11) with  $v_r$  and  $v_\infty$  unchanged). Therefore, one can differentiate both sides of Equation (B.11)

$$\Delta v = \frac{-v_r v_\infty}{v} \sin\theta \Delta\theta, \quad (\text{B.12})$$

Replace  $\Delta v$  with Equation (B.9) and rearrange the terms, I get the following equation for the fractional change in small body semimajor axis for a specific rogue encounter of  $b$  and  $\theta$ :

$$\frac{\Delta a}{a} = 4 \left( \frac{v_r}{v_\infty} \sin\theta \right) \left( \frac{m_r}{M_\odot} \right) \left( \frac{a}{b} \right). \quad (\text{B.13})$$

One can also write  $b$  as a multiple of the average Hill radius  $\beta \bar{R}_H$  (Equation (B.5))

$$\frac{\Delta a}{a} = 4\sqrt[3]{3} \left( \frac{v_r}{v_\infty} \sin\theta \right) \left( \frac{m_r}{M_\odot} \right)^{\frac{2}{3}} \beta^{-1}. \quad (\text{B.14})$$

To estimate the order of magnitude of the factor  $(\frac{v_r}{v_\infty} \sin\theta)$ , I assume at close encounters,  $v_r \sim \sqrt{2} v$ , which is basically assuming the rogue's trajectory is parabolic and the TNO's velocity is its circular velocity at  $r = a$ . Combining these assumptions, we have

tions with Equation (B.11), I obtain

$$\frac{v_r}{v_\infty} \sin\theta = \frac{\sin\theta}{-\cos\theta - \sqrt{\cos\theta^2 - 1/2}}, \quad (\text{B.15})$$

which is a function that only depends on a single angle  $\theta$  in the range of  $135^\circ < \theta < 180^\circ$ . The averaged value of Equation (B.15) over all available  $\theta$  is  $\simeq 1$ . Therefore, Equation (B.14) can be further simplified to

$$\frac{\Delta a}{a} \simeq 6 \left( \frac{m_r}{M_\odot} \right)^{\frac{2}{3}} \beta^{-1}. \quad (\text{B.16})$$

Having this result, estimating the typical  $\Delta e$  and  $\Delta i$  is more straightforward. Here, I only give rogue estimates under the assumption that the TNO affected by rogue encounters has a near-circular and co-planar orbit (i.e.  $e \approx 0$  and  $i \approx 0^\circ$ ). This is true for objects in the cold classical belt but can also be applied TNOs with small  $e$  and  $i$ .

The order-of-magnitude changes in  $e$  and  $i$  caused by a velocity change  $\Delta v$  are given by (Burns et al., 2022)

$$\Delta e = \Delta i \simeq \frac{\Delta v}{v}, \quad (\text{B.17})$$

Recall Equation (B.9), in which the fractional change in semimajor axis can also be rewritten as  $\Delta a/a = 2\frac{\Delta v}{v}$ , therefore, one simply has

$$\Delta e = \Delta i \simeq 3 \left( \frac{m_r}{M_\odot} \right)^{\frac{2}{3}} \beta^{-1}. \quad (\text{B.18})$$

Equation (B.16) and (B.18) basically state that for a typical rogue planet flyby, the induced fractional change in  $a$  and changes in  $e$  and  $i$  mainly depend on the mass of the planet  $m_r$  and the flyby distance in Hill radii  $\beta$ . One can thus combine these equations with the flyby frequency equation (B.7) to estimate the cumulative impact from an eccentric planet that repeatedly transverses the Kuiper Belt. To do this, I apply the equation from the random walk theory, where the expected distance over a series of random walk encounters is equal to  $\sqrt{N_{\text{enc}}}$  times the average ‘step

size'. Hence, the cumulative

$$\begin{aligned} \frac{|\Delta a|_c}{a} &= \sqrt{\frac{N_{\text{enc}}}{N}} \times \frac{\Delta a}{a}, \\ &\simeq 0.005 \left( \frac{T_r}{100 \text{ Myr}} \right)^{\frac{1}{2}} \left( \frac{m_r}{2M_{\oplus}} \right) \left( \frac{a_r}{300 \text{ au}} \right)^{-\frac{3}{4}}. \end{aligned} \quad (\text{B.19})$$

Similarly, the cumulative changes in  $e$  and  $i$  are given by

$$|\Delta e|_c = |\Delta i|_c \simeq 0.0025 \left( \frac{T_r}{100 \text{ Myr}} \right)^{\frac{1}{2}} \left( \frac{m_r}{2M_{\oplus}} \right) \left( \frac{a_r}{300 \text{ au}} \right)^{-\frac{3}{4}}. \quad (\text{B.20})$$